Quantum information processing and measurement in circuit quantum electrodynamics

Franz Ferdinand Helmer

SIGILL · UNIVERSITAT · LUDOVIC · MAXIM ·

München 2009

Quantum information processing and measurement in circuit quantum electrodynamics

Franz Ferdinand Helmer

Dissertation
an der Physik Fakultät
der Ludwig–Maximilians–Universität
München

vorgelegt von
Franz Ferdinand Helmer
aus München

München, den 18.05.2009

Erstgutachter: Dr. Florian Marquardt
Zweitgutachter: Prof. Dr. Rudolf Gross
Tag der mündlichen Prüfung: 08.07.2009

Contents

Abstract **xi**

1 Introduction **1**
- 1.1 Cavity QED as a tool to understand quantum mechanics . . . 2
- 1.2 Basics of quantum information processing . . . 4
  - 1.2.1 Quantum vs. classical information processing . . . 4
  - 1.2.2 Example algorithms . . . 4
  - 1.2.3 Present-day quantum computation architectures . . . 5
  - 1.2.4 Outlook . . . 7
- 1.3 The Josephson Effect and the Josephson Junction . . . 8
  - 1.3.1 The Josephson Effect . . . 8
  - 1.3.2 The Josephson Junction . . . 8
  - 1.3.3 The RCSJ-model of a Josephson Junction . . . 9
- 1.4 Qubit types . . . 12
  - 1.4.1 Phase qubits . . . 12
  - 1.4.2 Flux qubits . . . 13
  - 1.4.3 Charge qubits . . . 17
    - 1.4.3.1 The Cooper pair box . . . 17
    - 1.4.3.2 The Transmon . . . 19
- 1.5 From cavity QED to circuit QED . . . 23
  - 1.5.1 Derivation of the Jaynes-Cummings Hamiltonian . . . 24
  - 1.5.2 Cavity QED with real atoms . . . 27
  - 1.5.3 Cavity QED with quantum dots and photonic crystals . . . 34
  - 1.5.4 Cavity QED using superconducting circuits . . . 37
    - 1.5.4.1 Superconducting on-chip microwave resonators . . . 37
    - 1.5.4.2 Charge qubits/transmon qubits . . . 39
    - 1.5.4.3 Flux qubits . . . 44
    - 1.5.4.4 Phase qubits . . . 45

2 The Cavity Grid - a scalable architecture for quantum computation **49**
- 2.1 Introduction . . . 51
- 2.2 Basic architecture . . . 52
- 2.3 One-qubit operations . . . 53
- 2.4 Tunability . . . 53
- 2.5 Two-qubit gates . . . 53

2.6 Hardware . . . 56
2.7 Scalable, fault-tolerant architecture . . . 58
2.8 Conclusions . . . 58

3 Optimized gates for the Cavity Grid 61
3.1 Motivation - improving the Cavity Grid . . . 61
3.2 A resonant CPhase gate - master equation simulation . . . 61
  3.2.1 The CPhase protocol . . . 61
  3.2.2 Model . . . 63
  3.2.3 Expectations . . . 63
  3.2.4 Lindblad master equation to include dissipation . . . 64
  3.2.5 Simulation . . . 64
  3.2.6 Results . . . 65
    3.2.6.1 Medium coupling . . . 66
    3.2.6.2 Strong coupling . . . 68
3.3 Optimizing dispersive gates with optimal control theory . . . 69
  3.3.1 A short glance at the principle of optimal control theory . . . 69
  3.3.2 Optimal control theory results for two qubits in the same cavity . . . 71
  3.3.3 Optimal control theory results for three qubits in crossing cavities . . 72
  3.3.4 Analysis in terms of entanglement measures . . . 76

4 Quantum trajectory approach to weak measurement 77
4.1 Ideal and realistic measurement . . . 78
  4.1.1 Ideal measurements . . . 78
  4.1.2 More realistic description of a measurement . . . 78
4.2 Weak measurement . . . 80
4.3 Stochastic master equations . . . 81

5 Measurement-based synthesis of multi-qubit entangled states 91
5.1 Introduction . . . 92
5.2 Model . . . 93
5.3 Necessary conditions for the generation of given target states . . . 94
5.4 Stochastic master equation . . . 96
5.5 Examples of measurement-generated entangled states . . . 97
  5.5.1 Quantitative characterization . . . 97
  5.5.2 Bell states for two qubits - no decoherence . . . 98
  5.5.3 Three qubits - no decoherence . . . 102
    5.5.3.1 Generation of W-states . . . 102
    5.5.3.2 Generation of GHZ-states . . . 102
5.6 Effects of decoherence . . . 105
  5.6.1 Examples - two-qubit Bell-states including dissipation . . . 105
5.7 Effect of imperfections due to parameter spread . . . 107
5.8 Possibilities for experimental realization . . . 110
5.9 Conclusions . . . 110

6 Detection of single itinerant photons and the Quantum Zeno effect 113
6.1 Introduction . . . 114
6.2 Model . . . 115
6.3 Stochastic master equation . . . 116
6.4 Analysis of detection efficiency . . . 117
6.4.1 Numerical results . . . 118
6.4.2 Analytical results . . . 118
6.4.3 Possible realization in superconducting circuit quantum electrodynamics setups . . . 124

7 Conclusions 129

8 Appendix 131
8.1 Derivation of the adiabatically eliminated stochastic master equation . . . 132
8.1.1 Unravelling the master equation . . . 132
8.1.2 Adiabatic elimination of the detector mode . . . 135
8.2 How to efficiently simulate master equations . . . 138
8.2.1 Get a first fast idea about your system . . . 138
8.2.2 Solve a deterministic master equation . . . 140
8.2.3 Introduce decoherence . . . 143
8.2.4 Solve a stochastic master equation . . . 144
8.2.5 Initialization-file handling . . . 147
8.2.6 How to run more complicated gate sequences . . . 148
8.2.7 How to optimize/profile the code . . . 153

Bibliography 155

Acknowledgements 170

Curriculum Vitae 172

List of Figures

1.1 Josephson junction circuit element symbol 8
1.2 Resistively and capacitively shunted Josephson Junction circuit diagram . . . 9
1.3 Washboard potential for the phase particle in a Josephson junction modeled by the RCSJ 11
1.4 Circuit diagram of an archetypical phase qubit (current biased JJ) 12
1.5 SEM micrograph, Rabi oscillations, and avoided crossings of qubit transition and two-level fluctuators of a phase qubit 14
1.6 Circuit diagram of a prototypal qubit (rf-SQUID and SQUID designs) 15
1.7 Potential energy of an rf-SQUID flux qubit 16
1.8 Circuit diagram and typical hardware layout of a Cooper Pair Box qubit . . . 17
1.9 First two energy levels of a charge qubit as function of gate charge n_g and the ratio E_J/E_C 18
1.10 Circuit diagram and SEM picture of a transmon qubit 20
1.11 Transmon transition frequencies and anharmonicity as functions of E_J/E_C . 21
1.12 Cooper pair box/transmon energy bands for different values of E_J/E_C 22
1.13 Illustration of a typical optical cavity QED setup 23
1.14 Illustration of the energy level scheme of the Jaynes-Cummings Hamiltonian for atom and cavity mode in resonance 26
1.15 Schematic microwave cavity QED setup 28
1.16 Vacuum Rabi oscillations 30
1.17 Ramsey fringes of an atom due to a cavity state-dependent phase shift 32
1.18 Micrograph image of self-assembled quantum dots 34
1.19 Illustration of the photonic crystal cavity, its resonance curve and the vacuum Rabi splitting indicating the strong coupling between a photonic bandgap cavity and a self-assembled quantum dot 35
1.20 Illustration of a transmission line resonator 37
1.21 Two-qubit spectroscopy data showing the cavity-mediated qubit-qubit coupling 41
1.23 SEM micrograph of transmon qubits with local flux control lines [1] 42
1.22 Higher-order Jaynes-Cummings transitions observed in [2] 43
1.24 Fourier transform of vacuum Rabi oscillation signal depending on the prepared resonator state 46
1.25 Wigner function comparison of theory and experiment for different nontrivial superpositions of resonator number states 46

2.1 Photograph of a magnetic core memory array 49

2.2 Schematic Cavity Grid setup 50
2.3 Master equation simulation results for the cavity grid 54
2.4 Illustration of possible hardware setup for the cavity grid 57
2.5 Scalable, fault-tolerant quantum computation scheme based on the cavity grid 59

3.1 Cooper pair box/Transmon transition frequencies as function of the ratio E_J/E_C at gate charge $n_g = 1/2$ 62
3.2 ac-Stark level tuning scheme for resonant CPhase-gate 65
3.3 Evolution of the diagonal elements of the density matrix for the resonant CPhase gate at medium coupling 66
3.4 Barplot of $Re(\hat{\rho})$. Depicted are the initial state $|\Phi^+\rangle$ and the final state close to $|\Phi^-\rangle$ 67
3.5 Results for the master equation simulation for the resonant CPhase gate (strong coupling) 68
3.6 Quantum circuit for a CNOT and a SWAP gate 71
3.7 Maximum fidelity as a function of pulse duration for a 1-2 CNOT gate, and a 1-2 SWAP gate 72
3.8 Sample optimized pulse sequences for a 1-2 CNOT-gate 73
3.9 Fidelity as a function of gate run-time t_{gate} for a 1,3 iSWAP 74
3.10 Maximum fidelity as a function of pulse duration for a 1,3-CNOT gate and a 1,3-iSWAP gate 75
3.11 Restricted controls to implement a 1,3-iSWAP gate 75
3.12 Logarithmic negativity as a measure for entanglement for a 1-3 iSWAP comparing the standard decomposition of gates and the optimal control version . . 76

4.1 Schematic setup of a system qubit repeatedly interacting with environment qubits, effectively realizing a weak measurement of the system qubit state . . 81
4.2 Two example trajectories for the excited state probability according to a simple stochastic master equation 89
4.3 Densities of excited state probability and integrated measurement signal . . . 90

5.1 Schematic setup for the measurement-stabilized generation of entangled multi-qubit states 92
5.2 Generation of the Bell state $|\Psi^+\rangle = (|10\rangle + |01\rangle)/\sqrt{2}$ (the two-qubit W-state) 100
5.3 Generation of two-qubit Bell state $|\Phi^+\rangle = (|00\rangle + |11\rangle)/\sqrt{2}$ (the two-qubit GHZ-state) 101
5.4 Generation of three-qubit W-states 103
5.5 Generation of three-qubit GHZ states and the efficient production of two-qubit W-states as a by-product 104
5.6 Effects of adding decoherence to the dynamics of the two-qubit Bell state synthesis 106
5.7 Density plots for integrated signal and entanglement for added decoherence and relaxation to the creation of the Bell state $|\Phi^+\rangle \equiv \frac{1}{\sqrt{2}}(|00\rangle + |11\rangle)$ 107
5.8 Probability density of the time-averaged phase shift signal as an illustration of the effect of parameter spread in the couplings 109

6.1 Schematic sketch of the underlying transport situation for the photon detection scheme . . . 114
6.2 Example quantum trajectories illustrating dispersive photon detection 119
6.3 Detector profile: Rate of detected vs. incoming photons, at $\Gamma/\kappa = 0.6$, for two different thresholds X_{thr} . . . 120
6.4 Detector efficiency η, obtained from quantum trajectory simulations, as a function of Γ and X_{thr} . . . 121
6.5 Lin-log enlargement of the region of the maximum efficiency of the numerical results (Fig. (6.4)) . . . 121
6.6 Dependence of the detector efficiency on the averaging time τ_{avg} 122
6.7 Suppression of the signal photon number $\bar{n}$ inside the cavity as a function of measurement rate Γ/κ compared to perfect transmission ($\bar{n}_{\mathrm{ideal}}$) 123

List of Tables

3.1 Resonant CPhase-gate protocol 63
3.2 Parameters used in simulation of the resonant CPhase gate protocol 65
3.3 Compilation of minimum gate run-times obtained for different gates and qubit configurations 73

Abstract

In this thesis, experimentally relevant aspects and open questions of quantum information processing and measurement in circuit quantum electrodynamics have been investigated theoretically. Circuit quantum electrodynamics is a relatively young field combining superconducting transmission line resonators on-chip with superconducting quantum bits which serve as artificial atoms. Remarkable experiments have underlined the prospects of circuit QED as a possible architecture for quantum information processing as well as a framework within which quantum optics experiments can be performed. In contrast to their optical counterparts, these experiments reach the ultra-strong coupling limit and allow e.g. the generation of Fock states, the study of decoherence and the observation of quantum jumps.

We present the physics of superconducting circuits based on the Josephson junction as a non-linear circuit element. We discuss the various types of quantum bits (qubits) before turning to an introduction on cavity QED and conclude the introduction with a brief presentation of the most relevant experiments and a short introduction to the principles and prospects of quantum information processing.

Building on the pioneering theoretical and experimental work in which up to three qubits have been integrated on a chip and successfully coupled via a cavity mode, we propose a scheme to overcome the natural limits concerning scalability in these systems. Usually, scalability is severely limited by the resonance width of the qubit transitions and the attainable frequency range for both qubit transition and cavity resonance frequencies. This limits the present setups to at most ten qubits. As a possible solution, we propose and investigate a cross-bar grid layout of cavities with qubits at the intersections. It turns out that this setup, allowing for up to about 1000 qubits, offers significant advantages over e.g. nearest-neighbor coupling schemes. In addition, it can serve as a building block for a truly scalable scheme for fault-tolerant quantum information processing with superconducting circuits by combining 7x7 arrays in a staircase manner.

Furthermore, we discuss and simulate different possibilities to improve upon the suggested scheme by e.g. using resonant gates and optimal control theory.

Another focus of the present thesis is measurement physics. In order to investigate e.g. the possibilities of using a circuit QED system to dispersively detect single microwave photons or to generate multi-qubit entangled states, we introduce in a pedagogical manner the basics of stochastic master equations which generate quantum trajectories before turning to concrete applications. Quantum trajectories have proven to be a state-of-the-art tool to analyze measurement situations in a very realistic manner by giving access to both the measurement record as well as the internal quantum dynamics conditioned on this record.

Using the method of quantum trajectories as generated by stochastic master equations, we discuss a scheme to efficiently generate multi-qubit entangled states in a very flexible way. The method is based on a collective, dispersive qubit readout. By this measurement, a suitable product state of N qubits can be reliably converted into e.g. a N-qubit Greenberger-Horne-Zeilinger or W state. We propose and discuss the scheme and investigate the effects of decoherence and parameter spread as they would be encountered in experiment.

Last but not least, we propose and fully analyze a scheme to dispersively detect single itinerant microwave photons. While experiments to generate single microwave photons have already been successfully performed, their single-shot quantum non-demolition detection has not been possible so far. The scheme presented in this thesis closes this gap in the circuit QED toolbox and reaches detection efficiencies of 30% only limited by fundamental quantum mechanics in this case the Quantum Zeno effect. This detection scheme could be used in quantum communication or quantum cryptography applications.

Chapter 1

Introduction

In this chapter we first introduce and review the field of cavity quantum electrodynamics (cavity QED) based on superconducting circuits. To do so, we discuss the very basic, underlying physics, the Josephson effect and the derived circuit element, the Josephson junction.

Based on this non-linear circuit element and its quantum properties, three different classes of systems emerged which, due to their non-linear spectrum, can be utilized as artificial atoms or qubits. We will review the state of the art of those three types (Phase, flux and charge qubit).

Physicists realized that these systems are ideally suited to couple them to resonator modes of microwave cavities which can be fabricated on the same chip. The strong qubit-cavity coupling due to the small mode volume of the resonators suddenly made those systems a powerful superconducting, on-chip analogue to what is known in Quantum Optics as Cavity Quantum Electrodynamics. Traditionally, beams of real atoms would be sent through a cavity and interact with the quantized light field for some interaction time. Here the coupling is much stronger, and the interaction time is (apart from decoherence effects) in principle infinite.

To make the reader familiar with the essentials of cavity QED physics, the Jaynes Cummings model is introduced, describing the interaction of a two-level system with a single, bosonic mode of a resonator. To make the analogy clear, we will furthermore introduce the reader to some select ground-breaking achievements in “traditional” cavity QED, before turning to the details of the superconducting analogue. Finally, we present the state of the art in cavity QED experiments paying attention to the quantum-optical as well as the quantum information aspect of this relatively new area of solid-state physics.

1.1 Cavity QED as a tool to understand quantum mechanics

Before jumping right into the subject matter, it seems to be appropriate to motivate the study of cavity QED systems with a bigger perspective. This short section deliberately tries not to introduce concepts formally but from a physical, intuitive point of view. We will then formally deepen the concepts when introducing basics of measurement theory in Sec. (4).

The concept of coherence of a quantum system is at the very core of quantum mechanics and closely related to the comparably counter-intuitive concept of entanglement, often also referred to as non-classical correlations. Both can be viewed as a manifestation of the superposition principle. In a density matrix representation of a quantum state, the off-diagonal terms between states are termed 'coherence'. This means is that if an off-diagonal element in a density matrix is non-zero, a suitable experiment will show interference between the two states.

When the coherence of a system decays and finally vanishes (this process is termed 'decoherence') the remaining density operator describes a classical superposition which can be identified with the classical uncertainty about the microscopic state of a system as known from thermodynamics. Systems that show decoherence are usually modelled as *open systems,* meaning that their dynamics due to the interaction with a bath exhibit decoherence, such as dephasing and decay. These are irreversible processes and as we know from the Schrödinger equation, quantum mechanical time evolution is unitary and thus always reversible. This can be resolved if one traces out the bath degrees of freedom and only effectively takes the interaction with the bath into account. The rates of decoherence are contained in the coupling constants of the system with the bath which set the time-scale on which the coherence will vanish. Any attempt to observe coherent effects consequently has to happen on time-scales shorter than any dissipative rates of the system. This limit is usually called the *strong coupling limit.* This limit has been reached in cavity QED systems, enabling experimentalists to probe coherence e.g. by observing Rabi oscillations and Ramsey interference fringes.

Entanglement, however, is not as easy to detect or even to quantify. It is a consequence of the fact that the basis of a composite quantum system made of two systems A and B is given by e.g. the tensor product $\{|\phi_A\rangle\} \otimes \{|\phi_B\rangle\}$, where $\left\{\left|\phi_{A/B}\right\rangle\right\}$ are the original bases of systems A and B. If one is given a state $|\Psi_A\rangle \equiv \sum_i \alpha_i \left|\phi_{i,A}\right\rangle$ of system A and a state $|\Psi_B\rangle \equiv \sum_i \beta_i \left|\phi_{i,B}\right\rangle$ of system B, it is always possible to write down the compound system state $|\Psi_{AB}\rangle \equiv \sum_{i,j} \alpha_i \beta_j \left(\left|\phi_{i,A}\right\rangle \otimes \left|\phi_{i,B}\right\rangle\right)$. This resulting state is called a *product (separable) state.* However, the converse does not hold. Generally, one cannot write any state of the compound system as a product state. If the compound system is in such a state, then the subsystems are called *entangled* and these states are called *entangled (non-separable) states.* They contain (non-classical) correlations between the individual subsystems and thus more information than a product state. Product states are the exception rather than the rule for a compound quantum system. Thus, given a system in product state and an arbitrary interaction Hamiltonian, the system will evolve into a non-separable state as long as the initial state is not an eigenstate of the interaction Hamiltonian. Undisturbed (decoherence-free) quantum-mechanical interaction of subsystems will thus naturally lead to entanglement.

Entanglement and coherence also are the key resources that make a quantum computer conceptually more powerful than a classical computer. As the condition of strong coupling makes it possible to observe coherent interactions between e.g. an atom and a cavity mode in a cavity QED setup, basic quantum computing gates and algorithms can be implemented. While setups with real atoms somewhat suffer from the lack of scalability, their circuit QED counterparts offer more flexibility here. Consequently, circuit QED experiments, apart from reproducing and extending quantum optical results, have focussed on quantum computation applications and have by now successfully implemented first few-qubit algorithms.

Apart from reaching the strong coupling limit, the field profits from the fact that the two most basic and best-understood quantum mechanical systems, a qubit (two-level system) and a harmonic oscillator, suffice to describe the physics extremely well. Not only can one perform a zoo of beautiful experiments, theory is able to keep up with the experiments without making to many approximations - a rare case in modern physics.

1.2 Basics of quantum information processing

In this section, we will try to give a very short introduction to the field of quantum information processing[1]. We will review the key differences between quantum and classical information, how it is stored, manipulated and transmitted, briefly discuss the most prominent algorithms. We will present the famous di-Vincenzo criteria for a workable quantum computing architecture and some examples that have come more or less close to meeting those requirements. Finally, we offer a short outlook combined with a motivation for the work done in the scope of this thesis, mainly the proposal of the cavity grid (Sec. 2), the improvement of gates for the cavity grid architecture (Sec. 3) and the examined scheme for the efficient generation of multi-qubit entangled state in superconducting circuit QED (Sec. 5).

1.2.1 Quantum vs. classical information processing

The answer to the question what makes quantum information theory so much different from classical information theory has different aspects. All of them are rooted in fundamental principles of quantum mechanics such as the superposition principle, entanglement, unitary evolution and the dimensionality of Hilbert spaces. The most straight-forward difference is that the number of possible states for a string of N classical bits is 2^N and only N boolean parameters are needed to parametrise this state. In contrast, for a qubit (quantum bit) system 2^N is just the number of basis states. With qubit systems any qubit can be in an arbitrary “complex” continuous superposition of its ’0’ and ’1’ states such that the number of continuous parameters to specify a multi-qubit state also exponentially grows as 2^N. This is sort of an analogy for the fact that in classical information processing the exact representation of an arbitrary analog voltage needs generally an infinite number of classical bits while this could be mapped to a single qubit angle (which is a continuous variable just as the analog voltage).

The second difference is that while classical information is always separable - meaning that knowing the individual state of each bit amounts to the same information as knowing the state of the complete string of bits - in quantum mechanics there exist a vast measure of multi-qubit states which are non-separable, meaning that they cannot be written as (tensor) products of the states of the individual qubits. This phenomenon is called entanglement. So-called entangling two-qubit gates (such as the universal CNOT or $\sqrt{\mathrm{iSWAP}}$ gates) together with single-qubit gates form the building blocks for all quantum computational algorithms. In contrast to classical computing, quantum computing gates preserve and even create entanglement between qubits. Furthermore, the time evolution given by the Schrödinger equation is *unitary* meaning that it can be viewed as a simple length-preserving rotation in the Hilbert space the quantum system lives in. Thus, it is just a change of basis which preserves the quantum computing resources such as superposition and entanglement.

1.2.2 Example algorithms

In a way all this can from an intuitive point of view be seen as a possibility to massively parallelise a computation which suggests that there should be a significant speedup vs. doing the same calculation on a classical computer. For some problems for which all known classical algorithms take exponentially long time to solve it, it has been shown that there exist quantum algorithms that can do the same in polynomial time.

---

[1] More comprehensive introductions can be found e.g. in [3–5]

The most prominent example is certainly Shor's algorithm for the factoring of large numbers [6]. This is such an interesting task as all efficient encryption algorithms such as RSA depend on the difficulty to factor large numbers into their prime factors. One just chooses two large prime numbers such that their product will be so large that all the classical computing resources would need longer than the age of the universe to factor them by brute-force attack. To be more precise, the fastest known classical algorithm, the general number field sieve (e.g. found in [7]) needs $O(N^{1/3}log(N)^{2/3})$ computational steps to factor an integer N while Shor's quantum algorithm can do the same in $O(log(N)^3)$ computational steps. This speedup is called *exponential* as the scaling is logarithmic while the classical algorithm is still polynomial.

The user of a (sufficiently powerful) quantum computer could thus break almost all past classical past World-War II and present-day classical encryption. Luckily a quantum computer that can factorize more than a 2-digit number has not been constructed so far and quantum information technology already offers so-called quantum encryption devices which do not rely on 'hardness' of computation but on the fundamental physics of quantum mechanics (in essence measurement theory and entanglement) to make eavesdropping truly impossible.

The second prominent example is the so-called Grover database search algorithm [8, 9]. On a classical computer the fastest way to find a matching entry in an unsorted N-element database takes $O(N)$ computational steps. Grover's algorithm can do the same on a quantum computer in $O(\sqrt{N})$ computational steps thus providing a *quadratic* speedup. It has been shown that Grover's algorithm is optimal in the sense that there does not exist any other, faster quantum algorithm.

Those two algorithms have been inspired by the purely academic Deutsch-Josza algorithm which was already presented in 1992 [10] and represent the most revolutionary possible applications for quantum computers at the present-day.

1.2.3 Present-day quantum computation architectures

For any quantum computational architecture there is the famous di-Vincenzo list of criteria [11] which have to be satisfied such that the system can be actually made useful in practice. These are

1. Scalability - the system should be extendable to a large number of qubits. Today, taking error correction codes into account, this means a number of at least $O(10^3)$ but better $O(10^6 - 10^9)$ qubits should be theoretically reachable.

2. Initialization - The system must be designed such that it can be reliably initialized e.g. in the ground state.

3. Limited decoherence - The system must obey certain upper thresholds for the decoherence rates. Depending primarily on the topology and the resulting availability of more or less efficient error-correction algorithms, these threshold range in between $O(10^{-2} - 10^{-6})$ measured in single gate errors/infidelities. Once these thresholds are reached, adding levels of so-called fault-tolerant quantum computing can reduce the

error added by each added gate and thus allow for arbitrarily long computations. For more details, see Sec. 2.7.

4. Read-out - The system must be designed such that a qubit state can be efficiently read out in a single-shot fashion.
5. Availability of a universal set of quantum gates - This means that at the very least one needs a universal (entangling) two-qubit gates and the possibility to perform arbitrary local rotations of the Bloch sphere for each individual qubit. This criterion is probably the least restrictive at the present day. Examples for such entangling universal two-qubit gates are the CNOT gate which flips the state of the target qubit if and only if the control qubit has been in the excited state. It can be written as

$$\hat{U}_{\mathrm{CNOT}} \equiv \begin{pmatrix} 1 & 0 & 0 & 0 \\ 0 & 1 & 0 & 0 \\ 0 & 0 & 0 & 1 \\ 0 & 0 & 1 & 0 \end{pmatrix}$$

for the basis vectors ordered like this $(|00\rangle, |01\rangle, |10\rangle, |11\rangle)$. Another example which is used in this thesis is the so-called $\sqrt{\mathrm{iSWAP}}$ gate. Based on the iSWAP gate which is given by

$$\hat{U}_{\mathrm{iSWAP}} \equiv \begin{pmatrix} 1 & 0 & 0 & 0 \\ 0 & 0 & i & 0 \\ 0 & i & 0 & 0 \\ 0 & 0 & 0 & 1 \end{pmatrix},$$

the $\sqrt{\mathrm{iSWAP}}$ can be realized by aborting an iSWAP sequence at half the gate runtime. As one can see from the matrix representation of the iSWAP gate, the iSWAP gate is equivalent to a simple SWAP gate up to the phase factor i in some of the matrix elements. Sec. (2) presents a way how to decompose the SWAP gate into iSWAP gates and single-qubit gates [12].

Experimental quantum information processing was pioneered mostly by Nuclear Magnetic Resonance (NMR) based experiments performed on molecules in solution [13]. In this experiment, the number 15 was factored using Shor's algorithm. However, no clear indication of entanglement was measured. This was repeated using photonic qubits [14, 15] where entanglement has been confirmed. Later-on Shor's algorithm has been implemented in charge qubits [16] and there are proposals how to implement it on linear qubit systems which rely on nearest-neighbour coupling [17].

Another prominent example system consists of trapped ions where ions are cooled, electromagnetically trapped and manipulated using lasers. More recent proposals even suggest moving the ions around [18] or accessing ions stored in a two-dimensional optical lattice with a read/write head consisting of a flying trapped ion in order to ease the weakness of a nearest neighbour coupling topology [19].

Another interesting class of systems are superconducting circuits such as the circuit QED systems explored in this thesis. In the recent years they have made promising progress as is shown in Sec. (1.5). The main problem here lies again in the lack of scalability although in principle this problem seems easier to solve due to the integration of all experimental components on microchip surfaces.

1.2.4 Outlook

Building on the present-day experiments in superconducting circuit QED which are introduced in Sec. (1.5) we concluded that probably the weakest point in terms of satisfying the di-Vincenzo criteria for these systems is the lack of scalability. This problem is tackled with the proposal of the cavity grid, an architecture which allows to overcome the restrictions of having to place qubits in a single cavity which is used as a quantum bus as it is done in present-day experiments. Similar proposals for other superconducting systems may be the starting point for what is today referred to as quantum engineering, a scientific discipline that makes use of the principle findings in example systems to take on and solve the engineering and practical problems when scaling the systems and integrating them into a workable quantum computer. The point when such as computer is available might still be decades away but the prospects to succeed have probably never been better than today.

1.3 The Josephson Effect and the Josephson Junction

1.3.1 The Josephson Effect

Based on the well-known Bardeen-Cooper-Schrieffer (BCS) theory of a superconductor [20], electrons form pairs (so-called Cooper pairs) when they are condensed in the superconducting phase. The state of those electrons can be described by a single wave function, the Ginzburg-Landau superconducting order parameter $\Psi(\vec{x},t) = |\Psi(\vec{x},t)|\, e^{i\varphi(\vec{x},t)}$. The macroscopic quantum mechanical phase in a superconductor is of course never to be known absolutely, but phase differences e.g. between different parts of the superconductor or across an insulator are physical and have great implications.

Brian D. Josephson predicted in 1962 [21] that even at zero bias voltage, Cooper pairs would tunnel between two superconductors that are separated by a thin layer of insulating material (this layer is sometimes also called a 'weak link') . He showed that the tunneling supercurrent is given by the first Josephson equation

$$I_s = I_c \sin(\Delta\varphi), \tag{1.1}$$

where $\Delta\varphi$ is the phase difference between the two superconductors and I_c is the critical current, meaning that it is the maximum supercurrent that can flow across the insulating layer. It can be calculated [22, 23] from basic material parameters such as the temperature T, the superconducting energy gap $\epsilon(T)$, and the normal resistance per unit area ρ of the insulating material according to

$$I_c = \frac{\pi}{4}\frac{2\epsilon(T)}{\rho e}\tanh\left[\frac{\epsilon(T)}{2k_B T}\right]. \tag{1.2}$$

This simple setup of an insulator sandwiched in between two superconductors is since known as the Josephson Junction. The effect was first observed experimentally by Anderson and Rowell in 1963 [24]. The voltage across a junction is found to be given by

$$U(t) = \frac{\hbar}{2e}\frac{\partial\Delta\varphi}{\partial t} = \frac{\Phi_0}{2\pi}\frac{\partial\Delta\varphi}{\partial t}, \tag{1.3}$$

$\Phi_0 \equiv h/2e$ being the flux quantum [25, 26]. This equation is called the second Josephson equation.

The convention is to use a cross as the circuit symbol for a Josephson junction see Fig. (1.1).

Figure 1.1: Illustration of the commonly used circuit element symbol of a Josephson junction.

1.3.2 The Josephson Junction

Continuing the introduction of the Josephson effect and the Josephson junction as a nonlinear circuit element, it proves very useful (when one wants to discuss the effects of magnetic

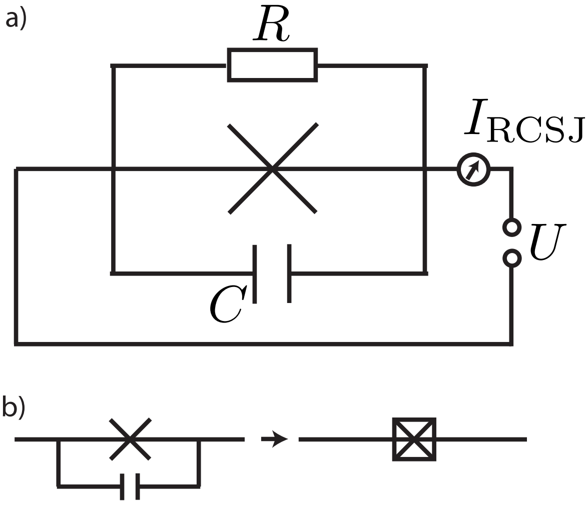

Figure 1.2: In the resistively and capacitively shunted Josephson Junction model the capacitance across the junction is modeled by a capacitor C in parallel to the junction while all dissipative effects are summed into a normal resistor R (also in parallel) (part (a)). A common way to depict a capacitively shunted Josephson junction in circuit diagrams in shown in part (b).

fields) to rewrite the superconducting phase difference by introducing the gauge invariant phase difference γ. It is defined as

$$\gamma \equiv \Delta\varphi - \frac{2\pi}{\Phi_0}\int A_i dx^i, \tag{1.4}$$

where (A^i) is the magnetic vector potential and the integration stretches from one superconductor across the weak link (the insulator) to the other superconductor [27]. In terms of γ, Eqs. (1.1,1.3) simply read:

$$I_s = I_c \sin(\gamma) \tag{1.5}$$

$$U(t) = \frac{\Phi_0}{2\pi}\frac{\partial\gamma}{\partial t} \tag{1.6}$$

and can be combined into the non-linear inductance L which is given by

$$L \equiv \frac{U(t)}{\frac{\partial I_s}{\partial t}} = \frac{\Phi_0}{2\pi I_c \cos(\gamma)}. \tag{1.7}$$

In reality, the two superconductors also realize a capacitor across the junction and in a reasonable circuit model, also the normal resistance across the junction (to include all dissipative effects) should be taken into account as well. This leads to the commonly used resistively and capacitively shunted Josephson Junction model (RCSJ model) [28, 29].

1.3.3 The RCSJ-model of a Josephson Junction

The equivalence circuit of a RCSJ is shown in Fig. (1.2). It accounts for Cooper pair tunneling, quasiparticle tunneling and the capacitance across the junction. The current across the

RCSJ can be found by applying Kirchoffs laws to the circuit depicted in Fig. (1.2) and using Eqs. (1.5,1.6) and reads

$$\begin{aligned} I_{RCSJ} &= I_c \sin\gamma + \frac{U(t)}{R} + C\frac{\partial U(t)}{\partial t} \\ &= I_c \sin\gamma + \frac{\Phi_0}{R\,2\pi}\frac{\partial\gamma}{\partial t} + \frac{\Phi_0 C}{2\pi}\frac{\partial^2\gamma}{\partial t^2}. \end{aligned} \tag{1.8}$$

Eq. (1.8) admits to be interpreted as an equation of motion for a so-called phase-particle. Using the mass of the phase particle given by

$$m \equiv \left(\frac{\hbar}{2e}\right)^2 C$$

allows to rewrite the equation of motion as

$$0 = m\frac{\partial^2\gamma}{\partial t^2} + \frac{m}{RC}\frac{\partial\gamma}{\partial t} + E_J\left(\sin\gamma - \frac{I_{RCSJ}}{I_c}\right), \tag{1.9}$$

where it should be noted that the mass m has units of $kg \cdot m^2$ in this definition. Furthermore, one can introduce a potential

$$V(\gamma) \equiv -E_J\left(\cos\gamma + \frac{I_{RCSJ}}{I_C}\gamma\right) \tag{1.10}$$

such that Eq. (1.9) describes the motion of a damped particle in this potential. For obvious reasons this potential is called washboard potential (see Fig. (1.3)).

Depending on the slope of the washboard potential and the temperature of the system, thermal excitations or quantum fluctuations can lead to the escape of the phase particle out of a well, corresponding to a finite voltage drop across the junction. Moreover, the case of an unbiased junction $I_{RCSJ} = 0$ corresponds exactly to the sinusoidal potential of a mathematical pendulum, such that both modes of motion, oscillatory and perpetually revolving can be studied in this system.

If the slope of the potential admits metastable wells ($0 < I_{RCSJ}/I_C < 1$) and thermal excitations are negligible ($k_B T \ll E_J$) it has been experimentally shown that the energy levels for the phase particle in such a metastable well are quantized and can be approximated by an anharmonic oscillator (energy levels are indicated in Fig. (1.3)) [30]. This was done by irradiating the system with microwaves of different frequencies and measuring the escape rates from the metastable well. The escape rates showed an enhancement whenever the microwave drive passed an energy level (lifting the phase particle to the corresponding excited state where the tunneling barrier would be smaller and hence making it easier to tunnel out).

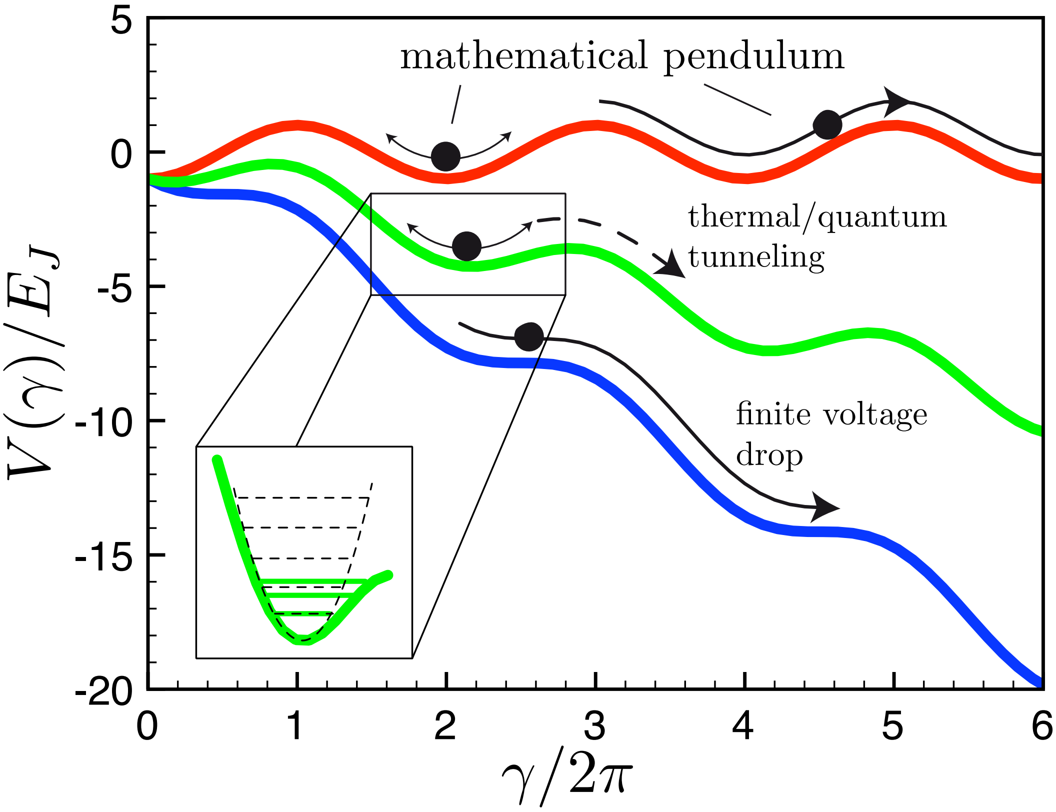

Figure 1.3: Washboard potential for the phase particle in a Josephson junction modeled by the RCSJ. The red line corresponds to the situation with no bias current across the junction, whereas the other curves show finite bias current (green $I_{RCSJ}/I_c = 0.5$, blue $I_{RCSJ}/I_c = 1$). The bound states inside the wells (green curve and red curve) can be approximated by the spectrum of an anharmonic oscillator (indicated by the blowup).

Looking at the energy levels in a metastable well, one finds that the level spacing is unequal, in contrast to a harmonic oscillator. The anharmonicity allows then to individually address one of the transitions and to use the system as an effective two-level system (qubit) (see Fig. (1.3)). This is the key feature that makes the system interesting for use as a two-level system, i.e. an artificial atom or qubit and stimulated the development of more intricate circuits based on Josephson junctions to offer better control and tunability while retaining the key feature of propagating quantum behaviour from the microscopic to mesoscopic scales.

1.4 Qubit types

Building on the basic physics of Josephson junctions which we have just discussed, several circuits have been developed for use as a qubit. In the following we will present their principal features, their circuit and their Hamiltonian. Among other circuit details the crucial parameter which determines the qubit type is the ratio of the Josephson energy E_J to the charging energy E_C. After presenting the three prevalent types (phase, flux, and charge qubit), we will also give a short overview of the experimental milestones for each qubit type (see e.g. [31] for a more detailed and more technical review).

1.4.1 Phase qubits

The simplest, most straightforward way to exploit the quantum physics of a Josephson junction (JJ) is a phase qubit. Here, e.g. a single junction is embedded in a superconducting ring and connected to a current source. The system is typically designed to be dominated by the Josephson energy E_J $(E_J \gg E_C)$ such that the phase is well defined and the charge degree of freedom suffers large quantum fluctuations. A typical circuit is schematically depicted in Fig. (1.4).

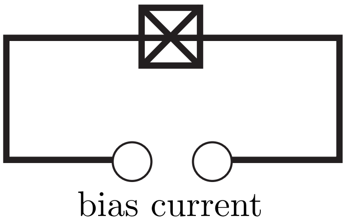

Figure 1.4: Circuit diagram of an archetypical phase qubit (current biased JJ).

Typically, this qubit loop is inductively coupled to driving and readout circuits. Two lowest lying levels of a metastable well of a washboard potential (see Fig. (1.3)) are used as the qubit states. The single junction is often replaced by two junctions in parallel, enclosing some finite area which can be threaded by an external, tunable magnetic flux. The system of the two junctions in parallel effectively behaves like a single junction, the critical current of which can be adjusted by tuning the external magnetic flux through the loop.

The Hamiltonian of a phase qubit can be easily found. One either reads off the Langrangian from Eq. (1.9), calculates the Hamiltonian by a Legendre transform and performs canonical quantization realizing that charge and flux are conjugate variables obeying $[\hat{\gamma}, \hat{Q}] = i\hbar 2e$. This straightforward procedure leads to the Hamiltonian

$$\hat{H} \equiv 4E_C\hat{n}^2 - E_J \cos\hat{\gamma} - \frac{\hbar I_B}{2e}\hat{\gamma}, \tag{1.11}$$

where $\hat{n} \equiv \hat{Q}/(2e)$ is the number of Cooper pairs. Another way to obtain the Hamiltonian would e.g. be to write down the total free energy of the system.

Furthermore, there is a generally valid, systematic approach how to quantize superconducting circuits which can be found in [32, 33]. In the vicinity of $I_B \leq I_c$, one of the metastable wells of the potential Eq. (1.10) can be well approximated by a cubic form

$$V(\hat{\gamma}) \approx \Phi_0 \left(\hat{\gamma} - \frac{\pi}{2}\right)(I_c - I_B) - \frac{I_C \Phi_0}{6}\left(\hat{\gamma} - \frac{\pi}{2}\right)^3 . \tag{1.12}$$

If we restrict ourselves to a two-level basis inside the metastable well, we can re-express this Hamiltonian in terms of Pauli spin operators.

$$\hat{H}_{\text{qubit}} \equiv \frac{\hbar\omega_{01}}{2}\,\hat{\sigma}_z + \sqrt{\frac{\hbar}{2\omega_{01} C_J}}\,\Delta I(t)\;(\hat{\sigma}_x + \chi\,\hat{\sigma}_z)\,,$$

where ω_{01} is the transition frequency of the qubit, C_J is the capacitance across the junction, $\Delta I(t) = I_B(t) - I_C(t)$, and $\chi \approx 1/4$ is a constant determined by material properties and the transition frequency [31]. Note that a low frequency drive $\Delta I(t)$ can be used to realize $\hat{\sigma}_z$-rotations while a high frequency drive will cause predominantly $\hat{\sigma}_x$-rotations. [2]

The junctions of phase qubits are typically big enough such that they can be fabricated using optical lithography which makes fabrication in principle easier than for other types that need smaller junctions. However, due to the large junction size, the number of defects (typically two-level fluctuators) in the oxide-layer constituting the insulator of the junctions is large. These defects couple to the qubit (which has been demonstrated by observing the avoided crossings of the individual fluctuators and the qubit levels, see Fig. (1.5)) and cause very high decoherence rates compared to e.g. charge qubits [34]. Only recently, improvements in the material for the insulating layers of the junctions and the fabrication processes made it possible to bring down the number of two-level fluctuators to $O(1)$, making the system a great qubit [35].

Phase qubits have an intrinsic advantage compared to their JJ-based competitors, namely that the readout is built-in. To read out a phase qubit, one applies a microwave drive field resonant to a transition frequency from the qubit excited state to some higher excited state (e.g. $1 \to 3$) and observes whether the JJ switches to the voltage state. The higher the excited state, the shallower the potential barrier that separates a metastable well from the down-hill part of the potential and the higher the probability (in state $|3\rangle$ the tunneling rate is about 500^2 enhanced) of tunneling and causing the JJ to switch to the voltage state. The switching will only happen if the qubit has previously been in the excited state. This readout allows for a remarkable fidelity of about 95% and is intrinsically single-shot - however it is a destructive measurement. After the readout the qubit needs to be reinitialized.

After macroscopic tunneling and the anharmonic level structure inside a metastable well were experimentally confirmed [30, 36], Rabi oscillations between the qubit levels were observed [37] (see Fig (1.5)), reaching a remarkable visibility of about 90% in more recent experiments using an evolved phase-qubit circuit [38]. Phase-qubits have been directly coupled capacitively, yielding evidence for qubit entanglement [39, 40]. Moreover, phase qubits have been successfully coupled via microwave on-chip cavities [41]. These experiments constitute the most promising road in coupling more qubits efficiently and will be discussed in more detail in Sec. 1.5.4.4.

1.4.2 Flux qubits

The second type of qubits we are discussing are the so-called flux qubits [42]. The two qubit states correspond to supercurrent flowing clockwise and counter-clockwise through the loop.

---

[2] $\chi \equiv \sqrt{\hbar\omega_{01}/(3\Delta V)}$, where ΔV is the barrier height of the potential given by $\Delta V = 2\sqrt{2}/3(I_C\Phi_0)(1 - I_B/I_C)^{3/2}$.

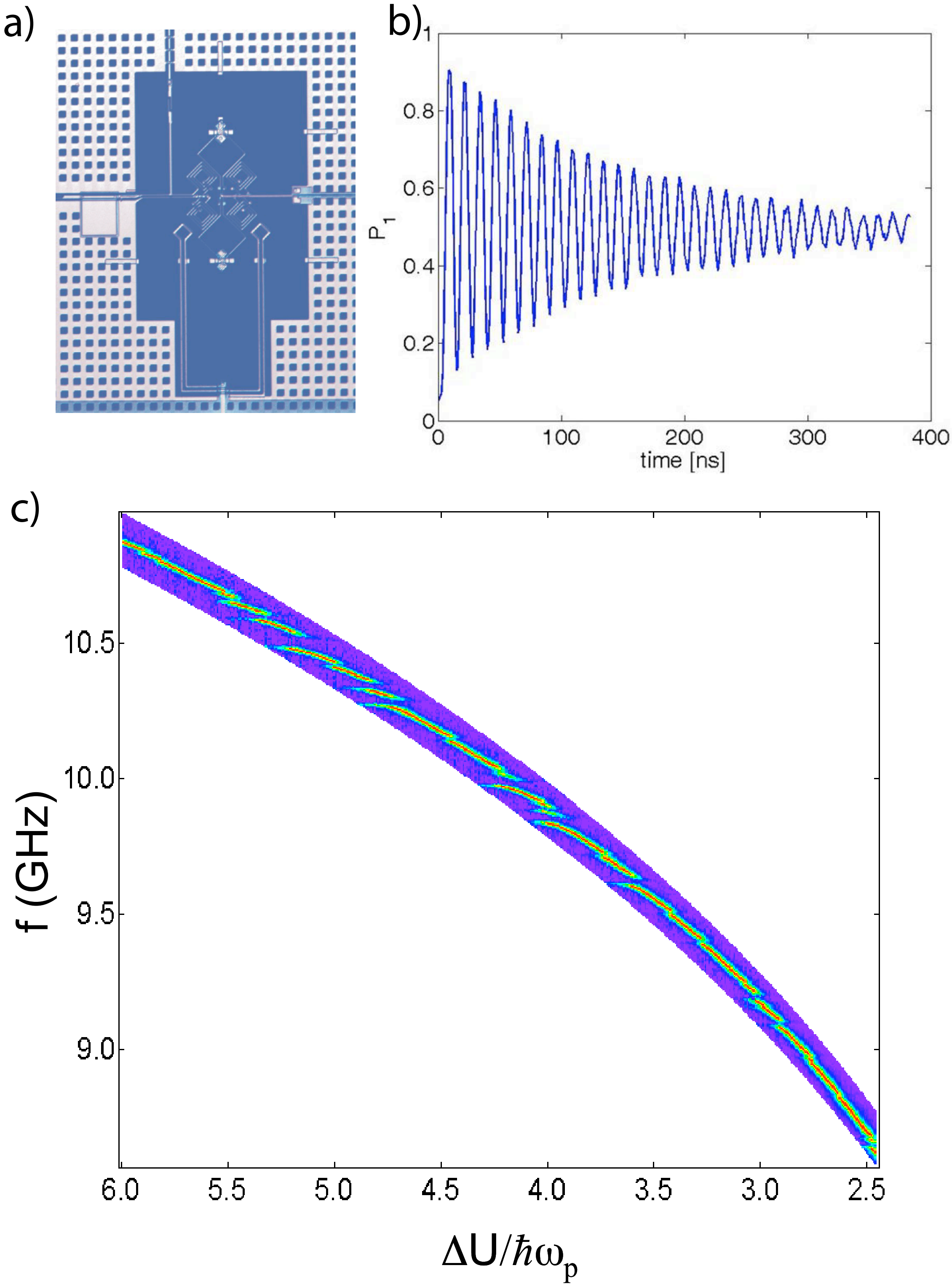

Figure 1.5: Part (a) shows a scanning electron micrograph of a Josephson phase qubit. Part (b) shows Rabi oscillations with a visibility of about 90%. Part (c): Avoided crossings of qubit transition and two-level fluctuators in a phase qubit. (Courtesy of Eva Weig)

Typically $E_J/E_C \gg 1$. The qubit loop, mostly containing one (rf-SQUID design [43]) or three Josephson Junctions [44, 45] can be inductively coupled to a tank circuit [46] which is used to adjust the flux through the qubit loop and to read out/drive the qubit.

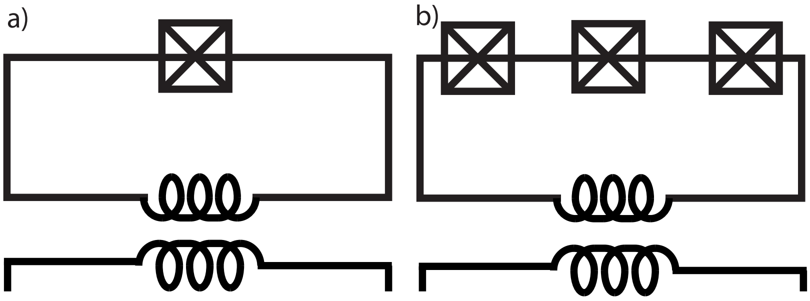

Figure 1.6: Part (a) shows an rf-SQUID design while part (b) shows a three JJ-SQUID design.

While for a charge qubit the gate voltage applied to one of the islands of the Josephson junction is used to tune the Hamiltonian, for a flux qubit the two superconducting leads of the JJ are connected to form a ring to couple to external flux. This external flux is then used to tune the parameters of the Hamiltonian. For simplicity we will write down and motivate the Hamiltonian of an rf-SQUID flux qubit. Here, the total flux through the loop Φ and the gauge-invariant phase γ are equivalent. The total energy of the system is given by:

$$H \equiv \frac{Q^2}{2C_J} - E_J \cos\left(2\pi\frac{\Phi}{\Phi_0}\right) + \frac{1}{2L}\left(\Phi - \Phi_x\right)^2,$$

where Q is the net charge on the two sides of the JJ and Φ_x is the externally applied flux ($\Phi - \Phi_x$ is the flux produced by the supercurrent in the loop), C_J is the capacitance across the JJ and L describes the self-inductance of the loop. The first term is the charging energy of the JJ, the second term is the JJ free energy (up to a constant) and the third term describes the magnetic energy stored in the loop. The potential part of the Hamiltonian reads

$$V(\Phi) \equiv V_0\left[\frac{1}{2}\left(\frac{2\pi(\Phi-\Phi_x)}{\Phi_0}\right)^2 - \frac{E_J}{V_0}\cos\left(2\pi\frac{\Phi}{\Phi_0}\right)\right].$$

where $V_0 \equiv \Phi_0^2/(4\pi^2 L)$.

Analogously to the discussion of the phase qubit (see Sec. 1.4.1), note that charge and flux are canonically conjugate variables. After promoting the variables Q, Φ to operators, we restrict ourselves to the two-level subspace which consists of the lowest-lying state in each well of the double-well potential. Note that the barrier height of the double-well can be tuned by choosing E_J, and the asymmetry by changing the external flux (see Fig. (1.7)).

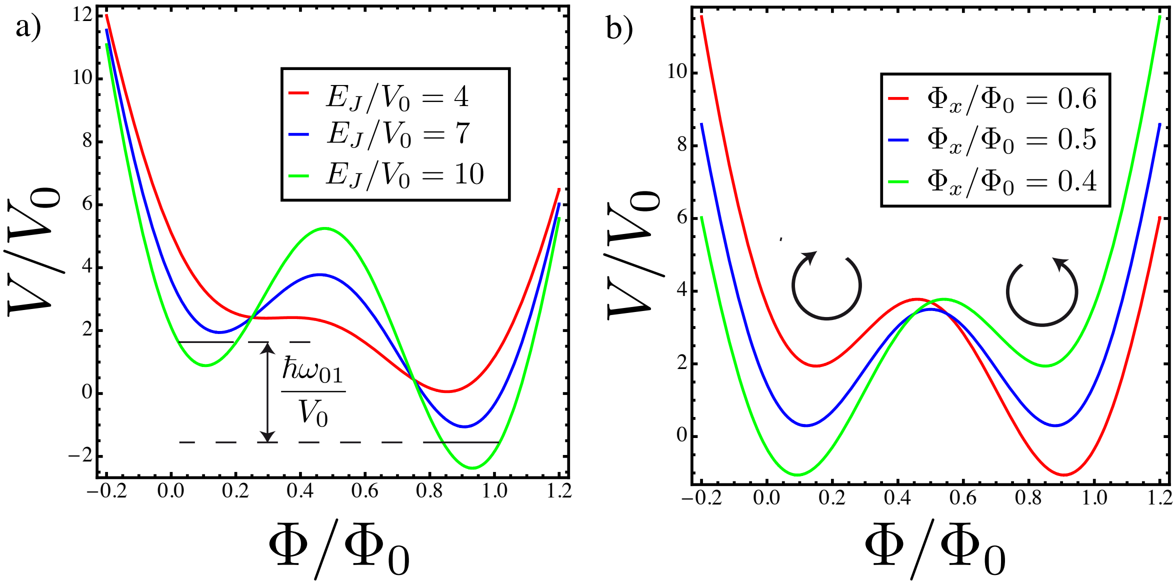

Figure 1.7: Potential energy of an rf-SQUID flux qubit. Part (a) shows the dependence of the barrier height on the Josephson energy while part (b) depicts the dependence of the asymmetry of the potential dependig on the external flux threading the loop. States which are localized in one of the two wells (like e.g. the two lowest-lying states constituing the qubit) correspond to clockwise and counter-clockwise supercurrent through the loop.

Truncating the basis yields an NMR-form of the Hamiltonian:

$$\hat{H}_{\text{qubit}} \equiv \frac{1}{2}\hbar\omega_{01}\hat{\sigma}_z + \frac{\Delta}{2}\hat{\sigma}_x$$

The tunnel coupling Δ between the two states can be calculated e.g. by the WKB-method [45] or can be measured in an experiment [47]. Another possibility is the summation of all possible tunneling paths [48]. The energy splitting of the qubit is given by

$$\hbar\omega_{01} \equiv 4\pi\sqrt{6\left(\frac{E_J}{V_0}-1\right)}\, E_J \left(\frac{\Phi_x}{\Phi_0}-\frac{1}{2}\right).$$

The drawback of rf-SQUID design flux qubits is that in order to achieve a sufficiently high barrier, one aims for the regime of $E_J/V_0 > 1$, which requires a large product of critical current and self-inductance. This requires a big loop-area in order to achieve a sufficiently large self-inductance and makes the qubit very susceptible to flux noise. On the other hand, a large critical current requires a large junction area which makes the qubit more susceptible to dielectric losses in the junction oxide layer. Problems related to large junctions are also a big issue for phase qubits (see Sec. 1.4.1). In practice, only a narrow parameter range proves to be useful, which is the main reason why experimentalists soon turned to more elaborate setups, e.g. the three Josephson junction design, to overcome those issues. These circuits exhibit the same basic physics and are the base for almost all sucessful experiments in the various groups around the world [44, 49–57].

First experiments demonstrated the qubit-suitable level structure and the macroscopic superposition of persistent current flowing clockwise- and counter-clockwise [58, 59]. Soon thereafter Rabi oscillations could be observed [46, 51, 60, 61] and more recently two and even more flux qubit have been coupled [62–65] and two-qubit quantum gates have been demonstrated [65]. These experiments already revealed the four two-qubit states and showed that coherent multi-qubit manipulations on flux qubits are possible. A more detailed discussion of the different static and tunable coupling schemes can e.g. be found in [66, 67]. The next step for flux qubits has been made by coupling them to on-chip microwave resonators and realize cavity QED experiments [60, 68]. Even a four-qubit sample has been sucessfully implemented [69].

1.4.3 Charge qubits

1.4.3.1 The Cooper pair box

The third and last archetypal superconducting qubit is the so-called charge-qubit. Also based on Josephson junction physics, the crucial difference to the aforementioned phase and flux qubits is that charge qubits are dominated by the charging energy, such that $E_C \gg E_J$[3]. As a consequence, these devices have energy levels defined by the number of Cooper pairs on either side of the junction while the phase (the conjugate variable) suffers large quantum fluctuations.

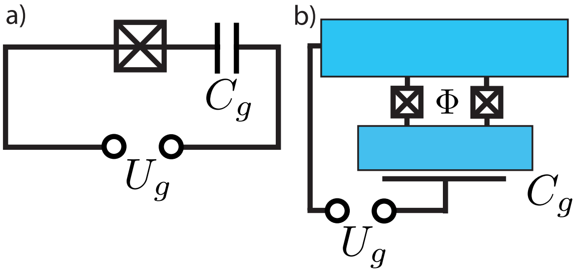

Figure 1.8: Part (a) shows a circuit diagram of a charge qubit. Part (b) shows the typical hardware layout of a Cooper Pair Box constituting the charge qubit. Cooper pairs can tunnel across the Josephson weak link(s) from one superconducting island to the other. This process is connected with a charging energy which can be tuned by an external gate voltage U_g. The other tunable parameter in the system is the flux through the loop enclosed by the two junctions and the islands which controls the tunnel coupling between neighbouring charge states.

The Cooper pair box Hamiltonian can be easily derived from the total Gibb's free energy in the circuit. It reads:

$$\hat{H} \equiv 4E_C(\hat{N} - n_g)^2 - E_J \cos\gamma, \tag{1.13}$$

which can, using the relation $\exp(\pm i\gamma)\left|n\right\rangle = \left|n \pm 1\right\rangle$, be transformed to

$$\hat{H} \equiv 4E_C(\hat{N} - n_g)^2 - \frac{E_J}{2}\left(\left|n\right\rangle\left\langle n+1\right| + h.c.\right).$$

---

[3] The transmon circuit does not obey this condition, however due to its topology, shares the Hamiltonian and many features of a charge qubit. The transmon is discussed at length in Sec. 1.4.3.2 and Sec. 3.2.

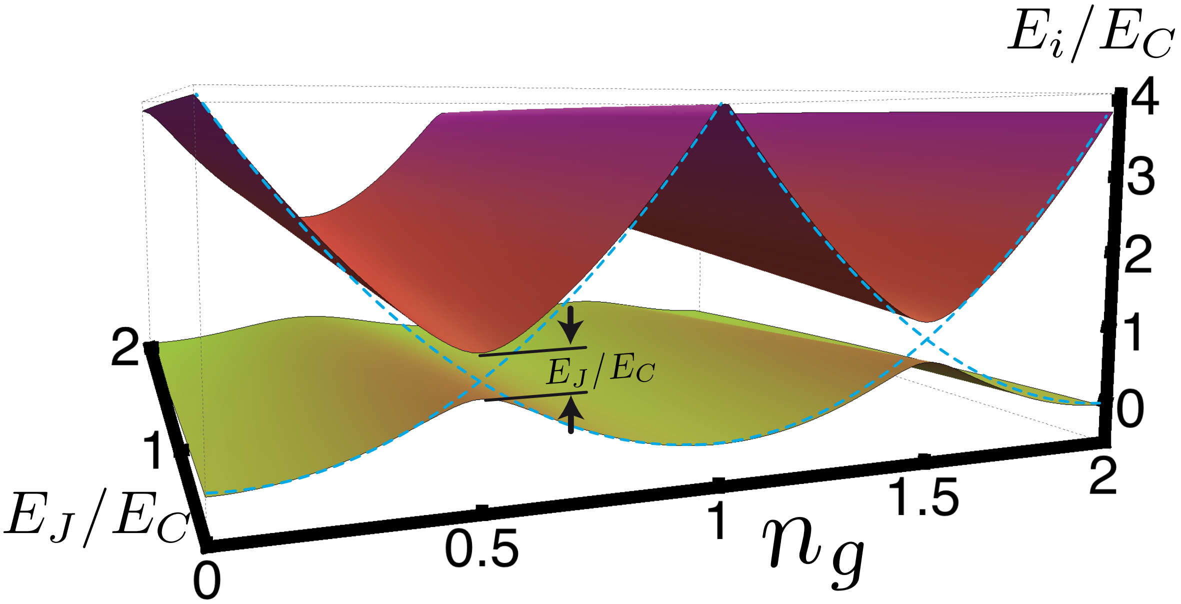

Figure 1.9: First two energy levels of a charge qubit as function of gate charge n_g and the ratio E_J/E_C. Note that the avoided crossings at half-integer values of n_g are pronounced sweet spots for small ratios E_J/E_C, while for larger values of E_J/E_C, the bands become more and more flat, a fact exploited in the design of the transmon qubit (see Sec. 1.4.3.2). In this regime, the whole band becomes a sweet spot and thus the qubit becomes insensitive to charge noise.

$\hat{N}$ is the operator that counts Cooper pairs ($\hat{Q} = 2e\hat{N}$), $n_g \equiv -V_g C_g/(2e)$ is the gate charge (in units of Cooper pairs), $E_C = e^2/(2(C_J + C_g))$ is the charging energy corresponding to one more excess Cooper pair on one island and E_J the Josephson tunneling energy associated with either the single junction or, in case of a split-junction SQUID geometry (Fig. (1.8), part (b)), a pair of junctions enclosing an external flux. In the latter case E_J can be tuned by the external flux threading the SQUID loop.

The Cooper pair box can in many ways be seen as the dual to the current-biased junction (the phase qubit). Here, two knobs are available to influence the spectrum of the qubit: It is possible to tune the ratio E_J/E_C e.g. by applying external magnetic flux, and to adjust the level splitting by varying the gate voltage (and thus the gate charge n_g). The spectrum exhibits avoided crossings at half-integer gate charge, while the ratio E_J/E_C influences the anharmonicity of the spectrum (see Fig. (1.9)). Typically, charge qubits are operated at the so-called sweet spot $n_g = 1/2$ in order to make the qubit to first order insensitive to charge noise, the most prominent source of decoherence. Unfortunately, in order to keep the qubit at the sweet spot, one essentially loses a great deal of experimental flexibility as the in-situ tunability of the Josephson energy by the application of external flux does not allow great variations of the spectrum.

Near this sweet spot at half-integer gate charge, and if we restrict ourselves to the lowest two eigenstates, we can truncate the basis of the Hamiltonian to two levels and cast it into NMR-form. It then reads

$$\hat{H} = -2\,E_C\,(1 - 2n_g)\,\hat{\sigma}_z - \frac{E_J}{2}\hat{\sigma}_x.$$

It is noteworthy that although termed charge-qubit, it is not a distinct difference in charge of the two islands that the qubit eigenstates are built from. On the contrary, at the sweet spot $n_g = 1/2$, the two levels correspond to $|0\rangle \pm | 1\rangle$, i.e. combinations of charge states.

Charge qubits proved to be very robust and to be ideally suited to strongly couple them to on-chip microwave resonators. Already the first experiments exhibited a very strong coupling that has by now been improved by another order of magnitude. The latest experiments rely on an improved design of the Cooper pair box, the so-called transmon, which we will have a closer look at in the following section.

Historically, a charge qubit was the first superconducting Josephson qubit ever to be realized [70–74] which had been previously proposed by Büttiker [75] followed by further theoretical investigations [76]. Quantum mechanical superpositions of charge states have been experimentally observed [77]. Soon thereafter, the first cavity QED proposals [78] and first encouraging experiments followed [79]. We will give a more detailed introduction to circuit QED in Sec. 1.5.

1.4.3.2 The Transmon

After the Cooper pair box had proven suitable as a qubit, groups around the world worked on design improvements. Among the goals for improvement was to reduce or even eliminate the necessity to keep each qubit at the magic point $n_g = 1/2$ in order to make it less susceptible to charge noise. The key idea is to shunt the two islands with an additional capacitance in order to operate the device in a regime of $E_J/E_C \gg 1$, where the charge dispersion in the energy level structure becomes more and more flat. By making the whole band a sweet spot, one eliminates the need of keeping the device tuned at half-integer gate charge. Thus, charge noise as a major source of decoherence can be reduced drastically. This design improvement was independently officially proposed by the Yale group [80] and Nori et. al. [81] at a point in time where the Yale group had already performed detailed measurements on such a device.

Although the $E_J/E_C = O(10^2)$ regime hints that the qubit could in fact be a phase qubit, there is a crucial difference. Phase qubits are based on current-biased junctions and by the current, the washboard potential is tilted. The phase can thus take all values on the real axis while for a transmon the phase only takes values between 0 and 2π. This topological difference between a transmon and a phase qubit explains why it is possible to map a CPB continuously into a transmon by changing E_J/E_C, but not into a phase qubit.

As shown in recent experiments [82–90], the transmon qubit is the superconducting qubit of choice at the moment and represents the state of the art. It has reached the dephasing limit of $T_2 = 2T_1$ and resulting dephasing times of up to $3\mu s$ [90]. Simultaneously, an enormous progress in the Jaynes-Cummings coupling strength to on-chip microwave resonators has been realized. While early Cooper pair box circuit QED experiments reached coupling values of about $2\pi \cdot 17MHz$ [91], recent transmon experiments have boosted this to values of about $2\pi \cdot 173MHz$ [2]. However, the increased coupling which allows faster gate operations also requires a stronger anharmonicity in order to prevent leakage to higher qubit levels.

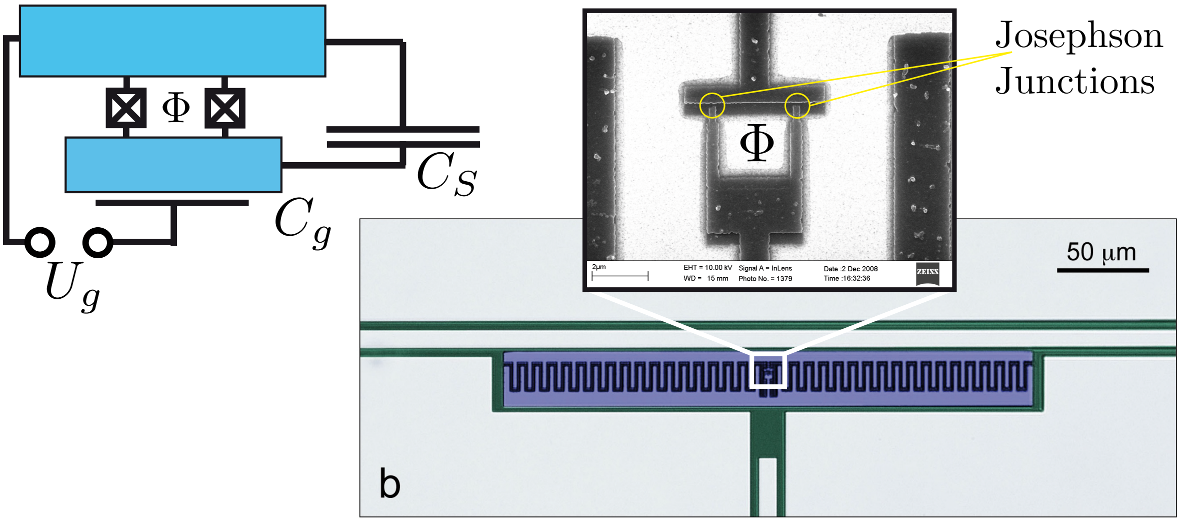

Figure 1.10: In addition to the usual Cooper pair box layout, the split Josephson junction between the superconducting islands is shunted by an additional, large capacitance C_S. This drastically reduces the charging energy and thus the ratio E_J/E_C. As a consequence, the energy levels are almost independent of the gate charge. This enhances coherence times while eliminating the need to tune the qubit to a sweet spot. The price to pay is a more harmonic spectrum which makes the consideration of higher qubit levels necessary.

In the following we will present a more detailed discussion of the trade-off between decreased sensitivity to charge-noise and increased coupling to the reasonator by operating in the transmon regime and the price which one has to pay - decreased anharmonicity. This will especially become important in Sec. 3.2, a proposal for the implementation of a resonant CPhase gate between two qubits coupled by a microwave cavity, where the individual addressing of different qubit transitions will be imperative.

Anharmonicity issues of the Transmon qubit In this section we discuss the energy level structure of the transmon in more detail and the resulting implications for the use as a qubit. As we have argued in the previous section, the transmon Hamiltonian is identical to the one of a Cooper pair box (Eq. (1.13)), although the device is operated at a different regime of E_J/E_C. As we could already infer from Fig. (1.9), charge dispersion (the variation of the energy levels with the gate charge n_g) is strongly reduced when increasing the ratio E_J/E_C, i.e. moving from the Cooper pair box to the transmon regime. At the same time, if we plot the transition frequencies of the lowest two qubit transitions at $n_g = 1/2$ as a function of E_J/E_C (see Fig. (1.11, part (a))), we realize that the anharmonicity (the difference in the transition frequencies) decreases with increasing E_J/E_C (see Fig. (1.11), part (b)). This makes a more detailed analysis necessary.

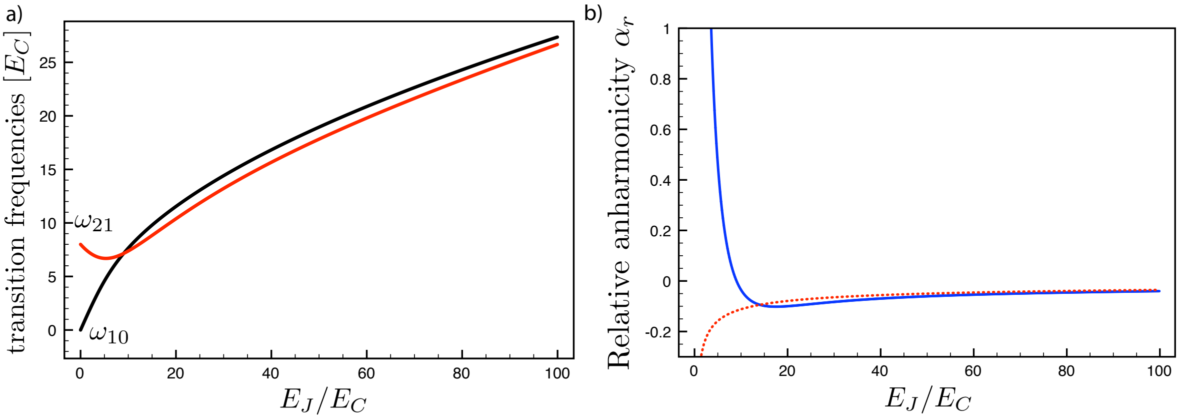

Figure 1.11: Transmon transition frequencies and anharmonicity as functions of E_J/E_C. Part (a) shows the two lowest transmon transitions while part (b) shows the relative anharmonicity $\alpha_r \equiv (\omega_{21} - \omega_{10})/\omega_{10}$. Note that around $E_J/E_C \approx 8$, the anharmonicity is zero, making this regime unfavourable. In the transmon regime $E_J/E_C = O(10^2)$, the anharmonicity is significantly smaller compared to the Cooper pair box charge qubit regime $E_J/E_C = O(1)$.

Following [80, 92], the CPB/transmon energy levels E_m can be found by exactly solving the Hamiltonian Eq. (1.13) and are expressed in terms of Mathieu functions:

$$E_m(n_g) = E_C a_{2[n_g+k(m,n_g)]}\left(-\frac{E_J}{2E_C}\right),$$

where $a_\nu(q)$ denotes Mathieu's characteristic value and the function k is sorting the eigenvalues appropriately. These functions can, in the limit of large E_J/E_C be well-approximated by more elementary functions. From the band structure and its dependence on the variations in the gate charge (see Figs. (1.9,1.12)) one can calculate the peak-to-peak value of the energy bands by approximating the Mathieu functions [80, 92].

This yields

$$\begin{aligned}\epsilon_m &\equiv E_m(n_g = 1/2) - E_m(n_g = 0)\\ &\simeq (-1)^m E_C \frac{2^{4m+5}}{m!}\sqrt{\frac{2}{\pi}}\left(\frac{E_J}{2E_C}\right)^{\frac{m}{2}+\frac{3}{4}} e^{-\sqrt{8E_J/E_C}}.\end{aligned}$$

Remarkably, the charge dispersion is suppressed exponentially with increasing E_J/E_C.

Now let us analyze how the absolute and relative anharmonicity scale with E_J/E_C. They are given simply by

$$\begin{aligned}\alpha &\equiv E_{21} - E_{10}\\ \alpha_r &\equiv \alpha/E_{10}.\end{aligned}$$

From a perturbative treatment [80, 92] of a quartic expansion of the cosine potential one obtains $\alpha \simeq -E_C$ and $\alpha_r = -1/\sqrt{8E_J/E_C}$. This result agrees well with the numerical data for $E_J/E_C \gg 1$. It is thus fair to conclude that while the decreased anharmonicity indeed poses a problem when one attempts to do fast gate operations, as higher transitions will be addressed unwantedly, the gain in noise insensitivity outweighs this disadvantage by far. This tradeoff has to be born in mind when considering the transmon as a quantum computation resource.

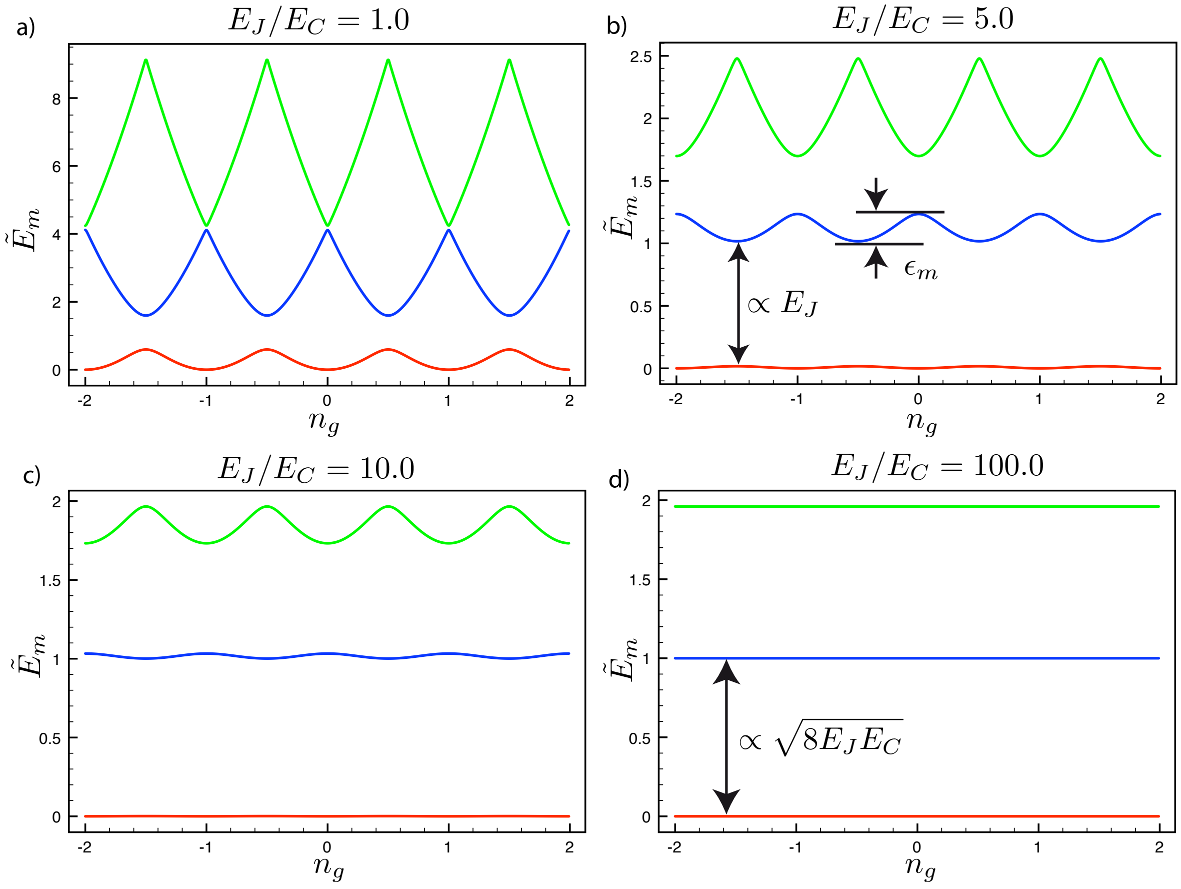

Figure 1.12: Cooper pair box/transmon energy bands for different values of E_J/E_C. We plot the lowest three energy eigenvalues $\tilde{E}_m(n_g) \equiv (E_m(n_g) - E_0(n_g = 0)) \,/\, (E_1(n_g = 1/2) - E_0(n_g = 1/2))$ as a function of gate voltage n_g. Note that with increasing E_J/E_C, we continuously follow the mapping of a charge qubit (part (a)) into a transmon (part (d)). Here, the energy bands are completely flat which reduces the suceptibility to charge fluctuations (charge noise) greatly. However, the spectrum also becomes more and more harmonic (almost equal level spacing). In part (b) we have visualized the peak-to-peak height ϵ_m of the m-th energy eigenvalue as a measure for the charge dispersion (see main text).

1.5 From cavity QED to circuit QED

The following section concludes the introduction with a short overview about the young field called 'circuit quantum electro-dynamics' (circuit QED). We will review basic physics (mostly the Jaynes-Cummings model and its extensions) as well as the experimental ancestors and closest relatives, namely cavity QED with real atoms, especially focusing on the experiments that have been performed with Rydberg atoms.

In this section, we will derive the Jaynes-Cummings Hamiltonian [93] which describes an atom (idealized as a two-level system) which is coupled to a single mode of the electromagnetic field (e.g. a cavity mode). A typical setup is sketched in Fig. (1.13). For most experiments, this model suffices to describe the experimental findings to great precision. In order to put the field of circuit QED - a promising and more recent physical implementation of a cavity QED setup - into physical and historical perspective, we will introduce the reader to some select experiments that have been performed with real atoms, in particular with Rydberg atoms and three-dimensional microwave resonators.

Circuit QED offers several advantages like e.g. even stronger coupling and unlimited interaction times compared to real (Rydberg) atoms and cavities operated at frequencies of visible light (microwaves). Here, the role of the atom is taken by some kind of superconducting qubit circuit as we have just discussed previously while the cavity can be realized by a coplanar waveguide or stripline resonator fabricated onto the same chip's surface.

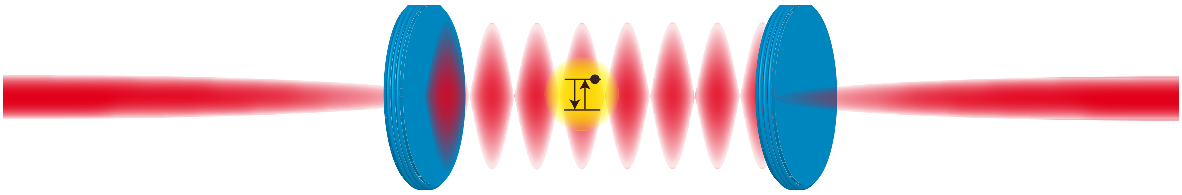

Figure 1.13: Illustration of a typical optical cavity QED setup. An atom, depicted in yellow, interacts with the electromagnetic field inside a cavity (red) that is formed by semi-transparent mirrors (blue) that allow to couple light in and out of the cavity.

1.5.1 Derivation of the Jaynes-Cummings Hamiltonian

The Jaynes Cummings model has been introduced by Jaynes and Cummings in 1963 [93] and has proven to be extremely useful. In the physical situation of Fig. (1.13), we start with writing a classical Hamiltonian for the electromagentic field inside the cavity.

$$H_{em} = \frac{1}{8\pi} \int dV \, \vec{E}^2(\vec{x},t) + \vec{H}^2(\vec{x},t), \tag{1.14}$$

into which we insert the field expansions for the magnetic and electric field

$$\begin{aligned} \vec{E}(\vec{x},t) &\equiv \sqrt{4\pi} \sum_a p_a(t) \vec{E}_a(\vec{x}) && (1.15) \\ \vec{H}(\vec{x},t) &\equiv \sqrt{4\pi} \sum_a q_a(t) \vec{H}_a(\vec{x}), && (1.16) \end{aligned}$$

suitably normalized such that $\int dV \, \vec{E}_a(\vec{x}) \, \vec{E}_b(\vec{x}) = \delta_{ab}$ and $\int dV \, \vec{H}_a(\vec{x}) \, \vec{H}_b(\vec{x}) = \delta_{ab}$. Upon writing the Maxwell equations

$$\nabla \times \vec{E}(\vec{x},t) = -\frac{1}{c} \frac{\partial \vec{H}(\vec{x},t)}{\partial t},$$

$$\nabla \times \vec{H}(\vec{x},t) = \frac{1}{c} \frac{\partial \vec{E}(\vec{x},t)}{\partial t},$$

we realize that they reduce to Hamiltonian equations of motion for the variables p_a and q_a respectively for this field expansion. The Hamiltonian 1.14 in terms of the field expansions Eqs. (1.15,1.16) reads

$$H_{em} = \frac{1}{2} \sum_a \left[p_a^2(t) + \omega_a^2 q_a^2(t) \right],$$

which can, imposing the usual canonical commutation relations $[q_a, q_b] = [p_a, p_b] = 0$, $[q_b, p_b] = i\hbar\delta_{ab}$, be immediately quantized to

$$\hat{H}_{em} = \sum_a \hbar\omega_a \hat{c}_a^\dagger \hat{c}_a,$$

where the annihilation operator

$$\hat{c}_a \equiv \frac{\hat{p}_a + i\omega_a \hat{q}_a}{\sqrt{2\hbar\omega_a}}$$

is defined in the usual way. In the following we restrict ourselves to one mode and drop the index a. This quantized field couples to a two-level system (an atom or a qubit), the Hamiltonian of which can be expressed in terms of Pauli spin operators and reads

$$\hat{H}_{atom} = \frac{\epsilon}{2} \hat{\sigma}_z.$$

It is assumed to couple to the EM-field via the interaction Hamiltonian

$$H_{int} \equiv \hbar g \hat{\sigma}_x (\hat{c} + \hat{c}^\dagger),$$

where the dipole moment is assumed to be along the electric field axis and $\hat{c} + \hat{c}^\dagger$ is proportional to the field amplitude. The atom dipole moment is given by $\hat{\mu} \equiv \mu\hat{\sigma}_x$ and we have defined a coupling constant $\hbar g \equiv \mu\sqrt{\frac{\hbar\omega}{V}}$ (V denotes the mode volume of the cavity). If we look at the matrix elements of the interaction Hamiltonian, we find

$$\left\langle m, n \left| \hat{H}_{int} \right| m', n' \right\rangle = \hbar g \left[\sqrt{n}\delta_{n,n'+1} + \sqrt{n+1}\delta_{n+1,n'} \right] (1 - \delta_{m,m'}) ,$$

where $n \in \mathbf{N}_0$ is the photon number in the oscillator and $m \in \{0, 1\}$ describes the atom excitation. From this expression it is evident that any dynamics involves (a) a state change of the atom and (b) only adjacent oscillator levels couple to each other via the atom. The complete Hamiltonian reads

$$\hat{H}_{JC} = \hat{H}_{em} + \hat{H}_{atom} + \hat{H}_{int} = \hbar\omega_a \left(\hat{c}^\dagger\hat{c}\right) + \frac{\epsilon}{2}\hat{\sigma}_z + \hbar g\hat{\sigma}_x(\hat{c} + \hat{c}^\dagger)$$

and can be made more instructive by introducing the atomic rising and lowering operators $\hat{\sigma}^\pm \equiv \frac{1}{2}\left(\hat{\sigma}_x \pm i\,\hat{\sigma}_y\right)$. It then reads

$$\begin{aligned} \hat{H}_{JC} &= \hbar\omega_a\hat{c}^\dagger\hat{c} + \frac{\epsilon}{2}\hat{\sigma}_z + \frac{\hbar g}{2}\left(\hat{\sigma}^+ + \hat{\sigma}^-\right)(\hat{c} + \hat{c}^\dagger) \\ &= \hbar\omega_a\hat{c}^\dagger\hat{c} + \frac{\epsilon}{2}\hat{\sigma}_z + \frac{\hbar g}{2}\left(\underbrace{\hat{\sigma}^+\hat{c} + \hat{\sigma}^-\hat{c}^\dagger}_{\mathrm{RWApart}} + \hat{\sigma}^-\hat{c} + \hat{\sigma}^+\hat{c}^\dagger \right) . \end{aligned} \tag{1.17}$$

One can immediately identify the excitation number conserving first two terms which lead to a coherent exchange of excitations between the atom and the oscillator, while the last two terms of the interaction correspond to generation of a photon while exciting the atom and the destruction of a photon while at the same time de-exciting the atom. The last two terms obviously do not conserve energy and thus they can often be neglected. This approximation is called the Rotating Wave Approximation (RWA). It is acceptable as long as e.g. the system is not very strongly driven. The term 'rotating wave' stems from making the argument in an interaction picture: Let us assume for the moment that the atom is in resonance with the oscillator such that $\omega = \epsilon$. It is then straightforward to see that while the $\hat{\sigma}^+\hat{c} + \hat{\sigma}^-\hat{c}^\dagger$ part of the Hamiltonian stays time independent, while the $\hat{\sigma}^-\hat{c} + \hat{\sigma}^+\hat{c}^\dagger$- part starts aquiring an oscillatory term, oscillating at twice the transition frequency and often much faster than anything else. In these cases the fast non-RWA oscillations average out on timescales one is interested in and thus can be neglected. The energy level scheme of the Jaynes-Cummings Hamiltonian is visualized in Fig. (1.14).

Note that only after approximating the superconducting qubit with an ideal two level system, the circuit QED systems conform to the Jaynes-Cummings Hamiltonian Eq. (1.17).

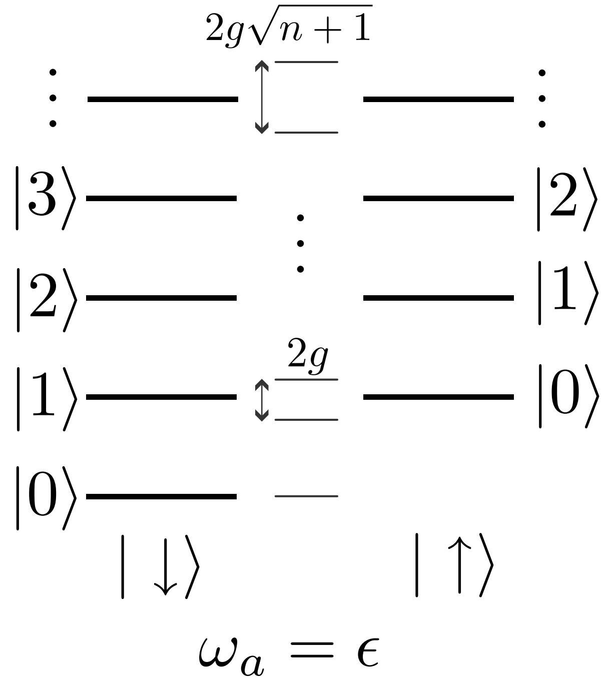
$2g\sqrt{n+1}$
$|3\rangle$
$|2\rangle$
$|1\rangle$
$|0\rangle$
$2g$
$|2\rangle$
$|1\rangle$
$|0\rangle$
$|\downarrow\rangle$
$|\uparrow\rangle$
$\omega_a = \epsilon$

Figure 1.14: Illustration of the energy level scheme of the Jaynes-Cummings Hamiltonian. Atom and cavity mode are assumed to be in resonance ($\omega_a = \epsilon$). The dressed states are split by $2g\sqrt{n+1}$, the so-called vacuum Rabi frequency.

1.5.2 Cavity QED with real atoms

This section is meant to give a short overview of cavity QED. It has been pioneered by quantum optics on the experimental side and clearly constitutes the base on which superconducting circuit QED and photonic crystal cavity QED thrive[4]. Many of the ground-breaking experiments in circuit QED have been already successfully performed in cavity QED with real (Rydberg) atoms, others are genuinely new in the circuit QED community.

The basic idea of the field is to perform experiments where a two-level system (the atom) is strongly coupled to an electromagnetic field mode [95]. Strong coupling in this sense means that the coupling constant of the atom-field coupling corresponds to a time-scale that is much shorter than any inverse decoherence rates (e.g. cavity loss rates, atom dephasing and decay rates).

This strong coupling limit has been reached in optical systems using high-finesse cavities and ordinary optical atomic transitions [96]. Interesting quantum effects such as e.g. the coherent interaction of the atom with the light-field in the cavity have been observed [97–99]. However, due to the extremely fast dynamics of optical systems in the $10^{-15}s$-range, entanglement could not be directly observed. Also the coherent control by suitable laser pulses and electric/magnetic fields is challenging on these time-scales. This is one of the reasons why a sibling called microwave cavity QED emerged. Here, a stream of Rydberg atoms is sent through a microwave cavity, each of them interacting with the cavity field. Rydberg atoms are atoms with a very high principal quantum number $n = O(10^2)$. This has several consequences such as very large electron orbits that are very close to a classical electron orbit which have diameters in the μm range and very long decay times. The transitions of the valence electron in such a state can be addressed with microwaves rather than with light at optical frequencies. Another advantage compared to trapped ions is that the quantum systems are spatially separated by distances in the millimeter range easily allowing for individual addressing. In trapped ion systems the strong coupling limit can only be reached by placing the ions very close to each other which makes individual addressing very difficult.

The strong coupling and the use of microwave technology suggest to focus on experiments conducted with Rydberg atoms, to present the setup and the most important results. This is done in the following.

---

[4] For a good introduction see [94] and references therein. This review article also covers more experimental details than this fairly qualitative introduction.

Experimental Setup

Rubidium atoms for microwave cavity QED are usually prepared in Rydberg states by first effusing from an oven and then applying laser and radiofrequency pulses to them to prepare the circular level [100]. Afterwards, the atoms are velocity-filtered in order to obtain control over the interaction times and to guarantee repeatable conditions.

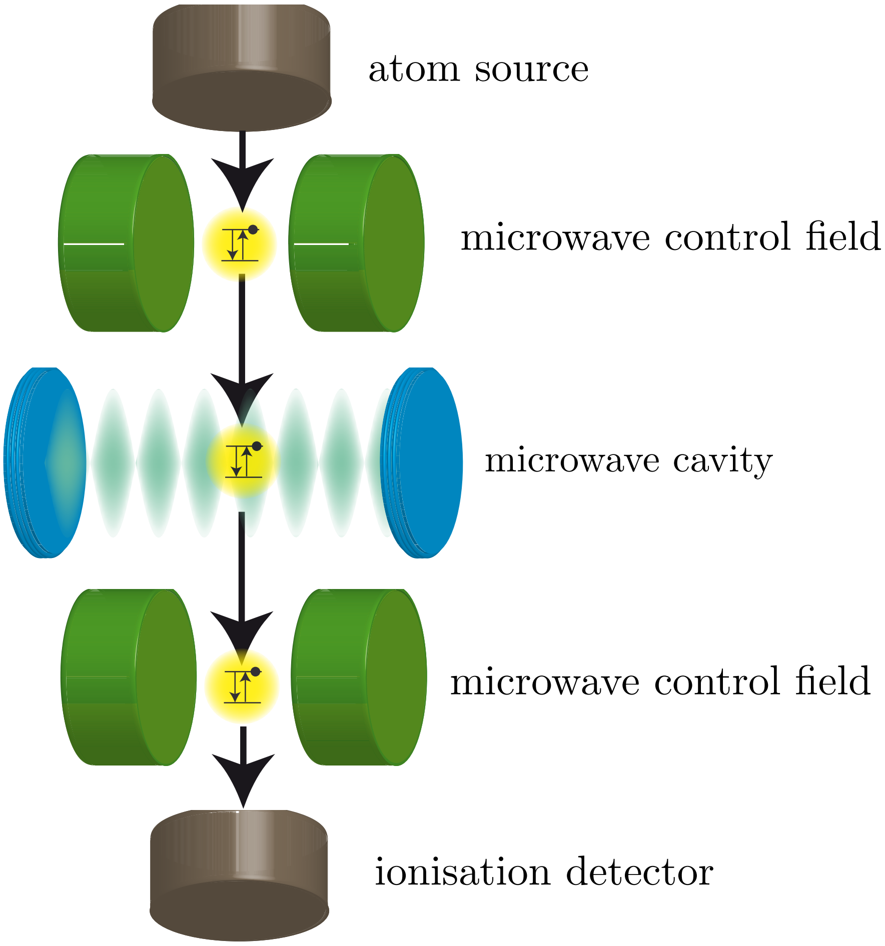

Figure 1.15: Schematic microwave cavity QED setup. Atoms (e.g. Rubidium) are effused from an oven, prepared in Rydberg states and velocity-filtered before they leave the atom source. Then they pass a first classical microwave control field which prepares the initial state of the atom. In the Fabry-Perot cavity they interact with a quantized microwave field according to the Jaynes-Cummings Hamiltonian before they leave the cavity, and, depending on the experiment, experience another control pulse. Finally, the atom state is determined using a field ionisation detector which can discriminate between the Rydberg states used as the atomic two-level system.

The atoms' initial state can then be controlled by applying a microwave pulse to them before they enter the superconducting microwave cavity. In the cavity they interact with the field mode according to the Jaynes-Cummings-Hamiltonian, both changing the atom and the field state. This leaves atom and field generally entangled when the atom leaves the cavity.

After it has left the cavity, the atom's state can be detected with high efficiency and precision, using a field ionisation detector.

The microwave cavity is a superconducting Fabry-Perot cavity with quality factors up to $Q = 3 \cdot 10^8$, corresponding to a photon lifetime of $O(1ms)$. Although the whole apparatus is cooled to $\approx 1K$ which corresponds to $O(1)$ thermal photons in the cavity, a procedure is needed in order to initialize the cavity in the ground state. Here, some atoms are sent through the cavity to absorb any thermal photon. Evidently, this cooling is temporary and limits the length of a single experimental sequence.

By suitably choosing microwave preparation pulses and interaction times with the cavity, many highly relevant experiments can be and have been performed. We will present the most promiment examples here without attempting to be complete.

Vacuum Rabi oscillations

Among the most prominent quantum effects are vacuum Rabi oscillations between an atom and the cavity involving entanglement of atom and cavity [101–103]. Here, during the time the atom is in the cavity, the initial excitation of the atom is swapped back and forth between the atom and the cavity. This can be readily seen from the Jaynes-Cummings-Hamiltonian Eq. (1.17) which after employing the rotating wave approximation, reads

$$\hat{H} = \hbar\omega \left(\hat{c}^\dagger \hat{c} + \frac{1}{2} \right) + \frac{\epsilon}{2}\hat{\sigma}_z + \frac{\hbar g}{2} \left(\hat{\sigma}^+ \hat{c} + \hat{\sigma}^- \hat{c}^\dagger \right).$$

As noted before (Sec. 1.5.1), this Hamiltonian has block-diagonal form with blocks of size 2x2, allowing for immediate diagonalizaion. Let us look at the block spanned by the coupled states $|n, \uparrow\rangle, |n+1, \downarrow\rangle$. Defining the detuning $\Delta \equiv \omega - \epsilon$, the eigenvalues read

$$\lambda_{1/2} \equiv \hbar\omega\,(n+1) \pm \frac{1}{2}\sqrt{\Delta^2 + (n+1)\,g^2}.$$

The corresponding eigenkets can be expressed as

$$\begin{aligned} |v_1\rangle &\equiv \sin\theta_n\,|n,\uparrow\rangle + \cos\theta_n\,|n+1,\downarrow\rangle \\ |v_2\rangle &\equiv \cos\theta_n\,|n,\uparrow\rangle - \sin\theta_n\,|n+1,\downarrow\rangle, \end{aligned}$$

which conveniently assures normalization. The angle θ_n is defined as

$$\tan 2\theta_n \equiv \frac{2g\sqrt{n+1}}{\Delta}.$$

Let us now assume that we initialize the system in the state $|\Psi(t=0)\rangle \equiv |n,\uparrow\rangle$ and ask for the probability $|\langle n,\uparrow|\,\Psi(t)\rangle|^2$ to return to this state after some interaction time t has elapsed. In the resonant case $\Delta = 0$, this probability is found to be

$$|\langle n,\uparrow|\,\Psi(t)\rangle|^2 = \cos^2\left(\frac{\sqrt{n+1}}{2}\,g\,t\right)$$

and the vacuum Rabi oscillations are plotted in Fig. (1.16).

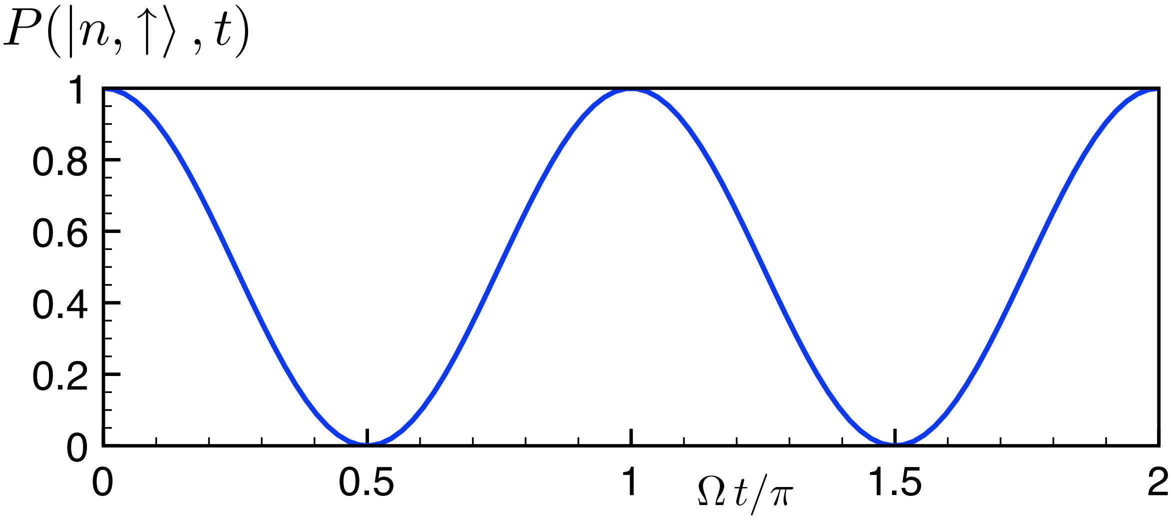

Figure 1.16: Vacuum Rabi oscillations between an atom and a cavity field mode. The plot shows the probability to find the atom in its excited state, given that we started in the excited state at $t = 0$. The frequency of oscillation is given by $\Omega \equiv \sqrt{n+1}\, g$.

Excitations are swapped at a rate given by the vacuum Rabi frequency $\Omega = \sqrt{n+1}\, g$. The interaction time t determines the state of the system when the atom leaves the cavity. Except for interaction times corresponding to integer multiples of π/Ω, the resulting state will be non-locally entangled, meaning that the entanglement between atom and cavity persists even when the atom has left the cavity. It can then be used to confer quantum information e.g. to a second cavity. Another possibility is to use this scheme to entangle subsequent atoms.

It is interesting to note that from the period of the vacuum Rabi oscillations, one can infer the number states of the cavity taking part in the oscillation by virtue of the $\sqrt{n+1}$ component in the frequency. A common method is thus to perform a spectral analysis (e.g. by Fourier transform) of the vacuum Rabi signal as depicted in Fig. (1.16). If the frequency components show a $\sqrt{n}$ pattern, this is a clear signature that vacuum Rabi oscillations based on Jaynes-Cummings dynamics are present in the system and that the electromagnetic field in the cavity is really quantized.

Generation of non-classical field states

Non-classical field states, e.g. Fock states, can be constructed by tuning the interaction time to e.g. $t_{int} = \pi/2\Omega^{-1}$. This leads to the conversion of an excitation in the atom to a photon in the cavity. Atom and cavity remain in a product state after the interaction. If done repeatedly, higher Fock states can be generated easily with this method. A similar method has been most recently used to construct arbitrary superpositions of photon Fock states using a phase qubit coupled to a microwave resonator. We will comment on this experiment in section 1.5.4.4 in more detail.

Observation of quantum jumps

Assuming the cavity has a small, but finite temperature, temperature driven creation of a photon competes with the usual cavity loss rate. Sending a stream of Rydberg atoms through the cavity at a rate fast compared to the cavity loss rate, it is possible to observe the quantum jumps of the photon field in the cavity in real-time [104]. When averaging the resulting jumpy traces, one nicely recovers the thermal population of the field mode known from e.g. an ensemble average master equation description.

The experiment is conducted as follows. The two zones before and after the cavity where microwave fields can be applied to the atoms, are used as a Ramsey interferometer. The first zone is used to apply a Hadamard gate (a $\pi/2$-pulse) to the atoms which leaves them in a superposition of ground and excited state

$$|\Psi_0\rangle \equiv \frac{1}{\sqrt{2}} \left(|\downarrow\rangle + |\uparrow\rangle \right) .$$

Employing the intuitive view on the Bloch sphere (see Fig. (1.17)), the qubit state vector is now precessing in the x-y plane. Unlike the vacuum Rabi experiment, the atom and the cavity mode are now detuned which prohibits the exchange of population.

The interaction with the cavity field shifts the qubit energy splitting which leads to a cavity-state dependent phase in the x-y plane that the qubit experiences. After the qubit has left the cavity, another $\pi/2$-pulse is applied to the qubit which, depending on the position of the qubit state vector in the x-y plane of the Bloch sphere, can lead to the atom being in any superposition of excited and ground state. Generally, one observes sinusoidal interference fringes for e.g. the excited state probability when the phase shift in between the two Ramsey zones is varied continuously.

If the atom detector is sufficiently efficient, it is thus possible to infer whether the cavity was in the state $|1\rangle$ or $|0\rangle$ when the atom passed. Such a detection event then marks a single data point in a quantum jump trajectory as recorded in [104][5]. In principle this experiment can also be viewed as a Quantum-Non-Demolition (QND) [105, 106] detector for the presence of a photon in the cavity [107]. In a QND measurement, repeated measurements give the same results. This is the case here if we disregard the loss rate of the cavity. In order for the measurement to be QND, the photon number state has to be fixed (the cavity field is projected onto a number state) while the phase of the cavity field is completely randomized. For more details on QND measurements and measurement theory as well as simulation please see Sec. (4).

---

[5] Note that in the actual experiment the cavity state was determined by a majority vote among 8 consecutive atoms impinging on the detector.

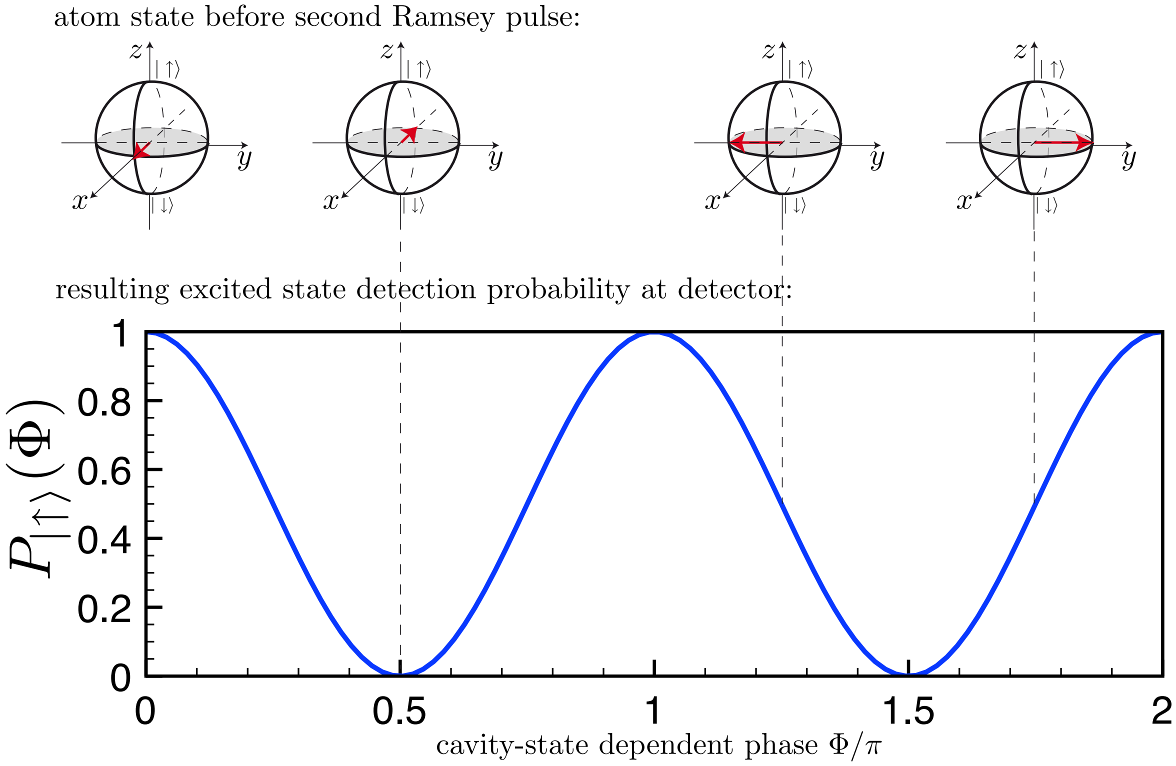

Figure 1.17: This illustration shows Ramsey fringes of an atom due to a cavity state-dependent phase shift. The atom state after passing the cavity and before the second $\pi/2$- Ramsey pulse is visualized on the Bloch sphere while below the probability to detect the atom in the excited state after the second Ramsey pulse is shown. The first Ramsey pulse has put the atom state vector into the x-y plane where it precesses with a frequency given by the atom level splitting. This splitting (if the cavity and atom are detuned from each other such that they do not exchange population) depends on the cavity state (and the detuning). Both detuning and interaction time of the atom with the cavity can be tuned such that e.g. the difference in phase between the cavity being in the $|0\rangle$ and in the $|1\rangle$ state leads to a phase differnce $\Phi = \pi$, yielding a maximum interference contrast. This makes it possible to QND-detect the state of the cavity with a single atom and thus to record quantum jump trajectories.

Controlled Phase gate as example for a universal two-qubit gate

Furthermore, a controlled-phase universal quantum two-qubit gate [108] has been demonstrated [109]. This gate can be implemented as follows: First the cavity is prepared in the one photon state $|1\rangle$ in the way just described above. Then, an atom in state $|\Psi_0\rangle$ is sent through the cavity with the interaction time adjusted such that it performs a full 2π-Jaynes-Cummings swap. Behind the cavity, another Ramsey pulse is applied and the atom detected. The action of the gate is the following: If, and only if the cavity is in the $|1\rangle$ state, the $|\uparrow\rangle$ −component of the atom state will suffer a phase shift of π, while if the cavity is in the vacuum, no state change takes place.

In principle the setup is very similar to the Ramsey interferometric setup but with the crucial difference that atom and cavity are in resonance while for the Ramsey experiment they are detuned.

Prospects for quantum information processing

In addition to a universal two-qubit gate, the full control over the atom state equivalent to the ability to perform arbitrary local rotations, is another requirement for quantum computation. This can be done with the Ramsey pulse zones adjacent to the cavity.

However, the prospects of these systems with respect to quantum information applications seem to be fairly limited. The most prominent limitation is the missing concept to scale the system to many qubits. While microwave cavity QED in principle allows to use the photon field inside the cavity or the atom as a qubit, it is desirable to have qubits where one can perform many operations on. This would either require many cavities or much longer interaction times within one cavity[6].

Taking the step from limited to infinite interaction times is the key improvement which circuit QED offers compared to microwave 'Rydberg' cavity QED or cavity QED at optical frequencies. Therefore circuit QED seems to be more adequate as a candidate for quantum computation applications.

---

[6] There are proposals about so-called 'sequential codes' which might relax this contraint a bit.

1.5.3 Cavity QED with quantum dots and photonic crystals

Compared to cavity QED experiments with superconducting circuitry, experiments with self-assembled quantum dots and photonic crystal cavities [110–112] are still in their infancy. However, given the remarkably long (spin)-relaxation times in the ms-range [113] measured in these systems, they are promising candidates to perform quantum memory, computation and communication operations. We will present the basic ingredients of experiments in this field and the experimental state of the art as far as cavity QED is concerned.

Self-assembled quantum dots as artificial atoms/qubits

In contrast to the commonly known way to engineer quantum wells/dots from a GaAs/AlGaAs heterostructure by depleting the two-dimensional electron gas beneath some gate electrodes, no gates are needed at all to form the dot.

The idea here is the following: By applying a very thin coating of e.g. InGaAs on top of a e.g. GaAs substrate, the slight mismatch of lattice spacings between the two materials induces a strain at the boundary which causes the thin, equally distributed upper layer to spontaneously relax into little spatially separated and randomly distributed droplets on the substrate, forming little 'hills' (this process is termed 'self-assembly', see Fig. (1.18)).

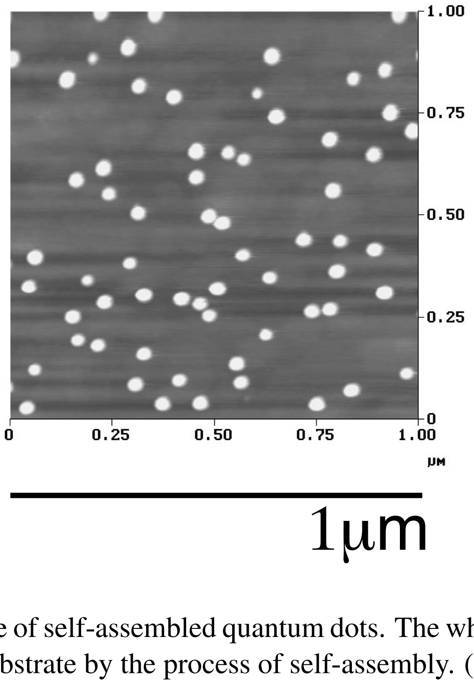

Figure 1.18: Micrograph image of self-assembled quantum dots. The white spots are the quantum dots randomly distributed on the substrate by the process of self-assembly. (Courtesy of Dirk Englund)

These hills locally change the band structure of the combined material, acting as a quantum well. As no gate electrodes are needed to trap e.g. excitons (bound electron-hole pairs) in such a dot, the coherence times do not suffer from e.g. gate charge fluctuations. One can then e.g. optically probe excitonic charge and spin degrees of freedom. The transition frequencies of these excitons are in the frequency interval of visible light.

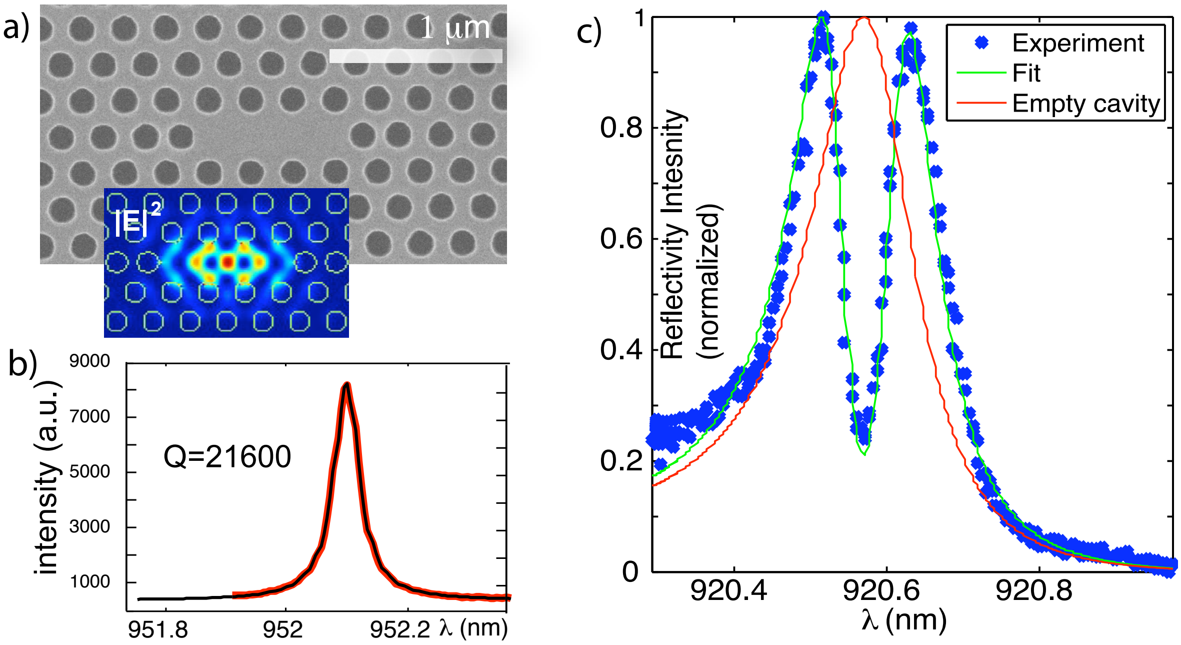

Figure 1.19: Part (a) shows the electric field intensity distribution in a photonic cavity formed by the interruption in the surface pattern. These cavities reach high Q factors as indicated by the resonance curve (part (b)). When a self-assembled quantum dot is located inside the cavity, it can couple to a cavity mode and the vacuum Rabi splitting can be observed (part (c)). (Courtesy of Dirk Englund)

Photonic bandgap cavities as on-chip resonators

In order to perform cavity QED experiments, one needs to engineer an on-chip cavity with a resonance frequency in the visible light wavelength domain. This can be done by using what is otherwise known as a 'meta-material'.

One uses e.g. lithography to pattern the surface of the heterostructure in such a way that electromagnetic waves travelling along the surface are strongly suppressed (this is called a photonic bandgap). If the pattern is interrupted at a certain site (see Fig. (1.19)), one has created a localized 'exception' to the rule that visible light waves cannot live on the surface of the structure and thus formed a cavity. If the material already has self-assembled quantum dots on it before applying the cavity pattern, chances are that a dot is right inside the cavity. In this case, cavity QED experiments can be performed with the sample.

Strong coupling of quantum dots to photonic crystal cavities

In [111, 112, 114] the vacuum Rabi splitting of a self-assembled quantum dot's excitonic charge excitation with a photonic bandgap cavity has been measured and confirmed that those system operate in the strong coupling limit (see Fig. (1.19)).

QND detection of the cavity photon population

A Kerr-type coupling $g\hat{n}_1\hat{n}_2$ between two cavity modes has been used to successfully detect that one photon was present in the cavity (on average) [115]. Although not a photon detector or counter, this experiment nicely illustrates the general applicability of the schemes investigated in this thesis. Based on the same type of coupling, I will show the possibility of itinerant single photon detection in circuit QED in Sec. (6). Although there is still considerable experimental ground to cover until single-shot photodetection will be possible in these systems, we will discuss the conditions and prerequisites in more detail in Sec. (6).

1.5.4 Cavity QED using superconducting circuits

1.5.4.1 Superconducting on-chip microwave resonators

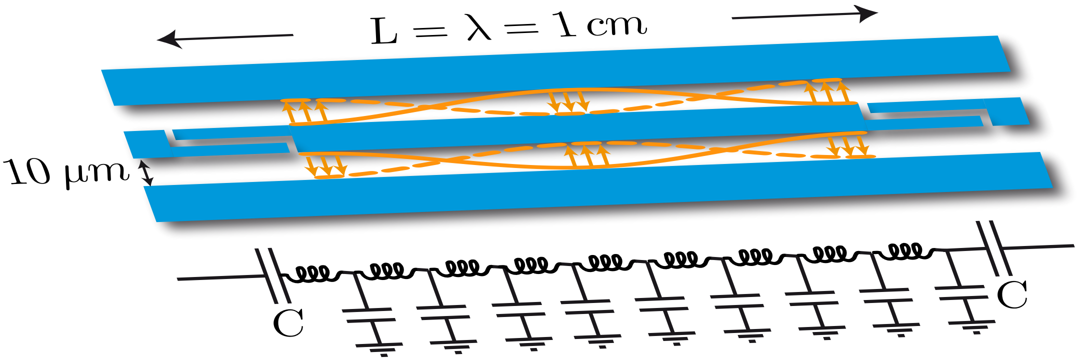

Figure 1.20: A transmission line resonator has the topology of a coaxial cable that has been cut in the middle. It consists of a center strip which is coupled to a transmission line on one or both sides by coupling capacitors C while being separated from ground-planes on either side by a gap which is about $10\mu m$ wide. The length of the resonator is in the cm-range which corresponds to GHz frequencies. Due to its extreme aspect ratio, it can be modeled by a one-dimensional network of inductors which are capacitively coupled to ground. The electric field distribution for one mode of the resonator is indicated in orange.

In order to perform cavity QED experiments with superconducting circuits which are integrated on the surface of a chip, suitable resonators are needed. As the artificial atoms (qubits) we have discussed have resonance frequencies in the GHz-range, resonator dimensions of about $1cm$ are needed. The resonator type we are going to discuss is called a co-planar waveguide (or transmission line) resonator and is the most commonly used in present-day experiments. Fig. (1.20) illustrates its dimensions and the basic physics. It can be viewed as a coaxial cable which has been cut such that there is a center conductor which is separated by an insulator from ground planes at either side. The center conductor has been cut in two places, forming an isolated strip about $1cm$ long. The resonator is then formed in between the cuts (which are coupling capacitors to the rest of the transmission line through which the cavity can be driven/read out).

Quantization of a one-dimensional transmission line resonator

The analogy to a coaxial cable extends even further, namely the lumped element network used to describe a coaxial cable can also be used to model a transmission line resonator (see Fig. (1.20)). This well-known derivation can e.g. be found in [78]. Let the transmission line resonator be of length L with a capacitance to ground per unit length given by c. The inductance per unit length be denoted by l. The Lagrangian density then reads

$$\mathcal{L} \equiv \frac{l}{2} j(x,t)^2 - \frac{1}{2c} q(x,t)^2, \tag{1.18}$$

where $q(x,t)$ is the charge density along the center conductor and $j(x,t)$ is the current density. The coupling to the rest of the transmission line has to be ignored at this stage, but could be phenomenologically added either classically into the equations of motion or in a Lindblad master equation in the quantum case to include losses or driving of the cavity. In order to simplify the Lagrangian (1.18), we use the one-dimensional continuity equation which states that

$$\frac{\partial}{\partial x} j(x,t) = -\frac{\partial}{\partial t} q(x,t).$$

Thus, the current density can be expressed by the charge density via

$$j(x,t) = -\frac{\partial}{\partial t} \int_{-L/2}^{x} dx' \, q(x',t) =: -\frac{\partial}{\partial t} \theta(x,t).$$

For convenience, we have introduced the new variable $\theta(x,t)$ in terms of which the Lagrangian reads

$$\mathcal{L} = \frac{l}{2} \dot{\theta}^2(x,t) - \frac{1}{2c} (\partial_x \theta(x,t))^2.$$

The Euler-Lagrange equation

$$\partial_\mu \left(\frac{\partial \mathcal{L}}{\partial \left(\partial_\mu \theta \right)} \right) - \frac{\partial \mathcal{L}}{\partial \theta} = 0$$

in this case reduces to the wave equation

$$\frac{\partial \theta(x,t)}{\partial t^2} = -\frac{1}{v^2} \frac{\partial \theta(x,t)}{\partial x^2}$$

which can be solved e.g. by a separation of variables upon imposing the boundary conditions $\theta(-L/2,t) = \theta(L/2,t) = 0$ for the spatial part. Teh velocity is given by $v \equiv \sqrt{1/(lc)}$.The result shows the typical even and odd modes of a resonator of length L with resonance frequency $\omega_n \equiv n\pi v/L$

$$\theta(x,t) = \sqrt{\frac{2}{L}} \left[\sum_{\text{nodd}} \Phi_n(t) \cos\left(\frac{n\pi}{L} x \right) + \sum_{\text{neven}} \Phi_n(t) \sin\left(\frac{n\pi}{L} x \right) \right].$$

When inserting this mode expansion back into the Lagrangian density, we can explicitly perform the spatial integration to obtain the Lagrangian (function)

$$\mathcal{L} = \sum_n \frac{l}{2} \dot{\Phi}_n(t) - \frac{1}{2c} \left(\frac{n\pi}{L} \right)^2 \Phi_n^2(t)$$

which is the expected set of harmonic oscillators that can be immediately quantized to

$$\hat{H} = \sum_n \hbar \omega_n \hat{a}_n^\dagger \hat{a}_n,$$

where $\hat{\Phi}_n(t) = \sqrt{\hbar \omega_n c/2}\, L/(k\pi) \left[\hat{a}_n + \hat{a}_n^\dagger \right]$ and its conjugated momentum ($\pi_n \equiv l\dot{\Phi}_n$) reads $\hat{\pi}_n(t) = -i\sqrt{\hbar \omega_n l/2}\, \left[\hat{a}_n - \hat{a}_n^\dagger \right]$. The spatial mode distribution can then be used to calculate the coupling qubits which can be inserted into the gap between the center conductor and the ground-planes (see e.g. Figs. (5.1,1.23)).

Coupling to charge qubits

The coupling to qubits placed inside the resonator is either capacitive (via the electric field, in case of charge qubits) or inductive (via the magnetic field, in case of flux qubits). For charge qubits, the Jaynes-Cummings coupling to the resonator is given by

$$\hbar g \equiv \frac{C_g}{C_J + C_g} e \sqrt{\frac{\hbar \omega_n}{cL}},$$

where C_g is the capacitance between the charge qubit and the transmission line resonator and C_J is the capacitance of the Josephson Junction of the qubit. The extreme aspect ratio confines the mode to such a small volume that vacuum field strengths of $O(1V/m)$ can be achieved which results in a coupling orders of magnitude greater than e.g. realized in experiments with Rydberg atoms. Most recently, the qubit-resonator coupling has been pushed to values of $2\pi \cdot 173.5\, MHz$ exceeding all dissipative rates in the system by two orders of magnitude[2].

Quality factors

Owing to the superconducting low-loss material and the freedom in the design of the coupling capacitors at either end of the resonator, a large parameter range is accessible for the typical decay rates of these resonators. They range from only a few kHz (high quality factor $Q = O(10^6)$, e.g. for many coherent operations between the cavity and the qubits) to a few MHz (low quality factor, e.g. for fast readout of a qubit) and can be chosen suitably depending on the experiment [116].

1.5.4.2 Charge qubits/transmon qubits

Soon after first theoretical proposals had been published [78, 117, 118], the Yale group started an impressive series of experiments which from 2004-2008 set the pace in superconducting circuit QED. More recently, the Wallraff group at ETH Zürich (a Yale spin-off) and the group at Saclay have met the pace and performed interesting experiments as well. In the following we will briefly present some of the most relevant experiments.

Strong coupling between a charge qubit and a microwave resonator

Strong coupling between a charge qubit and the coplanar waveguide resonator has been first reported in [79], where a Jaynes-Cummings coupling of $2\pi \cdot 17 MHz$ between qubit and resonator was measured. More recently this value has been pushed to values of $2\pi \cdot 173.5\, MHz$ [2]. Strong coupling here means that the coupling is much larger than any dissipative rates in the system. This yields Vacuum Rabi peaks that are separated by much more than a linewidth and thus are clearly visible.

Single atom laser

In [119], the Nakamura group showed that a single atom (a Cooper pair box qubit) coupled to a coplanar-waveguide resonator, can emit coherent, monochromatic microwave radiation. Typical lasing characteristics such as amplification and purification (line-width of the emitted radiation shrinks) have been observed. Only recently, comprehensive theory has been brought forward [120] which nicely explains all features of lasing and cooling in this setup.

Dispersive resolution of resonator number states

While the analysis of the number state distribution in the resonator can be done via the resonant qubit-cavity Jaynes-Cummings interaction (thus inevitably altering the resonator state), the very same thing can also be done dispersively utilizing the AC-Stark effect.

Starting from a Jaynes-Cummings Hamiltonian Eq. (1.17) and assuming strong detuning of qubit and cavity, one can transform the Hamiltonian using a unitary transformation $U \equiv \exp\left[\frac{g}{\Delta}\left(a\sigma^{+} + a^{\dagger}\sigma^{-}\right)\right]$ and keeping terms up to second order in g to a version that makes the effects of the ac-Stark shift/Lamb-shift clearly visible [78]:

$$H \approx \hbar\omega a^{\dagger}a + \frac{\hbar}{2}\left[\epsilon + 2\frac{g^{2}}{\Delta}(a^{\dagger}a + \frac{1}{2})\right]\sigma^{z}.$$

This result suggests that if the resonator is populated with a state consisting of more than just one number state, the qubit resonance in spectroscopy should be split up into equally spaced lines. To resolve those lines, the dispersive coupling $\frac{g^2}{\Delta} \approx 2\pi \cdot 17MHz$ has to be larger than the qubit linewidth (here $\approx 2\pi \cdot 1.9MHz$), a condition which has been fulfilled in [121], where this dispersive number splitting has been first observed. There is also an accompanying theory paper [122] interpreting the measurements in detail.

Single Photon generation

In this experiment [123], a cavity with asymmetric coupling to the transmission line has been coupled to the qubit in the same way as in previous experiments. The modification is that the input port for driving and spectroscopy tones has a much lower capacitance and hence decay rate than the output port.

Driving the qubit (which is tuned almost into resonance with the cavity) with Rabi (π)-pulses, the qubit, once excited, has a very large chance (enhanced by the Purcell effect) to radiatively decay into the cavity mode, resulting in a single photon inside the cavity.

Then, due to the fact that the cavity's output port has a very large decay rate, the chance that the photon will leave the cavity through the output is very high once the qubit excitation has been transferred to the cavity via spontaneous emission.

By carefully separating the signals of driving pulses and resulting single photons stemming from the qubit's spontaneous emission, an average efficiency of this single photon source of 39% has been established. However, as a remark to this experiment it should be noted that - strictly speaking - no evidence for a single photon has ever been presented. Due to the lack of a single-shot readout of the qubit, it only has been possible that on an ensemble average basis, a single photon has been generated with the reported efficiency. The missing ingredient is a single-shot photo-detection scheme which we have proposed and analyzed in Sec. (6).

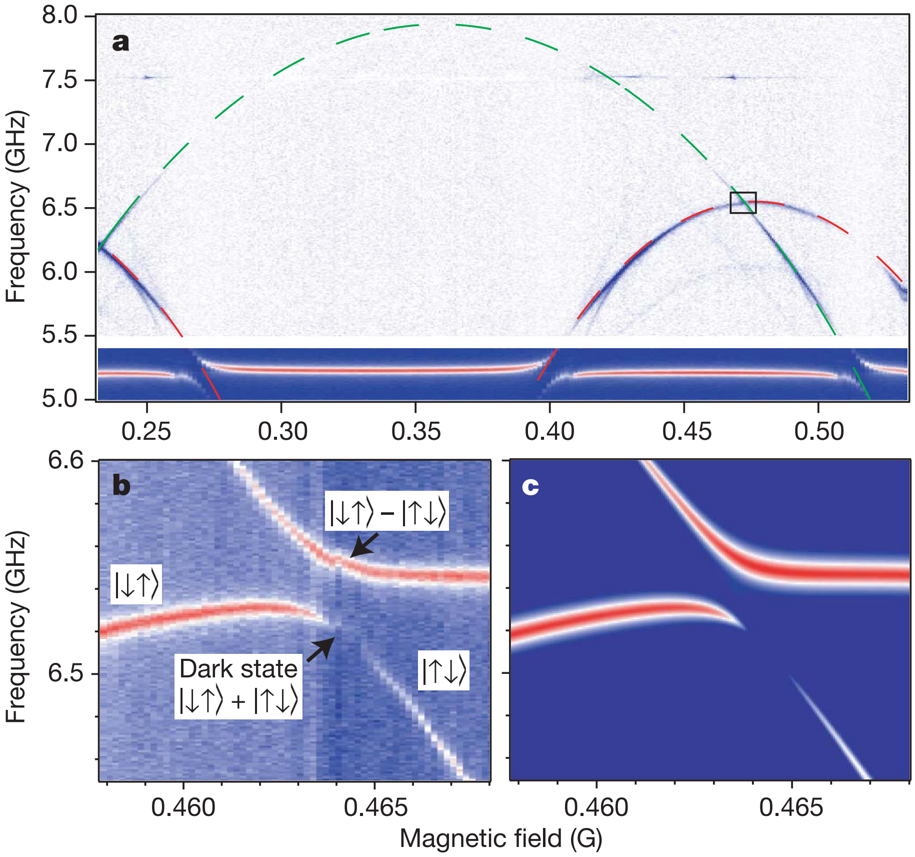

Figure 1.21: Two-qubit spectroscopy data showing the cavity-mediated qubit-qubit coupling. Part (a) shows the qubit transition frequencies as functions of the magnetic field, part (b) is a blow-up of the avoided crossing of the two- qubit arches which nicely fits the theoretical prediction (part (c)). (Courtesy of J. Majer et. al.)

Coupling two qubits via a cavity

Once the experiments using single qubits had advanced significantly, the next step towards a quantum computing application has been made by coupling two qubits via the same cavity using it as a bus [82]. As has been shown in [12], the Jaynes-Cummings interaction generates a flip-flop Hamiltonian between two qubits which are both detuned from the cavity, but in mutual resonance. The two qubits will exchange their population at a rate given by the dispersive coupling $J \equiv \frac{g^2}{\Delta}$ (For more details see Sec. 2 and [82]). This interaction is the natural generator of an iSWAP gate, which is, up to phases, equivalent to a SWAP gate. Aborting this gate at half the time realizes the so-called $\sqrt{\text{iSWAP}}$ gate which is a universal entangling two-qubit gate equivalent to a CNOT gate from a quantum information processing perspective. During the whole process, the cavity is never populated (except for virtual excitations).

Note that in this experiment no local flux or charge control lines (as suggested in [124] and later realized in [1, 125]) have been used. Instead, the qubits' transition frequencies were tuned pseudo-independently using the following trick: By manufacturing one qubit's Josephson-loop area significantly larger than the others, one of the effects is that the period of their transition frequency when ramping the magnetic field is different. This causes the arches to intersect at some value of the magnetic field. Here, an avoided crossing was observed spectroscopically by the usual transmission measurements which confirmed the cavity-mediated qubit-qubit coupling in excellent agreement with the theoretical predictions (see Fig. (1.21)).

Testing higher order Jaynes-Cummings transitions with high drive powers

The Jaynes-Cummings model, simple as it is, still holds for enourmously high driving powers as demonstrated in [2]. Here, many higher-order transitions between eigenstates of the Jaynes-Cummings model (up to seven photons in the cavity) have been observed and exactly matched to the theoretical predictions which have been obtained by solving a simple Lindblad-master equation taking up to seven resonator states into acount (see Fig. (1.22)).

Implementation of two-qubit algorithms

Building on the work where a two-qubit iSWAP gate was first realized [82], the design has been successfully completed by adding local flux control lines running past each qubit, allowing to tune the qubits' resonance frequencies independently and on a ns timescale [1].

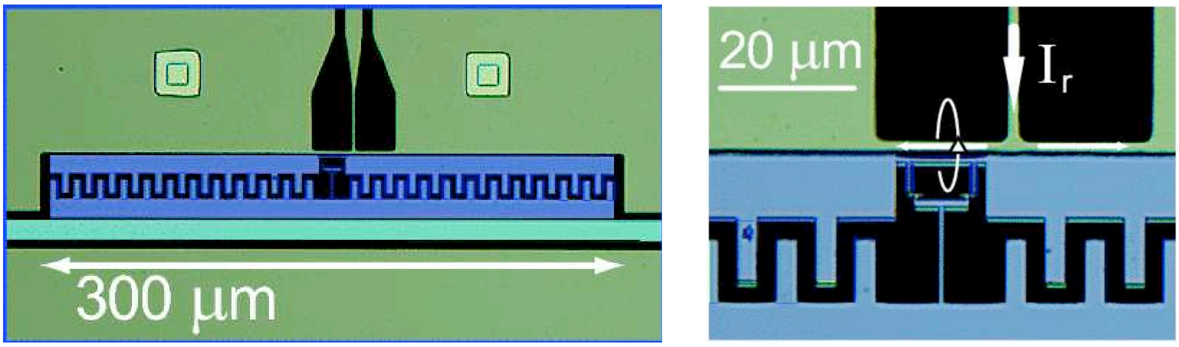

Figure 1.23: SEM micrograph of transmon qubits with local flux control lines [1]. (Courtesy of Leonardo di Carlo et al.)

Here, the Grover database search algorithm [8] as well as the Deutsch-Josza algorithm [10, 126] have been implemented. However, the main achievement in this experiment [1] is clearly the capability to perform single qubit gate sequences independently on the two qubits (owed to the local flux control).

These algorithms applied to two qubits remain rather academical in terms of 'real' application (they do only consist of O(5) gates anyway) and so this experiment is to be viewed rather as a proof-of-principle showing the possiblities offered by the newly introduced local flux control. In order to really perfom any useful computation, systems scaled up to at least

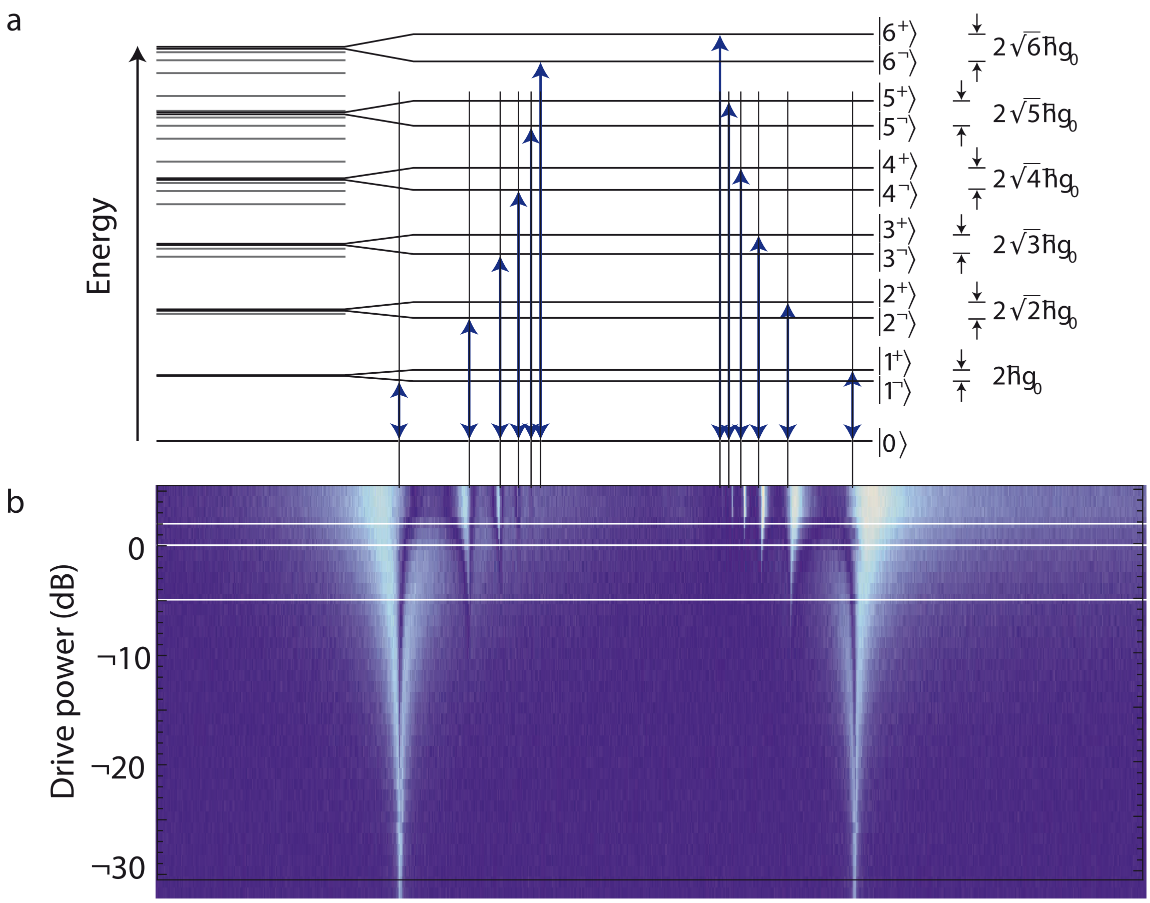

Figure 1.22: Higher-order Jaynes-Cummings transitions observed in [2]. Part (a) illustrates the measured transitions in the level diagram, part (b) shows the spectroscopy signal as a function of frequency (horizontal axis) and drive power (vertical axis). (Courtesy of L. Bishop et al.)

$O(100)$ qubits are needed. In this thesis, I will present an architecture for such a scalable system (see Sec. 2).

Three qubits coupled to a resonator

Combining three transmon qubits with local flux control at each qubit, the Wallraff group managed to explore in detail the multi-atom extension of the Jaynes-Cummings-model, the so-called Tavis-Cummings-Model [127]. One of the highlight features of this model is that the collective qubit-cavity coupling scales with $\sqrt{N}$,where N is the number of atoms/qubits. In this experiment [125], first one qubit, then two and at last all three qubits were tuned into resonance with the cavity and the resulting avoided crossing with the cavity line analyzed using transmission spectroscopy. The $\sqrt{N}$ scaling was nicely observed, confirming yet again how good a model the Jaynes-Cummings/Tavis-Cummings model is to describe the circuit QED systems.

Observation of Lamb shift - corrections to the Jaynes-Cummings dynamics

In the dispersive limit, the qubit-resonator dynamics is usually well-approximated by a RWA treatment of the Jaynes-Cummings interaction (see Sec. (1.5.1)). Similar to the ac-Stark shift interpretation of the dispersive energy shifts, given that the resonator is in its vacuum state, the very same effect can be interpreted as the Lamb-shift [128, 129] an atom experiences due to the vacuum energy density of the electromagnetic field.

While a dispersive treatment suggests that this energy shift scales with $\propto \frac{g^2}{\Delta}$, where g is the qubit resonator coupling and Δ is their mutual detuning, significant deviations from this scaling have been observed in this experiment in the Wallraff group [130]. Remarkably, when taking into account the counter-rotating terms dropped in the RWA, i.e. by numerically diagonalizing Eq. (1.17), the measurements and theoretical predictions are in excellent agreement.

1.5.4.3 Flux qubits

Flux qubits as introduced in 1.4.2 have been successfully coupled to on-chip microwave resonators only recently [60, 68, 131]. Here, the qubit was inductively coupled to an on-chip LC-oscillator. Qubit spectroscopy showed a strong qubit-cavity coupling of the order of $0.2GHz$ while all loss rates in the system are of the order of $0.01GHz$. Thus, vacuum Rabi oscillations indicating coherent evolution of the coupled qubit-cavity system and a hallmark of the so-called strong-coupling regime, could be observed.

In another experiment, the selection rules stemming from the symmetry/asymmetry of the flux qubit potential have been extensively studied in a two photon probe experiment [132].

1.5.4.4 Phase qubits

Experiments using phase qubits have suffered from their large and thus impure Josephson junctions for a long time. As already explained at length in 1.4.1, this had limited coherence times to a degree that experiments coupling them coherently to resonators were not reachable. However, in 2007, breakthrough improvements to both fabrication as well as materials [133] have jump-started circuit QED experiments with phase qubits. Here we are going to present the most prominent examples.

Coherent coupling of two qubits

Building on the experience gathered with an experiment in 2006 which coupled two phase qubits capacitively [134], simple capacitive coupling was replaced by a coplanar-waveguide resonator with the qubits at either end [41]. It was demonstrated that an excitation can be transferred back and forth between the qubits indirectly via their interaction with the cavity. The protocol for the state transfer is the following: One starts with both qubits and the cavity in the ground state and both qubits detuned from each other and the cavity. One qubit (qubit A) is pulsed into the excited state, then brought into resonance with the cavity for a time $t = \pi/g$, where g is the Jaynes Cummings coupling as introduced in Eq. (1.17). This will transfer the excitation fully into the cavity, leaving qubit A again in the ground state. After qubit A has been detuned again, qubit B is brought into resonance with the cavity for the same time $t = \pi/g$, yielding a complete cavity-mediated state transfer between the qubits. Similarly, by varying the interaction time and the sate of qubit A when starting the sequence, the qubits can as well be entangled or two-qubit gates - such as a CPhase gate (see Sec. 3.2) - performed.

High-fidelity single qubit gates

Single-qubit gates are one of the crucial ingredients for any quantum computing application. Consequently, it is necessary to show that a given architecture allows for individual addressing and at the same time a high fidelity for arbitrary single qubit gates (local rotations). In [135], the Martinis/Cleland group made the effort and managed to account for all gate and measurement errors and improved the single-qubit gate fidelity to a level of 0.98 setting the record for gate fidelities in solid state systems. The remaining infidelity can be fully explained by qubit relaxation and thus leaves room for further optimization (e.g. using optimal control pulse shaping techniques).

Generation and measurement of arbitrary resonator states

With excellent control of single-qubit rotations and built-in fast qubit readout and strong coupling to microwave resonators already demonstrated, the Martinis/Cleland group set a new reference [136, 137] for the quality of non-classical state-engineering not only in superconducting circuits but also when comparing to quantum optics. The basic idea is to pulse the qubit into its excited state and transfer the excitation to the resonator, thereby adding photons one-by-one and climbing the ladder of photon-number states in the resonator. This has been demonstrated up to photon numbers of $O(20)$. The presence of a number state was directly confirmed by analyzing the period of the resulting vacuum Rabi oscillations between the qubit and the resonator which scales with the $\sqrt{n}$ of the photon number as shown in Sec. (1.5.2). This scaling with the square root is shown in Fig. (1.24).

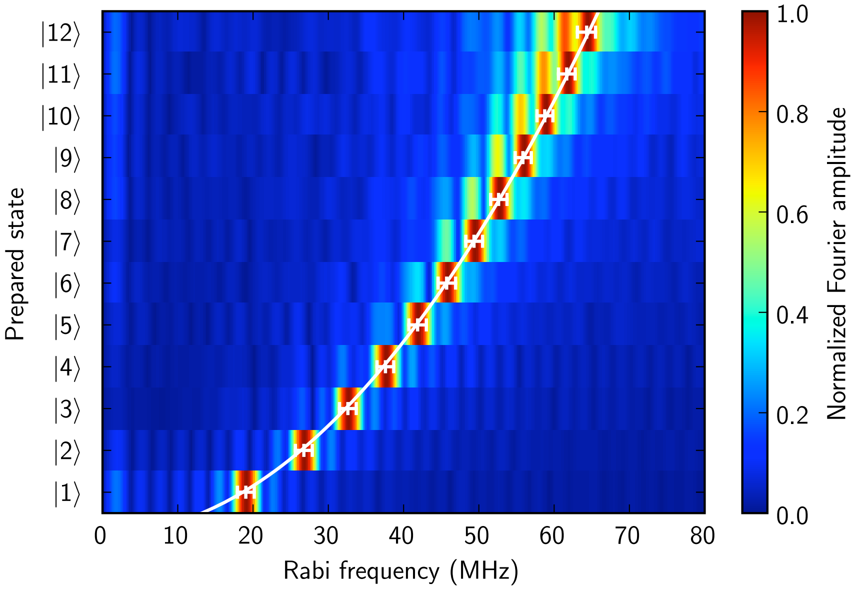

Figure 1.24: Fourier transform of vacuum Rabi oscillation signal depending on the prepared resonator state. The $\sqrt{n}$ scaling can be clearly observed which makes this experiment proof for the creation of non-classical field states using superconducting phase qubits and on-chip microwave resonators. (courtesy of Max Hofheinz et al.)

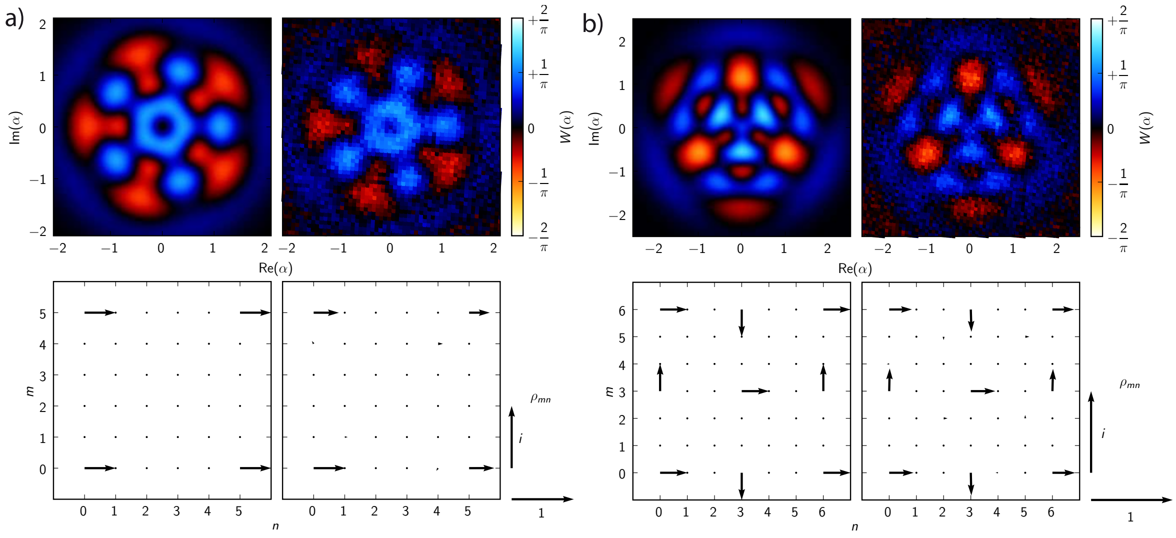

Figure 1.25: Wigner function and density matrix comparison of theory and experiment for different non-trivial superpositions of resonator number states. Part (a) shows the state $|0\rangle + |5\rangle$, part (b) shows the state $|0\rangle + i\,|3\rangle + |6\rangle$. (courtesy of Max Hofheinz et al.)

However, the possiblities to construct states go far beyond simple photon number states. In this experiment[7], an arbitrary resonator state can be constructed. The corresponding, possibly complex pulse sequence can be automatically determined by a straightforward state decompilation protocol M. Hofheinz et al. have developed. To confirm the quality of the state synthesis scheme, the complete Wigner function was reconstructed and excellent agreement to the theoretical prediction was found (see Fig. (1.25)).

---

[7] unpublished results submitted to Nature Physics. Presented by Max Hofheinz/Andrew Cleland at the QDDJ Conference at Lago di Garda, Italy (Oct. 2008), DPG march meeting (March 2009) and the CeNS Winterschool (March 2009, St. Christoph, Austria).

Chapter 2

The Cavity Grid - a scalable architecture for quantum computation

Circuit QED experiments have aimed at offering a platform for quantum computational tasks from the beginning [78]. Scalability is one of the di Vincenzo criteria (see Sec. 1.2) to be met before being able to perform useful tasks such as the factorisation of large numbers or efficient database search. In this chapter, we propose an architecture for quantum computing based on superconducting circuits.

We were inspired by early-day crossbar geometries in classical computing like e.g. magnetic core memory, where the current through intersecting wires running through magnetic loops allowed to individually address any bit on the grid to store and read out information (see Fig. (2.1)). Later on, cross-bar geometries were e.g. revived in molecular electronics as well as in addressing of pixels in early LCD displays.

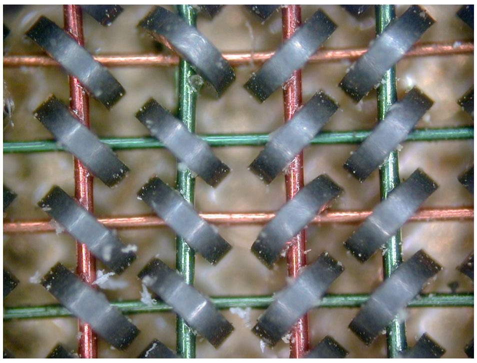

Figure 2.1: Photograph of a magnetic core memory array. The current sent through a pair of crossing wires can be used to induce a magnetic field at the crossing location which can be used to write or read out the magnetization of the magnetic loop at the crossing point. Magnetic core memories were widely used in the 1950s. It is the earliest form of so-called random access memory (RAM) in contrast to other, e.g. tape-based sequential memory architectures. (Courtesy of H.J. Sommer III, Professor of Mechanical Engineering, Penn State University)

As demonstrated e.g. in [82], transmission line resonators can be utilized as a quantum bus which offers a selective, global coupling between all qubits in the resonator. However, as we will argue, the number of qubits which can be placed inside a single resonator, is very limited and far from a number that satisfies the requirement of scalability. Consequently, we exploit the topological advantages of a crossbar geometry compared to e.g. nearest neighbour coupling schemes like in trapped ions and propose a scheme where on-chip planar microwave resonators are arranged in a two-dimensional grid with a qubit at each intersection. This allows any two qubits on the grid to be coupled at a swapping overhead independent of their distance. As it turns out, all fault-tolerant quantum computation schemes rely on reaching a certain error threshold per gate operation. Only once this criterion is met, adding layers of error correction actually reduce the over-all errors in the computation to arbitrarily small values. However, the value of this threshold depends strongly on the coupling topology. The semi-global coupling scheme the cavity grid offers suffices to serve as a building block for a truly scalable quantum computation architecture including error-correction.

We demonstrate no less than that this approach encompasses the fundamental elements of a scalable fault-tolerant quantum computing architecture.

This chapter has been published, essentially in the form presented here, in [124] (F. Helmer, M. Mariantoni, A.G. Fowler, J. von Delft, E. Solano, and F. Marquardt. Two-dimensional cavity grid for scalable quantum computation with superconducting circuits. Europhysics Letters, 85(5), 03 2009).

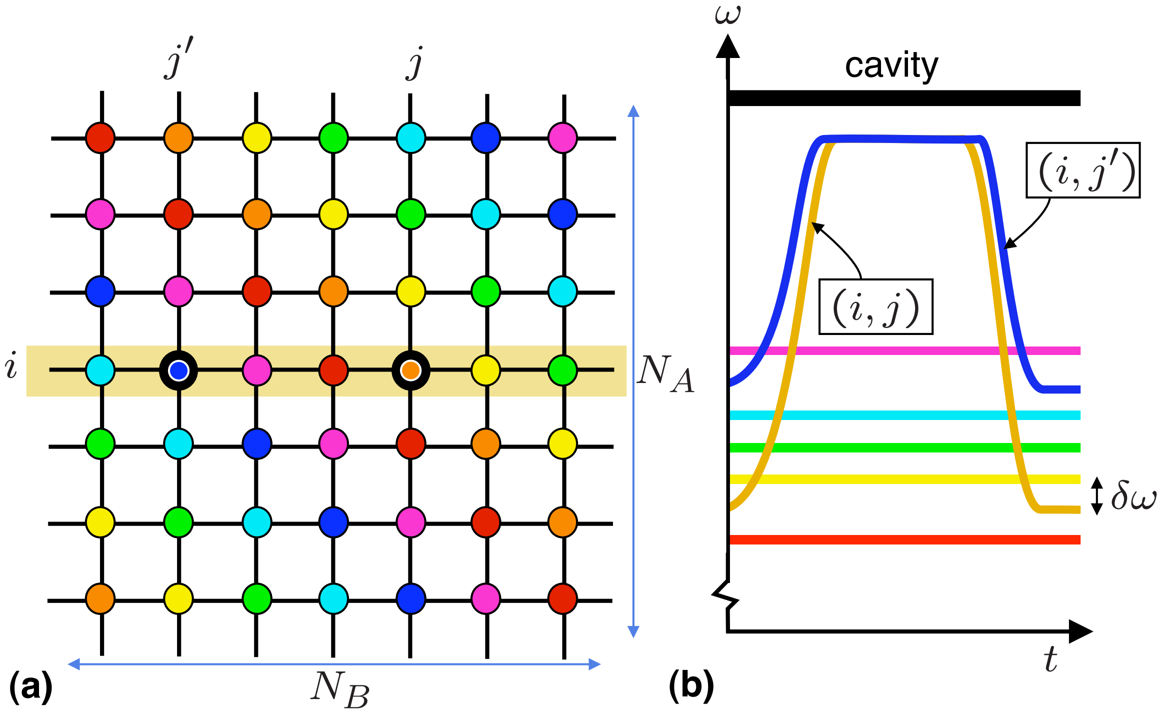

Figure 2.2: Schematic cavity grid setup. (a) The 2D cavity grid, with qubits depicted as circles and cavities shown as lines. Qubit (i, j) sits at the intersection of cavities i and j. Colors distinguish the transition frequencies, which differ within any column or row (in the 'idle state'). (b) A two-qubit operation is induced by tuning two qubits into mutual resonance to exploit the cavity-assisted dispersive coupling.

2.1 Introduction

Superconducting circuits are promising candidates for scalable quantum information processing [42, 58, 62, 71, 72, 134, 138–141]. This route was further strengthened with the advent of circuit quantum electrodynamics. Starting with early proposals for implementing the quantum-optical Jaynes-Cummings model in the context of superconducting circuits [118, 142, 143], this research direction became a major topic after it was pointed out that on-chip microwave transmission line resonators could be coupled to superconducting qubits [78]. Since then, a series of ground-breaking experiments have demonstrated these concepts [60, 68, 79], including achievements like dispersive qubit readout [144], photon number splitting [121], single-photon generation [123], or lasing by a single artifical atom [119].

Recent experiments [41, 82] have advanced to coupling two qubits via the cavity, yielding a flip-flop (XY) interaction permitting two-qubit gates. If multiple qubits share one cavity, arbitrary qubit pairs could be selectively coupled [145], which outperforms nearest-neighbor setups (no swapping overhead or disruption by single unusable qubits). However, moving towards more qubits requires suitable novel architectures.

In this section, we present and analyze an architecture that builds on these elements and extends them into the second dimension, by forming a crossbar-like geometry of orthogonal microwave resonators, with qubits sitting at the intersections (Fig. 2.2). The global coupling within each row and column makes this setup distinct from existing proposals for array-like arrangements in ion traps [18, 19], optical lattices [146], semiconductor spins [147] or superconductors [42, 148]. We show

1. how to couple any two qubits on the grid
2. with minimal swapping overhead using
3. an appropriately chosen ('Sudoku'-style) frequency distribution, and
4. suggest a scalable fault-tolerant quantum computing architecture.

Before we turn to a description of our proposal, we note that experiments right now are obviously still struggling to improve the fidelity of single- and two-qubit operations for superconducting qubits, and this painstaking work is crucial for further progress in the whole field. Nevertheless, the effort going into this endaveour is ultimately justified by the long-term goal of implementing large-scale circuits able to perform nontrivial quantum computation tasks, where the numbers of qubits may run into the thousands. While present-day experiments are still very far from this goal, it is worthwile to develop architectures that couple more than a handful of qubits in a nontrivial setup, and which represent a challenging medium term goal for the experiments to strive for. We will demonstrate that parameters (dephasing times, coupling strengths etc.) near those that are available nowadays would allow for a first proof-of-principle experiment in our proposed architecture, and further progress in the perfection of single qubits will enable truly useful larger scale versions. The basic ideas behind our scheme are sufficiently general so as to permit replacing individual building blocks (particular qubit types, two-qubit gates etc.) by improved versions that might be developed within the coming years.

In addition, we would like to emphasize that even though any working set of universal one- and two-qubit operations permits to implement arbitrary computations in principle, it is by no means clear that the resulting generic implementation is efficient. Rather, in order to make the most efficient use of resources, it is mandatory to come up with larger scale schemes that exploit the particular features of a given physical realization. In this sense, our proposal is similar in spirit to previous proposals for other physical systems that envisaged how well-known elementary operations could be extended to an efficient two-dimensional architecture [18, 19, 146].

2.2 Basic architecture

The cavity grid consists of cavity modes belonging to N_A horizontal (A) and N_B vertical (B) cavities,

$$\hat{H}_{\text{cav}} = \sum_{j=1}^{N_A} \hbar\omega_j^A \hat{a}_j^\dagger \hat{a}_j + \sum_{j=1}^{N_B} \hbar\omega_j^B \hat{b}_j^\dagger \hat{b}_j,$$

coupled to one qubit of frequency ϵ_{ij} at each intersection (i, j), generalizing [78] to a 2D architecture:

$$\hat{H}_{\text{cav}-\text{qb}} = \sum_{i,j} \hat{n}_{ij}[g_{ij}^A(\hat{a}_i + \hat{a}_i^\dagger) + g_{ij}^B(\hat{b}_j + \hat{b}_j^\dagger)]. \tag{2.1}$$

For definiteness we consider charge (or transmon) qubits, unless noted otherwise. Then the couplings $g_{ij}^{A(B)}$ between the horizontal (vertical) cavity mode $i\,(j)$ and the dipole operator $\hat{n}_{ij}$ of qubit (i, j) depend on the detailed electric field distribution and geometry of the qubit. Eq. (2.1) leads to the Jaynes-Cummings model and the cavity-mediated interaction between qubits [78]. It can be realized in different ways: A capacitive coupling was demonstrated for charge [79] (or 'transmon' [82, 121]) and phase qubits [41], while for flux qubits [60] $\hat{n}_{ij}$ is the magnetic moment coupling to the magnetic field.

It is well-known [78, 82] that the Hamiltonian (2.1) induces an effective flip-flop interaction of strength

$$J_{\alpha\beta} = g_\alpha g_\beta \frac{\Delta_\alpha + \Delta_\beta}{2\Delta_\alpha \Delta_\beta}$$

between each pair of qubits (α, β) in the same cavity (for couplings $g_{\alpha(\beta)}$ and detunings from the cavity $\Delta_{\alpha(\beta)}$, in the dispersive limit $|g| \ll| \Delta|$):

$$\hat{H}_{\alpha\beta}^{\text{flip}-\text{flop}} = J_{\alpha\beta} \left(\hat{\sigma}_\alpha^+ \hat{\sigma}_\beta^- + \text{h.c.} \right). \tag{2.2}$$

In the computational 'idle state' these interactions have to be effectively turned off by detuning all the qubits from each other. This requires a detuning $\delta\omega \gg J$ to avoid spurious two-qubit operations. Thus, the number N of qubits in a linear array is strongly restricted [145], since a frequency interval of order $N\delta\omega$ is required. In the present 2D architecture, this constraint is considerably relaxed. The required frequency range is reduced from $N\delta\omega$ to $\sqrt{N}\delta\omega$ (where N is the total number of qubits), while still ensuring a spacing of $\delta\omega$ within each cavity (the constraints being similar to the rules of the game "Sudoku"). This allows for grids with more than $20 \times 20 = 400 = N$ qubits, for realistic parameters. Figure 2.2 shows an acceptable frequency distribution. An extension to a fully scalable setup is discussed at the end of this paper.

2.3 One-qubit operations

We briefly review some ingredients that have already been implemented [60, 68, 79, 121, 144]. Operations on a selected qubit can be performed via Rabi oscillations [144] using a microwave pulse resonant with the qubit at $\epsilon_{ij}/\hbar$, but detuned from the cavity and all other qubits in the same cavity. Rotations around the z-axis can be performed via AC Stark shift [82], or by tuning the qubit frequency temporarily (see below). The cavities can be used for fast dispersive QND readout [144] of single qubits tuned close to the readout frequency or multiplexed readout of several qubits at once [78, 82].

2.4 Tunability

Additional charge and flux control lines (Fig. 2.4) reaching each qubit are needed for tunability. For split-junction charge qubits [42, 71], locally changing the magnetic flux sweeps the energy splitting $\epsilon_{ij} = E_{\mathrm{J}}(\Phi_{ij})$ (see [41, 69]), while keeping the qubit at the charge degeneracy point (to which it has been tuned via a separate charge gate line). This ensures maximum coherence through weak coupling to $1/f$ noise, although this requirement is relaxed in the new "transmon" design [89]. Individual addressability introduces some hardware overhead, but is essential both for two-qubit gates and for compensating fabrication spread.

2.5 Two-qubit gates

We use the effective flip-flop interaction of Eq. (5.3) (see [78, 149–151]) to induce two-qubit gates. In the 'idle state', the interaction is ineffective, since the qubits are out of resonance, $|\epsilon_\alpha - \epsilon_\beta| \gg J$. During the gate, the two qubit frequencies are tuned into mutual resonance near the cavity frequency to increase J, see Fig. 2.2 (b). After a waiting time $t = \hbar\pi/(2|J|)$, this realizes the universal two-qubit iSWAP gate (demonstrated experimentally in [82]), which can be used to construct CNOT and SWAP. Each SWAP(α, β) operation in the protocol (Fig. 2.3) can be decomposed into three iSWAP gates between qubits α and β [12]:

$$\text{SWAP} = \text{iSWAP} \cdot \text{R}_\beta \cdot \text{iSWAP} \cdot \text{R}_\alpha \cdot \text{iSWAP} \cdot \text{R}_\beta. \tag{2.3}$$

Here R_α rotates qubit α by an angle $-\pi/2$ around the x-axis via a Rabi pulse. Arbitrary gates between any two qubits (e.g., 1 and 3) in different cavities can be implemented via an intermediate qubit 2 at the junction of two orthogonal cavities containing 1 and 3 (see Fig. 2.3). The sequence

$$\text{SOPS}(1,3) \equiv \text{SWAP}(1,2)\,\text{OP}(2,3)\,\text{SWAP}(1,2), \tag{2.4}$$

leaves qubit 2 unchanged and performs the desired operation "OP" between 1 and 3.

We simulated such an operation (Fig. 2.3) for realistic parameters. Relaxation and pure dephasing for each qubit α, with rates γ and γ^φ, are modeled by a Lindblad master equation (where $\hat{P}_\alpha = |e_\alpha\rangle \langle e_\alpha|$ projects onto the excited state of qubit α):

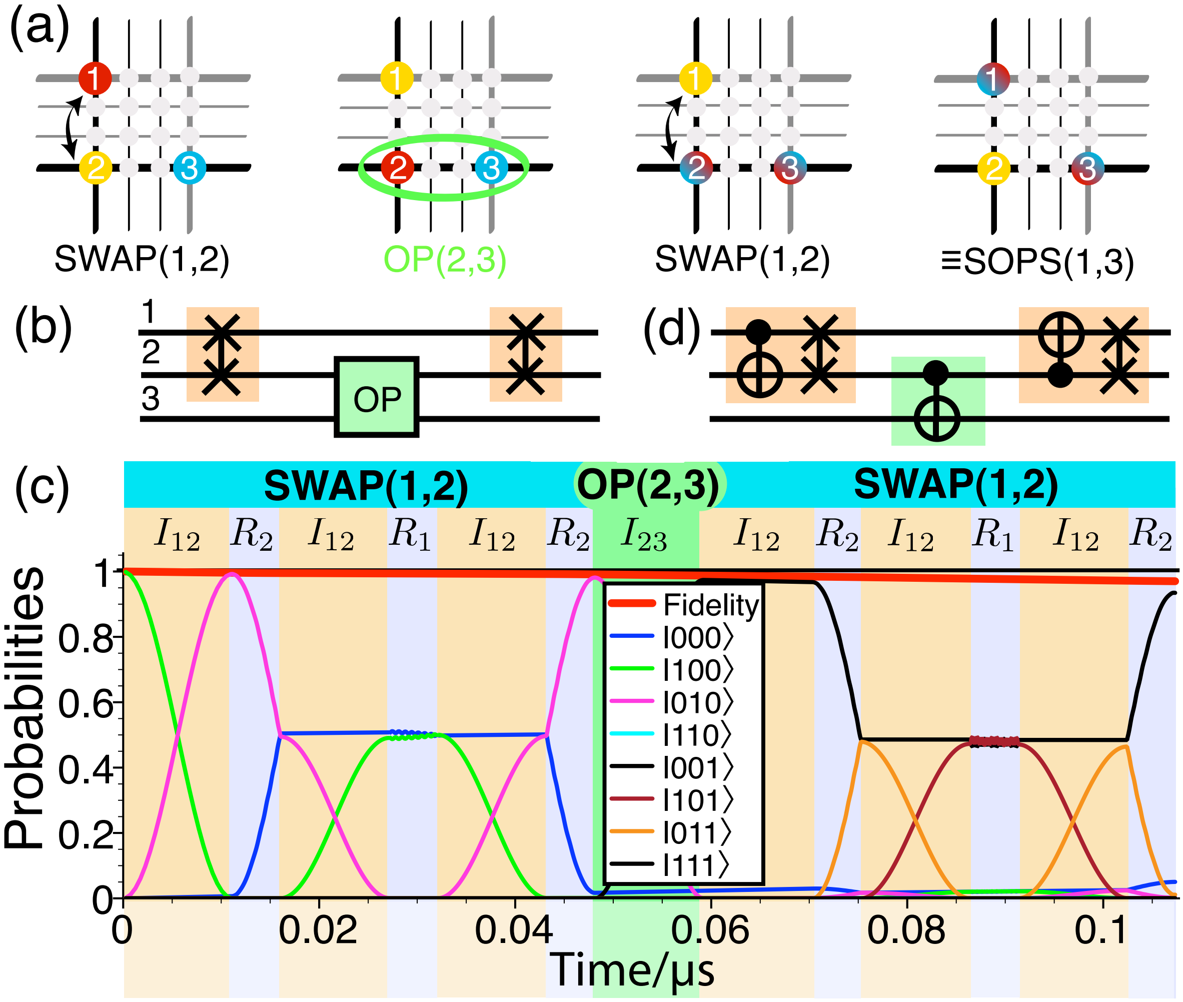

Figure 2.3: Operations between arbitrary qubits on the grid (I_{ij} denotes an iSWAP gate between qubits i and j, and R_i an x rotation by $-\pi/2$). (a) Sequence of operations for a two-qubit gate between two qubits (1 and 3), via an auxiliary qubit (2). (b) Corresponding quantum circuit, where each SWAP has to be decomposed into three iSWAPs and local gates, Eq. (2.3). (c) Master equation simulation of the full evolution for an operation according to (b), including relaxation and dephasing. The evolution of all three-qubit probabilities is shown together with the fidelity (topmost curve), for presently available experimental parameters. (d) For the important case OP $=$ CNOT, a speed-up can be obtained by noting that each SWAP/CNOT pair can be implemented using a single iSWAP and local gates (see [12]).

$$\dot{\hat{\rho}} = -\frac{i}{\hbar}[\hat{H},\hat{\rho}] + \sum_{\alpha}(\mathcal{L}_{\alpha}^{\varphi} + \mathcal{L}_{\alpha}^{\mathrm{rel}})\hat{\rho}\,, \tag{2.5}$$

$$\mathcal{L}_{\alpha}^{\varphi}\hat{\rho} = \gamma^{\varphi}\left[2\hat{P}_{\alpha}\hat{\rho}\hat{P}_{\alpha} - \hat{P}_{\alpha}\hat{\rho} - \hat{\rho}\hat{P}_{\alpha}\right]\,, \tag{2.6}$$

$$\mathcal{L}_{\alpha}^{\mathrm{rel}}\hat{\rho} = \gamma\left[\hat{\sigma}_{\alpha}^{-}\hat{\rho}\hat{\sigma}_{\alpha}^{+} - \frac{1}{2}\hat{\sigma}_{\alpha}^{+}\hat{\sigma}_{\alpha}^{-}\hat{\rho} - \frac{1}{2}\hat{\rho}\hat{\sigma}_{\alpha}^{+}\hat{\sigma}_{\alpha}^{-}\right]. \tag{2.7}$$

We consider three qubits, where $(1,2)$ and $(2,3)$ are coupled via flip-flop terms [see Eq. (5.3)] after adiabatic elimination of the cavities.

During two-qubit gates, the qubit energy is ramped and will cross other qubit energies (Fig. 2.2), potentially leading to spurious population transfer to other qubits if the process is too slow, while ramping too fast would excite higher qubit levels.

For a $10\,\mathrm{ns}$ switching time (during which a sweep over $\delta\epsilon/\hbar = 2\pi\cdot 10\,\mathrm{GHz}$ is accomplished), the probability of erroneous transfer during one crossing is estimated to be less than 10^{-2} from the Landau-Zener tunneling formula, and thus could be safely disregarded for the present simulation, where energies were instead switched instantaneously. Although several crossings may occur during one sweep, the scalable setup to be introduced further below keeps this kind of error under control by having only eight qubits per cavity.

For the simulation we used the following parameters: Initially, the qubit transition frequencies are at $\epsilon/\hbar = 2\pi\cdot 4,\ 5,\ 6\,\mathrm{GHz}$. A resonant classical drive yields a Rabi frequency of $\Omega_{\mathrm{R}} = 150\,\mathrm{MHz}$. A qubit-cavity coupling $g = 2\pi\cdot 150\,\mathrm{MHz}$ and a detuning $\Delta = 2\pi\cdot 1\,\mathrm{GHz}$ (from a cavity at $2\pi\cdot 15\,\mathrm{GHz}$) produce $J/\hbar = 2\pi\cdot 21\,\mathrm{MHz}$. The dephasing and decay rates are $\gamma^{\varphi} = 0.16\,\mathrm{MHz}$ and $\gamma = 0.6\,\mathrm{MHz}$ (i.e. $T_1 = 1.7\,\mu s$ and $T_{\varphi} = 6.3\mu s$), consistent with recent experiments on transmon qubits [89]. Note that in the idle state the actual J is reduced by a factor of 10 (due to larger detuning from the cavity). Employing a qubit spacing of $\delta\omega \sim 500\,\mathrm{MHz}$, this yields a residual coupling strength of $J^2/\hbar^2\delta\omega \sim 0.4\,\mathrm{MHz}$, which may be reduced further by refocusing techniques. To check the accuracy of adiabatic elimination, we performed an additional simulation of an iSWAP operation between two qubits taking the cavity fully into account, observing an error below the level brought about by dissipation.

A measure of the fidelity of the operation is obtained [152] by computing

$$F(\hat{\rho}_{\mathrm{real}}(t), \hat{\rho}_{\mathrm{ideal}}(t)),$$

where

$$F(\hat{\rho}_1,\hat{\rho}_2) \equiv \mathrm{tr}\left|\sqrt{\hat{\rho}_1}\hat{\rho}_2\sqrt{\hat{\rho}_1}\right|,$$

and $\hat{\rho}_{\mathrm{ideal}}$ denotes the time-evolution in the absence of dissipation. Fig. 2.3 shows a fidelity of about 95%, confirming that presently achievable parameters suffice for a first proof-of-principle experiment.

We emphasize that the swapping overhead does not grow with the distance between the qubits. Furthermore, multiple operations may run in parallel, even if they involve the same cavities, provided no qubit is affected simultaneously by two of the operations and the qubit pairs are tuned to different frequencies.

Here we have chosen the dispersive two-qubit gate that relies on proven achievements. Faster resonant gates (e.g. CPHASE [109, 145]) might be implemented, with a time scale on the order of $1/g$ instead of Δ/g^2.

2.6 Hardware

For illustration, we discuss one out of many conceivable setups (Fig. 2.4). The cavities can be coplanar wave guides or microstrip resonators. Available multi-layer technology allows the fabrication of thin films stacked on top of each other.

For example, consider waveguide layers of Nb or Al, separated by $100\,\mathrm{nm}$ of dielectric, which can be optimized for good decoherence properties (e.g. [35]). The inner grid area for 10×10 wave guides (each with $20\mu\mathrm{m}$ inner conductor and $10\mu\mathrm{m}$ gaps) would have a width of about $1\,\mathrm{mm}$, whereas the full resonator lengths are above $10\mathrm{mm}$, allowing all the qubits to be placed near the cavity mode central field antinode, with comparable couplings (see Fig. 2.4).

The qubit-cavity coupling remains similar to single-layer designs, owing to the small layer thickness of only $100\,\mathrm{nm}$. Good isolation between two orthogonal cavities was estimated in a previous theoretical work [153, 154], and unwanted cross-talk may be reduced further by choosing different cavity frequencies. The qubits can be placed above all layers to minimize fabrication problems.

Weak coupling between qubits and control lines (e.g. cross-capacitance $\sim 0.01\mathrm{fF}$) suppresses sufficiently unwanted Nyquist noise from these lines, which could lead to decoherence. Indeed, for a Cooper pair box of total capacitance C_Σ , this cross-capacitance yields a relaxation rate $\sim (C_g/C_\Sigma)^2 e^2\omega Z/\hbar$ for radiation into a control line of impedance Z at the qubit splitting frequency ω, leading to estimates that are small compared to the intrinsic qubit relaxation rate for the present parameters (the same holds for dephasing).

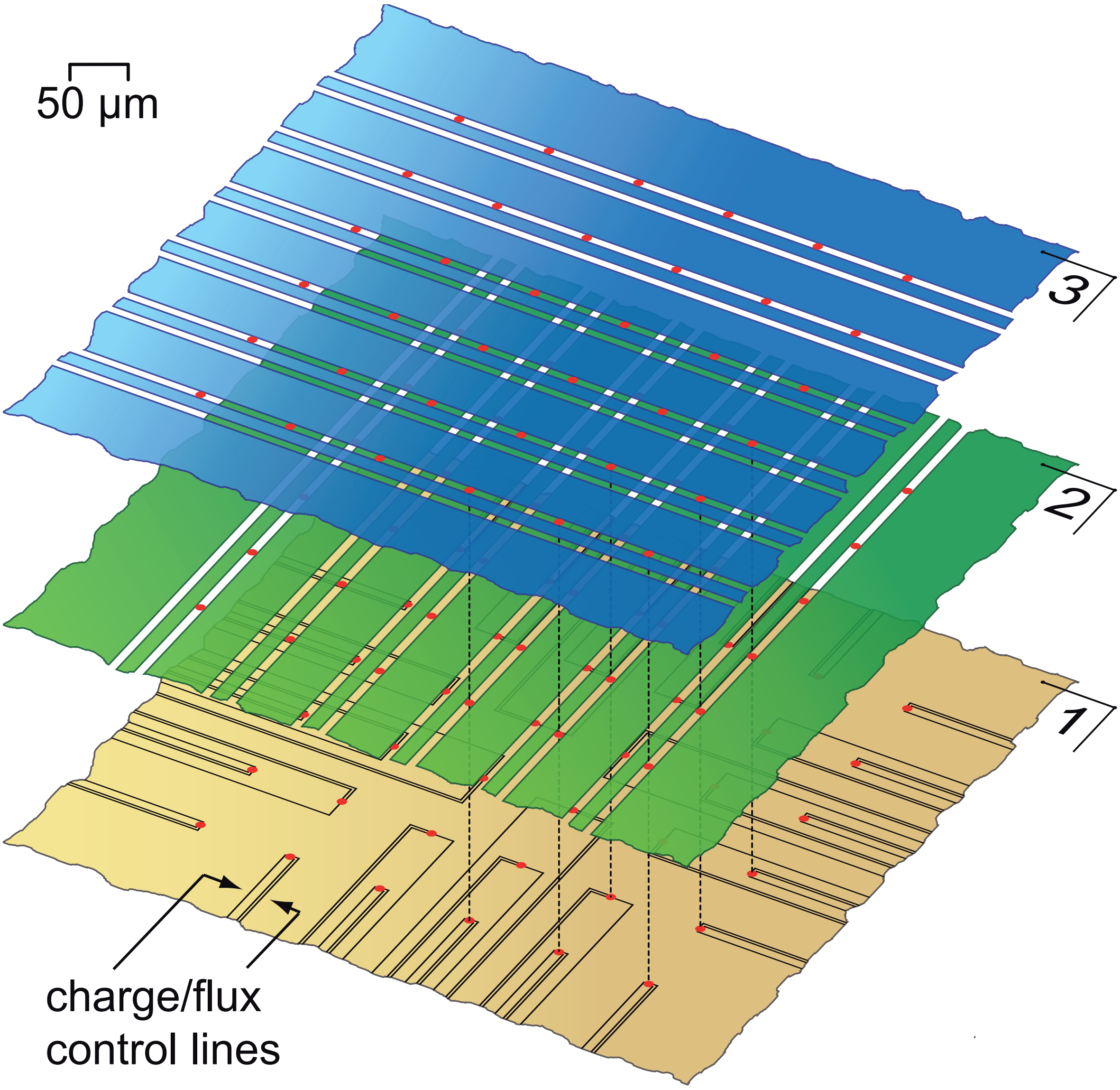
50 µm
3
2
1
charge/flux
control lines

Figure 2.4: A possible multilayer architecture. The layers 2 and 3 with coplanar wave guides are positioned above a ‘control line layer’ 1. The qubit positions are indicated as red dots within each layer only for reference (they would be fabricated above layer 3).

2.7 Scalable, fault-tolerant architecture[1]

The cavity grid is a building block for a truly scalable, fault-tolerant architecture. Scalability means that, at a minimum, the physics of initialisation, readout, single- and two-qubit gates does not depend on the total number of qubits. Fig. 2.5 shows a scalable architecture requiring only eight different qubit frequencies. In each unit cell of 64 qubits (Fig. 2.5) we choose two arrays of seven data qubits and use each array to store a single logical qubit, employing the Steane quantum error correction code [155]. Clean logical states can be prepared in additional ancilla qubits. Moreover, errors in the data qubits can be copied into the ancillae, which are then measured, locating the errors and enabling correction [156]. All other qubits are placeholders which are crucial: Swapping a pair of data qubits directly could corrupt both if the SWAP gate fails, resulting in a pair of errors that may not be correctable by the seven qubit Steane code. Using three SWAP gates with a placeholder qubit for temporary data storage solves this problem. We ignore errors in placeholder qubits as they contain no data.

A logical CNOT gate is illustrated in Fig. 2.5. The final arrangement of qubits differs from the initial one and can be returned to it by swapping. However, if all logical qubits undergo similar logical gates, explicitly swapping back may be unnecessary as subsequent gates will do this automatically. A broad range of single logical qubit gates are possible. Full details of our chosen set of logical gates and their associated circuits including error correction can be found elsewhere [157, 158].

2.8 Conclusions

In this section, we have proposed a novel architecture for quantum computation using a 2D grid of superconducting qubits coupled to an array of on-chip microwave cavities. A "Sudoku"-type arrangement of qubit frequencies permits global coupling of a large number of qubits while suppressing spurious interactions. These basic ideas could be implemented in a wide variety of hardware implementations. Elementary operations within this scheme could be demonstrated in the near future on small grids, while the setup has the potential to form the basis for truly scalable fault-tolerant architectures.

---

[1] The fault-tolerant scheme was contributed to this work by Austin Fowler.

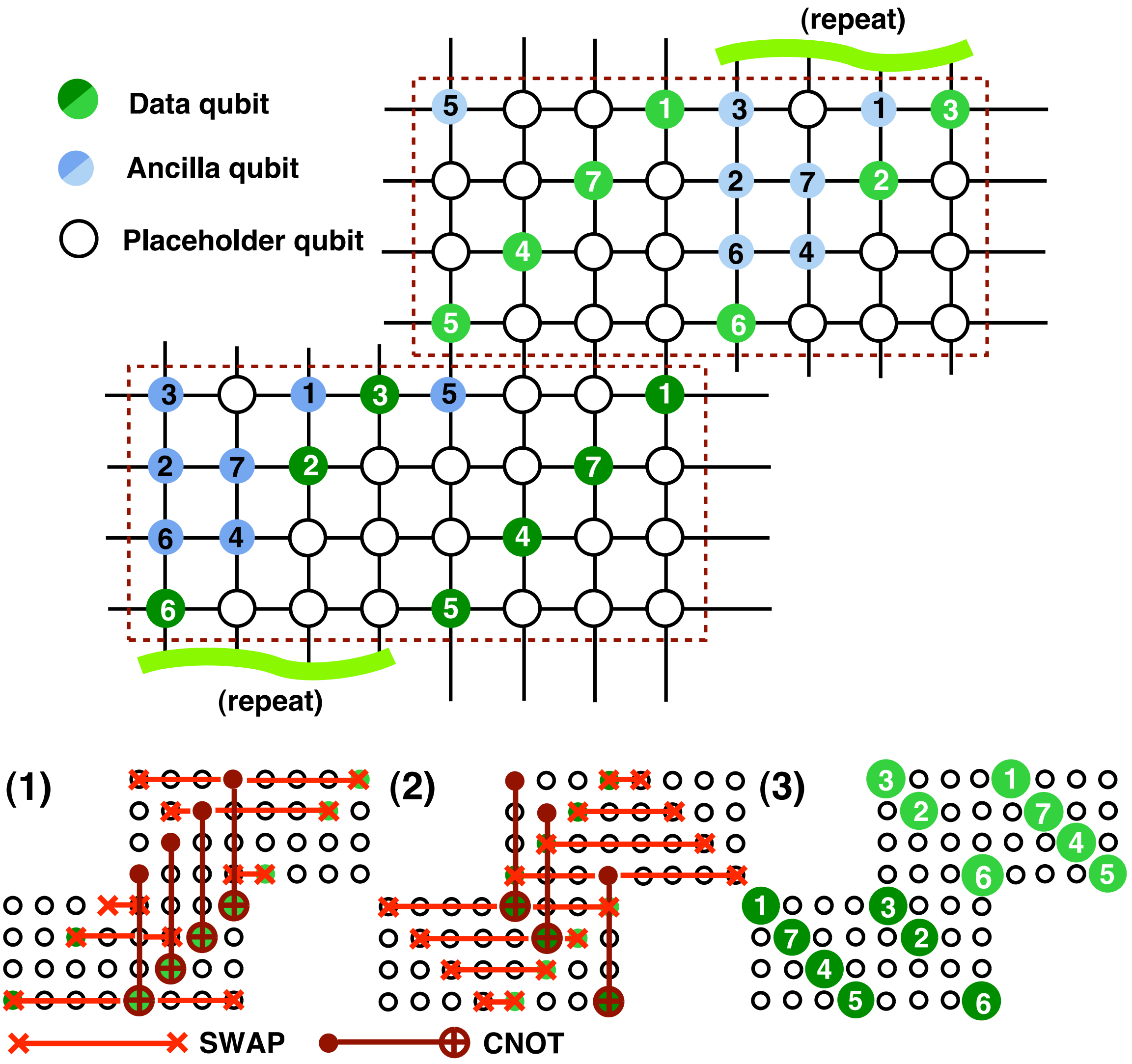
Data qubit
Ancilla qubit
Placeholder qubit
(repeat)
(repeat)
(1)
(2)
(3)
SWAP
CNOT

Figure 2.5: A possible fault-tolerant scalable architecture based on the cavity grid. Top: The unit cell of a periodic arrangement, with two logical qubits, each made up of seven data qubits (grouping indicated by dashed rectangles), together with ancilla and placeholder qubits. Bottom: The sequence of SWAP and CNOT gates shown in (1) and (2) implements a transversal CNOT between the logical qubits, producing the final arrangement (3); see main text.

Chapter 3

Optimized gates for the Cavity Grid

3.1 Motivation - improving the Cavity Grid

Based on the idea of the cavity grid as an architecture for quantum information processing which has been introduced in 2, schemes to improve upon a purely dispersive set of quantum gates have been devised in [159]. Basically two approaches are possible:

1. Improving the gate run-times and thus the fidelity by moving from dispersive gates (qubit strongly detuned from the cavity, only virtual excitations in the cavity) to purely resonant gates (qubit in resonance with the cavity, real excitations in the cavity) and

2. improving upon simple gate sequences and the corresponding pulse schemes using optimal control theory techniques, i.e. the numerical optimization of e.g. qubit driving and detuning pulse shapes (discussed in Sec. 3.3).

In this section we focus on the improvement that can be gained by performing all operations resonantly to the cavity. In order to assess the fidelity gain that can be expected from moving from the dispersive iSWAP to the proposed purely resonant CPhase gate as the basic two-qubit unitary, a master equation simulation of an example system of two qubits and a cavity has been performed.

3.2 A resonant CPhase gate - master equation simulation

3.2.1 The CPhase protocol

As introduced in [159], a CPhase gate between the two qubits can be realized by applying the protocol presented in Tab. (3.1). It is assumed that in the beginning of the protocol, the cavity which is solely used as a cache for the quantum information contained in the second qubit, is in its ground state. Imagine this protocol acting on a general two-qubit state: $|\Psi\rangle \equiv \alpha|00\rangle + \beta|01\rangle + \gamma|10\rangle + \delta|11\rangle$ would be transformed to $|\Psi\rangle \equiv \alpha|00\rangle + \beta|01\rangle + \gamma|10\rangle - \delta|11\rangle$, where the only difference is the sign change before the $|11\rangle -$ component of the state as can be read off from looking at the matrix elements of the CPhase gate

$$U_{\text{CPhase}} \equiv \begin{pmatrix} 1 & 0 & 0 & 0 \\ 0 & 1 & 0 & 0 \\ 0 & 0 & 1 & 0 \\ 0 & 0 & 0 & -1 \end{pmatrix}.$$

The tuning required by the protocol can be done either by changing the resonator frequency [145] or by changing the qubit transition frequencies. If one chooses to do the latter, there are again two possibilities

1. changing the ratio E_J/E_C by e.g. applying a magnetic or electric control field locally to the qubit in question (see Fig. (3.1) or by

2. irradiating the cavity off-resonantly with a strong microwave field to change the qubit level-positions via the ac-Stark effect [78].

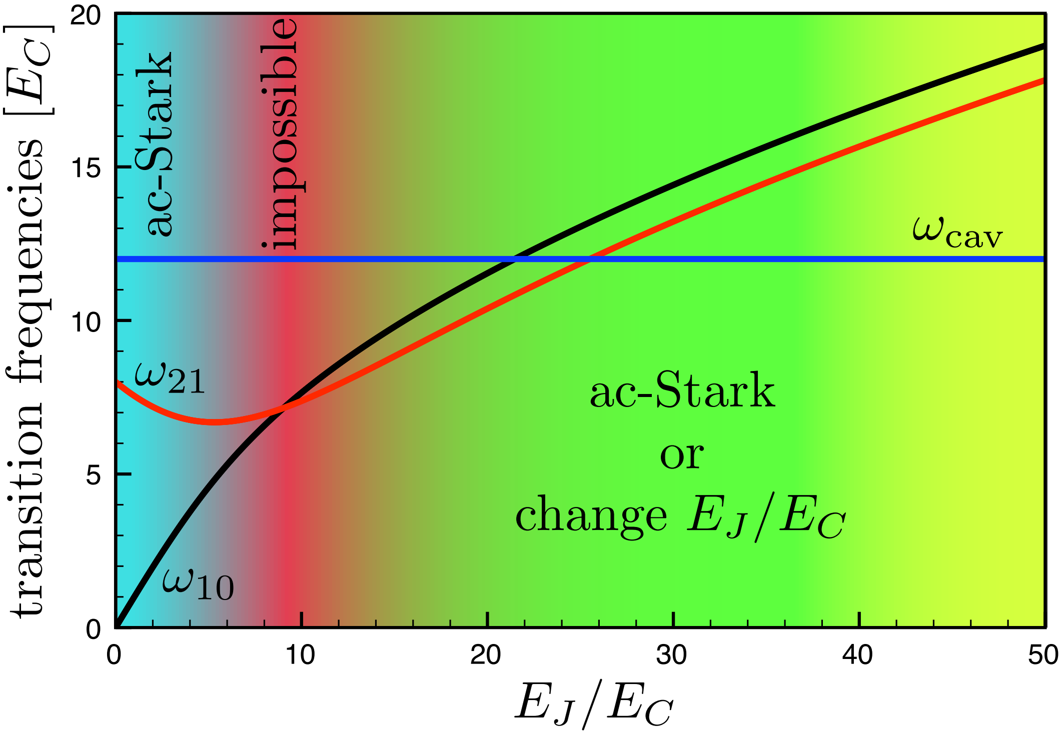

Figure 3.1: Cooper pair box/Transmon transition frequencies as function of the ratio E_J/E_C at gate charge $n_g = 1/2$. Tuning both the two needed transitions into resonance if needed requires different tuning schemes depending on the regime of E_J/E_C. The cavity transition frequency remains fixed. In the small E_J/E_C regime tuning the qubit levels e.g. by ac-Stark shift is possible while tuning E_J/E_C will not work. For $E_J/E_C \gg 1$, both ac-Stark shifting and changing E_J/E_C works. For the intermediate regime of $E_J/E_C \approx 10$, the two transitions are almost degenerate, which makes it impossible to individually address them.

As one can see from Fig. (3.1), the first option only exists in the transmon regime and thus suffers leakage due to the small anharmonicity of the transmon qubit type[1].We therefore chose to use the ac-Stark scheme and operate in the charge qubit regime where $E_J/E_C \approx O(1)$.

Step	tuning	duration	effect
(1)	$\omega_{10}^{(2)} = \omega_{\text{cav}}$	$\pi \cdot g_{10}^{(2)}$	Perform Jaynes-Cummings SWAP to map the quantum information in qubit 2 into the (empty) cavity
(2)	$\omega_{21}^{(1)} = \omega_{\text{cav}}$	$2\pi \cdot g_{21}^{(1)}$	Change the phase of the $\left\|1_{\text{qubit 1}}\right\rangle \otimes \left\|1_{\text{cavity}}\right\rangle$ state
(3)	$\omega_{10}^{(2)} = \omega_{\text{cav}}$	$\pi \cdot g_{10}^{(2)}$	Map back from the cavity to the second qubit

Table 3.1: Resonant CPhase-gate protocol. When tuning certain frequencies into mutual resonance, all other transitions have to be kept detuned. The couplings refer to the effective coupling of some qubit transition to the cavity given by $g_{nn'}^{(i)} \equiv g_0^{(i)} \left\langle n \middle| \hat{N}_{\text{diag}} \middle| n' \right\rangle$.

3.2.2 Model

The model we base our simulation of the resonant CPhase gate on is the following. It consists of two charge qubits and a harmonic oscillator coupling to both qubits. Its Hamiltonian reads:

$$\begin{aligned}\hat{H} \;\equiv\; & 4 \sum_{i=0}^{2} E_J^{(i)} \, (\hat{N}^{(i)} - n_g^{(i)})^2 + \sum_{i=0}^{2} \frac{E_C^{(i)}}{2} \left(\left| n^{(i)} \right\rangle \left\langle n^{(i)} + 1 \right| + h.c. \right) \\ & + \hbar\omega_{\text{cav}} \, \hat{a}^\dagger \hat{a} + \sum_{i=0}^{2} g_o^{(i)} \, \hat{N}^{(i)} \, (\hat{a} + \hat{a}^\dagger) \\ & + \hat{H}_{drive+decay}. \end{aligned} \tag{3.1}$$

Here, $E_J^{(i)}$ is the Josephson energy of the i-th qubit, $E_C^{(i)}$ is the capacitive energy between the two qubit islands and $\hat{N}^{(i)}$ is its Cooper pair number operator that describes the number of excess Cooper pairs on one of the islands.

In the actual simulation we will move to the eigenbasis of the system by diagonalizing the qubit subspace (the cavity is already diagonal). This will enable us to mimic ac-Stark shifting of energy levels by simply adiabatically changing the level posititions. One has to be careful with this method as the number operator cannot be changed accordingly and thus only small level shifts will yield sufficiently correct simulation results.

3.2.3 Expectations

From using only resonant gates, one can expect an improvement in gate runtimes compared to dispersive gates as e.g. introduced in Sec. 2 roughly by a factor given by Δ/g, where Δ

---

[1] The leakage to unwanted transmon levels can be significantly reduced by applying simple additional pulses as examined in [160].

is the qubit-cavity detuning and g is the qubit-cavity coupling. This is the ratio of the typical dispersive two-qubit gate runtime given by $J^{-1} \equiv (g^2/\Delta)^{-1}$ to the typical resonant two-qubit gate runtime given by the time of a Jaynes-Cummings swap g^{-1}. Recent experiments [82, 84, 121] have demonstrated a qubit-cavity coupling of about $2\pi \cdot 100MHz$, while typical cavity detunings are found to be in the GHz range. Therefore one can reasonably expect to gain one order of magnitude in gate runtime. Translating this to the expected fidelity gain is straightforward. As the fidelity (to a first approximation, see Sec. 2) decreases exponentially as time advances, one can expect a fidelity gain by a factor of $F_{new} \approx F_{old}^{1/10} \approx 0.95^{1/10} \approx 0.99$. We will find these expectations confirmed by our master equation simulation for which we considered two different parameter sets.

3.2.4 Lindblad master equation to include dissipation

To assess the fidelity of the protocol presented in Tab. (3.1), we extend the model represented by Eq. (3.1) to include pure dephasing and decay. This can be done by writing down the corresponding Lindblad master equation

$$\begin{aligned}
\dot{\hat{\rho}} &= -\frac{i}{\hbar}[\hat{H}_{diag}, \hat{\rho}] + \sum_{i=1}^{2}(\mathcal{L}_i^{\varphi} + \mathcal{L}_i^{\text{rel}})\hat{\rho} + \kappa_{\text{cav}}(\hat{a}\hat{\rho}\hat{a}^{\dagger} - \frac{1}{2}\hat{a}^{\dagger}\hat{a}\hat{\rho} - \frac{1}{2}\hat{\rho}\hat{a}^{\dagger}\hat{a}), \\
\mathcal{L}_i^{\varphi}\hat{\rho} &= \gamma^{\varphi}\sum_{n=1}^{N}\left[2\hat{P}_i^{(n)}\hat{\rho}\hat{P}_i^{(n)} - \hat{P}_i^{(n)}\hat{\rho} - \hat{\rho}\hat{P}_i^{(n)}\right], \\
\mathcal{L}_i^{\text{rel}}\hat{\rho} &= \gamma\sum_{n_i=1}^{N}\sum_{m_i=1}^{n_i}\left[|n_i - m_i\rangle\langle n_i|\hat{\rho}|n_i\rangle\langle n_i - m_i| - \frac{1}{2}|n_i\rangle\langle n_i|\hat{\rho} - \frac{1}{2}\hat{\rho}|n_i\rangle\langle n_i|\right],
\end{aligned}$$

where the index i is the qubit index and the index n denotes its excited states. Note that we have assumed equal dephasing and decay rates for the qubits and all their decay channels. For the purpose of our simulation, we have restricted ourselves to $N = 2$, i.e. taking three qubit levels into account.

3.2.5 Simulation

In between the three time intervals where the actual protocol is performed, we need to mimic an ac-Stark shift on the qubit transition frequencies such that after the tuning, the right transition is in resonance with the cavity mode. This has to be done slowly (adiabatically) enough such that the speed of tuning of some transition between levels n and n', $\frac{\partial(\hbar\omega_{nn'})}{\partial t}$ is small compared to the square of any other transition frequency of the system. On the other hand it needs to be fast compared to the Jaynes-Cummings interaction time given by the couplings $g_{nn'}^{(i)} \equiv g_0^{(i)}\left\langle n\left|\hat{N}_{\text{diag}}\right|n'\right\rangle$. The reason is that if one tunes too slowly, the Jaynes-Cummings dynamics sets in before the tuning has ended, if one tunes too fast, one changes the state of the system while an adiabatic transition was aimed for. Keeping this balance, we simply changed the qubit spectra linearly in time yielding the tuning pattern as can be see from Fig. (3.2).

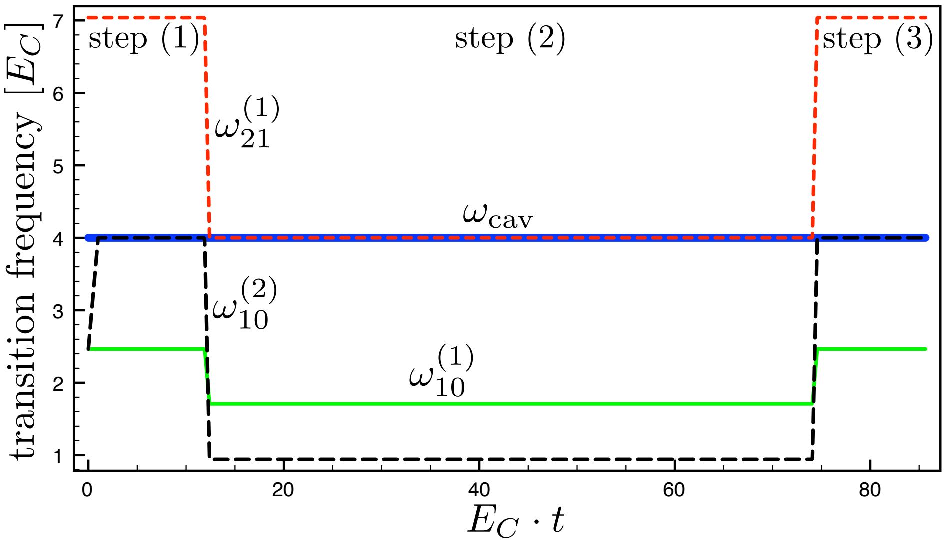

Figure 3.2: Example ac-Stark level tuning scheme for the resonant CPhase-gate. In step 1 the state of qubit 2 is mapped onto the cavity, in step 2 the CPhase gate is realized and step 3 realizes the back-mapping of the quantum information stored in the cavity to the seond qubit, using another Jaynes-Cumming swap.

The parameters for the simulation were taken from actual experiments [91] and are compiled in Tab. (3.2) .

quantity	symbol	value
Ratio of Josephson- vs. Charging Energy	E_J/E_C	2.53
Qubit decay rate	γ	$0.14\,MHz$
Qubit pure dephasing rate	γ_φ	$1.93\,MHz$
Resonator frequency	ω_{cav}	$2\pi \cdot 5.5\,GHz$
Resonator intensity decay rate	κ_{cav}	$10kHz$
bare coupling (medium)	g_0	$2\pi \cdot 43\,MHz$
Jaynes-Cummings coupling transition 1 → 0 (medium)	$g_{10} \equiv g_0 \left\langle 1 \middle\vert \hat{N} \middle\vert 0 \right\rangle$	$2\pi \cdot 17\,MHz$
Jaynes-Cummings coupling transition 2 → 1 (medium)	$g_{21} \equiv g_0 \left\langle 2 \middle\vert \hat{N} \middle\vert 1 \right\rangle$	$2\pi \cdot 6.6\,MHz$
bare coupling (strong)	g_0	$2\pi \cdot 191\,MHz$
Jaynes-Cummings coupling transition 1 → 0 (strong)	$g_{10} \equiv g_0 \left\langle 1 \middle\vert \hat{N} \middle\vert 0 \right\rangle$	$2\pi \cdot 100\,MHz$
Jaynes-Cummings coupling transition 2 → 1 (strong)	$g_{21} \equiv g_0 \left\langle 2 \middle\vert \hat{N} \middle\vert 1 \right\rangle$	$2\pi \cdot 38.8\,MHz$

Table 3.2: Parameters used in simulation of the resonant CPhase gate protocol.

3.2.6 Results

To verify that we have indeed performed a CPhase gate and assess the fidelity of the operation, we compute the fidelity between the evolution without dissipation compared to the evolution with dissipation according to $F \equiv \mathrm{tr}\left|\sqrt{\hat{\rho}_{ideal}}\hat{\rho}\sqrt{\hat{\rho}_{\mathrm{ideal}}}\right|$. Note that the evolution without dissipation is not a priori equal to the action of the unitary CPhase gate. However, we have checked the deviations from the ideal unitary to be orders of magnitude smaller than the errors induced by dissipation. We start the simulations with the two qubits in the Bell-state $|\Phi^+\rangle \equiv 1/\sqrt{2}(|00\rangle + |11\rangle)$ and the cavity in the ground state. After the CPhase operation this state will be converted into $|\Phi^-\rangle \equiv 1/\sqrt{2}(|00\rangle - |11\rangle)$.

3.2.6.1 Medium coupling

Using the parameters as presented in Tab. (3.2), we find that a CPhase gate can be performed with a fidelity of about 93% (see Figs. (3.4)). Note that the coupling g_0 is not the usually discussed coupling of the $1 \longrightarrow 0$-transition to the resonator. This coupling is given by $g_{10} \equiv g_0 \left\langle 1 \middle| \hat{N} \middle| 0 \right\rangle$ and amounts to $g_{10} = 2\pi{\cdot}17\,MHz$. In turn, the coupling of the $2 \longrightarrow 1$-transition is found to be $g_{21} = 2\pi \cdot 6.6\,MHz$. In Fig. (3.3) we see the time evolution of relevant state occupation probabilities (selected diagonal elements of the density matrix) for this protocol. The overall gate performance can be assessed from Fig. (3.4) where the full density matrix (the real part, sufficient in this case) of the initial and final state are depicted.

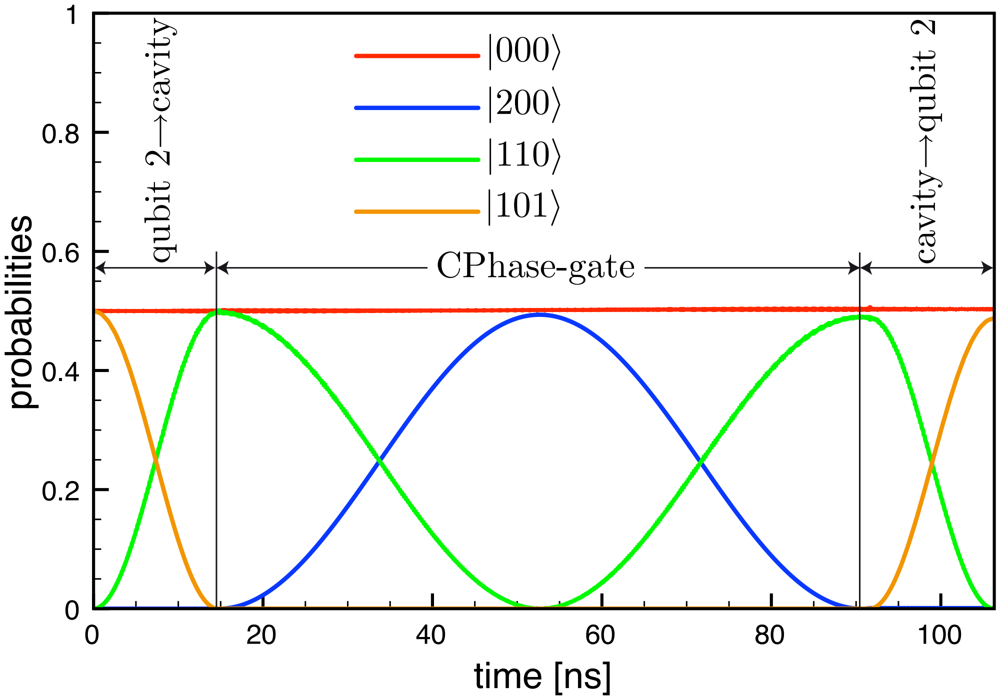

Figure 3.3: Evolution of the diagonal elements of the density matrix for the resonant CPhase gate at medium coupling $g_0 = 2\pi \cdot 33MHz$. The overall fidelity of this operation is found to be 93%.

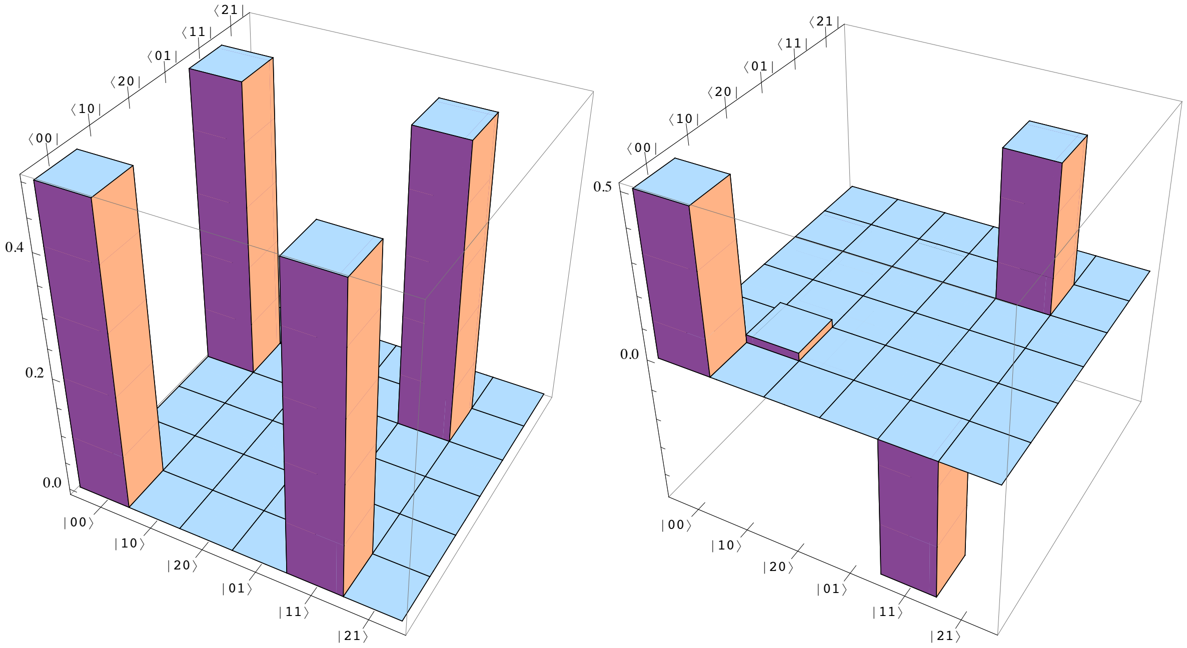

Figure 3.4: Barplot of $Re(\hat{\rho})$. Depicted are the initial state $|\Phi^+\rangle$ and the final state close to $|\Phi^-\rangle$.

3.2.6.2 Strong coupling

To make a fair comparison to the dispersive schemes discussed in 2, we repeat the simulation with a larger qubit-resonator coupling of $g_0 = 2\pi \cdot 191 MHz$ which is even lower than the latest achievements in circuit QED experiments [2], where a coupling of $g_{10} = 2\pi \cdot 173.5\, MHz$ has been reported. For this parameter set a fidelity of about 98.5% is found for the CPhase gate sequence. The coupling of the $1 \longrightarrow 0$-transition to the resonator is given by $g_{10} \equiv g_0 \left\langle 1 \middle| \hat{N} \middle| 0 \right\rangle$ and amounts to $g_{10} = 2\pi \cdot 100\, MHz$. The coupling of the $2 \longrightarrow 1$-transition is found to be $g_{21} = 2\pi \cdot 38.8\, MHz$. The results for this parameter set are compiled in Fig. (3.5).

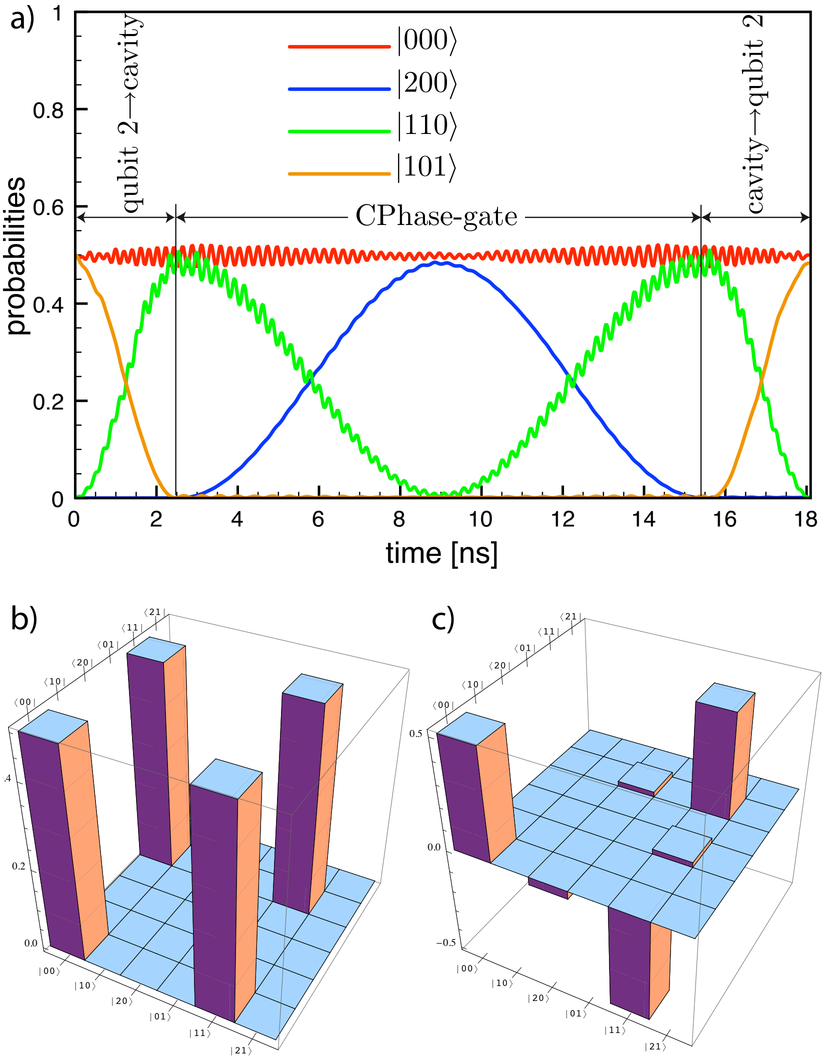

Figure 3.5: Part (a): Evolution of the diagonal elements of the density matrix for the resonant CPhase gate at strong coupling $g_0 = 2\pi \cdot 191 MHz$. The overall fidelity of this operation is found to be 98.5%. Part (b) displays the real part of the initial density matrix, part (c) the real part of the final density matrix.

3.3 Optimizing dispersive gates with optimal control theory

As already mentioned in the introduction to this chapter, apart from improving the toolbox for the cavity grid architecture by moving from dispersive to purely resonant gate operations, both of them rely on straightforward decompositions into the gates that are naturally available in the system and/or need some fixed swapping overhead in order to be performed between an arbitrary couple of qubits on the cavity grid. in this section, we have applied optimal control theory to numerically find the optimal pulses and thus the optimal time one can perform a certain target gate operation on the grid. We find that the use of optimal control theory can greatly improve upon any simple decomposition (such as e.g. the decomposition of the iSWAP gate presented in Sec. 2)

In particular, we have used a Gradient Ascent Pulse Engineering (GRAPE [161, 162]) algorithm to analyze the possibilities of optimising upon the sequential decomposition schemes of an iSWAP gate, a SWAP and CNOT combination and a SOPS operation implementing an iSWAP 'around the corner' between qubits belonging to different cavities on the grid. We also look at the impact of sensible restrictions on the minimal times and pulse-shapes found. The numerical optimization has been performed by Robert Fisher at the Department of Chemistry at Technical University of Munich. The results presented in this chapter are to be published in a manuscript currently in preparation [Robert Fisher, Ferdinand Helmer, Florian Marquardt and Thomas Schulte-Herbrüggen, manuscript in preparation, 2009].

3.3.1 A short glance at the principle of optimal control theory

Let us first briefly motivate the problem one tries to solve with optimal control theory. Usually in an quantum computation experiment where one wants to manipulate a quantum register (one or more qubits), one knows the initial and the target state of the system, i.e. one knows the unitary operation that corresponds to this gate. Then one faces the problem that the experimental knobs one can turn are very specific and usually limited. E.g. one can apply microwave driving, but only collectively on all qubits, not individually. In addition one can maybe shift the qubits' frequencies individually. In addition to the goal and the knobs (the controls) one has at hand, there might be additional restrictions such as the maximum drive power, maximum speed that qubit energies can be reliably tuned, etc. .

Now let us formalize this a bit. The knobs on the one hand correspond to certain terms in the Hamiltonian containing parameters which can be tuned in time (turning the knobs). These controls are thus parametrized by a set of functions of time $\{f_i(t)\}$. The gate as mentioned before is given by a certain unitary action on our system specified by U_{target}. We said that one is looking for the minimal time the gate can be performed within a certain admissible error range. Technically, one tries the optimization for a run-time t_{gate} in which this gate operation is to be realized, and the algorithm will find a set of control functions leading to an evolution given by U_{opt}. The one computes the error (the distance between U_{target} and U_{opt}) and sees if one is still in the acceptable error range. If so, one might shorten the time t_{gate} and repeat the procedure.

One therefore starts from a Hamiltonian which is separated into a free part (called 'drift term', the system without the Hamiltonian terms corresponding to the knobs) and the parts containing the control functions $\{f_i(t)\}$ (e.g. amplitudes of single qubit rotation driving fields or energy shifts, called 'control part'), which can be written as

$$\hat{H}(t) \equiv \hat{H}_{\mathrm{drift}}(t) + \hat{H}_{\mathrm{control}}[\{f_i(t)\}] = \hat{H}_{\mathrm{drift}}(t) + \sum_i f_i(t)\hat{H}_{\mathrm{control},i},$$

one divides the gate run-time t_{gate} into N discrete slices indexed by m, such that the continuous Hamiltonian is approximated by a discrete, piecewise constant Hamiltonian [162]. Now the optimal control algorithm has to start from some arbitrary, user specified initial set of control functions $\{f_i(t)\}$. The goal is to optimize a certain performance function, usually given by a measure for the overlap of the desired unitary operation with the synthesized unitary at a certain step in the optimization process. Most generally and formally one can derive a scalar Hamiltonian function used to compute gradients and introduces a Lagrange multiplier in order to enforce the equation of motion for the unitary operation $i\dot{U}_{\mathrm{opt}}(t) = \hat{H}U_{\mathrm{opt}}(t)$ while the performance functional is optimized. The concrete optimization equation can then be calculated from the so-called Pontryagin's maximum principle [163].

However, in the cases considered in this thesis, it is possible to simplify the argument mainly because the performance function does only depend on the unitary at the final time T. We use the performance function

$$\Phi = \left|\langle U_{\mathrm{target}} | \, U(T)\rangle\right|^2 \ ,$$

where T is the final time of the pulse sequence and the inner product $\langle X | \, Y\rangle$ is defined as $\mathrm{tr}\left[X^\dagger Y\right]$. By optimizing the squared magnitude of this inner product, it is guaranteed that a global phase will be unimportant in the optimzation process.

We discretize the pulse sequence into N suitably small steps which allows to write the performance function as

$$\Phi = \langle U_{\mathrm{target}} | \, U_N \cdots U_1\rangle \langle U_1 \cdots U_N | \, U_{\mathrm{target}}\rangle \, .$$

Rewriting the previous expression we can define operators P_j, X_j as

$$\Phi = \langle \underbrace{U_{j+1}^\dagger \cdots U_N^\dagger U_{\mathrm{target}}}_{\equiv P_j} | \underbrace{U_j \cdots U_1}_{\equiv X_j} \rangle \langle X_j | \, P_j\rangle \, .$$

Now the corresponding gradients for the time-sliced control functions read to first order in the time step $\Delta t \equiv T/N$:

$$\frac{\partial \Phi}{\partial f_k(j)} = -2\mathrm{Re}\left\{\langle P_j | \, i\Delta t H_{\mathrm{control,k}} X_j\rangle \langle X_j | \, P_j\rangle\right\} .$$

This equation supplies the gradients to iteratively update the initially guessed or randomly chosen control functions. A more detailed introduction into the method, underlying derivations can be found e.g. in [161, 164].

It is intuitively clear that this optimization procedure is very non-trivial and cannot possibly guarantee to find a global optimum. If it converges, it rather flows to a local optimum given the gate run-time t_{gate}, the initial set of control functions and, most importantly, the algebraic nature of the control and drift Hamiltonian. If those Hamiltonians do not allow to produce the desired unitary operation, then it is clear that no optimization procedure can help. However, given the huge success in Nuclear Magnetic Resonance (NMR) experiments, the field that this method has come from, it seems to be a good tool from a pragmatic point of view despite its principal shortcomings.

3.3.2 Optimal control theory results for two qubits in the same cavity

As a first test of the method applied to the cavity grid, we consider the case of two qubits in a cavity obeying the Hamiltonian

$$H_1(t) = \frac{\pi J}{2}\left(\sigma_x^1\sigma_x^2 + \sigma_y^1\sigma_y^2\right) + \sum_{i=1}^{2}\frac{1}{2}\Delta_i(t)\,\sigma_z^i + \frac{1}{2}\,\Omega(t)\left(\sigma_x^1 + \sigma_x^2\right). \tag{3.2}$$

Here, there are three control functions, the local energy splittings of the qubits $\Delta_i(t)$ and a (global) microwave drive that can be applied to the qubits via the cavity. This is the situation e.g. found in the Yale group's two-qubit iSWAP experiment [82]. As we have argued before in Sec. (2), the iSWAP-gate is the natural two-qubit gate given the flip-flop interaction between the qubits specified by Eq. (3.2). So, we can expect that the optimal control approach will coincide with the analytically known result [165], namely that the optimal time in which the iSWAP

$$\exp\left\{i\frac{\pi}{4}\left(\sigma_x^1\sigma_x^2 + \sigma_y^1\sigma_y^2\right)\right\} = \begin{pmatrix} 1 & 0 & 0 & 0 \\ 0 & 0 & i & 0 \\ 0 & i & 0 & 0 \\ 0 & 0 & 0 & 1 \end{pmatrix}$$

is realized is given by

$$t_{\text{gate}} = \frac{1}{2J},$$

if the qubits are in resonance ($\Delta_1 = \Delta_2$) and no microwave drive is applied ($\Omega(t) = 0$). This was very nicely confirmed.

The next, non-trivial task for the optimal control approach was to optimize a CNOT and SWAP gate which, in a straightforward and 'pedestrian' way, can be decomposed [12] into

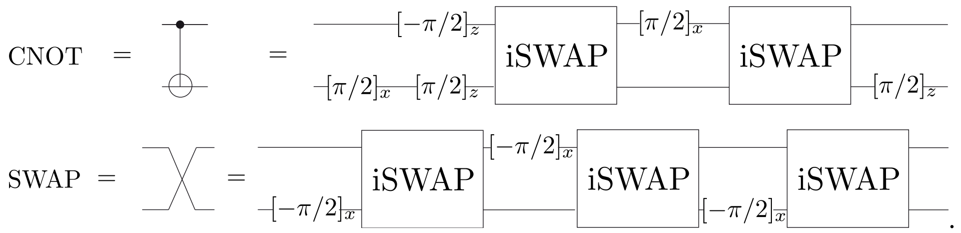

Figure 3.6: Quantum circuit for a CNOT and a SWAP gate. E.g. $[-\pi/2]_x$ denotes a $-\pi/2$ local rotation about the x-axis of the Bloch sphere. The right direction in these diagrams symbols time.

Given the particular situation we consider and the decomposition into elementary gates according to Fig. (3.6), one could realize the Hadamard gates by first detuning the qubits from each other strongly to (i) effectively switch off the flip-flop interaction and (ii) address only one qubit with the $\hat{\sigma}_x$-driving. The energy shifts and the iSWAP interaction can be directly realized.

Employing the optimal control scheme we have introduced, we have analyzed two situations:

1. No restrictions on the control functions.
2. Amplitudes of the control functions restricted:

$$\begin{aligned} |\Delta_i(t)| &\leq 6\,GHz \pm 2\pi \cdot 1GHz \\ |\Omega(t)| &\leq 300\,Mrad/s \approx 2\pi \cdot (48MHz) \end{aligned}$$

The results are compiled in Fig. (3.7). The key finding is that all local rotations can be done (almost) simultaneously to the iSWAP gate which in turn is fundamentally limited in time by $t_{\text{gate}} = 1/(2J)$. In Fig. (3.8) we show examples of optimized pulse sequences for a CNOT gate in restricted and unrestricted cases.

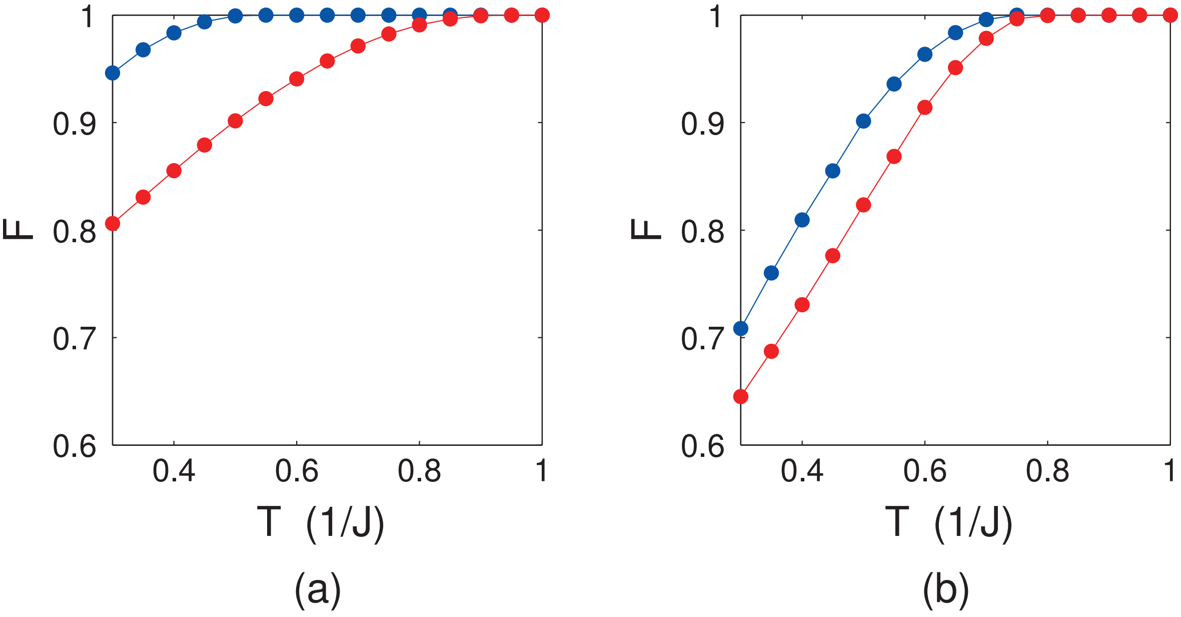

Figure 3.7: Maximum fidelity as a function of pulse duration, in both unrestricted case (i) (blue) and restricted case (ii) (red), for (a) a CNOT gate, and (b) a SWAP gate.

3.3.3 Optimal control theory results for three qubits in crossing cavities

As a next step, we take the findings for two qubits to the grid and look at the basic and most general two-qubit operation on a grid, namely the SOPS operation introduced in Sec. 2 which implements an arbitrary two-qubit gate between arbitrary two qubits on the grid involving at most one mediating qubit at the crossing of the cavities of the two qubit.

Simplified model without pulse restrictions

The Hamiltonian considered here reads:

$$H_2(t) = \frac{\pi J}{2} \left(\sigma_x^1 \sigma_x^2 + \sigma_y^1 \sigma_y^2 + \sigma_x^2 \sigma_x^3 + \sigma_y^2 \sigma_y^3 \right) \tag{3.3}$$

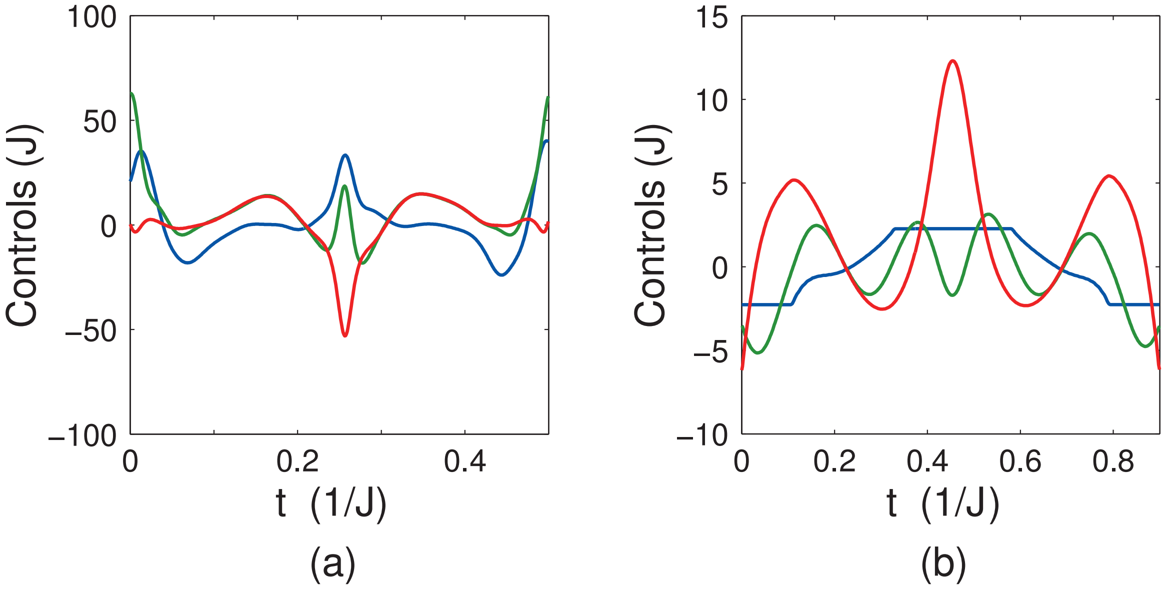

Figure 3.8: Controls Δ_1 (red), Δ_2 (green), and Ω (blue) in (a) unrestricted, and (b) restricted cases. Observe the visible restriction on the Rabi frequency (plateaus) in part (b). These pulses correspond to the fidelity curves shown in Fig. (3.7), part (a)

$$+ \sum_{i=1}^{3} \frac{1}{2} \left(\Omega_x^i(t)\, \sigma_x^i + \Omega_y^i(t)\, \sigma_y^i \right) .$$

Note that qubit 1 and qubit 3 cannot directly interact but instead have to use their interaction with qubit 2. Here, the speedup is about a factor of 3.5, just considering the two-qubit interactions. The 1-3 iSWAP-gate presented in Sec. 2 in a 'pedestrian' way, can be realized using the time of just two iSWAPs versus the 7 iSWAPs in the 'pedestrian' scheme (see Fig. (3.9)).

A summary of two- and three-qubit minimal times for the idealized model can be found in Tab. (3.3).

Gate	$T_{\text{pedestrian}}(1/J)$	$T_{\text{opt}}(1/J)$
CNOT_{12}	1.0	0.5
SWAP_{12}	1.5	0.75
iSWAP_{12}	0.5	0.5
CNOT_{13}	2.0	1.00
SWAP_{13}	4.5	1.15
iSWAP_{13}	3.5	1.00

Table 3.3: For the optimized 3-qubit cases, the time given is the shortest time in which our algorithm can reach a fidelity of $1 - 10^{-5}$, with time resolution $0.05/J$.

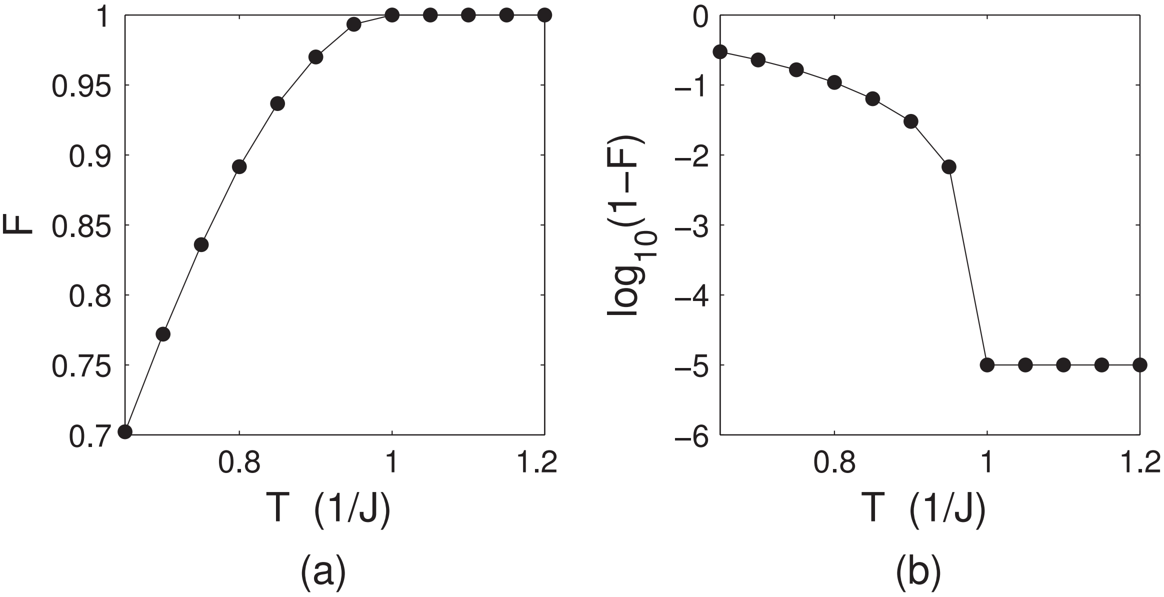

Figure 3.9: Fidelity as a function of gate run-time t_{gate} for a 1,3 iSWAP.

More realistic model including pulse restrictions

In a real experimental setup using the cavity grid, the single qubit rotations would most probably be done as follows: One qubit would be tuned to a certain frequency off-resonant from the cavity and also detuned from all other qubits in the cavity. Then one would apply a microwave tone to the cavity resonant to the qubit. Although this tone affects in principle all qubits in the cavity, there is a strong frequency selection that allows to more or less perfect individual addressing of a single qubit. This is the reason why we consider the following Hamiltonian instead of (3.3):

$$\begin{aligned} H_3(t) &= \frac{\pi J}{2}\left(\sigma_x^1\sigma_x^2+\sigma_y^1\sigma_y^2+\sigma_x^2\sigma_x^3+\sigma_y^2\sigma_y^3\right) \\ &\quad +\sum_{i=1}^{3}\frac{1}{2}\Omega_z^i(t)\,\sigma_z^i \\ &\quad +\frac{1}{2}\Omega_x^{12}(t)\left(\sigma_x^1+\sigma_x^2\right)+\frac{1}{2}\Omega_x^{23}(t)\left(\sigma_x^2+\sigma_x^3\right). \end{aligned}$$

Again, the first term describes the flip-flop interaction between all qubits as found in the 1-3 ’around-the-corner’ topology. The second term allows to tune the qubit transition frequencies independently from each other while the last two terms represent the aforementioned ability to drive the qubits per-cavity.

In addition to this more realistic structure, we have also applied restrictions to the control functions as follows:

$$\begin{aligned} |\Delta_i(t)| &\leq 6\,GHz \pm 2\pi\cdot 1GHz \\ |\Omega(t)| &\leq 300\,Mrad/s \approx 2\pi\cdot(48MHz). \end{aligned}$$

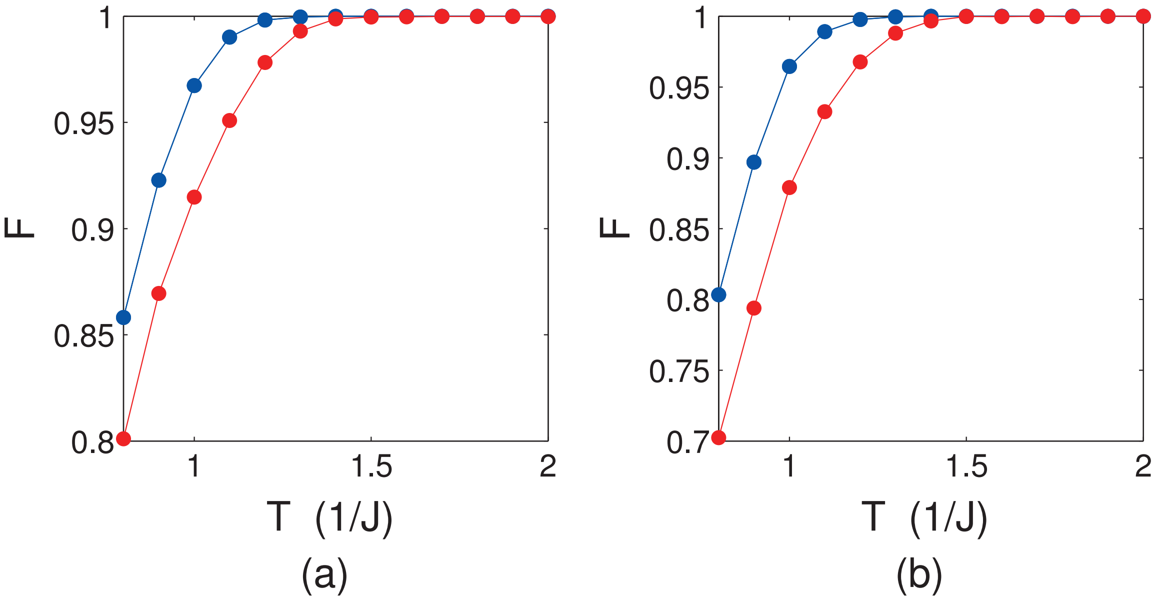

Figure 3.10: Maximum fidelity as a function of pulse duration, in both unrestricted case (i) (blue) and restricted case (ii) (red), for (a) a 1,3-CNOT gate, and (b) a 1,3-iSWAP gate.

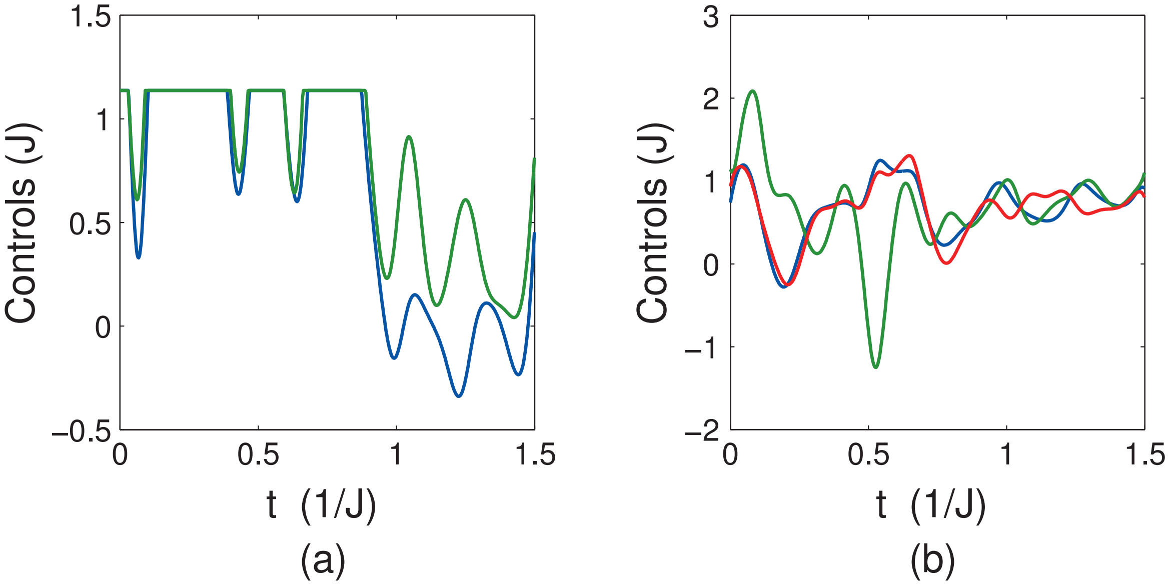

Figure 3.11: Restricted controls to implement a 1,3-iSWAP gate: (a) Ω_x^{12} (green), Ω_x^{23} (blue). (b) Ω_z^1 (blue), Ω_z^2 (green), Ω_z^3 (red). Restrictions are hit in the single-qubit driving powers shown in part (a) while the restrictions on the qubit transition frequencies are not actually limiting here.

As shown in Fig. (3.10) and comparing to the less restricted case examined before (see Fig. (3.9)), one observes that the restrictions and especially the more realistic control paradigm indeed play a role and reduces the speed-up from 3.5 to about 2.1 which is still considerable if one is looking at example pulse shapes corresponding to part (b) of Fig. (3.10) as shown in Fig. (3.11).

3.3.4 Analysis in terms of entanglement measures

In order to understand the pulses generated by the optimal control algorithm to a certain degree, it is a good idea to look at the entanglement between qubits during the sequence to see when they are actually entangled. As the $\sqrt{\text{iSWAP}}$-gate (letting the flip-flop interaction switched on for a time $t = 1/(4J)$) is a universal entangling gate we know that this has to be the case in some part of the sequence. We therefore compute the entanglement using the logarithmic negativity which is given by

$$E_N(\rho) = \log_2 \left|\left|\rho^{\Gamma_A}\right|\right|_1$$

where Γ_A is the partial transpose, $||\cdot||_1$ is the trace norm, and ρ is the reduced density matrix of the two-qubit subsystem from the initial state $|100\rangle$. The fidelity is

$$F(U) = \left|\mathrm{tr}\left\{U_T^\dagger U\right\}\right|$$

where U_T is the target 1,3-iSWAP gate.

This short demonstration already strongly suggests that a lot of fidelity and gate runtime can be gained by applying optimal control theory. However, a lot of care has to be exercised in choosing the model and the restrictions realistically. Like any optimization method, it tends to be slaved to a certain degree to the way those restrictions are implemented (hard wall vs. penalty function, etc.). Another interesting application for this method is to compensate e.g. for complicated distortions that happen to a signal when sending it through all cryogenic stages down to a sample. Simply inserting the transfer functions into the control Hamiltonians will take those effects into account naturally.

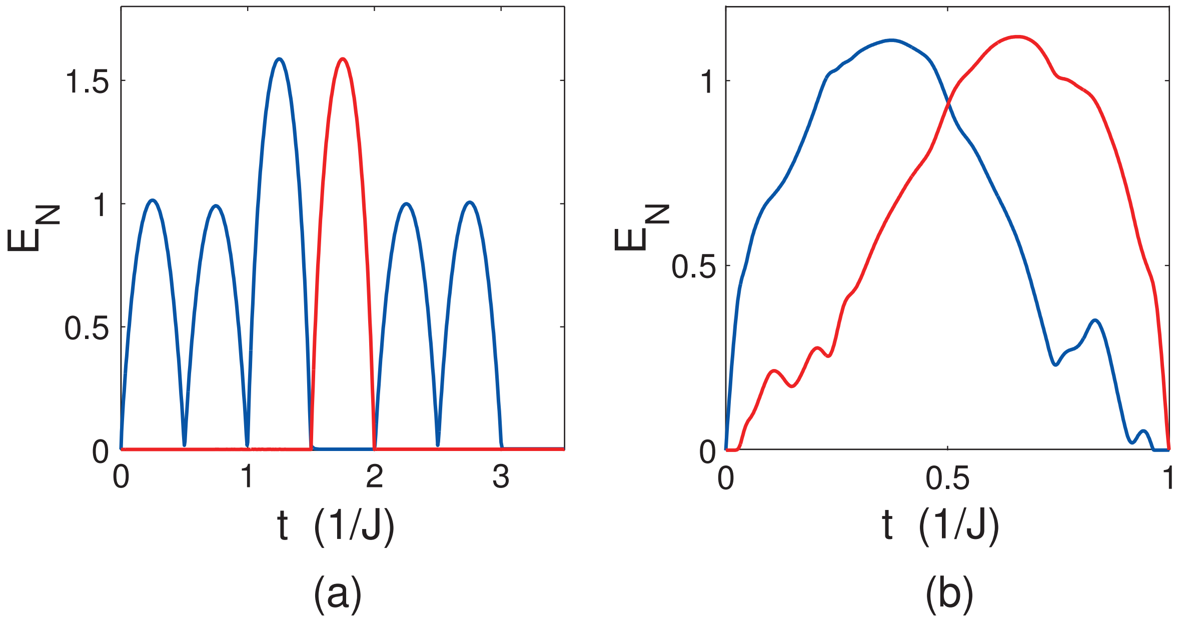

Figure 3.12: Logarithmic negativity between qubits 1-2 (blue line) and 2-3 (red line) for (a) pedestrian and (b) optimized ($F > 99.9\%$) implementations of a 1,3-iSWAP from the initial state $|100\rangle$. Note that while the pedestrian scheme involves 7 iSWAPs, the optimized version needs roughly two iSWAPs. These results are for the ideal, unrestricted control paradigm as presented in Eq. (3.3).

Chapter 4

Quantum trajectory approach to weak measurement

In this chapter we will introduce the method of quantum trajectories as generated by stochastic master equations. Before we start to derive formulas, we will give a small overview of the aspects of a measurement that are vital for the understanding of the concept of a measurement back-action. Especially we will focus on QND measurements and the class of so-called weak measurements. It is important to realize that using this technique is not some purpose on its own, but gives access to an extremely realistic and thus experimentally relevant description of measurement. When using this technique, the focus is not on the method, but on the physics involved in the experiment that one is simulating.

This chapter is supposed to be a rather pedagogical introduction to the technique which is later used in more complex setups, e.g. in the scheme for the measurement-based generation of multi-qubit entangled states (Sec. 5) and in the scheme for the detection of single itinerant microwave photons in Sec. 6.

4.1 Ideal and realistic measurement

4.1.1 Ideal measurements

Measurement in a reasonably realistic description is usually quite a bit more complicated than depicted in an introductory quantum mechanics textbook. The notion there is the following: If a measurement of some system observable is performed, one applies a projector $\hat{P}$ onto the system state which changes the state of the system instantly to the eigenstate that corresponds to the reported real number (the measurement result which is the corresponding eigenvalue of the measured observable[1]). This measurement is called 'projective' or a 'von-Neumann' measurement. The sudden change of state involved is usually referred to as 'collapse of the wavefunction'. One of the consequences of this sudden state-change is that if we were to repeat the same measurement, we would get exactly the same result. This is due to the fact that $\hat{P}^2 = \hat{P}$. A von-Neumann measurement shares this property with another very important class of measurements, the so-called 'Quantum Non-Demolition Measurements' (QND) [105, 106, 166].

It is noteworthy that this aspect of a quantum mechanical measurement poses a litmus test to the different philosophical interpretations of quantum mechanics. While the so-called 'collapse of the wavefunction'-theory ascribes ontological reality to this inherently random (stochastic) process and thus makes the universe a place ontologically dominated by randomness, there also exists the so-called 'multiverse' theory which claims that *all* possible measurement outcomes are realized - just in different universes which split/branch every time a measurement is performed.

Without trying to side with one of the interpretations, it remains unclear what the benefit of the multiverse theory is (we only live through one randomly selected path of universes and essentially could never experience the difference to a single random universe). It seems to face two major problems: a) The principle of economics of a theory seems to be heavily violated by the multiverse theory and its exponential "multiplication of universes". b) It seems to be unclear in what basis the branching occurs, leaving it yet again ontologically indefinite and thus not evidently ontologically preferable to the collapse of wavefunction theory. In the end it seems to be a) irrelevant to concrete research and b) a pure matter of personal taste which intepretation one prefers.

The act of measurement is a singular process which is *not* described by the Hamiltonian evolution according to the Schrödinger equation because this could never introduce any irreversible element (e.g. projection) into the theory.

While the fact that Hamiltonian dynamics is not sufficient to describe measurements well is certainly true, this picture is far too simplistic to be of use in describing most realistic situations as found in experiments. It merely constitutes a building block from which a realistic measurement process can be constructed.

4.1.2 More realistic description of a measurement

Now imagine a general measurement situation where the system in question cannot be directly projectively measured, but instead one has to couple a measurement apparatus (most often meso- or macroscopic) to the system. Only this apparatus can then be projectively measured.

---

[1] That is the reason why only Hermitian operators can be reasonably called observables, otherwise the real-valuedness of the eigenvalues is not guaranteed.

Assuming that the apparatus and the coupling to the system are indeed suitable to extract information about a certain system observable via a projective measurement on an apparatus observable, the following will happen during such a measurement:

We let system and apparatus, initially assumed to be in a *product* state, evolve according to the coupling Hamiltonian for some time interval Δt. Afterwards, the state will have changed, generally into an *entangled* state between system and measurement apparatus. It is by this entanglement that information about the system state is transferred into the measurement apparatus and reflected in the state of the measurement apparatus.

Then we imagine to projectively measure some *apparatus* observable. This has several consequences:

1. The measurement apparatus experiences a projection onto one of the (usually smoothly distributed) eigenstates of the *apparatus* observable.
2. The system and the measurement apparatus are now again in a product state.
3. This has evidently also changed the system state (this process is called measurement back-action), however not necessarily into an eigenstate of the *system* observable. It is important to realize that this change is also in so far *random,* as it is *conditional* on the measurement result we obtained when projectively measuring the apparatus observable.

4.2 Weak measurement

Very often and especially in situations considered in this thesis, the coupling between system and measurement apparatus is weak, meaning that during one measurement as we just described, the system state only changes very little. This is then referred to as a 'weak' measurement. If we take the continuum limit $\Delta t \to 0$, it is intuitively clear that the infinitesimally small kicks the system experiences should lead to stochastic dynamics adding to the Hamiltonian dynamics. We can therefore expect

1. Having a stochastic term enter the Schrödinger/master equation which leads to
2. diffusion- and/or jump-like behaviour of the system state and
3. eventually to the *system* being in an eigenstate of the *system* observable we have indirectly measured.

The timescale on which this *indirect* projection happens corresponds exactly to the timescale on which we can extract enough information from the measurement signal (the sequence of results from projectively measuring the apparatus) to infer the value of the *system* observable with certainty. On this timescale, we have indirectly performed a QND measurement of the system. No matter how much longer we keep on measuring, the result of subsequent measurements will always give the same result because the system has been projected.

In addition to the back-action modifying the quantum dynamics in a meaningful way, we also obtain the classical measurement signal (the sequence of measurement results). It is again intuitively clear that this signal should be noisy (it is a sequence of random projections of the measurement apparatus) and should contain the same realization of the noise as the internal back-action-modified dynamics.

To summarize, this framework of analyzing weak measurements gives us access to concrete realizations of the classical noisy signal while we simultaneously obtain the system-internal, measurement back-action-modified quantum dynamics for each of those realizations. This allows to design and validate detection schemes in a quite powerful way and makes this the method of choice for the topics examined in the present thesis. In the following section we will derive a stochastic master equation for a simple example system before turning to realistic applications.

4.3 Stochastic master equations

In this section we are going to introduce the concept of a stochastic master equation using a simple example[2] as illustrated in Fig. (4.1). The equation which we will derive will be of the same structure as the equations encountered in more difficult measurement setups, such as the ones which will be discussed in the following chapters.

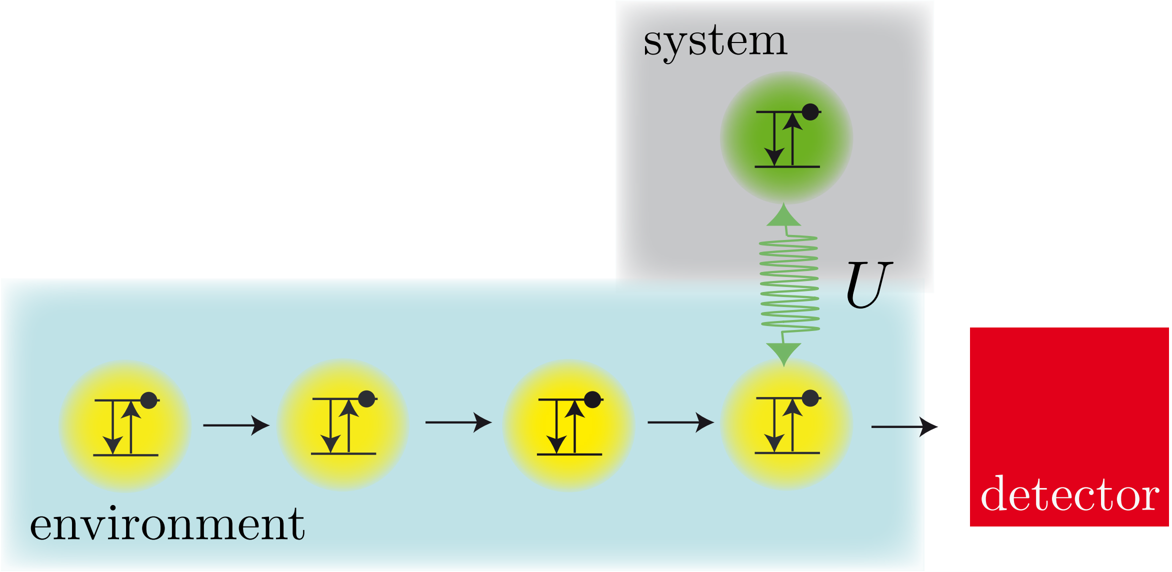

Figure 4.1: We imagine the following situation: A system qubit repeatedly interacts with identically prepared environment qubits. Each of them interacts with the system qubit according to the unitary transformation U. After system and environment qubits have interacted, the environment qubit's state is detected in e.g. a Stern-Gerlach detector.

Basic measurement theory for weak measurements

Depending on the strength of the interaction of environment qubit and system qubit, the environment qubits' initial state and measurement axis, different measurement situations can be realized. We will particularly focus on an implementation of a weak measurement which leads to state diffusion described by a stochastic master equation for the system qubit. First, we briefly need to introduce the concept of a Positive Operator Valued Measurement (POVM). Here, unlike with projective measurements, the measurement is not specified by a complete set of projectors which sum up to the identity operator, but instead by specifying some set of positive operators $\{\hat{E}_n\}$ such that

$$\sum_n \hat{E}_n = \hat{1}.$$

---

[2] The main steps of this introduction can also be found in [167], although the over-all focus of the paper is on stochastic Schrödinger equations rather than stochastic master equations.

The probability of a certain measurement outcome with subscript n is given by $p_n \equiv \left\langle \Psi \left| \hat{E}_n \right| \Psi \right\rangle$ or, in terms of the density operator $\hat{\rho}$, by $p_n \equiv \mathrm{tr}\hat{E}_n\hat{\rho}$. In order to assess the system state after a POVM, we need to additionally specify a set of operators $\{\hat{A}_{nk}\}$, from which the operators $\{\hat{E}_n\}$ are constructed according to

$$\hat{E}_n = \sum_k \hat{A}^\dagger_{nk}\hat{A}_{nk}.$$

The system state $\hat{\rho}'$ after the measurement is then given by

$$\hat{\rho}' = \frac{1}{p_n}\sum_k \hat{A}_{nk}\hat{\rho}\hat{A}^\dagger_{nk}.$$

Note that this measurement does not preserve the purity of the system state unless $\hat{E}_n = \hat{A}^\dagger_n\hat{A}_n$.

A weak measurement as introduced conceptually in the previous chapter can be described by a POVM in which each individual measurement result reveals only very little information about the system state. An example for such a POVM would be the following set of operators

$$\begin{aligned} \hat{E}_0 &\equiv |0\rangle\langle 0| + (1-\epsilon)|1\rangle\langle 1| \equiv \hat{A}_0^2 \\ \hat{E}_1 &\equiv \epsilon|1\rangle\langle 1| \equiv \hat{A}_1^2 \end{aligned}$$

where $\epsilon \ll 1$, such that the measurement outcomes for an initial state $|\Psi\rangle \equiv \alpha|0\rangle + \beta|1\rangle$are found with probabilities

$$\begin{aligned} p_0 &= 1 - \epsilon|\beta|^2 \\ p_1 &= \epsilon|\beta|^2. \end{aligned}$$

and the corresponding states of the system (conditional on the measurement outcome)

$$\begin{aligned} |\Psi_0\rangle &= \frac{\hat{A}_0|\Psi\rangle}{\sqrt{p_0}} = \frac{\alpha|0\rangle + \beta\sqrt{1-\epsilon}|1\rangle}{\sqrt{p_0}} \\ |\Psi_1\rangle &= |1\rangle. \end{aligned}$$

We can conclude that if one were to repeat this measurement, most of the time the system state would be almost unchanged corresponding to the '1' result, whereas the system will very rarely collapse into the $|1\rangle$ state which can be associated with a quantum 'jump'.

If one were to choose a POVM with a more symmetric set of operators, jumps would not occur at all. Instead, averaging over many successive measurements is needed here to extract information about the system. Such a set of operators would e.g. be

$$\begin{aligned} \hat{E}_0 &\equiv \left(\frac{1+\epsilon}{2}\right)|0\rangle\langle 0| + \left(\frac{1-\epsilon}{2}\right)|1\rangle\langle 1| \equiv \hat{A}_{10}^2 \\ \hat{E}_1 &\equiv \left(\frac{1-\epsilon}{2}\right)|0\rangle\langle 0| + \left(\frac{1+\epsilon}{2}\right)|1\rangle\langle 1| \equiv \hat{A}_1^2, \end{aligned}$$

and the conditional system states

$$\left|\Psi_0\right\rangle = \frac{1}{\sqrt{1+\epsilon(|\alpha|^2-|\beta|^2)}}(\alpha\sqrt{1+\epsilon}\left|0\right\rangle+\beta\sqrt{1-\epsilon}\left|1\right\rangle \approx \alpha(1+\epsilon|\beta|^2)\left|0\right\rangle+\beta(1-\epsilon|\alpha|^2)\left|1\right\rangle$$

$$\left|\Psi_1\right\rangle = \frac{1}{\sqrt{1-\epsilon(|\alpha|^2-|\beta|^2)}}(\alpha\sqrt{1-\epsilon}\left|0\right\rangle+\beta\sqrt{1+\epsilon}\left|1\right\rangle \approx \alpha(1-\epsilon|\beta|^2)\left|0\right\rangle+\beta(1+\epsilon|\alpha|^2)\left|1\right\rangle .$$

From these results we can already read off that a result '1' makes the system drift towards the $\left|1\right\rangle$ state and vice versa. The overall probability to end up in $\left|0\right\rangle$ or $\left|1\right\rangle$ is given by $|\alpha|^2$ and $|\beta|^2$, as we would expect for any quantum measurement.

Ensemble average description with the master equation

Although a general introduction to the concept of a weak measurement is certainly very useful, in practice it proves valuable to analyze a given measurement situation from an open systems perspective rather than just postulating a set of measurement operators. Instead, one divides the world into the system and the environment. Here, the environment consists of the qubits flying by the system qubit (see Fig. (4.1)). The interaction between system and environment is then specified by an interaction Hamiltonian $\hat{H}_{\text{int}}$ which generically entangles system and environment qubit. This entanglement is the resource that transfers information about the system state onto the environment qubit such that we can learn about the system state by analyzing the state of the environment qubits.

Let us assume that, initially, system and environment are in a product state

$$\left|\tilde{\Psi}\right\rangle \equiv \left|\Psi\right\rangle \otimes \left|E\right\rangle ,$$

which corresponds to a pure state density operator given by

$$\hat{\rho} = \left|\tilde{\Psi}\right\rangle \left\langle\tilde{\Psi}\right| .$$

Now we have to specify the way the unitary transformation U acts on the density operator, according to which system and environment interact. It can be written as

$$U \equiv \sum_j \hat{A}_j \otimes \hat{B}_j .$$

where $\hat{A}_j$ are system operators and $\hat{B}_j$ are environment operators. The density matrix after U has acted is then given by

$$\begin{aligned} \hat{\rho}_s' &\equiv \operatorname{tr}_E\left\{\hat{U}\left|\tilde{\Psi}\right\rangle\left\langle\tilde{\Psi}\right|\hat{U}\right\} && (4.1)\\ &= \sum_{j,j'} \operatorname{tr}_E\left\{\left(\hat{A}_j\left|\Psi\right\rangle\left\langle\Psi\right|\hat{A}^\dagger_{j'}\right)\otimes\left(\hat{B}_j\left|E\right\rangle\left\langle E\right|\hat{B}^\dagger_{j'}\right)\right\} \\ &= \sum_{j,j'} \hat{A}_j\left|\Psi\right\rangle\left\langle\Psi\right|\hat{A}^\dagger_{j'} \qquad \underbrace{\left\langle E\left|\hat{B}^\dagger_{j'}\hat{B}_j\right|E\right\rangle}_{\text{defines self-adjoint matrix } M_{jj'}} \qquad . && (4.2) \end{aligned}$$

The matrix $M_{jj'}$ is self-adjoint which means that it can be spectrally decomposed into real eigenvalues $\{\lambda_k\}$ and eigenvectors $\{\vec{\mu}_k\}$ such that

$$M_{jj'} = \sum_k \lambda_k \mu_{kj} \mu^*_{kj'}.$$

The residue of the environment entering the system dynamics can this way be included into the system operators by defining a new set of operators

$$\hat{O}_k \equiv \sqrt{\lambda_k} \sum_j \mu_{kj} \hat{A}_j,$$

such that Eq. (4.2) simply becomes

$$\hat{\rho}'_s = \sum_k \hat{O}_k \left|\Psi\right\rangle \left\langle\Psi\right| \hat{O}^\dagger_k. \tag{4.3}$$

Now we consider the very important special case when the unitary transformation only perturbs the system state weakly, i.e. it is close to the identity. It is then convenient to reintroduce the Hermitian operators $\hat{A}_j, \hat{B}_j$ as

$$\hat{U} \equiv \exp\left\{-i\theta \sum_j \hat{A}_j \otimes \hat{B}_j\right\},$$

with $\theta \ll 1$, one can expand Eq. (4.1) to second order in θ:

$$\hat{\rho}'_s = \left|\Psi\right\rangle \left\langle\Psi\right| + \frac{\theta^2}{2} \sum_{jj'} \left\langle E \left| \hat{B}_j \hat{B}^\dagger_j \right| E\right\rangle \left[2\hat{A}_j \left|\Psi\right\rangle \left\langle\Psi\right| \hat{A}_{j'} - \hat{A}_{j'}\hat{A}_j \left|\Psi\right\rangle \left\langle\Psi\right| - \left|\Psi\right\rangle \left\langle\Psi\right| \hat{A}_{j'}\hat{A}_j\right], \tag{4.4}$$

where we have without loss of generality assumed $\sum_j \hat{A}_j \left\langle E \left| \hat{B}_j \right| E\right\rangle = 0$, such that the first order term vanishes[3]. Using the same reasoning as before, we define a new set of (Lindblad) operators

$$\hat{L}_k \equiv \sqrt{\frac{\theta^2 \lambda_k}{\delta t}} \sum_j \mu_{kj} \hat{A}_j \tag{4.5}$$

in order to re-express Eq. (4.4) in terms of a Lindblad master equation

$$\frac{\hat{\rho} - \rho}{\delta t} = \sum_k \left[\hat{L}_k \hat{\rho} \hat{L}^\dagger_k - \frac{1}{2}\hat{L}^\dagger_k \hat{L}_k \hat{\rho} - \frac{1}{2}\hat{\rho}\hat{L}^\dagger_k \hat{L}_k\right], \tag{4.6}$$

assuming that the duration of the interaction of a single environment qubit with the system qubit is δt. This master equation describes the evolution from a pure state density matrix into the mixed state describing the statistical mixture of measurement outcomes. In order to 'unravel' this master equation w.r.t. the measurement, some additional considerations are needed. This will be done in the next paragraph. Unraveling in this context means to write down an equation that does not describe the ensemble average outcome of many measurements but instead a single, random realisation of the measurement process. The random variable introduced by such a process has exactly the properties that guarantee that averaging aver many of these single random realisations gives the same result as the original description before the unraveling. This is especially interesting if one aims at evaluating the measurement outcomes of single measurements with non-linear filters as it is done in e.g. Sec. 5 and Sec. 6.

---

[3] This is always possible by considering local rotations in addition to the unitary U.

Unraveling of the master equation

Unraveling the master equation with respect to the measurement means that instead of the ensemble average over many measurements which is described by Eq. (4.6), we go back a step and realize that the change in the density operator conditioned on a certain measurement result is given by

$$\hat{\rho}_{c,k}(t+\delta t) = \frac{\hat{O}_k \hat{\rho} \hat{O}_k^\dagger}{\mathrm{tr} \hat{O}_k \hat{\rho} \hat{O}_k^\dagger}.$$

As in the first example, for simplicity we consider a system qubit that repeatedly and weakly interacts with environment qubits which are prepared in a definite input state. We imagine to measure the environment qubit after the interaction in some basis with corresponding results ’0’ and ’1’. As mentioned before, for this case there are two operators $\hat{A}_1$ and $\hat{A}_2$ which for this simple case of qubits are equivalent to the operators $\hat{O}_k$. To specify these operators, it is necessary to know (a) the interaction of system and bath (b) the initial state of the bath qubits and (c) the basis the measurement on the bath qubits is performed.

Before turning to a concrete example, we want to sketch the line of the calculation that follows. First, we write the system state after one environment qubit has passed in terms of the conditional states, introducing a random variable $\delta N \in \{0, 1\}$ which is a point process (and thus non-Gaussian). The system state then reads

$$\hat{\rho}(t+\delta t) = \frac{\hat{A}_1 \hat{\rho}(t) \hat{A}_1^\dagger}{\mathrm{tr} \hat{A}_1 \hat{\rho}(t) \hat{A}_1^\dagger} \delta N + \frac{\hat{A}_2 \hat{\rho}(t) \hat{A}_2^\dagger}{\mathrm{tr} \hat{A}_2 \hat{\rho}(t) \hat{A}_2^\dagger} (1 - \delta N). \tag{4.7}$$

In principle one could now rewrite the terms on the right hand side by introducing a new random variable which has zero mean and variance δt. To do so, our knowledge is sufficient as the statistics of δN is completely known. Note that δN is also the measurement record (our ’signal’). It takes the value 1 with probability p_1 and 0 with probability p_0. Thus all moments of δN can be calculated. The new stochastic variable is then defined as

$$\delta Z \equiv \sqrt{\delta t} \left(\delta N - E[\delta N] \right) / \sqrt{Var(\delta t \delta N)}. \tag{4.8}$$

The next step is to imagine that we look at the system change after many of those random steps have occurred, each of which takes time δt. If it is ensured that this larger time $dt = n\delta t$ is still small compared to all system timescales while $n \gg 1$, then we can appeal to the central limit theorem and replace δZ by a Wiener increment dW (a Gaussian random variable with zero mean and variance dt). It has been rigorously shown in [168] that the form of Eq. (4.7) is preserved in this procedure and the only changes are $\delta Z \to dW$ and $\delta t \to dt$. The measurement signal $X \propto \delta N/\delta t$ can in general expressed using Eq. (4.8). With the same argument as before this can be written as a continuous function $X \rightarrow X(t)$ which contains white noise dW/dt rather than a point process.

In order to give live to the very abstract concept we will now derive the stochastic master equation in w this way for a concrete, simple example. We assume the environment qubits to be initialized in the state $|y_-\rangle \equiv \frac{1}{\sqrt{2}}(|0\rangle - i|1\rangle)$. After interacting with the system qubit (general state $|\Psi\rangle = \alpha|0\rangle + \beta|1\rangle$) according to the unitary $\hat{U} = \hat{R}_z(\theta)\hat{U}_{\text{CNOT}}(\theta)$, the environment qubit is measured in the $\hat{\sigma}_x$- basis. $\hat{R}_z(\theta)$ denotes a rotation about the z-axis with an angle θ while $\hat{U}_{\text{CNOT}}(\theta)$ is the usual CNOT gate parametrized by the angle $\theta \ll 1$. It can be written as

$$\hat{U}_{\text{CNOT}}(\theta) \equiv \exp\left\{-i\theta\hat{U}_{\text{CNOT}}\right\} = \hat{\mathbf{1}}\cos\theta - i\hat{U}_{\text{CNOT}}\sin\theta,$$

where

$$\hat{U}_{\text{CNOT}} \equiv \begin{pmatrix} 1 & 0 & 0 & 0 \\ 0 & 1 & 0 & 0 \\ 0 & 0 & 0 & 1 \\ 0 & 0 & 1 & 0 \end{pmatrix}$$

for the basis vectors ordered like this $(|00\rangle, |01\rangle, |10\rangle, |11\rangle)$. The measurement operators are given by

$$\begin{aligned} \hat{A}_0 &= \frac{1}{\sqrt{2}}(|0\rangle\langle 0| + (\cos\theta - \sin\theta)|1\rangle\langle 1|) \\ \hat{A}_1 &= \frac{1}{\sqrt{2}}(|0\rangle\langle 0| + (\cos\theta + \sin\theta)|1\rangle\langle 1|). \end{aligned}$$

The key computational tool is that we will consider everything up to order $O(\theta^2)$ which reduces the operators to

$$\begin{aligned} \hat{A}_0 &= \frac{1}{\sqrt{2}}\left(\hat{\mathbf{1}} + \theta|1\rangle\langle 1| - \theta^2(|1\rangle\langle 1|)^2\right) \\ \hat{A}_1 &= \frac{1}{\sqrt{2}}\left(\hat{\mathbf{1}} - \theta|1\rangle\langle 1| - \theta^2(|1\rangle\langle 1|)^2\right). \end{aligned}$$

The probabilities to obtain the results are given by

$$\begin{aligned} p_0 &\equiv \frac{1}{2} - \theta|\beta|^2 \\ p_1 &\equiv \frac{1}{2} + \theta|\beta|^2. \end{aligned}$$

Now we write Eq. (4.7) explicitly in orders of θ. In order to make it more readable, we introduce an operator $\hat{L} = \hat{L}^\dagger \equiv \sqrt{\frac{\theta^2}{\delta t}}|1\rangle\langle 1|$, following Eq. (4.5). The result reads

$$\begin{aligned} \hat{\rho}(t+\delta t) &= \frac{1}{2p_1}\left[\hat{\rho} + \sqrt{\delta t}\left(\hat{L}^\dagger\hat{\rho} + \hat{\rho}\hat{L}\right) + \delta t\left(\hat{L}^\dagger\hat{\rho}\hat{L} - \frac{1}{2}\hat{\rho}\hat{L}^\dagger\hat{L} - \frac{1}{2}\hat{L}^\dagger\hat{L}\hat{\rho}\right) + O(\theta^3)\right]\delta N \quad (4.9) \\ &+ \frac{1}{2p_0}\left[\hat{\rho} - \sqrt{\delta t}\left(\hat{L}^\dagger\hat{\rho} + \hat{\rho}\hat{L}\right) + \delta t\left(\hat{L}^\dagger\hat{\rho}\hat{L} - \frac{1}{2}\hat{\rho}\hat{L}^\dagger\hat{L} - \frac{1}{2}\hat{L}^\dagger\hat{L}\hat{\rho}\right) + O(\theta^3)\right](1-\delta N). \end{aligned}$$

Now the normalization factors have to be taken into account as well to order $O(\theta^2)$. Eq. (4.9) becomes

$$\begin{aligned}\hat{\rho}(t+\delta t) &= \left[\left(1-2|\beta|^2\theta+4|\beta|^4\theta^2\right)\hat{\rho}+\sqrt{\delta t}\left(1-2|\beta|^2\theta\right)\left(\hat{L}^\dagger\hat{\rho}+\hat{\rho}\hat{L}\right)+O(\theta^3)\right]\delta N \\ &+\left[\left(1+2|\beta|^2\theta+4|\beta|^4\theta^2\right)\hat{\rho}-\sqrt{\delta t}\left(1+2|\beta|^2\theta\right)\left(\hat{L}^\dagger\hat{\rho}+\hat{\rho}\hat{L}\right)+O(\theta^3)\right](1-\delta N) \\ &+\delta t\left(\hat{L}^\dagger\hat{\rho}\hat{L}-\frac{1}{2}\hat{\rho}\hat{L}^\dagger\hat{L}-\frac{1}{2}\hat{L}^\dagger\hat{L}\hat{\rho}\right)+O(\theta^3)\end{aligned}$$

By inspection we conclude that there is a measurement induced dephasing term $\hat{L}^\dagger\hat{\rho}\hat{L}-\frac{1}{2}\hat{\rho}\hat{L}^\dagger\hat{L}-\frac{1}{2}\hat{L}^\dagger\hat{L}\hat{\rho}$ which is of Lindblad ($\hat{L}$ is indeed a Lindblad operator) form and has the correct order in the time step $O(\delta t)$. Moreover, it does not depend on the stochastic variable and represents what would remain if we would average over the realisations of the measurement outcome. Sorting the stochastic terms simplifies the equation a lot:

$$\begin{aligned}\hat{\rho}(t+\delta t)-\hat{\rho}(t) &= \left[\hat{L}^\dagger\hat{\rho}+\hat{\rho}\hat{L}-2|\beta|^2\frac{\theta}{\sqrt{\delta t}}\hat{\rho}\right]\left[2\delta N-1-2|\beta|^2\theta\right]\sqrt{\delta t} \\ &+ \delta t\left(\hat{L}^\dagger\hat{\rho}\hat{L}-\frac{1}{2}\hat{\rho}\hat{L}^\dagger\hat{L}-\frac{1}{2}\hat{L}^\dagger\hat{L}\hat{\rho}\right)+O(\theta^3).\end{aligned} \tag{4.10}$$

Now we define a new stochastic variable (still a point process) as

$$\delta Z \equiv \left(2\delta N-1-2|\beta|^2\theta\right)\sqrt{\delta t}. \tag{4.11}$$

One can easily verify that this variable has the following properties

$$\begin{aligned}E[\delta Z] &= 0 \\ \mathrm{Var}[\delta Z]=E[\delta Z^2] &= \delta t+O(\theta^2).\end{aligned}$$

One might wonder why we have not taken the term of order θ^2 in the variance into account and redefined the variable accordingly to absorb it. The reason is that upon inserting it into Eq. (4.10), all terms stemming from the $O(\theta^2)$-term in the variance will multiply terms that are already of order $O(\theta)$ and can thus be disregarded.

As mentioned before, one can now make the step from one detection event to many and replace δZ by dW, which is a Gaussian random variable. Upon taking the continuum limit, the resulting equation contains a white noise variable $\xi(t)\equiv dW/dt$ and is of Ito-Form. Dephasing as well as the stochastic dynamics take place on a timescale given by $\Gamma\equiv\theta^2/dt$ which we call 'measurement rate'. To make this apparent, we redefine the Lindblad operators as $\hat{L}\rightarrow\sqrt{\Gamma}\hat{L}$ such that $\hat{L}=|1\rangle\langle 1|$. This complete stochastic master equation, the main result of this section reads

$$\begin{aligned}\frac{\hat{\rho}(t+dt)-\hat{\rho}(t)}{dt} &= \sqrt{\Gamma}\left[\hat{L}^\dagger\hat{\rho}+\hat{\rho}\hat{L}-2\mathrm{tr}\left(|1\rangle\langle 1|\hat{\rho}\right)\hat{\rho}\right]\xi(t) \\ &+ \Gamma\left(\hat{L}^\dagger\hat{\rho}\hat{L}-\frac{1}{2}\hat{\rho}\hat{L}^\dagger\hat{L}-\frac{1}{2}\hat{L}^\dagger\hat{L}\hat{\rho}\right).\end{aligned} \tag{4.12}$$

Remembering that the sequence of measurement results is encoded in the realisation of the stochastic variable δN, we can define the measurement signal conveniently as

$$X = \frac{2\delta N - 1}{2\delta t}.$$

From the derivation of the stochastic master equation (esp. Eq. (4.11)) we know that $2X = -2|\beta|^2\sqrt{\Gamma} + \delta Z/\delta t$. Making the same argument of taking $\delta t \to dt$ which takes $\delta Z/\delta t \to dW/dt = \xi(t)$, the signal (which can now be validly interpreted as a continuous function) reads

$$X(t) = \sqrt{\Gamma}\frac{\langle\hat{\sigma}_z\rangle(t) + 1}{2} + \frac{1}{2}\xi(t).$$

It is conveniently scaled such that the deterministic part takes values in the interval $[0, 1]$. The stochastic master equation (4.12) describes a diffusive behaviour for the system state whith the energy eigenstates $|0\rangle$ and $|1\rangle$ as attractors. Thus, the stochastic term vanishes for the system being in the $|0\rangle\langle 0|$ state or the $|1\rangle\langle 1|$ state or a statistical mixture of them.

We simulate Eq. (4.12) and find exactly this behaviour. In the simulation, we start with the system in an initial state $|\Psi\rangle \equiv \frac{1}{\sqrt{2}}(|0\rangle + |1\rangle)$ and observe that, depending on the realization of the noise, the system behaves diffusively on a timescale given by Γ^{-1} before it is either projected onto the $|0\rangle$ or the $|1\rangle$-state (see example trajectories in Fig. (4.2)). This can also be seen from a density plot where we averaged over 10^4 realisations of the actually measured, integrated signal which is given by

$$X_{\text{int}}(\tau) \equiv \frac{1}{\tau}\int_0^\tau X(\tau')d\tau',$$

(see Fig. (4.3)). One can nicely see that only after accumulating the signal longer than the timescale set by the measurement rate, we have gained enough signal-to-noise ratio to distinguish the two states. In addition we have also plotted the density of $|\beta|^2$ which shows that after the initial phase of diffusion, all the weight is contained in the eigenstates indicating that the system has on average evolved into a statistical mixture of $|0\rangle$ and $|1\rangle$.

With this very simple example, we have attempted to give a feeling about how a weak measurement results in gradual information increase on the observer side while gradually projecting the system onto an eigenstate. The beauty of the method clearly lies in the fact that it allows simultaneous and self-consistent simulation of a measurement record and the quantum dynamics of the systems conditioned on this record. We will now apply this method to more complex and realistic problems.

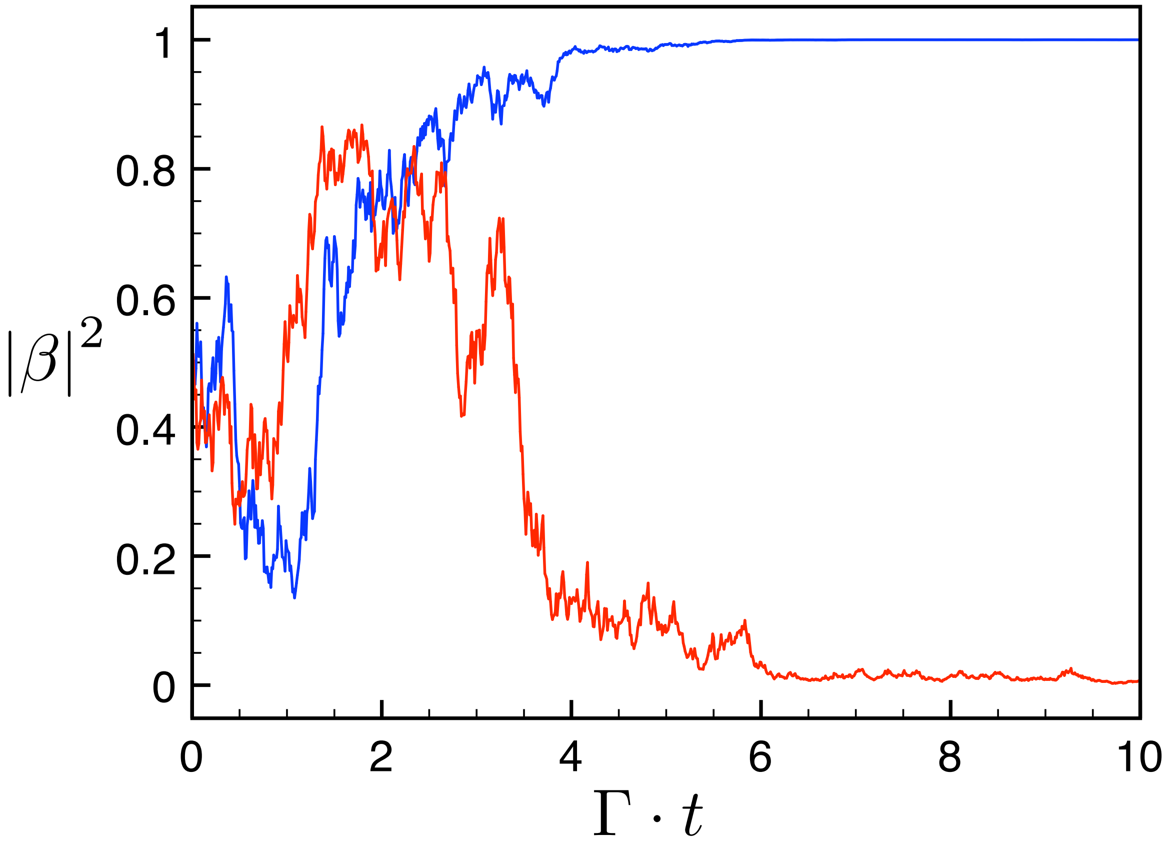

Figure 4.2: We plot the solution to Eq. (4.12) for the excited state probability $|\beta|^2 = \hat{\rho}_{11}$ for two different realisations of the noise (corresponding to two different measurement records) for an initial value of $\hat{\rho}_{11} = 1/2$. One can observe the timescale of projection set by the measurement rate Γ and that the states $|0\rangle$ and $|1\rangle$ are attractors.

Although the example here was very simplistic as it involved only two-level systems, the structure of the stochastic master equation and the measurement induced dephasing term is the same as found in the more complex setups discussed in the following chapters. They involve harmonic oscillators (the cavity modes) and the concept of homodyne/heterodyne detection in order to measure field quadratures. In particular, in Sec. 5 we exploit the structure of this stochastic master equation in so far as the projection always happens on a subspace which is specified by the observable eigenbasis. By carefully choosing this observable as a combination of single-qubit excitation numbers, we can use the measurement as a tool to generate entanglement from an initial product state and even stabilize it with the measurement. This should serve as an interesting tool for quantum information processing/quantum cryptography.

Then, in Sec. 6 we focus on the QND aspect of weak measurements. We propose and extensively analyze a scheme how to dispersively detect single itinerant microwave photons, essentially building on the measurement physics in form of a stochastic master equation as presented in this section.

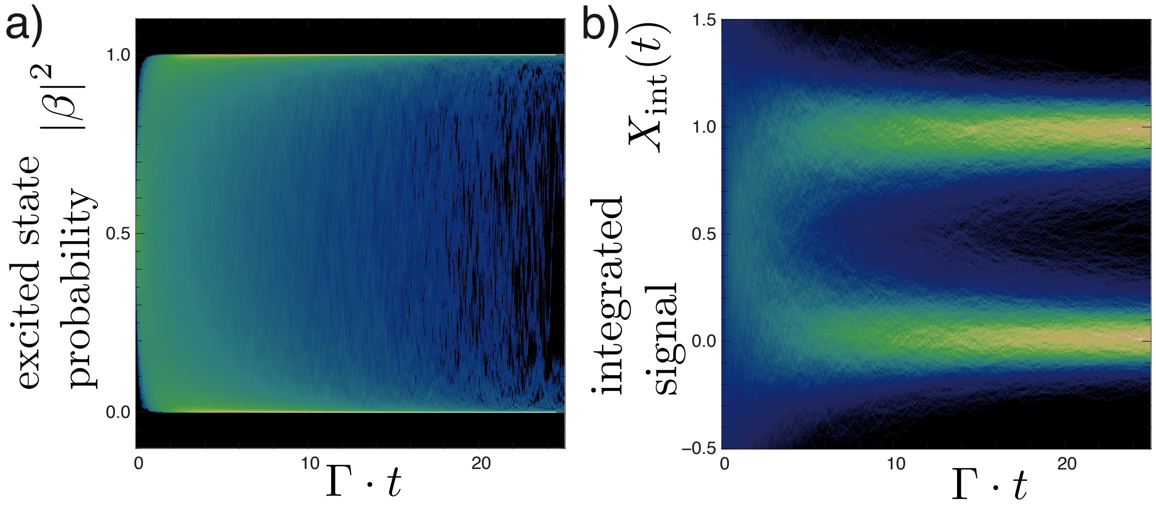

Figure 4.3: Densities of excited state probability and integrated measurement signal. Part (a) illustrates that all the probability density weight is concentrated near the states $|0\rangle$ and $|1\rangle$ on a timescale set by the measurement rate Γ. Part (b) shows the density of the integrated measurement signal $X_{\text{int}}(t)$. Again, we can directly observe that, on average, it is only possible to decide which state the system qubit is in after the measurement time Γ^{-1} has elapsed. For these plots, 10^4 realisations of the solution to Eq. (4.12) have been used.

Chapter 5

Measurement-based synthesis of multi-qubit entangled states

Entanglement is a key resource in quantum information processing. Instead of complicated pulse sequences on the individual qubit in a cavity, almost arbitrary states can be generated and stabilized in a much simpler manner. Among those states are the famous maximally entangled Greenberger-Horne-Zeilinger and W states. Building on the dispersive readout scheme of circuit QED, we analyze how those states may be generated through a dispersive collective QND measurement of superconducting qubits coupled to a microwave transmission line resonator.

The target state is determined by choosing sign and magnitude of the qubit detuning with respect to the cavity as well as the product state the qubits are initalised in. The scheme under evaluation here is directly applicable to an arbitrary number of qubits connected through a cavity quantum bus.

Using the quantum trajectory approach, we analyze the stochastic measurement traces that would be observed in experiments. We illustrate the synthesis of three-qubit W- and GHZ states, and we analyze how the fidelity and the entanglement evolve in time during the measurement. We discuss the influence of decoherence and relaxation, as well as of imperfect control over experimental parameters. We show that the desired states can be generated on timescales much faster than the qubit decoherence rates.

The contents of this chapter have been published in essentially the form presented here in [Ferdinand Helmer and Florian Marquardt, Measurement-based synthesis of multiqubit entangled states in superconducting cavity QED, Physical Review A, 79(5) , (2009), [169]].

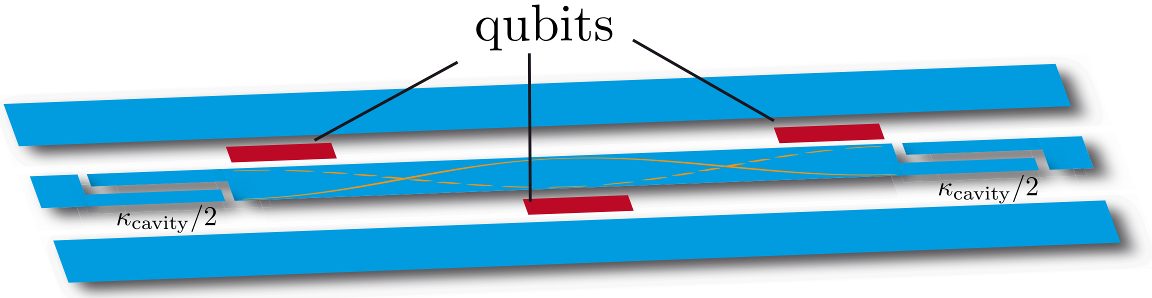

Figure 5.1: Schematic setup: Three superconducting qubits (red) are coupled to a mode of a coplanar microwave resonator (blue). The measurement of the phase shift of a transmitted microwave beam can be utilized to rapidly synthesize e.g. maximally entangled multi-qubit states like GHZ and W-states.

5.1 Introduction

The realization of quantum-optical concepts in condensed matter systems has led to remarkable progress during the past few years. One of the prime examples is the study of quantum electrodynamics (QED) in superconducting circuits. Earlier suggestions to implement the Jaynes-Cummings model in the solid state [118, 142, 143] were followed by a proposal [78] to employ on-chip microwave resonators and couple them to artificial atoms in the form of superconducting qubits.

This seminal idea was, soon thereafter, realized experimentally [79], creating a solid-state analogue of conventional optical cavity QED [170]. The tight confinement of the field mode and the large electric dipole moment of the "atom" yield extraordinary coupling strengths. As a result, these highly tunable systems have been employed to demonstrate experimentally a variety of achievements, including: The Jaynes-Cummings model in the strong-coupling regime [60, 68, 79], Rabi and Ramsey oscillations and dispersive qubit readout [144, 171], generation of single photons [123] and Fock states [136, 137], cavity-mediated coupling of two qubits [41, 82], setups with three qubits [125], Berry's phase [172], and the measurement of the photon number distribution [121].

The strong coupling makes dispersive quantum non-demolition (QND) readout possible, both for qubit states and for detecting single photons [173]. QND measurements are ideal projective measurements that reproduce their outcome when repeated [106, 166]. Any QND measurement may be applied to (probabilistically) generate states. In particular, having several qubits inside a common cavity (as realized in recent circuit QED experiments [41, 82], for a schematic setup see Fig. (5.1))), one may produce entangled multi-qubit states, even without employing directly any qubit-qubit coupling. In the context of circuit QED, this option has been investigated previously in a series of remarkable studies [174–176]. However, these consider primarily two qubits, with a recent work [175] discussing the extension to more qubits in general terms. The present work aims to go beyond these studies in several aspects. First, we present necessary conditions for being able to generate arbitrary multi-qubit states out of a given subspace of the total multi-qubit Hilbert space, using only single qubit operations and subsequent collective measurement. Second, we carry out detailed quantum jump trajectory simulations also for the case of three qubits, where W and GHZ states may be produced. We show how entanglement is generated in the course of the measurement process, paying attention to the effects of relaxation and decoherence. Moreover, we analyze how imprecise fine-tuning of experimental parameters would lead to a loss of entanglement after its initial, transient generation. Finally, we comment on possible experimental realizations. Such a measurement-based scheme complements other approaches for entanglement-generation in circuit QED [78, 126, 145, 148, 177–181] , based on unitary dynamics, and may prove advantageous for some purposes, since generation and measurement are combined into one step. It might also be used to generate entanglement between qubits in spatially separated cavities, without any direct interaction.

5.2 Model

We investigate a QND scheme utilizing the coupling of superconducting qubits to a bosonic field mode of a microwave resonator as examined in [78, 79]. The presence of excitations in the qubits inside the cavity gives rise to a frequency shift of the cavity mode, which can be observed dispersively via its phase shift. In turn, the measurement back-action leads to a projection of the qubits on a state that depends fully a) on the chosen set of couplings and b) the initial (product) state the qubits are prepared in.

We proceed as follows: (i) We derive a stochastic master equation for the situation of N qubits coupled to a cavity subject to phase shift measurement and give an analytical approach to the success rates and state lifetime, given the imperfections due to parameter spread and qubit decoherence. (ii) We give examples of interesting states which can be synthesized in this way and comment on the lifetimes and success rates for those particularly interesting states. (iii) Finally, we comment on possible experimental realizations.

We consider a system of a driven cavity mode coupled to N qubits

$$\begin{aligned}\hat{H} &= \hbar\omega\left(\hat{a}^\dagger\hat{a}+\frac{1}{2}\right)+\sum_{i=1}^{N}\frac{\epsilon_i}{2}\left(\hat{\sigma}_i^z+1\right)\\ &+ \sum_{i=1}^{N} g_i^0(\sigma_i^+ a+\sigma_i^- a^\dagger)+\frac{\kappa_{\text{cavity}}}{2}\left(\varepsilon\hat{a}^\dagger+\hat{a}\varepsilon^*\right)\\ &+ \hat{H}_{\text{decay}}\,, \qquad (5.1)\end{aligned}$$

a model commonly known as the Tavis-Cummings model which has been recently experimentally realized for $N = 2$ [41, 82] and $N = 3$ [125]. The first term of this Hamiltonian describes the cavity mode with a frequency ω, the second all qubit energies, the third term realizes the Jaynes-Cummings coupling for each qubit to the cavity with bare coupling constants g_i^0, while the last term describes the driving of the cavity with the readout microwave tone which will yield $|\varepsilon|^2$ photons in the resonator on average (κ_{cavity} is the intensity decay rate for the cavity).

In the limit where all the qubits are strongly detuned from the cavity, it is well-known [78] that the qubits impart a state-dependent phase shift on the cavity mode and the effective Hamiltonian can be written as:

$$
\begin{aligned}
\hat{H} &= \hbar\omega\left(\hat{n}+\frac{1}{2}\right)+\sum_{i=1}^{N}\frac{\epsilon_i}{2}\left(\hat{\sigma}_i^z+1\right)\\
&+ \sum_{i=1}^{N}\frac{(g_i^0)^2}{\Delta_i}\frac{\left(\hat{\sigma}_i^z+1\right)}{2}\hat{n}+\frac{\kappa_{\text{cavity}}}{2}\left(\varepsilon\hat{a}^\dagger+\hat{a}\varepsilon^*\right)+\hat{H}_{\text{decay}}\\
&= \hbar\left[\omega+\sum_{i=1}^{N}\frac{(g_i^0)^2}{\Delta_i}\frac{\left(\hat{\sigma}_i^z+1\right)}{2}\right]\left(\hat{n}+\frac{1}{2}\right)+\sum_{i=1}^{N}\frac{\epsilon_i}{2}\left(\hat{\sigma}_i^z+1\right)\\
&+ \frac{\kappa_{\text{cavity}}}{2}\left(\varepsilon\hat{a}^\dagger+\hat{a}\varepsilon^*\right)+\hat{H}_{\text{decay}}\,. \qquad (5.2)
\end{aligned}
$$

Here, $\hat{n}=\hat{a}^\dagger\hat{a}$ denotes the number operator of the cavity mode. Hamiltonian (6.1) also induces an effective flip-flop interaction [78, 82] of strength $J_{\alpha\beta}=g_\alpha g_\beta(\Delta_\alpha+\Delta_\beta)/(2\Delta_\alpha\Delta_\beta)$ between each pair of qubits (α,β) in the same cavity (for couplings $g_{\alpha(\beta)}$ and detunings from the cavity $\Delta_{\alpha(\beta)}$, in the dispersive limit $|g|\ll|\,\Delta|$):

$$
\hat{H}_{\alpha\beta}^{\text{flip-flop}}=J_{\alpha\beta}\left(\hat{\sigma}_\alpha^+\hat{\sigma}_\beta^-+\text{h.c.}\right). \qquad (5.3)
$$

When simulating the master equation (8.14) to be derived from the Hamiltonian (5.2), we neglect this interaction for several reasons. (i) In a concrete experiment the qubit energies could always be chosen very different, such that this unwanted interaction does not play a role, since the qubits are non-resonant. (ii) As we will argue later in more detail, the measurement rate $\bar{\Gamma}$ is usually much larger than $J_{\alpha\beta}$, thus making the effects of the interaction negligibly small even when the qubits are in resonance with each other. (iii) We note that all the states we consider as examples are eigenstates of the flip-flop interaction, Eq. (5.3). Therefore, even if the qubits are chosen to be in resonance (as is ultimately assumed in our simulations), the interaction will not have any important effect on the dynamics besides trivial phases between subspaces that are rendered mutually incoherent by the measurement anyway. Thus, we will neglect the flip-flop interaction.

5.3 Necessary conditions for the generation of given target states

The protocol we are envisaging is to first produce a product state, using local operations on the individual qubits, and then to project on an entangled state by measurement. This scheme will be successful with a certain probability. Our aim in the present section is to briefly discuss the necessary conditions that must be met to be able to generate a given class of entangled states. It goes without saying that once an entangled state has been reached, one may then apply further local operations to reach a corresponding subspace of the full multi-qubit Hilbert space.

Let us first fix notation. The coupling strengths g_i determine the phase shifts induced by the individual qubits,

$$
g_i\equiv\frac{(g_i^0)^2}{\Delta_i}, \qquad (5.4)
$$

and for convenience we will collect them into the coupling vector

$$\overrightarrow{G} \equiv \left(\frac{g_i}{\bar{g}}\right), \; i = 1...N\,, \tag{5.5}$$

where the overall strength $\bar{g}$ just determines the measurement time-scale, but does not affect the reachable states.

Using qubit excitation operators $\hat{n}_i \equiv \frac{\left(\hat{\sigma}_i^z+1\right)}{2}$, we define the measurement operator $\hat{N}$ as

$$\hat{N} \equiv \sum_{i=1}^{N} \frac{g_i}{\bar{g}} \hat{n}_i\,. \tag{5.6}$$

Note that even in current experiments, the g_i are tunable in magnitude and sign simply by choosing the detuning Δ appropriately. The phase shift on the microwave cavity will then be

$$\hat{\Phi} = \sum_{i=0}^{N} \hat{\phi}_i = \bar{g}\hat{N} = \sum_{i=1}^{N} g_i \hat{n}_i \tag{5.7}$$

where n_i is the excitation number of the i-th qubit.

The desired entangled state $|\Psi\rangle \equiv \sum_{j=1}^{2^N} \alpha_j |\varphi_j\rangle$ has complex amplitudes

$$\overrightarrow{\alpha} \equiv (\alpha_j)\,, \; j = 1...2^N \tag{5.8}$$

in the energy eigenbasis of the qubits (a product basis that diagonalizes $\hat{n}_i$).

In the following we derive *necessary* conditions for being able to produce arbitrarily chosen states out of some M-dimensional Hilbert space that is spanned by a subset of M basis states $|\varphi_j\rangle$. In order to generate a certain target state given by arbitrary $\overrightarrow{\alpha}$, we need to adjust the couplings such that all base kets with non-vanishing α_j yield the same phase shift. Assume the amplitude vector of the target state has

$$M \in \{1, ..., 2^N\}$$

non-zero entries $\alpha_j, j \in \{1, .., 2^N\}$, where the corresponding indices can be written as a family F_α with $\dim(F_\alpha) = M$. Then the goal is to use the measurement to project the system onto the subspace given by

$$\mathrm{span}\left(\{|\varphi_\mathrm{j}\rangle\, |\mathrm{j} \in \mathrm{F}_\alpha\}\right).$$

In the simplest case this is directly possible by choosing (i) an appropriate initial product state of the three qubits (to fix the amplitudes) and (ii) a suitable coupling vector (to project onto the correct subspace).

Choosing an arbitrary initial product state allows for the choice of $2N$ complex amplitudes. Due to normalization of the N single qubit states and an arbitrary global phase for each of those states, we essentially have $2N$ real parameters to choose.

The amplitude vector of the target state will - up to a constant common factor due to the renormalization after projection - be determined by the amplitudes of this initial state. This suggests that, in general (i.e. for arbitrary target states), we can only aim at reaching states that satisfy

$$2M - 2 \leq 2N. \tag{5.9}$$

Again, we had to subtract 2 to account for the irrelevant global phase and normalization.

Note that for the maximal value of $M = 2^N$, the last inequality does not hold for any $N > 1$ and we recover the fact that arbitrary states are in general not product states. Note that we have just found a necessary condition for constructing *arbitrary* states out of an M-dimensional subspace. When choosing particular states, e.g. trivially separable states, one may still be able to construct those even if they formally violate Eq. (5.9)).

We now turn to the question when it is possible to choose the couplings such that the measurement cannot distinguish the components of the target state from each other. This requirement of equal phase-shifts formally corresponds to a set of $M - 1$ equations

$$\langle\varphi_i|\,\hat{N}\,|\varphi_i\rangle = \langle\varphi_j|\,\hat{N}\,|\varphi_j\rangle \tag{5.10}$$

where i,j denote successive indices out of F_α.

As tunable parameters to our disposal we effectively have $N - 1$ couplings (discounting the overall strength $\bar{g}$), so this set of equations will in general be solvable as long as $M \leq N$ is fulfilled.

As we will demonstrate below by constructive proof, the most interesting entangled states, such as W and GHZ states, can always be synthesized in a single step. Indeed, they have $M = N$ for the W- and $M = 2$ for the GHZ states and thus satisfy the necessary conditions discussed in this section.

5.4 Stochastic master equation

In this section we present a stochastic master equation for the system presented above. This enables us to model the back-action of the phase shift measurement as well as the measured homodyne signal.

In the case of a cavity mode that decays much faster both than the qubit decoherence rates ($\kappa_{cavity} \gg \gamma_1, \gamma_\phi$) and the couplings to the cavity mode $\kappa_{cavity} \gg g_i \forall i \in \{0, 1, .., N\}$, it is possible to adiabatically eliminate the cavity mode from the system and find for the stochastic master equation (in the interaction picture) for the qubits alone

$$\begin{aligned}
\dot{\hat{\rho}} &= \sum_{i=0}^{N} \gamma_1 \left(\hat{\sigma}_i{}^- \hat{\rho} \hat{\sigma}_i{}^+ - \frac{1}{2} \hat{\sigma}_i{}^+ \hat{\sigma}_i{}^- \hat{\rho} - \frac{1}{2} \hat{\rho} \hat{\sigma}_i{}^+ \hat{\sigma}_i{}^- \right) \\
&+ \sum_{i=0}^{N} \gamma^{\varphi} \left[2\hat{P}_i \hat{\rho} \hat{P}_i - \hat{P}_i \hat{\rho} - \hat{\rho} \hat{P}_i \right] \\
&- 2\bar{\Gamma} \left[\hat{N}, \left[\hat{N}, \hat{\rho} \right] \right] \\
&- \sqrt{4\bar{\Gamma}} \left(\hat{N} \hat{\rho} + \hat{\rho} \hat{N} - 2\hat{\rho} \left\langle \hat{N} \right\rangle (t) \right) \xi(t).
\end{aligned} \tag{5.11}$$

Here $\bar{\Gamma} \equiv \frac{\bar{g}^2|\varepsilon|^2}{\kappa_{cavity}}$ is the measurement rate, and $|\varepsilon|^2$ is the average photon number circulating inside the cavity mode. See [182, 183] for a detailed derivation. The stochastic master equation is conditioned on the measured signal

$$X(t) \equiv \langle \hat{N} \rangle (t) + \frac{1}{4}\sqrt{\frac{1}{\bar{\Gamma}}}\xi(t), \tag{5.12}$$

where ξ represents the fundamental, unavoidable vacuum noise (with $\langle \xi(t)\xi(t') \rangle = \delta(t - t')$). Physically, $X(t)$ is the appropriate (suitably normalized) quadrature component of the electric field transmitted through the cavity, which is proportional to the phase shift that indicates the multi-qubit state. Experimentally, this signal would be measured in a homodyne detection scheme, Note that, for a two-sided cavity, information is contained both in the transmitted and the reflected signal, and we have assumed that both parts of the signals are superimposed symmetrically to extract the maximum possible information content [173].

5.5 Examples of measurement-generated entangled states

In this section we discuss the most relevant examples for the case of two and three qubits in the cavity. More precisely we will show that it is possible to generate Bell states, W states, and Greenberger-Horne-Zeilinger states (GHZ-states) as well as other maximally entangled states.

We will be able to observe that the measurement indeed first drives the system to one of its attractor solutions (among them the desired state) which are then stabilized by the measurement. The attractor nature of the subspaces selected by the coupling vector $\overrightarrow{G}$ can be immediately understood from the structure of the stochastic master equation (8.14), by realizing that the stochastic term and the measurement induced dephasing term both vanish if the density matrix is in the desired state. Only relaxation and dephasing can take the system out of this final state, and we will discuss their influence later.

5.5.1 Quantitative characterization

In order to characterize the time-evolution during the measurement process, we have plotted several quantities. We plot the phase shift signal $X(t)$ and the excitation number n_i in each qubit as functions of time. To verify that we have indeed obtained the desired state, we will compute the state fidelity $\mathcal{F}$ between the density matrix from the simulation, ρ_{sim}, and the ideal state density matrix σ, according to $\mathcal{F} \equiv \mathrm{tr}\left|\sqrt{\rho_{sim}}\sigma\sqrt{\rho_{sim}}\right|$. Finally, the two-qubit entanglement between two qubits A and B will be measured by the log-negativity. Given the density matrix ρ of the two qubits (after tracing out other qubits, if needed), this is defined as $E_N(\rho) = \log_2 \left\|\rho^{T_A}\right\|$. Here ρ^{T_A} is the partial transpose with respect to qubit A, and $\|\mu\| = \mathrm{tr}[\sqrt{\mu^\dagger \mu}]$ is the trace norm.

Before discussing the individual examples, we briefly point out the general features. Looking at the results [e.g. in Fig. (5.2)], we find that in those cases where we end up in the right state the fidelity as well as the log-negativity are 1. Furthermore, the state is stabilized by the measurement, meaning that, due to the absence of any non-vanishing terms in the master equation's right hand side, it is frozen. We observe that the state is generated on a timescale given by the measurement rate $\bar{\Gamma}^{-1}$.

While discussing the examples we will also analyze plots that show the probability density of various quantities evolving over time. This point merits a brief discussion. The time-evolution of the distribution for any simple quantum-mechanical observable can be immediately obtained from the time-evolution of the *average* density-matrix, i.e. from the standard, non-stochastic master equation. In that case, simulating a large number of stochastic trajectories and then averaging over the results would be unnecessarily cumbersome. However, that argument becomes void as soon as one considers signals that depend on the entire pre-history of the trajectory. An important example is the time-averaged phase-shift signal,

$$\bar{X}(t) \equiv \frac{1}{t}\int_0^t X(t')dt' \,. \tag{5.13}$$

This quantity has the advantage of tending towards a well-defined limit in the course of a QND measurement, with the fluctuations around that limiting value decreasing like $1/\sqrt{t}$. It is not possible to obtain the distribution of $\bar{X}$ from the average density-matrix ρ, and quantum jump trajectory simulations are needed.

Another example is represented by quantities that depend non-linearly on the density matrix. In those cases, the average density matrix is irrelevant since obviously $\langle f(\rho)\rangle \neq f(\langle\rho\rangle)$ for a nonlinear function f. An important case is the entanglement measure E_N. In fact, the average density matrix is never entangled ($E_N(\langle\rho\rangle) \equiv 0$) for our examples. Thus, it is indeed necessary to obtain E_N for a large number of trajectories in order to discuss its statistical behaviour and plot the probability density.

5.5.2 Bell states for two qubits - no decoherence

In the case of two qubits and vanishing decoherence rates $\gamma, \gamma_\phi = 0$, the generation of Bell states is straightforward [175]. We imagine starting the experiment with all qubits in the ground state $|00\rangle$ applying a Hadamard gate ($\pi/2$ - σ_x rotation) at some time t_0, leaving the system in the product state $|\Psi_0\rangle \equiv \prod_\otimes \frac{1}{\sqrt{2}}(|0\rangle + |1\rangle) = \frac{1}{2}(|00\rangle + |01\rangle + |10\rangle + |11\rangle)$. We want to generate the Bell state

$$\left|\Psi^+\right\rangle \equiv \frac{1}{\sqrt{2}}\left(|01\rangle + |10\rangle\right), \tag{5.14}$$

which is the two-qubit version of a W-state. Clearly the amplitude vector for this state is simply $\sqrt{2}\overrightarrow{\alpha} = (0,1,1,0)^T$, and the resulting Eq. (5.10) for the couplings is given by

$g_1 = g_2$, thus $\overrightarrow{G} = (1,1)^T$. The desired state will be generated with a success rate η given by

$$\eta \equiv \left|\left\langle \Psi^+ \right| \Psi_0\rangle\right|^2 = \frac{1}{2}, \tag{5.15}$$

meaning that the experiment will in 50% of all runs end up in the correct state (as confirmed by observation of the correct phase shift).

Likewise, for the Bell state vector $|\Phi^+\rangle \equiv \frac{1}{\sqrt{2}}(|00\rangle + |11\rangle)$, we find for the amplitude vector $\sqrt{2}\overrightarrow{\alpha} = (1,0,0,1)^T$, and for the characteristic equation for the couplings $g_1 = -g_2$, which is fulfilled by the choice of coupling vector $\overrightarrow{G} = (1, -1)^T$. Note that in principle $|\Phi^+\rangle$ could also be generated by first producing $|\Psi^+\rangle$ and then applying local unitary operations, and the same is true for the two other Bell states, $|\Psi^-\rangle$ and $|\Phi^-\rangle$.

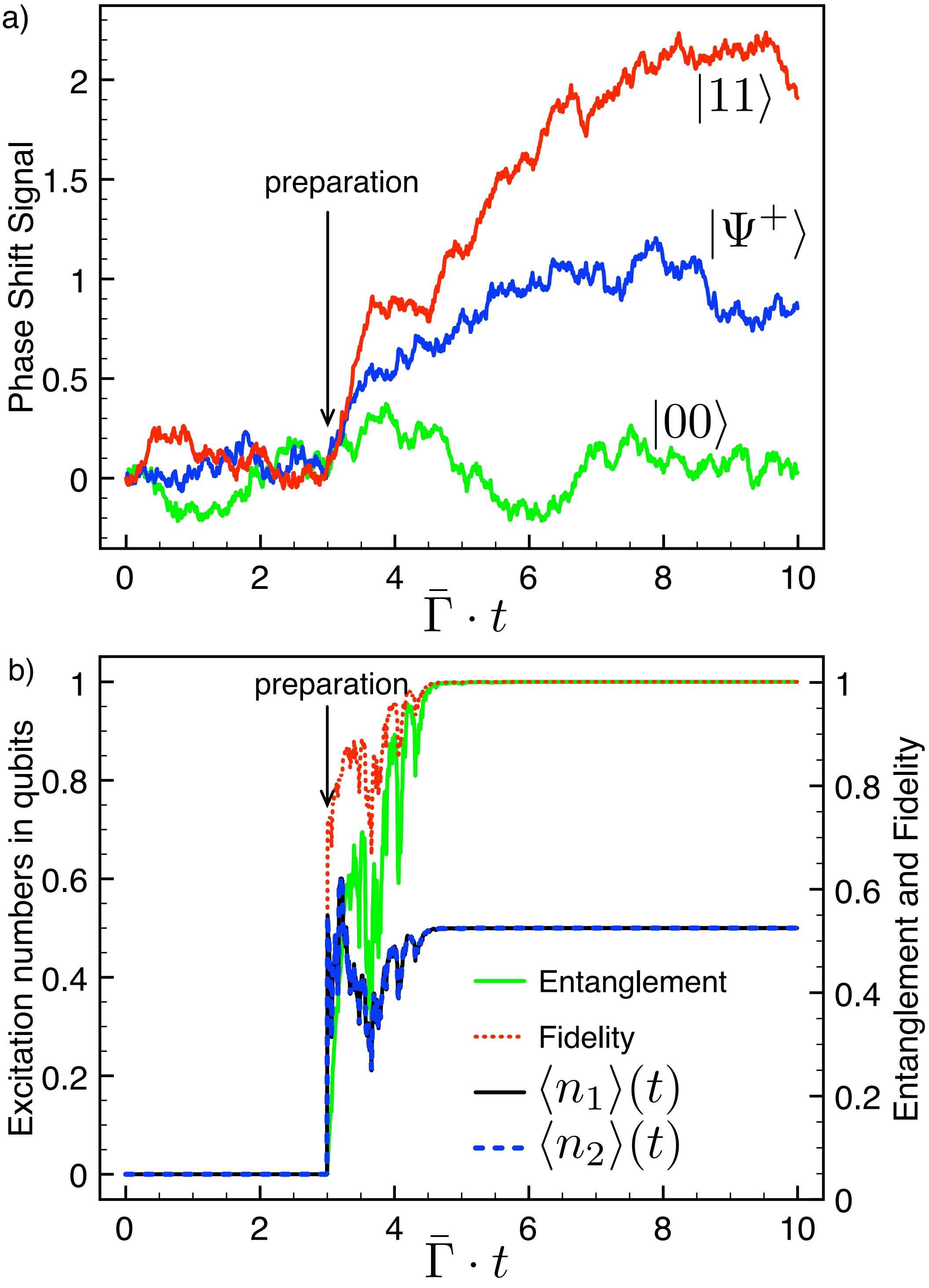

Figure 5.2: Generation of the Bell state $|\Psi^{+}\rangle = (|10\rangle + |01\rangle)/\sqrt{2}$ (the two-qubit W-state): (a) Quantum trajectories illustrating the different phase shift signal traces $X(t)$. Three traces have been selected, corresponding to the possible outcomes of the measurement given the same input state $|\Psi_0\rangle$. At time $\bar{\Gamma}t_0 = 3$, Hadamard gates are applied to both qubits, starting from the ground state. As in every real measurement of field quadratures, the signal $X(t)$ is smoothed by doing a windowed average over a suitable time-span, $\bar{\Gamma}\tau_{avg} = 1.0$. Part (b) displays the excitation numbers, state synthesis fidelity and the entanglement (log-negativity) for the one trajectory of plot (a) that ended up in the desired state.

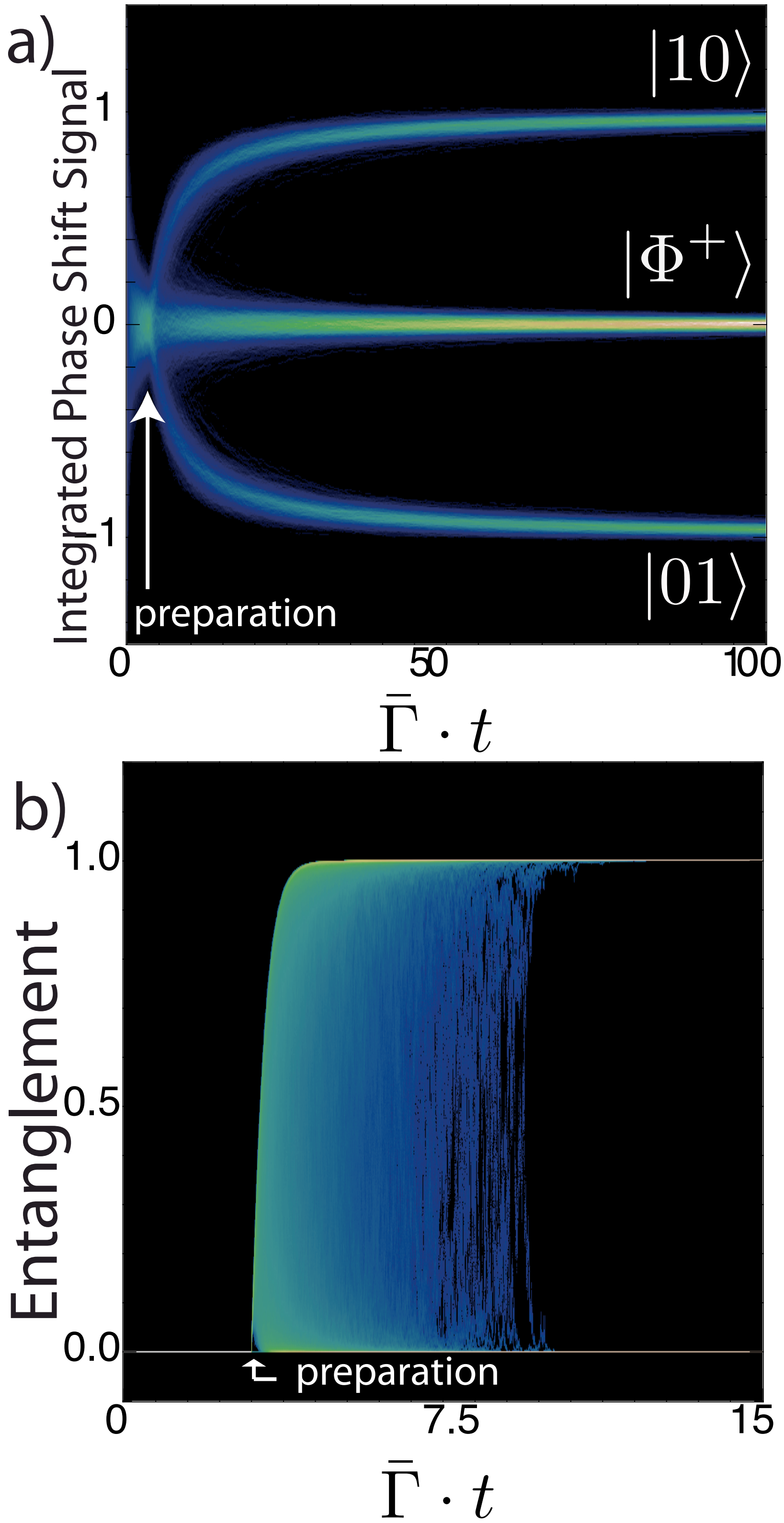

Figure 5.3: Generation of two-qubit Bell state $|\Phi^+\rangle = (|00\rangle + |11\rangle)/\sqrt{2}$: (a) Probability density of the average phase shift signal $\bar{X}(t) = t^{-1}\int_0^t X(t')dt'$ from 6000 runs of the simulation. At time t_0 Hadamard gates are applied to both qubits. Part (b) displays the probability density of the entanglement measure E_N, the log-negativity. Note that neither of these plots can be obtained from the standard, non-stochastic master equation (see main text), i.e. quantum jump trajectory simulations are essential.

5.5.3 Three qubits - no decoherence

5.5.3.1 Generation of W-states

Similarly, for three qubits, the generation of W-states is straightforward as well. We imagine starting the experiment with all qubits in the ground state $|0\rangle$, applying a Hadamard gate ($\pi/2$ - σ_x rotation) at some time t_0, leaving the system in the state

$$\begin{aligned}|\Psi_0\rangle &\equiv \prod_{\otimes}\frac{1}{\sqrt{2}}\left(|0\rangle+|1\rangle\right)\\ &= \frac{1}{\sqrt{8}}\left[|000\rangle+|001\rangle+|010\rangle+|011\rangle\right.\\ &+ \left.|100\rangle+|101\rangle+|110\rangle+|111\rangle\right].\end{aligned}$$

We aim to generate a W-state which for three qubits is given by

$$|W\rangle \equiv \frac{1}{\sqrt{3}}\left(|001\rangle+|010\rangle+|100\rangle\right).$$

We find the corresponding amplitude vector $\sqrt{3}\overrightarrow{\alpha}=(0,1,1,0,1,0,0,0)^T$, and the resulting equations for the couplings, $g_1=g_2=g_3$, solved by equal couplings to all qubits, $\overrightarrow{G}=\begin{pmatrix}1,1,1\end{pmatrix}^T$. The W state will be generated with a success rate η given by

$$\eta \equiv |\langle W|\,\Psi_0\rangle|^2=\frac{3}{8}.$$

Note that with the same success rate the dual W state is generated (see Fig. (5.4)) which is given by

$$\left|\bar{W}\right\rangle \equiv \frac{1}{\sqrt{3}}\left(|011\rangle+|110\rangle+|101\rangle\right).$$

5.5.3.2 Generation of GHZ-states

Extending the two-qubit scheme to three qubits, we find for the amplitude vector $\sqrt{3}\overrightarrow{\alpha}=(1,0,0,0,0,0,0,1)^T$, and for the characteristic equation for the couplings in case of a desired GHZ state as the target state $|GHZ\rangle\equiv\frac{1}{\sqrt{2}}\left(|000\rangle+|111\rangle\right)$: $0=g_1+g_2+g_3$, which is fulfilled, for example, by the choice of coupling vector $\overrightarrow{G}=(1,-1/2,-1/2)^T$. The success rate is $\eta=\frac{1}{4}$. Again we plot phase shift signal, excitation numbers, log-negativity and fidelity to illustrate the correctness of our considerations (see Fig. (5.5)). Note that due to the unequal couplings, the qubit excitations and pairwise entanglement do depend on the qubit index, in contrast to all our previous examples, where the couplings had been equal in magnitude.

It is noteworthy that this three-qubit GHZ scheme yields a 75% chance of obtaining a Bell-state between qubits 2 and 3 as a by-product. So this might in fact be also considered an even more efficient scheme to generate two-qubit Bell-states than just with two qubits in the cavity.

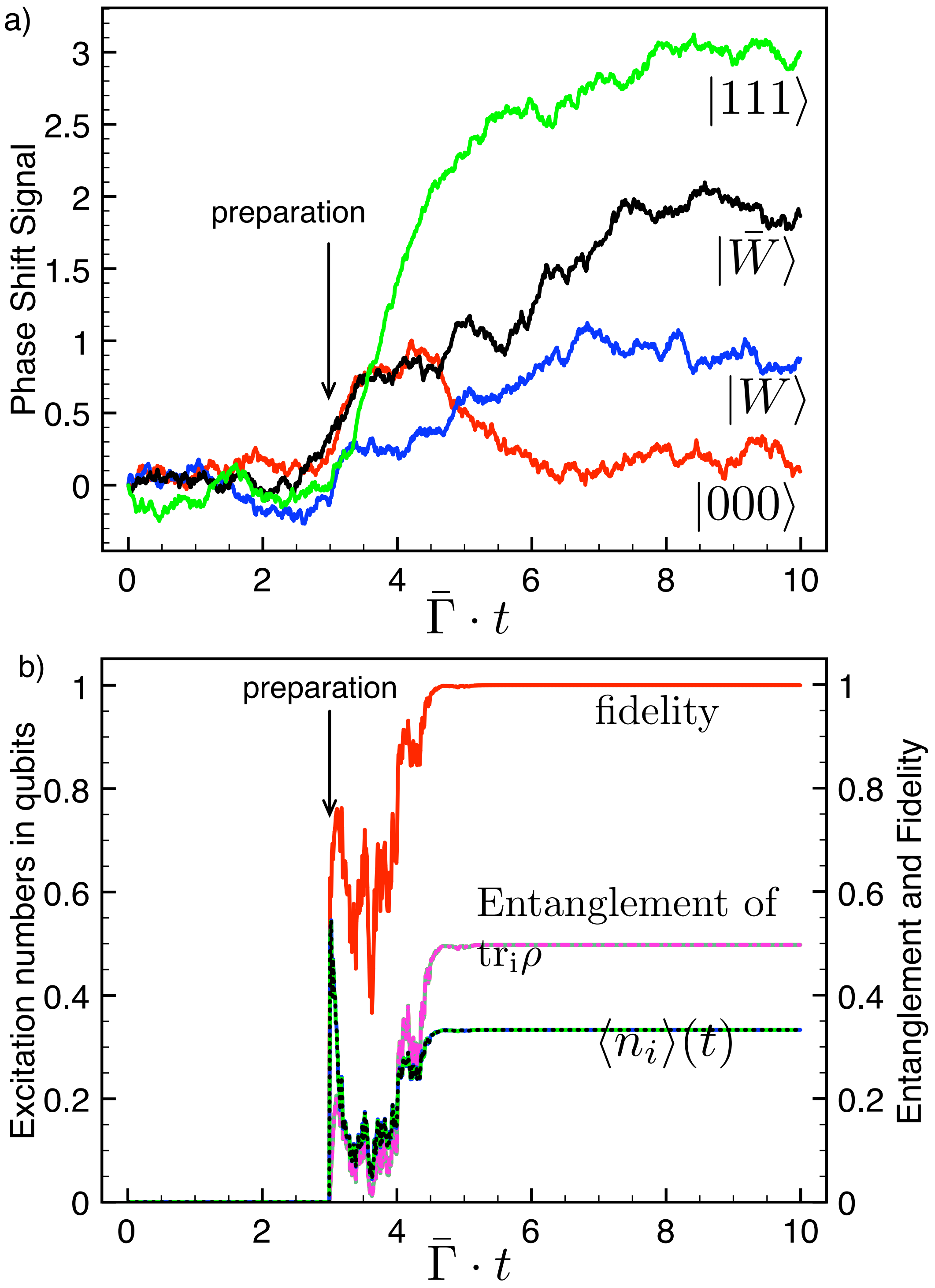

Figure 5.4: Generation of three-qubit W-states: (a) Quantum trajectories for the different states that can arise from the given input state $|\Psi_0\rangle$. At time $\bar{\Gamma} t_0 = 3$, Hadamard gates are applied to all qubits. Windowed averaging is performed as in Fig. (5.2). Part (b) displays the excitation numbers, state synthesis fidelity and the log-negativity for the one trajectory of plot (a) that ended up in the desired W-state. Here $tr_i \rho$ denotes the partial trace over qubit number i, and the resulting pairwise entanglement happens to be the same for all choices of qubit pairs in this example. Note that in the target state all pairs of qubits are mutually entangled which is characteristic for the W-state and the reason for the robustness of its entanglement compared to the GHZ state.

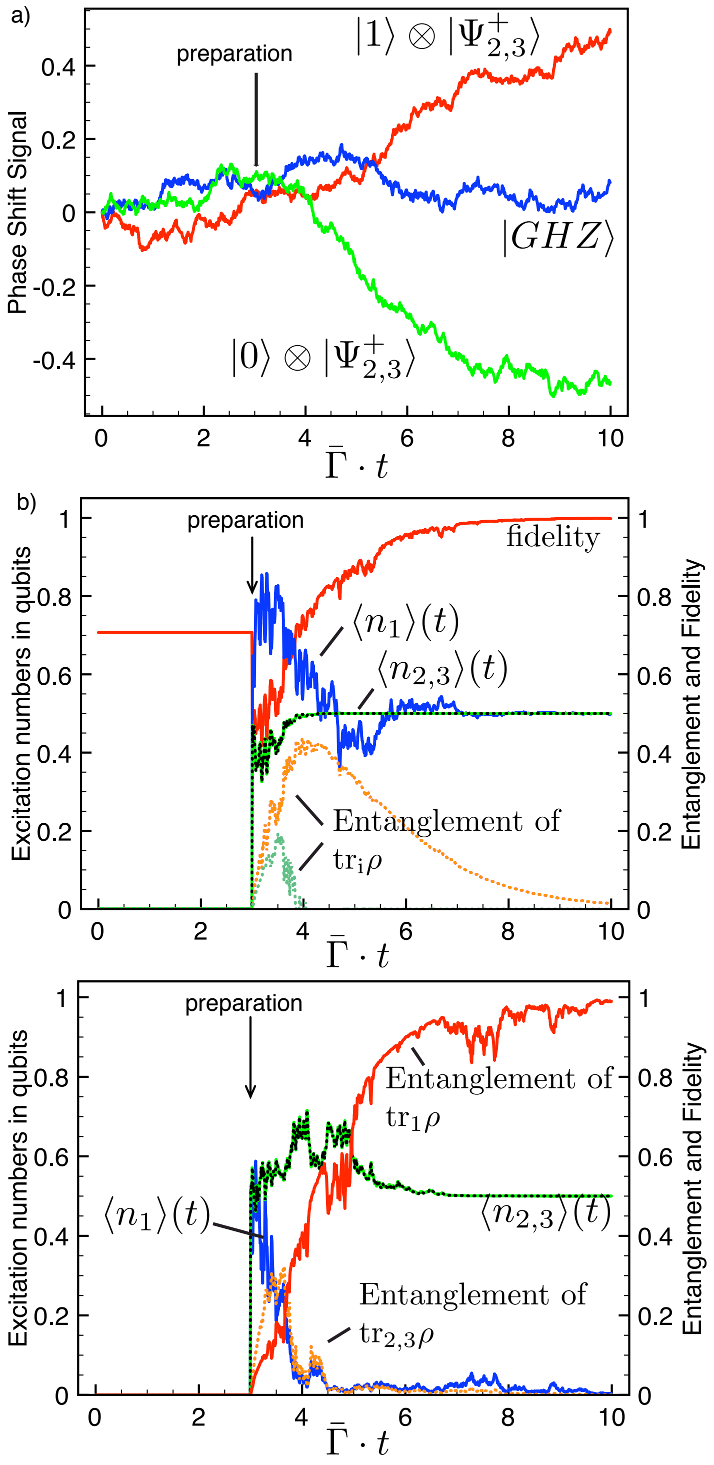

Figure 5.5: Generation of three-qubit GHZ states: (a) Quantum trajectories corresponding to the different states that can arise from the given input state. At time t_0, Hadamard gates are applied to both qubits. Note that among the unwanted outcomes there are two-qubit $|\Psi^+\rangle$ Bell-states. These are actually generated with a success rate of $\eta = 3/4$, which is higher than in the original two-qubit scheme. Part (b) displays the excitation numbers, state synthesis fidelity and the log-negativity for all pairs of qubits for the trace of part (a) that ended up in the desired GHZ-state. Note that once the GHZ-state is reached, *all* pairwise entanglement is lost. This is a typical feature of GHZ states, which contain only genuine three-particle entanglement. Part (c) shows the evolution for the particular trajectory that reaches the Bell-state between qubits 2 and 3, which can be generated very efficiently as a by-product using this 3-qubit GHZ scheme.

5.6 Effects of decoherence

We include decoherence into our model by considering the stochastic master equation Eq. (8.14) with the Lindblad decay and dephasing rates now different from zero. Assuming equal rates for all the qubits, evidently entanglement will be on average destroyed on a timescale set by $T_2 = (\gamma_1/2 + \gamma_\phi)^{-1}$. When considering experimentally reachable parameters, which we will do further below, we will find that indeed the time needed to synthesize states is orders of magnitude shorter compared to T_2. It is thus clear that the simulation of the examples will look like above with a weak decay of coherence superimposed on the trajectories.

In contrast to the decay due to decoherence, the decay due to relaxation (at a rate γ_1) is stochastic, in the sense that it leads to sudden quantum jumps. This can be understood by considering that the phase shift measurement stabilizes a certain subspace. Doing so, certain configurations of diagonal elements in the density matrix constitute attractors that compete with the exponential decay due to γ_1. More formally speaking, the master equation is unravelled with respect to the γ_1-process, but still an ensemble average description of the pure dephasing physics. The result is that the decay is stochastic when looking at single trajectories and the usual exponential γ_1-decay is recovered when averaging over many trajectories. Conversely, in a single trajectory the off-diagonal elements decay on a timescale set by T_2, showing the following behavior: As long as the relaxation jump process has not happened, one observes a decay *solely* due to pure dephasing (see Fig. (5.6)). Once the relaxation process has happened, coherence and thus entanglement are also lost completely.

5.6.1 Examples - two-qubit Bell-states including dissipation

To demonstrate the influence of decoherence and relaxation, we repeat the example for a two-qubit Bell-state, $|\Psi^+\rangle \equiv \frac{1}{\sqrt{2}}(|01\rangle + |10\rangle)$, assuming comparatively low values of $\bar{\Gamma}/\gamma_1 = 10$ and $\bar{\Gamma}/\gamma_\phi = 20$ to illustrate the effects and make all the dynamics visible. Experimental ratios would be at least about a factor 100 higher and thus the fidelity and lifetime are higher in experiment than they appear from the following simulations.

We have plotted the time-evolution for the choice of couplings that leads to the creation of a two qubit Bell-state $|\Psi^+\rangle \equiv \frac{1}{\sqrt{2}}(|10\rangle + |01\rangle)$. The results are shown in Fig. (5.6), which should be compared against Fig. (5.2). Likewise, we have considered the probability density for the time-averaged phase shift signal and the entanglement measure, for the Bell state $|\Phi^+\rangle$, see Fig. 5.7. There, the strict upper envelope for the entanglement is particularly noteworthy, corresponding to the decay of coherence within the subspace selected by the measurement.

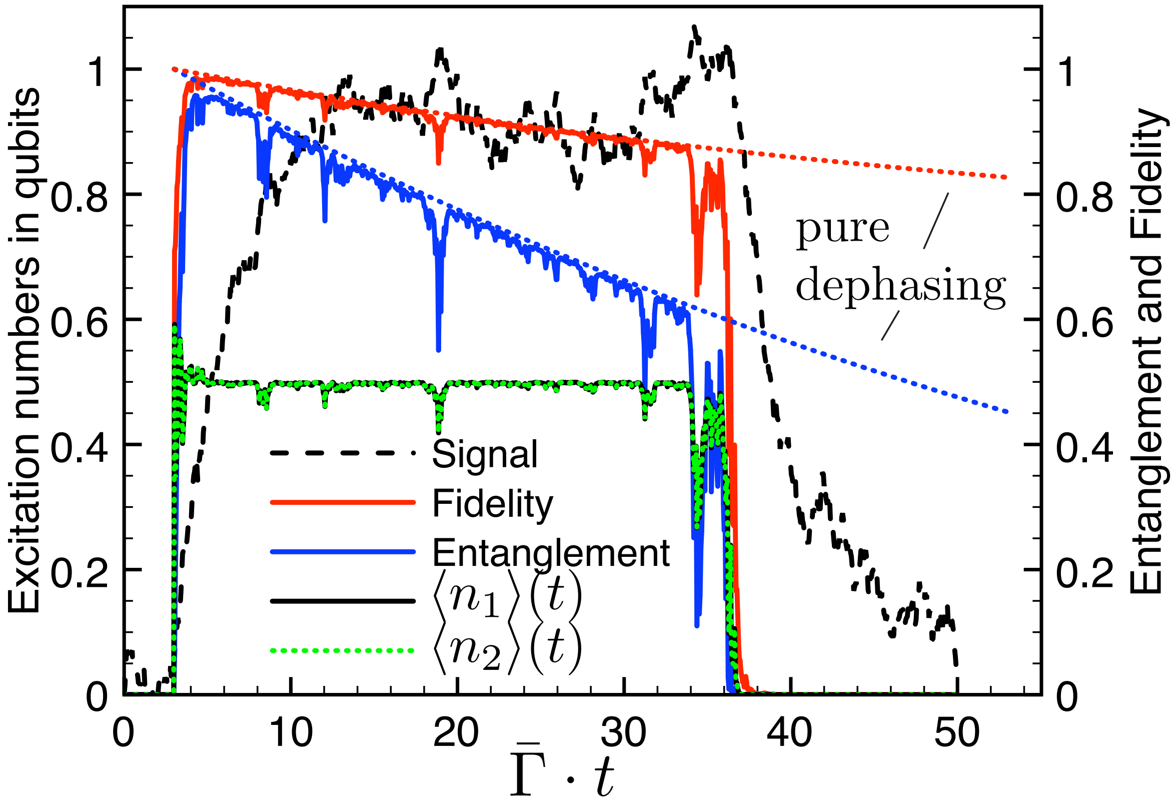

Figure 5.6: Effects of adding decoherence to the dynamics. The situation is identical to the simulation of Fig. (5.2), with the target state $|\Psi^+\rangle$, except for the added relaxation rate $\gamma_1 = 0.01 \cdot \bar{\Gamma}$ and pure dephasing rate $\gamma_\phi = 0.02 \cdot \Gamma$. We can observe that the subspace of choice is stabilized before the eventual decay due to relaxation. However, even before the sudden jump due to relaxation, one observes a slow decay of the fidelity and entanglement between the qubits, due to the pure dephasing rate γ_ϕ (dashed lines).

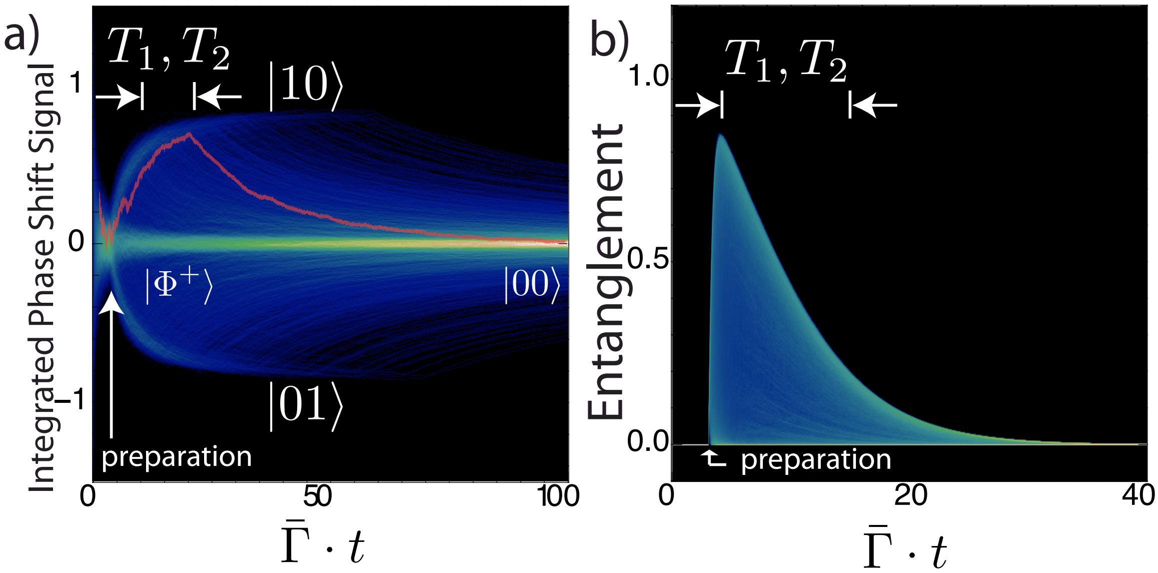

Figure 5.7: Effects of adding decoherence and relaxation to the creation of the Bell state $|\Phi^+\rangle \equiv \frac{1}{\sqrt{2}}(|00\rangle + |11\rangle)$. The situation is identical to the simulation of Fig. (5.3), except for the added relaxation rate $\gamma_1 = 0.1 \cdot \bar{\Gamma}$ and pure dephasing rate $\gamma_\phi = 0.05 \cdot \Gamma$. Part (a) shows the probability density of the time-averaged phase shift signal $\bar{X}(t)$ with an example trajectory shown in red. Note the build-up of finite probability at finite signal values, before relaxation back to zero phase shift, which represents the vacuum state $|00\rangle$ at long times. Part (b) shows the probability density of the entanglement (log-negativity). We can observe that the entanglement is lost on a timescale given by $T_2 = (\gamma_1/2 + \gamma_2)^{-1}$. Note in particular the sharply defined, exponentially decaying envelope that defines a *strict* upper bound for the entanglement at any given time. This is due to the pure dephasing.

5.7 Effect of imperfections due to parameter spread

In order to prepare states in this way experimentally, one faces the problem that it might not always be possible to fix important parameters perfectly. If the scheme one has in mind in turn relies on exact matching of parameters too much, one quickly ends up with a proposal that may be interesting but not very realistic. We therefore examine the effects on the fidelity and entanglement properties of this state synthesis scheme in the presence of small deviations in the couplings of the qubits to the cavity

$$\overrightarrow{G} = \overrightarrow{G_0} + \left(\frac{\delta g_i}{\bar{g}}\right), \tag{5.16}$$

where $\overrightarrow{G_0}$ is the ideal coupling vector from solving the characteristic equations Eq. (5.10) for the target state. $\delta g_i/\bar{g}$ are the deviations from that ideal coupling for each qubit. Without loss of generality we first look at the case where all couplings are equal to their ideal value, except one which differs by $\delta g/\bar{g}$. We focus on the stochastic term in the master equation Eq. (8.14) which is responsible for the projection onto a set of states, one of which is our target state.

Let us rewrite this term a bit by inserting the definitions of $\bar{\Gamma}$ and $\hat{N}$:

$$\begin{aligned}\dot{\hat{\rho}}_{\mathrm{st}} &= -\sqrt{4\bar{\Gamma}}\left(\hat{N}\hat{\rho}+\hat{\rho}\hat{N}-2\hat{\rho}\left\langle\hat{N}\right\rangle(t)\right)\xi(t)\\ &= -\sqrt{4\frac{\bar{g}^2|\alpha|^2}{\kappa_{cavity}}}\sum_{i=1}^{N}\frac{g_i}{\bar{g}}\left(\hat{n}_i\hat{\rho}+\hat{\rho}\hat{n}_i-2\hat{\rho}\left\langle\hat{n}_i\right\rangle(t)\right)\xi(t). \qquad (5.17)\end{aligned}$$

From this form of Eq. (5.17), it is evident that due to the linearity in the couplings g_i, we can pull out all deviating couplings into separate terms which have the same form. This reads

$$\begin{aligned}\dot{\hat{\rho}} &= -\sqrt{4\bar{\Gamma}}\sum_{i=1}^{N}\frac{g_i^{(0)}}{\bar{g}}\left(\hat{n}_i\hat{\rho}+\hat{\rho}\hat{n}_i-2\hat{\rho}\left\langle\hat{n}_i\right\rangle(t)\right)\xi(t)\\ &- \sqrt{4\bar{\Gamma}}\sum_{i=1}^{N}\frac{\delta g_i}{\bar{g}}\left(\hat{n}_i\hat{\rho}+\hat{\rho}\hat{n}_i-2\hat{\rho}\left\langle\hat{n}_i\right\rangle(t)\right)\xi(t)\\ &= -\sqrt{4\bar{\Gamma}}\left(\hat{N}\hat{\rho}+\hat{\rho}\hat{N}-2\hat{\rho}\left\langle\hat{N}\right\rangle(t)\right)\xi(t)\\ &- \sum_{i=1}^{N}\sqrt{4\delta\Gamma_i}\left(\hat{n}_i\hat{\rho}+\hat{\rho}\hat{n}_i-2\hat{\rho}\left\langle\hat{n}_i\right\rangle(t)\right)\xi(t),\end{aligned}$$

which means that in addition to the ideal behaviour captured by the first term, each individual qubit with deviating coupling will be projected on its ground or excited state on a timescale given by the inverse of the individual measurement rate $\delta\Gamma_i \equiv \frac{|\varepsilon|^2\delta g_i^2}{\kappa_{\mathrm{cavity}}}$ (we have assumed positive δg_i for simplicity; otherwise the signs in the last line would change for those qubits with $\delta g_i < 0$). This has two consequences: The first consequence concerns the measured phase shift: Instead of being equal for all the base kets that form our target state, there will be deviations in the phase shift from base ket to base ket. This means that we will be able to observe the breakdown of the target state. Therefore, second, the lifetime of the desired entangled state will now also be limited by the inverse of the maximum of the individual measurement rates, in addition to the effects of decoherence.

In other words: As soon as we have gained enough signal to noise ratio to discriminate the different base kets from each other (i.e. resolve the different corresponding phase shifts), our target state will be destroyed.

To illustrate this effect in a fairly drastic way, we choose an example of three qubits with a W-state as a target state and the coupling vector $\overrightarrow{G} = (1,1,1)^T + (\sqrt{2}/10, 0, -\sqrt{2}/10)^T$. This yields an individual measurement rate for the second qubit of $\delta\Gamma_2/\bar{\Gamma} = 1\ /50$. Therefore, we expect the target state and especially its entanglement properties to be destroyed on a timescale of 50 times the preparation time $\bar{\Gamma}^{-1}$. As we will argue in the following section, present experiments allow a ratio $\bar{\Gamma}/\gamma_{decoh} = O(10^4)$, which justifies to ignore decoherence for the moment. The resulting simulation beautifully confirms the expectations, see Fig. 5.8.

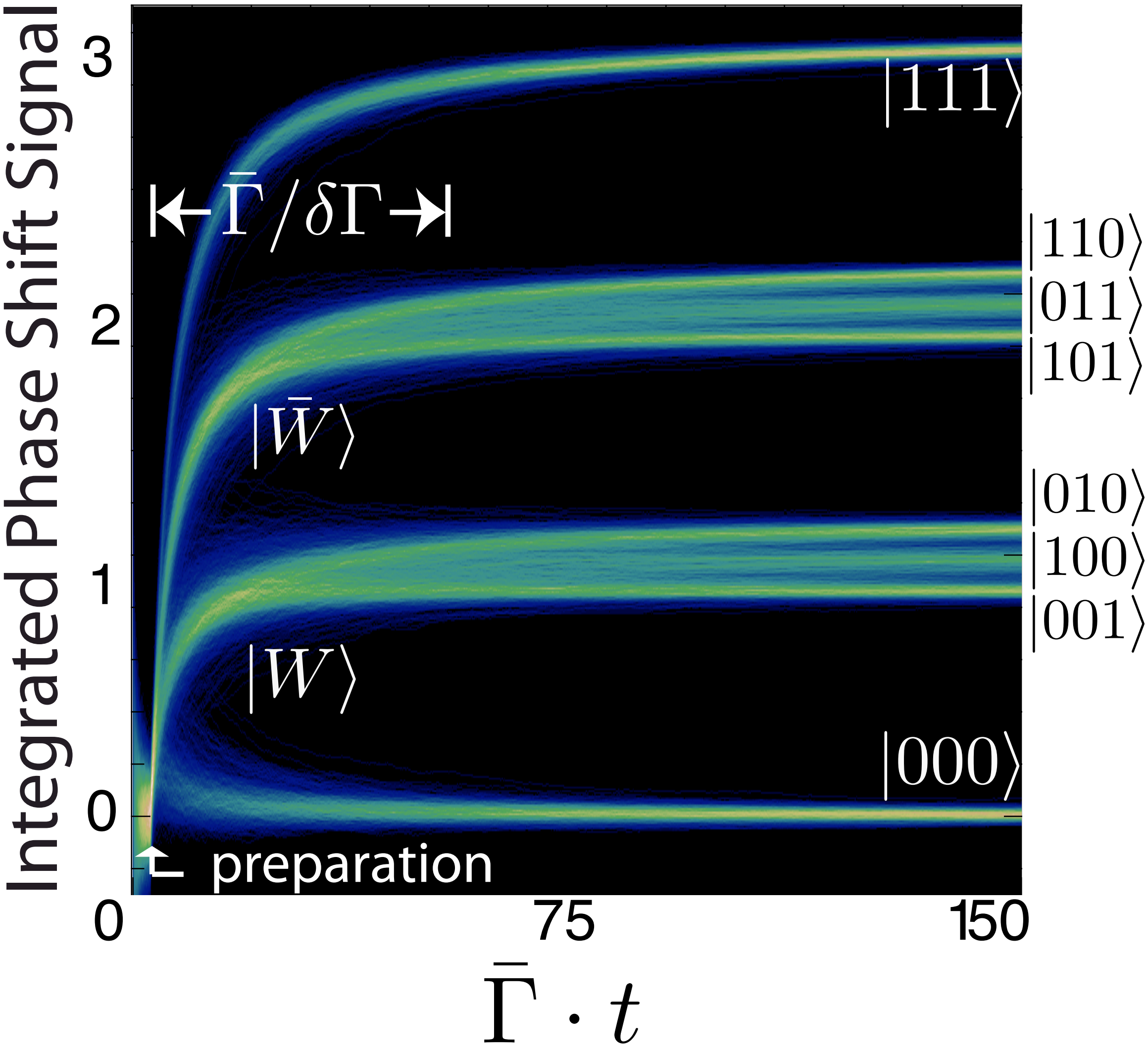

Figure 5.8: Probability density of the time-averaged phase shift signal $\bar{X}$ as an illustration of the effect of parameter spread in the couplings. Apart from the deviation in couplings from the ideal values, the setup is identical to the example in which we aimed for a three-qubit W-state, as seen in Fig. 5.4. Hadamard gates are applied to all qubits at time $t_0 = 3\cdot\bar{\Gamma}^{-1}$. During the following time interval of length $\bar{\Gamma}^{-1}$ all trajectories are projected onto the W-state, $|\bar{W}\rangle$,$|000\rangle$, or $|111\rangle$. Meanwhile the competing projection on the individual number states of the qubits becomes more pronounced and dominates the dynamics on a time scale $\delta\Gamma_2^{-1} = 50\bar{\Gamma}^{-1}$. This is exactly the timescale on which we can be sure to identify all the product base states by their phase shift values individually.

We conclude that in order to observe the full dynamics of the system one should strive for a regime where the condition

$$\bar{\Gamma} \gg \delta\Gamma_i > \gamma_1, \gamma_\phi \forall i \in 1, ..., N \tag{5.18}$$

is met. In the next section we will show that this is indeed possible with present day experimental parameters.

As a side remark we state that the situation of one coupling deviating from the others is in principle already found when synthesizing GHZ states for an odd number of qubits (e.g.

3) as examined in the previous sections (see Fig. (5.5, a))). We had chosen a coupling vector $\overrightarrow{G} = (1, -1/2, -1/2)^T$. Here the larger magnitude of the coupling for the first qubit is responsible for the generation of two-qubit W-states. As a consequence, we can learn about the state of the first qubit while we can still not distinguish qubits 2 and 3 from each other. Following our previous reasoning in this section, we find that the state of qubit 2 should be discerned on a timescale set by $\left(\delta\Gamma_2/\bar{\Gamma}\right)^{-1} = 4$ (in units of $\bar{\Gamma}^{-1}$), which matches the simulation results shown in the previous section (see Fig. (5.5, a))).

5.8 Possibilities for experimental realization

Cavity QED setups in superconducting circuits [68, 79, 123, 184] have been used to implement ideas of quantum optics on the chip, and are considered a promising candidate for scalable, fault tolerant quantum computing (e.g. [124]). Proposals for generating and detecting non-classical photon states exist or have been implemented [121, 123, 173, 185, 186].

These experiments realize a Jaynes-Cummings coupling between qubit and resonator of up to $2\pi \cdot 100\,\mathrm{MHz}$, resonators with frequencies of about $2\pi \cdot 5\mathrm{GHz}$, and a large range of resonator decay rates κ between $10\,\mathrm{kHz}$ and $100\,\mathrm{MHz}$. Given this parameter space and assuming a bare qubit coupling of $g_0 \approx 2\pi \cdot 100\,MHz$, detunings in the GHz range, $|\epsilon|^2 \approx 10$ photons in the readout cavity, and a qubit decay rate $\gamma_1 \approx 0.6\,MHz$, it is easily possible to reach values of $\bar{\Gamma}/\kappa \approx 10^4$. This gives ample time for the state synthesis before decoherence starts playing a role.

Furthermore, couplings can be adjusted with enough accuracy such that the state generation is also not limited by this factor. We can examine the sensitivity of the ratio $\delta\Gamma/\bar{\Gamma}$ to small deviations in the parameters. From $\delta\Gamma \propto \delta g^2$ and $\delta g = \delta(g_0^2/\Delta)$, we find $\delta\Gamma/\bar{\Gamma} = [2\delta g_0/g_0 - \delta\Delta/\Delta]^2$. Assuming an uncertainty about the bare value of the coupling of the qubits to the cavity and an uncertainty about the qubit detuning of about 5% each, we find that $\delta\Gamma \sim 0.05^2\bar{\Gamma}$. Note that this value is obtained without even considering the possibility of actively compensating for the spread in the couplings by suitably adjusting the detuning. This hints that under presently available optimal experimental conditions, the infidelity due to parameter spread becomes visible only long after the system has been severely decohered anyway. However, one can always intentionally choose parameters such that Eq. (5.18) is fulfilled and the full dynamics discussed here can be experimentally observed, including the ultimate measurement-induced decay of the temporarily produced entangled state.

The main challenging step to be taken experimentally before realizing this scheme in the lab is to operate in the single-shot qubit readout limit. This has been demontrated very recently by the Saclay group using a Josephson bifurcation amplifier setup [187].

5.9 Conclusions

We have analyzed a very general, experimentally directly relevant way to generate entangled multi-qubit states using a dispersive phase shift measurement of the collective state of several qubits inside a cavity. We have given criteria for the possibility to synthesize a given target state and studied the most relevant examples of Bell-states as well as W- and GHZ-states for two and three qubits. We have also discussed, and analyzed by extensive numerical simulations, the two major sources of imperfections in this setup, namely decoherence and parameter spread. Finally, we have compared with presently reachable experimental parameters and conclude that this scheme could soon be tested in the laboratory.

This chapter also represents the first non-trivial application of stochastic master equations and the quantum trajectory method in this thesis. In the following chapter, we will present a slightly more involved measurement scheme which we analyze using the same method. In addition to the model components of this section, a non-linear filter will be used to quantitatively analyze the measured signal. The goal of the next chapter is to present a workable single itinerant microwave photon detection scheme based on the available experimental tools in circuit QED.

Chapter 6

Detection of single itinerant photons and the Quantum Zeno effect

Circuit QED provides a rich toolbox to perform experiments known from quantum optics on-chip as argued in the introduction. Special attention has been drawn to the possibility to generate single microwave photons on-demand. However, up to now there is no detector which could detect those generated single photons on a single-shot basis. Thus, strictly speaking the claim to have generated a single photon can not be proven on an ensemble average basis. Be this as it may, single photons have great application e.g. when it comes to quantum cryptography where entangled single photon pairs are used to communicate making eavesdropping impossible. In order to perform such experiments, a single photon detection scheme is highly desirable. In this work, we extend and transfer ideas which have been around in optics for a long time, namely to use a dispersive cross-Kerr coupling (in optics via some non-linear medium) to detect the photon number in one beam (the signal) by the phase shift imparted on a reference beam.

In order to provide this missing tool in circuit QED, we analyze the detection of itinerant photons using a quantum non-demolition (QND) measurement. Here, the dispersive detection can be realized via the nonlinear interaction between photons inside a superconducting transmission line resonator.

Using quantum trajectory simulations, we show that the back-action due to the continuous measurement imposes a limit on the detector efficiency in such a scheme. We find that the restrictions on the fidelity of detection are a consequence of the Quantum Zeno effect caused by photon reflection, and we discuss both analytical results and quantum trajectory simulations of the measurement process.

One particularly important and feasible implementation would be in superconducting circuit QED, where this scheme would enable the on-chip detection of single microwave photons. We have shown how the Quantum Zeno effect enters the detection efficiency, a result that will be relevant to many other situations, such as the detection of electrons tunneling through a quantum dot by current passing through a nearby quantum point contact [188], the detection of itinerant phonons entering a micromechanical cantilever or membrane (e.g. in an optomechanical setup [189]), and other similar settings in mesoscopic physics, quantum optics, and atomic physics. Another possible application migh be in photonic crystal cavity QED with self-assembled quantum dots.

This work, essentially in the form presented here, has been published in [Ferdinand Helmer, Matteo Mariantoni, Enrique Solano and Florian Marquardt, Physical Review A, 79(5), (2009), [173]].

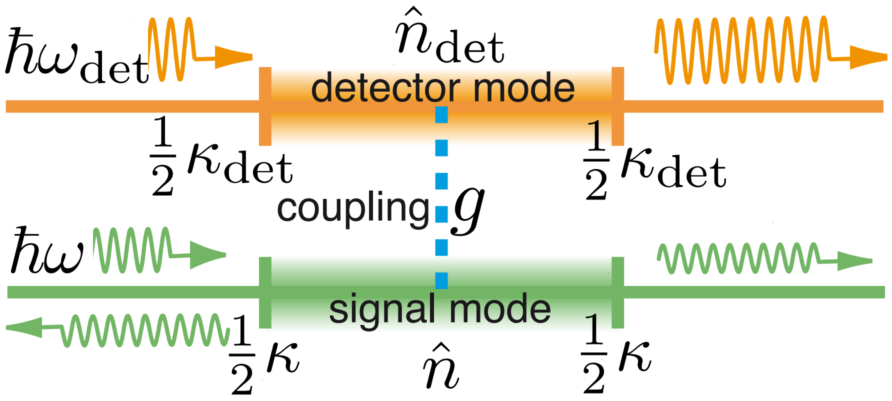

Figure 6.1: Schematic sketch of the model. Two cavity modes are coupled anharmonically. The detector mode is irradiated with a strong coherent field that suffers a phase shift whenever a photon is present in the signal mode.

6.1 Introduction

Quantum non-demolition (QND) measurements are ideal projective measurements that reproduce their outcome when repeated [106, 166]. Using them, it is possible to measure the state of a system with the minimal disruption required by quantum mechanics. Recent successful experimental demonstrations of QND detection for superconducting qubits and microwave photons [121, 144, 190, 191] are both of fundamental interest and crucial to the development of quantum communication and information processing. When QND detection is applied continuously to a system that would otherwise undergo some intrinsic dynamics, quantum jumps are observed, tracing the quantum evolution in real-time [104, 192–195]. As a consequence, the dynamics tends to be frozen, a result now known as the Quantum Zeno effect [184, 196–200].

In the present section, we show that the interplay of these phenomena may put interesting constraints on the detection of *itinerant* quanta. The specific minimal example we will discuss concerns the continuous dispersive QND detection of single photons passing through a cavity.

The crucial distinction to be recognized is the following: For localized quanta (e.g. a photon already created inside a cavity [104, 183]), the Quantum Zeno effect could presumably only enhance the detection by suppressing the decay. However, this no longer holds for the detection of itinerant quanta, if we require that our detector is always working and can detect the quantum without knowing the arrival time in advance. As we will show, in this case the unavoidable back-action of the measurement device produces a Quantum Zeno effect, suppressing the fidelity of measurements.

Such dispersive photon detection schemes could have a particularly important application in the field of quantum electrodynamics (QED) in superconducting circuits. Circuit QED setups [68, 79, 123, 184] offer the possibility to implement ideas of quantum optics using microwave photons propagating in transmission lines, and they could also form the basis of novel architectures capable of scalable, fault tolerant quantum computing [124]. Proposals for generating nonclassical photon states exist or have been implemented [121, 123, 185, 186]. However, the on-chip single-shot detection of itinerant photons is still missing.

Recent experiments have demonstrated dispersive qubit detection [144] and measurements of photon statistics [121]. Based on the dispersive coupling strengths demonstrated there, one could employ a superconducting qubit inside a microwave transmission line resonator to induce a nonlinear coupling between two modes of the resonator (or alternatively couple two cavities), thus creating a dispersive photon detector of the type discussed here. Even though we find a limit for the photon detection fidelity of about 30% for the simplest scheme considered here, this would still be a considerable improvement on the present state of the art.

In the following we present a simple model and analyze it analytically and numerically.

6.2 Model

We investigate a QND scheme utilizing the non-linear, Kerr-type coupling [201–203] of two discrete localized modes of a bosonic field. The presence of a quantum inside the signal mode gives rise to a frequency shift of the detection mode, which can be observed dispersively via the phase shift of a beam transmitted through that mode (see Fig. 6.1). In turn, the signal mode frequency fluctuates due to the detection beam's shot noise. As a consequence, the incoming signal photon will be reflected with a probability that rises with coupling strength and detection beam intensity.

This incarnation of the Quantum Zeno effect generates a trade-off that yields the highest detection efficiency at intermediate coupling strengths. In that way, such dispersive schemes for itinerant quanta turn out to be similar to weak measurements using general linear detectors and amplifiers [106].

We proceed as follows:

1. We numerically evaluate quantum jump trajectories for the phase-shift signal in a minimal model of a QND photon detector and analyze the fraction of detected photons, observing the trade-off described above.
2. We interpret these findings using an analytical approximation.
3. Finally, we briefly comment on possible experimental realizations.

We consider a system of two cavity modes with a Kerr-type coupling of strength g:

$$\begin{aligned}\hat{H} &= \hbar\omega\left(\hat{n}+\frac{1}{2}\right)+\hbar\omega_{\mathrm{det}}\left(\hat{n}_{\mathrm{det}}+\frac{1}{2}\right)+ \\ &\quad \hbar g\,\hat{n}\,\hat{n}_{\mathrm{det}}+\hat{H}_{\mathrm{drive+decay}}\,. \qquad (6.1)\end{aligned}$$

These modes might represent two different electromagnetic field modes inside an optical or microwave cavity, the modes of two adjacent cavities, or even two anharmonically coupled modes of a nanomechanical resonator. Photons in the signal mode (frequency ω, number operator $\hat{n}$) and the detector mode ($\omega_{\rm det}$, $\hat{n}_{\rm det}$) decay by leaking out of the cavity. The anharmonic Kerr-type coupling arises generically when introducing any nonlinear medium, such as an atom, a qubit or a quantum dot, into a cavity and has been studied for the purpose of QND measurements in quantum optics [201–203]. It induces a phase shift in the strong detection beam ($\langle \hat{n}_{\rm det}\rangle \gg 1$) upon presence of a signal photon.

We are interested in analyzing individual realizations of the phase shift signal as a function of time. The phase shift can be observed by continuously measuring an appropriate field quadrature of the detection beam (e.g. in a homodyne setup). As the beam passes through the cavity, the beam becomes entangled weakly with the cavity's state. Thus, the stochastic measurement outcomes reveal information about that state, feeding back into the time-evolution of the cavity's density matrix. This physics is described by a stochastic master equation [106, 183, 204–206] for the density matrix $\hat{\rho}$ conditioned on the output signal (see [183]).

In order to assess the performance of this detection scheme, we need to gain access to the individual measurement records for each run of the experiment. By construction, a usual master equation, which is an ensemble average description, is able to capture e.g. measurement dephasing but does not give access to individual measurement records and the corrspodning conditional state evolution. This is especially true if one aims at applying a non-linear filter to this record because non-linear functions and averaging cannot be interchanged. The threshold detection we are going to introuce is such a non-linear function. Thus, we have to use the concept introduced in Sec. 4.3 to unravel the master equation into a stochastic master equation which generates so-called quantum trajectories.

6.3 Stochastic master equation

In this derivation we follow [182, 183, 207, 208], adapted to the case of zero temperature and a two-sided cavity. As a starting point we write down a master equation to model the quantum dynamics of the system introduced in Fig. (6.1) and Eq. (6.1):

$$\begin{aligned}\dot{\hat{\rho}} &= -i[\frac{\kappa_1}{2}(\alpha\hat{a}_1^\dagger + \alpha^*\hat{a}_1) + g\hat{a}_1^\dagger\hat{a}_1\hat{a}_0^\dagger\hat{a}_0, \hat{\rho}] \\ &+ \kappa(\hat{a}_0\hat{\rho}\hat{a}_0^\dagger - \frac{1}{2}\hat{a}_0^\dagger\hat{a}_0\hat{\rho} - \frac{1}{2}\hat{\rho}\hat{a}_0^\dagger\hat{a}_0) \\ &+ \kappa_1(\hat{a}_1\hat{\rho}\hat{a}_1^\dagger - \frac{1}{2}\hat{a}_1^\dagger\hat{a}_1\hat{\rho} - \frac{1}{2}\hat{\rho}\hat{a}_1^\dagger\hat{a}_1) \\ &- i\sqrt{\dot{N}_{\rm in}/2\kappa}[\hat{a}_0 + \hat{a}_0^\dagger, \hat{\rho}]. \end{aligned} \tag{6.2}$$

The first Hamiltonian term describes driving of the detector mode (annihilation operator $\hat{a}_1$, decay rate κ_1) as well as the Kerr-type nonlinear coupling between the modes. The driving amplitude α results in a coherent state in the signal mode with an average photon number $|\alpha|^2$. The signal mode annihilation operator is denoted $\hat{a}_0$ and its decay rate is labelled κ. The second and third terms are the Lindblad-decay terms for both modes reflecting the finite Q-factor of the cavity. The fourth term is a weak driving of the signal mode to model the itinerant photons impinging onto the cavity. Here, $\dot{N}_{\rm in}$ describes the rate of itinerant photons impinging onto the cavity from the outside. Although the drive is coherent, after a suitable unravelling of the master equation it will become apparent that the Poissonian nature of the coherent drive will indeed model the situation we have in mind correctly - namely that once a while a photon comes along the transmission line, hits the cavity and can then be detected or not. Note that we have chosen to work in an interaction picture and in a rotating frame to eliminate the explicit time-dependece of the drives.

It is convenient to follow the steps of [182, 183, 207–209] to (i) derive the unravelled version of Eq. (8.1) and to (ii) adiabatically eliminate the detector mode from this equation assuming $\kappa_{\text{det}} \gg \kappa$. This is done in Appendix 8.1. Finally, we obtain a stochastic master equation for the signal mode alone, greatly facilitating the numerical study of the detection efficiency. Its stochastic term accounts for the back-action of the measurements performed on the field quadrature leaking out of the detector mode correctly and reads

$$\begin{aligned}\dot{\hat{\rho}}_s &= -i\sqrt{\frac{\dot{N}_{\text{in}}\kappa}{2}}\left[\hat{a}+\hat{a}^\dagger,\hat{\rho}\right]+\kappa\left(\hat{a}\hat{\rho}\hat{a}^\dagger-\frac{1}{2}\hat{n}\hat{\rho}-\frac{1}{2}\hat{\rho}\hat{n}\right)\\ &\quad -2\Gamma\left[\hat{n},\left[\hat{n},\hat{\rho}\right]\right]-\sqrt{4\Gamma}\left(\hat{n}\hat{\rho}+\hat{\rho}\hat{n}-2\hat{\rho}\left\langle\hat{n}\right\rangle(t)\right)\xi(t), \qquad (6.3)\end{aligned}$$

while the classical noisy measurement signal that corresponds to this internal dynamics is given by

$$X(t) \equiv \langle\hat{n}\rangle(t)+\frac{1}{4}\sqrt{\frac{1}{\Gamma}}\xi(t). \qquad (6.4)$$

6.4 Analysis of detection efficiency

We analyze a situation with a continuous weak coherent beam of photons entering at a rate $\dot{N}_{\text{in}}$ into the signal mode, whose intensity decay-rate is κ (first line of Eq. (8.14)). We have chosen to work in the limit of a large detector mode decay rate, $\kappa_{\text{det}} \gg \kappa$, which is favorable for the detection process and makes it possible to adiabatically eliminate that mode [183], keeping only the signal mode $\hat{n} = \hat{a}^\dagger\hat{a}$ and drastically reducing the numerical effort. After adiabatic elimination, the coupling strength g and the detection beam intensity are combined into the measurement rate [183]

$$\Gamma \equiv g^2\left\langle\hat{n}_{\text{det}}\right\rangle/(4\kappa_{\text{det}}), \qquad (6.5)$$

where $1/\Gamma$ is the time-scale needed to resolve different photon numbers. The last, stochastic term in Eq. (8.14), describes the measurement back action.

It contains a systematic term depending on the average number of signal photons, as well as a stochastic term representing the unavoidable vacuum noise, where $\langle\xi\rangle = 0$ and $\langle\xi(t)\xi(t')\rangle = \delta(t-t')$. In deriving Eqs. (8.14,6.4), we have assumed that the transmitted and reflected signals are superimposed symmetrically to extract the maximum information.

As in any measurement of field quadratures, temporal filtering is required to suppress the noise. We average over a timespan τ_{avg}, which should be as large as possible while still remaining smaller than the expected temporal extent of the phase shift signal due to a single photon, i.e. τ_{avg} not much bigger than κ^{-1}. We denote the averaged signal as $\bar{X}(t)$. We have made sure that this moving average (a necessary but technical step to cope with white noise) does not interfere with the physics involved (see Fig. (6.6)). From another point of view, this averaging is inherent in *any* experimental device and merely represents the UV-cutoff in the bandwith of the devices used. As in a real experiment one needs to make sure that the interesting phsyics does not happen too near or outside the bandwith of e.g. the amplifiers used.

6.4.1 Numerical results

In order to obtain results, we numerically solve the master equation, and use it to compute the signal $\bar{X}(t)$ and the occupation of the signal mode $\langle \hat{n} \rangle (t)$ as a function of time. We then implement the minimal model of a threshold detector: Time-points when the quantum jump trajectory $\bar{X}(t)$ first exceeds the threshold X_{thr} are counted as detection events, and the detector is then set insensitive for a dark-time τ_{dark}, suitably chosen to avoid multiple detection, i.e. $\dot{N}_{\mathrm{in}}^{-1} \gg \tau_{\mathrm{dark}} \gg \kappa^{-1}$.

Our discussion will focus on small values of $\dot{N}_{\mathrm{in}}$, making the results independent of τ_{dark}, while we will analyze the dependence on X_{thr} in some detail. In figure 6.2 we show two example trajectories. Whereas the expected number of signal photons is the same for both cases, the increase in the measurement rate Γ/κ decreases the number of photons actually detected, while at the same time enhancing the signal to noise ratio in the trajectory. This is an indication of the Quantum Zeno effect in the detection of itinerant quanta, which we now want to study in more quantitative detail.

We plot the rate of photon detection events $\dot{N}_{\mathrm{det}}$ versus the rate of incoming photons $\dot{N}_{\mathrm{in}}$ (see Fig. 6.3). The detection efficiency η is naturally defined as the ratio of detected vs. incoming photons, obtained at small input rates $\dot{N}_{\mathrm{in}}$:

$$\eta \equiv \left. \frac{d\dot{N}_{\mathrm{det}}}{d\dot{N}_{\mathrm{in}}} \right|_{\dot{\mathrm{N}}_{\mathrm{in}}=0} . \tag{6.6}$$

Fig. 6.4 displays the efficiency η as a function of Γ/κ and X_{thr}. The statistics for this figure were obtained from extensive numerical simulations by generating $O(10^4)$ trajectories of length $10^2/\kappa$ for seven different rates $\dot{N}_{\mathrm{in}}$ at each value of Γ/κ. Apparently, the detector efficiency η is strongly suppressed both for $\Gamma/\kappa \ll 1$ (low signal to noise ratio) and $\Gamma/\kappa \gg 1$.

The pronounced peak is shown enlarged in a lin-log plot in Fig. (6.5).

Now we have discussed at length the dependence of the detector efficiency in terms of all inherent physical parameters, such as the threshold and the measurement rate. However, when performing the analysis, we have used an averaged signal, such that there could be a dependence on this averaging time as well. In order to exclude this, we have examined the dependence of the efficiency η along a line of constant measurement rate Γ/κ. This line is depicted as the yellow cut in the 3D-inset of Fig. (6.4). As can be seen from Fig. (6.6), changing the averaging time just shifts the value of the threshold where we get maximum efficiency whereas the height of the maximum only changes negligibly.

6.4.2 Analytical results

Now, in order to corroborate and interpret these results, we calculate the total transmission probability through the signal mode, whose frequency fluctuates due to the shot noise in the

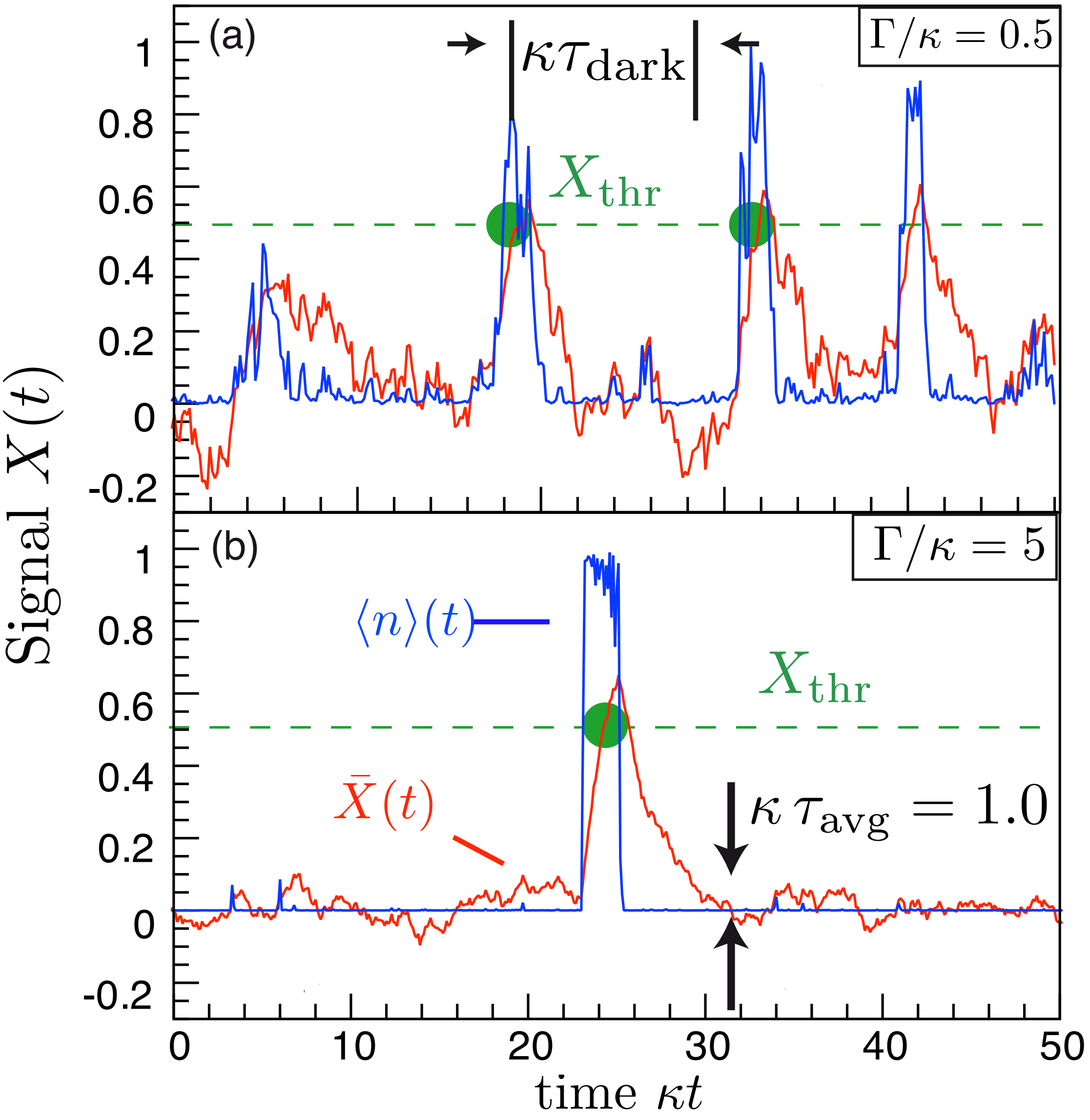

Figure 6.2: Quantum jump trajectories illustrating dispersive photon detection: The observable homodyne signal $\bar{X}(t)$ (red lines) and the corresponding signal mode occupation $\langle\hat{n}\rangle(t)$ (blue lines), for two different values of the measurement rate Γ/κ at a fixed input rate $\dot{N}_{\mathrm{in}}$. Photon detection events are indicated as filled circles. The relative noise strength $\propto (\Gamma\tau_{\mathrm{avg}})^{-1/2}$ is suppressed with increasing Γ/κ, but the number of photons actually detected also decreases, due to the Quantum Zeno effect (see main text). The size of the noise floor, the detector threshold X_{thr} (green dashed line), and the dark time are indicated. Here and in the following plots $\kappa\tau_{\mathrm{avg}} = 2$.

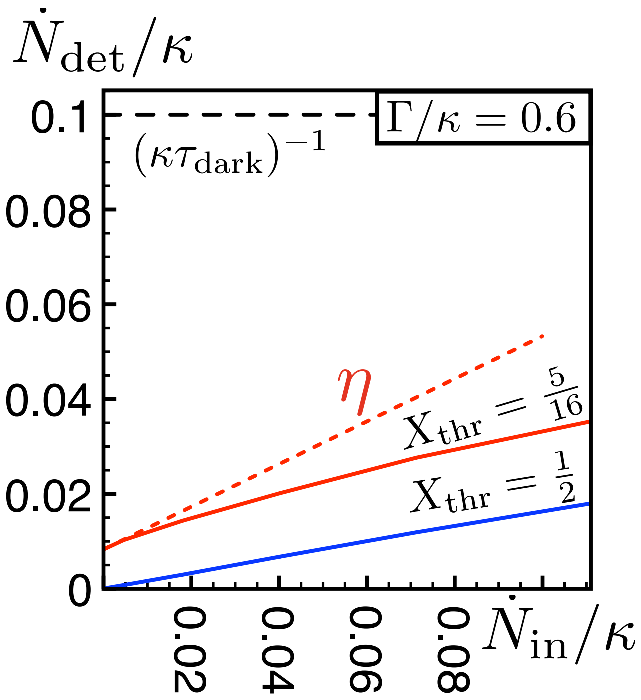

Figure 6.3: Observe the dark count rate (offset at $\dot{N}_{\rm in} = 0$), the detector efficiency η defined from the slope at $\dot{N}_{\rm in} = 0$, and the saturation for large $\dot{N}_{\rm in} \sim \tau_{\rm dark}^{-1}$.

detection mode, which is treated as classical noise. We start from the semiclassical equation of motion for the complex field amplitude $\alpha(t)$ in the signal mode,

$$\dot{\alpha}(t) = \left(-i\,\delta\omega(t) - \frac{\kappa}{2}\right)\alpha(t) + \sqrt{\frac{\kappa}{2}}\alpha_{\rm L}^{\rm in}. \tag{6.7}$$

Here $\alpha_{\rm L}^{\rm in}$ is the amplitude of the signal photon field entering the cavity from the left side, and $\delta\omega(t) \equiv g n_{\rm det}(t)$ is the fluctuating frequency shift ($n_{\rm det} \gg 1$). The correlator of the noise is given by

$$\langle\delta\omega(t)\delta\omega(0)\rangle - \langle\delta\omega\rangle^2 = g^2 \bar{n}_{\rm det} e^{-\kappa_{\rm det}|t|/2}\,. \tag{6.8}$$

To obtain an expression for the transmission probability, we write down the formal solution for $\alpha(t)$,

$$\frac{\alpha(t)}{\sqrt{\kappa_L}\alpha_{\rm L}^{\rm in}} = \int_{-\infty}^{t} dt' \exp\left[-i\int_{t'}^{t}\delta\omega(t'')dt'' - \frac{\kappa}{2}(t-t')\right]. \tag{6.9}$$

Note that the fluctuations $\delta\omega(t)$ themselves are non-Gaussian. Still, the integral in the exponent is approximately Gaussian for time-intervals that fulfill $\kappa_{\rm det}|t-t'| \gg 1$, due to the central limit theorem. These times yield the main contribution under our assumption of a "fast detector", $\kappa_{\rm det} \gg \kappa$. Thus, we can evaluate $\langle|\alpha|^2\rangle$ using the formula $\langle\exp[-iY]\rangle = \exp[-i\langle Y\rangle - \frac{1}{2}{\rm Var}Y]$ for a Gaussian random variable Y, and inserting Eq. (6.8). From this,

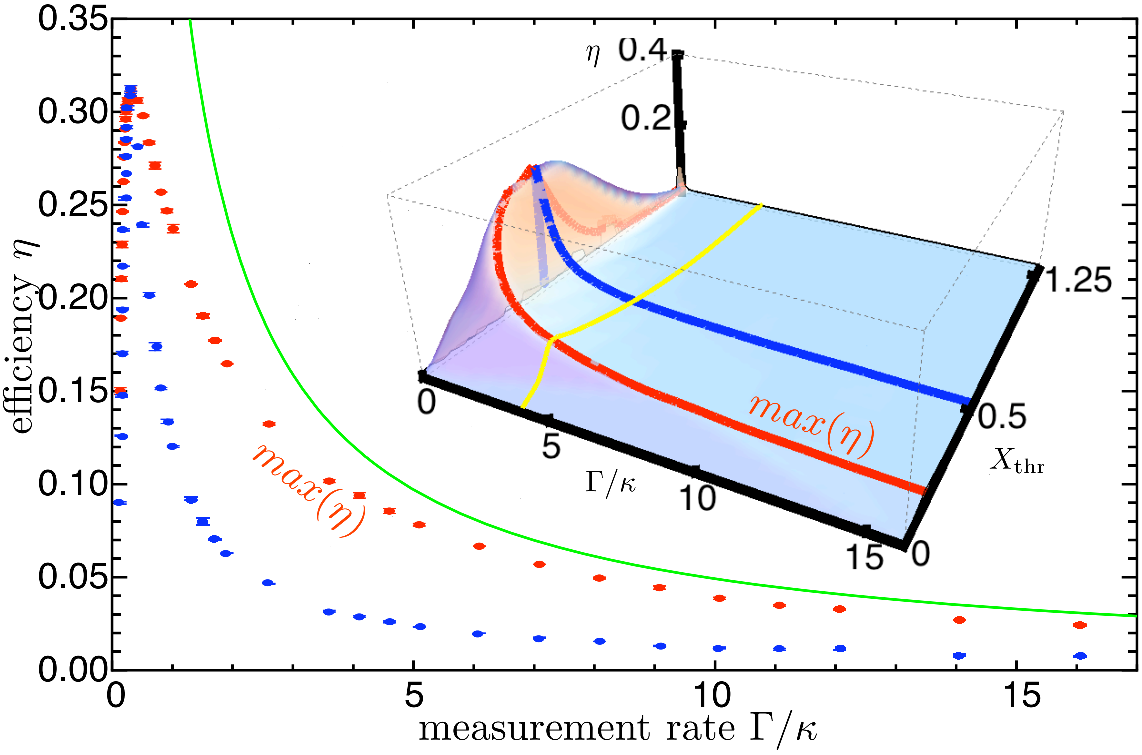

Figure 6.4: Detector efficiency η, obtained from quantum trajectory simulations, as a function of Γ and $X_{\rm thr}$ (3D-inset), and comparison with the analytical results (main plot). The blue data points display η for fixed $X_{\rm thr} = 0.5$ (blue cut in 3D-inset). When maximizing the η over $X_{\rm thr}$ for any given Γ/κ, the red data points are obtained (labeled "$\max(\eta)$"), agreeing well with the analytical asymptote (green thin line) at higher values of Γ/κ.

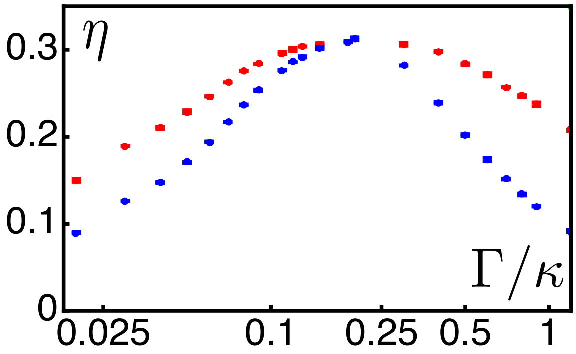

Figure 6.5: Lin-log enlargement of the region of the maximum efficiency of the numerical results (Fig. (6.4)). Shown are data and statistical errors from the averaging over many quantum trajectories and the fitting procedure.

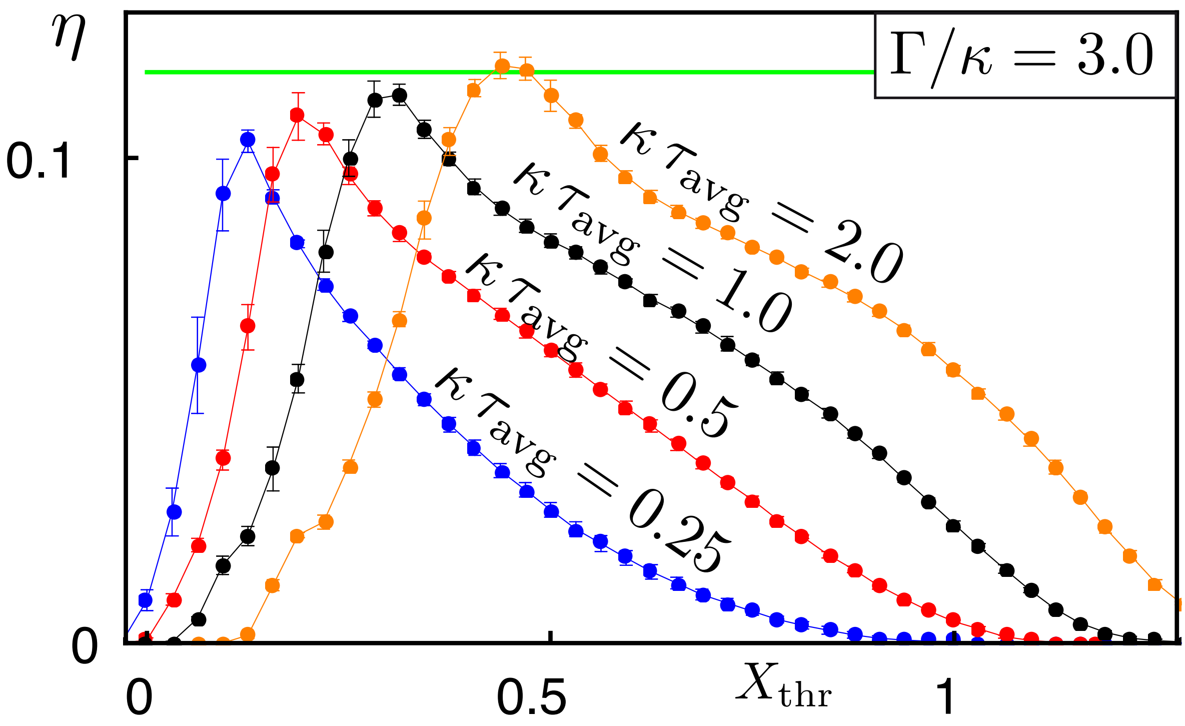

Figure 6.6: Dependence of the detector efficiency on the averaging time $\tau_{\rm avg}$. Shown are curves for different values of $\kappa\tau_{\rm avg}$ and thresholds $X_{\rm thr}$ while the measurement rate $\Gamma/\kappa = 3.0$ is kept fixed (corresponds to yellow cut in 3D-inset of Fig. (6.4)). The green line represents the analytical result from the transmission calculation (which does not depend on any thresholds or averaging).

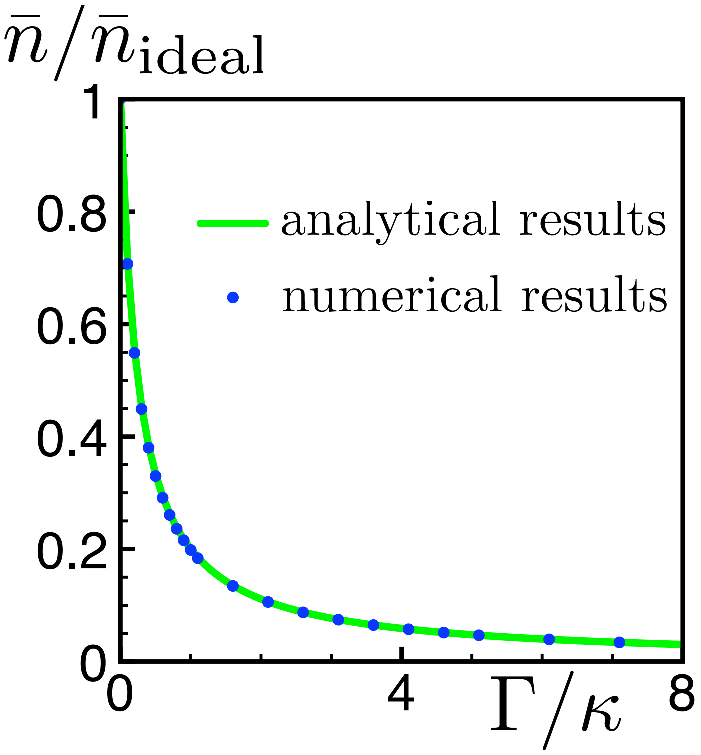

Figure 6.7: Suppression of the signal photon number $\bar{n}$ inside the cavity as a function of measurement rate Γ/κ compared to perfect transmission ($\bar{n}_{\text{ideal}}$)

we obtain the average transmitted intensity

$$\langle |a_{\mathrm{R}}^{\mathrm{out}}|^2 \rangle = \frac{\kappa}{2} \langle |\alpha|^2 \rangle = \langle \mathcal{T} \rangle \, |\alpha_{\mathrm{L}}^{\mathrm{in}}|^2, \tag{6.10}$$

and the average transmission probability (see Fig. (6.7))

$$\langle \mathcal{T} \rangle = \left(1 + 4 \frac{\Gamma}{\kappa} \right)^{-1}. \tag{6.11}$$

Before we can correlate the suppression of the transmission with the reduction of the detector efficiency η in the limit of $\Gamma/\kappa \gg 1$, one more consideration is necessary. In this limit, any photon that has entered the cavity will almost certainly be detected. Once detected, the photon loses the coherence with the incoming beam, which is needed for perfect transmission on resonance in the ideal, coherent case. As a consequence, it acquires an *equal* probability to leave the cavity through the left or the right port. This means that, on average, the number of detected photons is *twice* the number of transmitted photons. The expected relation is thus $\eta = 2\langle \mathcal{T} \rangle$, which is indeed observed nicely when comparing with the numerical data (Fig. 6.4).

The reduction of detector efficiency at $\Gamma/\kappa \gg 1$ thus has found its explanation in the Quantum Zeno effect: Many photons remain undetected, because they are reflected due to detector back-action. As low values of Γ/κ are also unfavorable, due to a bad signal-to-noise ratio, the maximum efficiency is found near the intermediate value $\Gamma/\kappa = 1/4$ (see Fig. 6.4).

6.4.3 Possible realization in superconducting circuit quantum electrodynamics setups

Having seen that the scheme is indeed workable with reasonable detection efficiencies if operated in the right regime, we want to investigate the possibilities to reach this regime in actual experiments.

Cavity QED setups in superconducting circuits [68, 79, 123, 184] have been used to implement ideas of quantum optics on the chip, and are considered a promising candidate for scalable, fault tolerant quantum computing [124]. While proposals for generating nonclassical photon states exist or have been implemented [121, 123, 185, 186], the on-chip single-shot detection of itinerant photons is still missing.

Building on recent experiments that demonstrated dispersive qubit detection [144] and measurements of photon statistics [121], one could employ the superconducting qubit to induce a nonlinear coupling between two modes of the microwave transmission line resonator (or coupling two cavities [1]), thus creating a dispersive photon detector of the type discussed here.

These experiments realize a Jaynes-Cummings coupling between qubit and resonator of up to $2\pi \cdot 100\mathrm{MHz}$, resonators with frequencies of about $2\pi \cdot 5\mathrm{GHz}$, and a large spread of resonator decay rates κ between $1\mathrm{MHz}$ and $100\mathrm{MHz}$.

To make the example more concrete we suggest to employ the qubit as a non-linear coupler between two modes of a transmission line cavity.

Imagine the qubit being tuned into resonance with the signal mode, such that their resonances hybridize, as described by the Jaynes-Cummings model. The detector mode is assumed to be far detuned from the qubit and the signal mode, i.e. we consider the case of dispersive coupling. The unperturbed Hamiltonian $\hat{H}_0$ (redefined to absorb the vacuum energy of the harmonic oscillators and using RWA) thus reads

$$\hat{H}_0 \equiv \hbar\frac{\omega_q}{2}\hat{\sigma}_z + \hbar\omega_\alpha\hat{a}_\alpha^\dagger\hat{a}_\alpha + \hbar\omega_\beta\hat{a}_\beta^\dagger\hat{a}_\beta + g_{0,\alpha}(\hat{\sigma}^+\hat{a}_\alpha + \hat{a}_\alpha^\dagger\hat{\sigma}^-).$$

This contains the resonant coupling of the qubit to the signal mode (mode index α), while the coupling to the detection mode (index β) will be considered perturbatively. Now imagine the incoming signal photon being on resonance with one of the states of the coupled system (qubit/signal mode), e.g. $|\alpha^-\rangle \equiv 1/\sqrt{2}(|0,\uparrow\rangle + |1,\downarrow\rangle) \otimes |n_\beta\rangle$. This state is an eigenstate of the qubit-signal mode system which is only weakly (dispersively) coupled to the detector mode. Provided we only consider situations with at most one signal photon inside the signal mode (α) and n_β photons in the detection (β) mode (as was the case in the preceding discussion), we can restrict ourselves to the subspace $\{|0,\downarrow\rangle \otimes |n_\beta\rangle, |\alpha^-\rangle\}$. This set of states will effectively represent the two lowest states of the signal mode in our detection scheme (photon absent/present).

The state $|\alpha^-\rangle$ has energy $\omega_{|\alpha^-\rangle} = \omega_\alpha + g_{0,\alpha} + n_\beta\omega_\beta$. Resonantly irradiating with $\omega_{|\alpha^-\rangle}$ will populate the corresponding state $|\alpha^-\rangle$ only and, being an eigenstate, will not induce any internal dynamics.

Now we consider populating the β-mode with n_β photons to dispersively detect the difference between the states $|vac, n_\beta\rangle \equiv |n_\alpha = 0, \downarrow, n_\beta\rangle$ and $|\alpha^-\rangle$ and thus the fact whether an α-mode photon has entered the cavity or not. So, we consider the coupling to the β-mode via the perturbation Hamiltonian

---

[1] A. Blais, J. Gambetta, C. Cheung, R. Schoelkopf, and S. M. Girvin, manuscript in preparation (priv. communication)

$$\hat{H}_{int} = g_{0,\beta}(\hat{\sigma}^{+}\hat{a}_{\beta} + \hat{a}_{\beta}^{\dagger}\hat{\sigma}^{-}). \tag{6.12}$$

The idea is that the second-order energy shift of the transition frequency between states $|vac, n_\beta\rangle$ and $|\alpha^-\rangle$ will contain a term $\propto n_\beta$ which can be used to read off the effective coupling g between the hybrid system of α-mode/qubit and the β-mode. The idea is that the second-order energy shift of the state $|\alpha^-\rangle$ will contain a term $\propto n_\beta$ which can be used to read off the effective coupling between the hybrid system of α-mode and qubit and the β-mode. As usual, the energy shift is given by

$$E^{(2)}_{|\alpha^-\rangle} = \sum_{|\Psi\rangle \neq |\alpha^-\rangle} \frac{\left|\langle \alpha^- | \hat{H}_{int} | \Psi\rangle\right|^2}{E_{|\alpha^-\rangle} - E_{|\Psi\rangle}}. \tag{6.13}$$

Substituting Eq. (6.12) and the definition of the state $|\alpha^-\rangle$ into Eq. (6.13), we find

$$\begin{aligned} E^{(2)}_{|\alpha^-\rangle} &= \sum_{|\Psi\rangle \neq |\alpha^-\rangle} \frac{1}{2} |g_{0,\beta}|^2 \frac{\left|\langle 0,\uparrow,n_\beta | \hat{\sigma}^{+}\hat{a}_{\beta} |\Psi\rangle - \langle 1,\downarrow,n_\beta | \hat{\sigma}^{-}\hat{a}^{\dagger}_{\beta} |\Psi\rangle\right|^2}{\omega_\alpha + g_{0,\alpha} + n_\beta \omega_\beta - E_{|\Psi\rangle}} \\ &= \sum_{|\Psi\rangle \neq |\alpha^-\rangle} \frac{1}{2} |g_{0,\beta}|^2 \frac{\left|\sqrt{n_\beta+1}\langle 0,\downarrow,n_\beta+1 | \Psi\rangle - \sqrt{n_\beta}\langle 1,\uparrow,n_\beta-1 | \Psi\rangle\right|^2}{\omega_\alpha + g_{0,\alpha} + n_\beta \omega_\beta - E_{|\Psi\rangle}}, \end{aligned}$$

where the two terms in the numerator contain disjunct Kronecker-deltas and thus the magnitude squared can be evaluated per term and the expression reads:

$$\begin{aligned} E^{(2)}_{|\alpha^-\rangle} &= \frac{1}{2} |g_{0,\beta}|^2 \left[\frac{n_\beta + 1}{\omega_\alpha + g_{0,\alpha} + n_\beta\omega_\beta - (n_\beta + 1)\omega_\beta} + \frac{n_\beta}{\omega_\alpha + g_{0,\alpha} + n_\beta\omega_\beta - (2\omega_\alpha + (n_\beta - 1)\omega_\beta)} \right] \\ &= \frac{1}{2} |g_{0,\beta}|^2 \left[\frac{n_\beta + 1}{\omega_\alpha + g_{0,\alpha} - \omega_\beta} - \frac{n_\beta}{\omega_\alpha - g_{0,\alpha} - \omega_\beta)} \right], \end{aligned} \tag{6.14}$$

where the last expression can be simplified if we explicitly use again that the coupling is weak $g_{0,\alpha} \ll \omega_{0,\alpha}$. We introduce a small parameter $\varepsilon \equiv g_{0,\alpha}/\omega_\alpha$ and realize that Eq. (6.14) becomes

$$E^{(2)}_{|\alpha^-\rangle} = \frac{|g_{0,\beta}|^2}{\omega_\alpha} n_\beta \left[\frac{-\varepsilon}{\left(\frac{\beta}{\alpha} - 1\right)^2} \right] + \frac{|g_{0,\beta}|^2}{2\omega_\alpha \left(1 - \frac{\beta}{\alpha}\right)} + O(\varepsilon^2). \tag{6.15}$$

Similarly, one finds

$$E^{(2)}_{|0,\downarrow,n_\beta\rangle} = \frac{|g_{0,\beta}|^2}{\omega_\beta - \omega_\alpha} n_\beta$$

Thus the new transition frequency $\tilde{\omega}$ of the hybrid system of qubit and mode α in the presence of the perturbation will be to second order in the coupling $g_{0,\beta}$:

$$\tilde{\omega}_{\text{hybrid}} \equiv \omega_\alpha + g_{0,\alpha} + E^{(2)}_{|\alpha^-\rangle} - E^{(2)}_{|0,\downarrow,n_\beta\rangle},$$

and we define the transition frequency for the hybrid system as

$$\omega_s \equiv \omega_\alpha + g_{0,\alpha} - \frac{|g_{0,\beta}|^2}{2\left(\omega_\beta - \omega_\alpha\right)}$$

and the effective coupling

$$\begin{aligned} g &\equiv -\frac{|g_{0,\beta}|^2}{(\omega_\beta - \omega_\alpha)}\left[1 + \frac{g_{0,\alpha}}{(\omega_\beta - \omega_\alpha)}\right] \\ &\approx -\frac{|g_{0,\beta}|^2}{(\omega_\beta - \omega_\alpha)}. \end{aligned} \tag{6.16}$$

Analogous to Eq. (5.2), the corresponding effective Hamiltonian reads

$$H_{\text{eff}} = \hbar\omega_s \hat{a}_s^\dagger \hat{a}_s + \hbar\omega_\beta \hat{a}_\beta^\dagger \hat{a}_\beta + g\, \hat{a}_s^\dagger \hat{a}_s\, \hat{a}_\beta^\dagger \hat{a}_\beta, \tag{6.17}$$

where the new system with index s is our hybrid system with only one excitation possible such that $|n_s = 1\rangle \equiv |\alpha^-\rangle$. In order to evaluate the result numerically for different modes, it is appropriate to assume the following scaling relations

$$\begin{aligned} g_{0,j} &= \sqrt{j} g_0 \\ \omega_j &= j \cdot \omega_0 \\ \kappa_j &= j \cdot \kappa_0, \end{aligned}$$

which lead to the following expression for the coupling and for the dimensionless measurement rate:

$$g = -\frac{|g_0|^2}{\omega_0} \cdot \frac{\beta}{\beta - \alpha}.$$

$$\frac{\Gamma}{\kappa_\alpha} = \frac{|g|^2 \langle \hat{n}_\beta \rangle}{4\kappa_\alpha \kappa_\beta} = \langle \hat{n}_\beta \rangle \frac{|g_0|^4}{4\omega_0^2 \kappa_0^2} \cdot \frac{1}{\alpha\beta} \left(\frac{\beta}{\beta - \alpha}\right)^2.$$

Assuming $g_0 = 2\pi \cdot 50MHz$, $\kappa_0 = 10\,MHz$, $\omega_0 = 2\pi \cdot 6GHz$, and $(\alpha, \beta) = (3, 5)$ we observe that the optimal measurement rate of $\Gamma/\kappa = 1/4$ is reached at a measurement mode photon number of $\langle \hat{n}_\beta \rangle \approx 35$, well below the critical photon number, where the dispersive approximation starts to break down as discussed e.g. in [122]. Note that the dropped term in Eq. (6.16) amounts to a correction of only about 2% in the needed photon number.

Simply adjusting the decay rate of the cavity or the qubit resonator coupling will enable the experimentalist to observe all the features discussed in this section as the full range of measurement rates are available, starting from the ideal detection limit $\Gamma/\kappa = 1/4$ to the Quantum Zeno limit $\Gamma/\kappa \gg 1$.

The detector efficiency, although limited by the Quantum Zeno effect as shown before, can then reach values of about 30% even without considering more elaborate detector and signal analysis schemes.

We note that in an alternative scheme, both the signal and the detection mode can be dispersively coupled to the qubit, although generically this would lead to a weaker overall coupling g. Finally, we remark that having control over the individual mode frequencies involved (e.g. in a setup with two cavities instead of one) would be advantageous for two reasons: First, it could avoid spurious higher-order processes in which the signal mode is contaminated by the decay of photons from the detection mode, by making those processes strongly off-resonant. Second, it would allow to tune the signal and detection modes relatively close to each other, thereby enhancing the coupling.

Another experiment in which essentially the same physics could be observed is the detection of single photons in a microwave cavity by employing the dispersive interaction with a stream of Rydberg atoms [104].

Chapter 7

Conclusions

In this thesis, experimentally relevant aspects and open questions of quantum information processing and measurement in circuit quantum electrodynamics have been investigated theoretically.

Building on the pioneering theoretical and experimental work in which up to three qubits have been integrated on a chip and successfully coupled via a cavity mode, we propose a scheme to overcome the natural limits concerning scalability in these systems. As a possible solution, we have proposed and investigated a cross-bar grid layout of cavities with qubits at the intersections. In addition, it can serve as a building block for a truly scalable scheme for quantum information processing with superconducting circuits by combining 7x7 arrays in a staircase manner. Hand in hand with current experiments that have succeeded in eliminating charge noise as a source of decoherence and combined with the methods to improve upon simple dispersive gates by e.g. using resonant gates and optimal control theory the cavity grid can be implemented in experiments in the very near future. Sample layouts combining two cavities and multiple qubits have already been designed by the leading groups.

Quantum trajectories have proven to be a state-of-the-art tool to analyze measurement situations in a very realistic manner by giving access to both the measurement record as well as the internal quantum dynamics conditioned on this record.

In order to extend the toolbox available for quantum information processing in circuit QED we have proposed and investigated in detail a scheme how a suitable product state of N qubits can be reliably converted into e.g. a N-qubit Greenberger-Horne-Zeilinger or W state by performing a collective dispersive readout of the qubits.

Access to the ultra-strong coupling regime has made it possible to perform quantum optics experiments on-the-chip. In this thesis we have presented the first workable scheme to dispersively detect single itinerant microwave photons. Presenting a way how to close this gap in the experimental toolbox will prove valuable to strengthen experimental claims about e.g. the deterministic generation of single photons. The scheme presented reaches detection efficiencies about 30% only limited by fundamental quantum mechanics in this case the Quantum Zeno effect. This detector could e.g. be used in quantum communication or cryptography applications.

Finally it should be mentioned that a comprehensive software package has been developed which will make future simulation of master equations easier. It provides the needed performance to investigate stochastic master equations while keeping the programming for the user at a comfortably high level otherwise only known from commercial software packages.

Chapter 8

Appendix

8.1 Derivation of the adiabatically eliminated stochastic master equation

8.1.1 Unravelling the master equation

Motivation

The goal of this procedure is to obtain a stochastic master equation which models the system including the measurement back-action and the corresponding noisy measurement signal in a consistent way starting from Eq. (6.2) which reads:

$$
\begin{aligned}
\dot{\hat{\rho}} &= -i[\frac{\kappa_1}{2}(\alpha\hat{a}_1^\dagger + \alpha^*\hat{a}_1) + g\hat{a}_1^\dagger\hat{a}_1\hat{a}_0^\dagger\hat{a}_0, \hat{\rho}] \\
&+ \kappa(\hat{a}_0\hat{\rho}\hat{a}_0^\dagger - \frac{1}{2}\hat{a}_0^\dagger\hat{a}_0\hat{\rho} - \frac{1}{2}\hat{\rho}\hat{a}_0^\dagger\hat{a}_0) \\
&+ \kappa_1(\hat{a}_1\hat{\rho}\hat{a}_1^\dagger - \frac{1}{2}\hat{a}_1^\dagger\hat{a}_1\hat{\rho} - \frac{1}{2}\hat{\rho}\hat{a}_1^\dagger\hat{a}_1) \\
&- i\sqrt{\dot{N}_{\mathrm{in}}/2\kappa}[\hat{a}_0 + \hat{a}_0^\dagger, \hat{\rho}]. \qquad (8.1)
\end{aligned}
$$

This way, we will gain insights beyond the ensemble average description of the usual master equation which is crucial for the analysis the detection efficiency.

Remark on Stochastic Master Equations

The master equation in general is an ensemble average description of a quantum system. It can be thought of as arising from averaging a stochastic, 'unravelled' master equation.

Note that there is, without a physical concept of the processes involved, no unique way of obtaining a stochastic master equation from the averaged master equation [182, 207, 210], a process which is known as "unravelling". However, once we consider the physical details of the measurement, quantum mechanics allows us to unravel the master equation Eq. (8.10) in such a way that we obtain (i) a classical measurement signal as produced by homodyne detection of the light-field leaking out the detector mode and (ii) simultaneously a master equation *conditioned* on this measurement signal. This enables us to self-consistently simulate the measured signal and the quantum dynamics of our system which gave rise to exactly this signal.

Outline of Calculation

We will observe that pure number states of the signal mode are attractor-solutions. As a result of the measurement, the signal mode's state is stochastically forced towards a pure number state on a timescale that corresponds to the time that we need to extract the information about this number state from the measured signal. The attractor nature of the number states also becomes apparent from the fact that the stochastic term in the master equation becomes strictly zero as can be seen from Eq. (8.14).

In the following derivation, we follow Refs. [182, 183, 207–209]. Note that the choice of unravelling formally corresponds to projecting the field leaking out of the detector mode into the free space field modes (which we also call the measurement bath) onto the correct basis states. In this case we project onto the eigenstates of the field quadrature we are interested in to extract the phase shift imposed by a signal photon in the cavity. We start by writing the measurement bath as an infinite set of harmonic oscillators (e.g. the modes of a transmission line),

$$\hat{H}_{\text{bath}} = \sum_n \omega_{d,n} \hat{b}^\dagger_{d,n} \hat{b}_{d,n}, \tag{8.2}$$

interacting with the detector mode by the Hamiltonian

$$\hat{H}_{int} = i \sum_n g_d(\omega_n) \left(\hat{b}^\dagger_{d,n} \hat{a}_1 - \hat{b}_{d,n} \hat{a}^\dagger_1 \right). \tag{8.3}$$

We employ the usual continuum and Markovian limit and define the detector mode decay rate $\kappa_{\text{det}} \equiv \pi D(\omega_1) |g_d(\omega_1)|^2$ where D is the density of states. [Note that this assumption cannot be easily relaxed for the purpose of deriving a stochastic master equation. It guarantees that the projective measurement of the bath will always disentangle system and bath which is not true for general non-Markovian baths. Details have been recently discussed in [210].] The operator of the measured signal is then

$$\begin{aligned} \hat{X}(t) &= \sum_n \left(\hat{b}^\dagger_{d,n}(t) + \hat{b}_{d,n}(t) \right) \\ &= \sqrt{\kappa_{\text{det}}} \left[\hat{a}_1(t) + \hat{a}^\dagger_1(t) \right] \\ &+ \sum_n \left(\hat{b}^\dagger_{d,n}(t_0) e^{i\omega_n (t-t_0)} + \hat{b}_{d,n}(t_0) e^{-i\omega_n (t-t_0)} \right), \end{aligned}$$

where the last two lines represent the inhomogeneous and homogeneous parts of the solution of the equations of motion for the Heisenberg operators $\hat{b}_{d,n}$, respectively. Using $\langle \hat{b}_n(t_0) \rangle = \langle \hat{b}^\dagger_n(t_0) \rangle = 0$, the average signal can be expressed as

$$\langle \hat{X}(t) \rangle = \sqrt{\kappa_{\text{det}}} \left\langle \hat{a}(t) + \hat{a}^\dagger_1(t) \right\rangle.$$

Now the idea is to let this interaction Hamiltonian (8.3) act for a small time Δt before projecting the bath onto an eigenstate. Every time the bath is projected, the previously generated entanglement between bath and system ensures that this will also have a (slight) effect on the system state. By this mechanism it becomes clear that the random choice of an eigenvalue of the bath will in the continuum limit give rise to a stochastic term in the measured signal (noise) as well as in the system dynamics (back-action). This random choice of eigenvalue/eigenstate of $\hat{X}$ happens according to the probability distribution given by

$$P(X) = \langle X | \hat{\rho}(t + \Delta t) | X \rangle$$

and projects the density matrix onto the eigenstate such that

$$\hat{\rho} \mapsto \frac{|X\rangle \langle X| \hat{\rho}(t + \Delta t) |X\rangle \langle X|}{\langle X| \hat{\rho}(t + \Delta t) |X\rangle} \tag{8.4}$$

In order to simplify the notation, we introduce global bath operators defined as $\hat{B}(t) \equiv \frac{1}{\sqrt{2\pi D(\omega_1)}} e^{+i\omega_1 t} \sum_n \hat{b}_{d,n}(t)$. We are interested in the evolution of the operator $\hat{B}(t)$ over the time-scale Δt which is much shorter than the internal time-scale of the intrinsic dynamics of $\hat{B}(t)$. Thus we can define an operator $d\hat{B}(t)$ as

$$d\hat{B}(t) \equiv \frac{1}{\sqrt{\Delta t}} \int_t^{t+\Delta t} \hat{B}(\tau) d\tau \, .$$

. To leading order in Δt, the evolution of the density matrix will then have the following form:

$$\begin{aligned} \hat{\rho}(t+\Delta t) &= \hat{\rho}(t) \otimes \rho_{\text{bath}}(t) \\ &+ \sqrt{\kappa_{\text{det}} \Delta t} \left[d\hat{B}\hat{a}_1^\dagger + \hat{a}_1 d\hat{B}^\dagger, \hat{\rho}(t) \otimes \hat{\rho}_{\text{bath}}(t) \right] \\ &+ O(\Delta t). \end{aligned}$$

Note that we have already worked out all $O(\Delta t)$ terms which constitute the deterministic evolution so we can focus on the $O(\sqrt{\Delta t})$ terms. If one does so, and keeps all the terms up to order $O(\sqrt{\Delta t})$, one realizes that the state after measurement and projection will have the form

$$\begin{aligned} \Delta\hat{\rho}(t+\Delta t) &= \frac{|X\rangle \langle X| \, \hat{\rho}(t+\Delta t) \, |X\rangle \langle X|}{\langle X| \, \hat{\rho}(t+\Delta t) \, |X\rangle} - \hat{\rho}(t) \\ &= \sqrt{\Delta t} X \left(\hat{a}_1 \hat{\rho}(t) + \hat{\rho}(t) \hat{a}_1^\dagger - \langle \hat{a}_1 + \hat{a}_1^\dagger \rangle (t) \hat{\rho}(t) \right) \\ & +O(\Delta t). \end{aligned} \tag{8.5}$$

Similarly we find for the signal X, assuming zero temperature, that the bath state at time t is a Gaussian centered at $X = 0$ and with width 1. At time $t + \Delta t$, after interaction and projection, the bath will still be in a Gaussian state, but centered around $\sqrt{\kappa_{\text{det}}} \langle \hat{a}_1 + \hat{a}_1^\dagger \rangle \Delta t$. Thus we can identify the functional form of the noisy signal. It reads in differential form

$$X(t) = \sqrt{\kappa_{\text{det}}} \langle a_1 + a_1^\dagger \rangle (t) + \xi(t), \tag{8.6}$$

where $\xi(t)$ is white noise, with $\langle \xi(t) \rangle = 0$ and $\langle \xi(t)\xi(t') \rangle = \delta(t - t')$. Writing Eq. (8.5) in differential form and inserting Eq. (8.6) and again keeping terms up to $O(\Delta t)$, we find the stochastic contribution $\dot{\hat{\rho}}_{st}(t)$ of the master equation that describes the measurement back-action given we have measured a certain signal trajectory $X(t)$ as

$$\dot{\hat{\rho}}_{st}(t) = \sqrt{\kappa_{\text{det}}} \left(\hat{a}_1 \hat{\rho}(t) + \hat{\rho}(t) \hat{a}_1^\dagger - \langle \hat{a}_1 + \hat{a}_1^\dagger \rangle (t) \hat{\rho}(t) \right) \xi(t).$$

Together with the deterministic evolution of Eq. (8.1), the unravelled master equation reads:

$$\begin{aligned} \dot{\hat{\rho}} &= -ig[\hat{a}_1^\dagger \hat{a}_1 \hat{a}_0^\dagger \hat{a}_0, \hat{\rho}] \\ &- ig[(\alpha^* \hat{a}_1^\dagger + \alpha \hat{a}_1) \hat{a}_0^\dagger \hat{a}_0, \hat{\rho}] \end{aligned}$$

$$
\begin{aligned}
&+ \kappa(\hat{a}_0\hat{\rho}\hat{a}_0^\dagger - \frac{1}{2}\hat{a}_0^\dagger\hat{a}_0\hat{\rho} - \frac{1}{2}\hat{\rho}\hat{a}_0^\dagger\hat{a}_0) \\
&+ \kappa_1(\hat{a}_1\hat{\rho}\hat{a}_1^\dagger - \frac{1}{2}\hat{a}_1^\dagger\hat{a}_1\hat{\rho} - \frac{1}{2}\hat{\rho}\hat{a}_1^\dagger\hat{a}_1) \\
&- i\sqrt{\dot{N}_{\text{in}}/2\kappa}[\hat{a}_0 + \hat{a}_0^\dagger, \hat{\rho}] \\
&+ \sqrt{\kappa}\left(\hat{a}_1\hat{\rho}(t) + \hat{\rho}(t)\hat{a}_1^\dagger - \langle\hat{a}_1 + \hat{a}_1^\dagger\rangle(t)\hat{\rho}(t)\right)\xi(t). \qquad (8.7)
\end{aligned}
$$

The last steps of this procedure can be found in more detail in [182]. Note that the stochastic term is not of Lindblad form but has nonlinear superoperator form [182].

8.1.2 Adiabatic elimination of the detector mode

The key assumption for the adiabatic elimination procedure to be correct and appropriate is that the dynamics of the ancilla system, in our case the detector mode, is much faster than the dynamics of the system, in our case the signal mode. In this limit $\kappa_{\text{det}}/\kappa \gg 1$, the detector mode will relax to its displaced, driven state on a timescale that is much faster than the intrinsic timescales in the signal mode.

The first step to be taken is to transform the master equation such that the phase space origin for the detector mode is centered at its steady state under the coherent drive. This can be done by applying the displacement operator $\hat{D}(-\alpha) = \exp[-\alpha\hat{a}_1^\dagger + \alpha^\star\hat{a}_1]$ to Eq. (8.1). As a result, we have eliminated the driving term for the detector mode and obtain as the new master equation:

$$
\begin{aligned}
\dot{\hat{\rho}} &= -ig[\hat{a}_1^\dagger\hat{a}_1\hat{a}_0^\dagger\hat{a}_0, \hat{\rho}] \\
&- ig[(\alpha\hat{a}_1^\dagger + \alpha^*\hat{a}_1)\hat{a}_0^\dagger\hat{a}_0, \hat{\rho}] \\
&+ \kappa(\hat{a}_0\hat{\rho}\hat{a}_0^\dagger - \frac{1}{2}\hat{a}_0^\dagger\hat{a}_0\hat{\rho} - \frac{1}{2}\hat{\rho}\hat{a}_0^\dagger\hat{a}_0) \\
&+ \kappa_1(\hat{a}_1\hat{\rho}\hat{a}_1^\dagger - \frac{1}{2}\hat{a}_1^\dagger\hat{a}_1\hat{\rho} - \frac{1}{2}\hat{\rho}\hat{a}_1^\dagger\hat{a}_1) \\
&- i\sqrt{\dot{N}_{\text{in}}/2\kappa}[\hat{a}_0 + \hat{a}_0^\dagger, \hat{\rho}]. \qquad (8.8)
\end{aligned}
$$

Note that the new vacuum state that the detector mode relaxes to is actually the coherent state $|\alpha\rangle$. The first two terms capture the fluctuations in the ancilla excitation while we have eliminated the frequency renormalization term $-i|\alpha|^2 g[\hat{a}_0^\dagger\hat{a}_0, \hat{\rho}]$ by absorbing it into the interaction picture.

The adiabatic elimination [182, 183, 207, 208] is a well-controlled approximation and can be expressed as an expansion of the density matrix in a small parameter. Introducing this small parameter $\epsilon \ll 1$ such that $\kappa/\kappa_{\text{det}} = O(\epsilon)$ and $g|\alpha|/\kappa_{\text{det}} = O(\epsilon)$ are satisfied, we can formally expand the density matrix in orders of ϵ as follows:

$$
\begin{aligned}
\hat{\rho} &= \hat{\rho}_{\text{s}}^{(00)} \otimes \hat{\sigma} + \hat{\rho}_{\text{s}}^{(10)} \otimes \hat{a}_1^\dagger\hat{\sigma} \\
&+ \hat{\rho}_{\text{s}}^{(01)} \otimes \hat{\sigma}\hat{a}_1 + \hat{\rho}_{\text{s}}^{(11)} \otimes \hat{a}_1^\dagger\hat{\sigma}\hat{a}_1 \\
&+ \hat{\rho}_{\text{s}}^{(20)} \otimes \hat{a}_1^{\dagger 2}\hat{\sigma} + \hat{\rho}_{\text{s}}^{(02)} \otimes \hat{\sigma}\hat{a}_1^2 + O(\epsilon^3). \qquad (8.9)
\end{aligned}
$$

Up to now, we have just rewritten the density matrix in a form that makes the different orders of ϵ as well as off-diagonal terms and diagonal terms apparent. $\hat{\sigma} \equiv |\mathrm{vac}\rangle \langle \mathrm{vac}|$ denotes the displaced coherent state of the detector mode which is a vacuum state. Using this decomposition, one can straightforwardly realize that taking the trace over the detector mode results in the following form for the signal mode density matrix:

$$\hat{\rho}_s = \hat{\rho}_{\mathrm{s}}^{(00)} + \hat{\rho}_{\mathrm{s}}^{(11)}.$$

We now evaluate Eq. (8.8) term by term using Eq. (8.9), $[\hat{a}_1, \hat{a}_1^\dagger] = 1$ and the fact that the coherent state $\hat{\sigma}$ is a vacuum state. After lengthy, but simple manipulation of the expressions we can eliminate all detector mode operators from the master equation. Key steps in this calculation are (a) replacing the off-diagonal terms in the signal mode density matrix by their steady state solution, i.e. setting $\dot{\hat{\rho}}_{\mathrm{s}}^{(10)} = \dot{\hat{\rho}}_{\mathrm{s}}^{(01)} = \dot{\hat{\rho}}_{\mathrm{s}}^{(02)} = \dot{\hat{\rho}}_{\mathrm{s}}^{(20)} = 0$ and (b) disregarding off-diagonal terms in the detector mode density matrix like e.g. $\hat{a}_1^\dagger \hat{a}_1^\dagger \hat{a}_1^{\dagger\,\mathrm{coh}} \hat{\rho}_{det}$ which are further away from the diagonal than the expansion range of the ancilla state. The result (see [183]) reads:

$$\begin{aligned} \dot{\hat{\rho}} &= -i\sqrt{\frac{\dot{N}_{\mathrm{in}}\kappa}{2}} \left[\hat{a} + \hat{a}^\dagger, \hat{\rho}\right] + \kappa \left(\hat{a}\hat{\rho}\hat{a}^\dagger - \frac{1}{2}\hat{n}\hat{\rho} - \frac{1}{2}\hat{\rho}\hat{n}\right) \\ &- 2\frac{g^2 \left|\alpha\right|^2}{\kappa_{\mathrm{det}}} \left[\hat{n}, \left[\hat{n}, \hat{\rho}\right]\right]. \end{aligned} \tag{8.10}$$

From now on we will introduce the measurement rate $\Gamma \equiv g^2 \left|\alpha\right|^2 / \kappa_{\mathrm{det}}$ which is the coefficient of the measurement induced diffusion term. This simplified master equation (Eq. (8.10)) for the signal mode alone later enables us to perform detailed numerical studies due to the more manageable size of the density matrix. Furthermore, only in the adiabatically eliminated version of the master equation we will be able to *explicitly* see that the chosen limit of $\kappa_{\mathrm{det}} \gg \kappa$ exactly corresponds to measuring the photon number of the signal mode by looking at the phase shift on the detection mode.

The last step of the calculation follows the lines of the elimination of the detector mode operators from the deterministic terms in the master equation. However, to adiabatically eliminate the detector mode operators from the stochastic term, one more consideration is necessary. Simply replacing the off-diagonal terms by their stationary solution will not be enough as the stochastic term averages to zero. Instead we have to compute the variance of the stochastic term and integrate it over the timescale of the diagonal terms $\Delta t = \kappa_{\mathrm{det}}^{-1}$. Doing so, we find that the resulting master equation Eq. (8.14) reads

$$\begin{aligned} \dot{\hat{\rho}}_s &= -i\sqrt{\frac{\dot{N}_{\mathrm{in}}\kappa}{2}} \left[\hat{a} + \hat{a}^\dagger, \hat{\rho}\right] + \kappa \left(\hat{a}\hat{\rho}\hat{a}^\dagger - \frac{1}{2}\hat{n}\hat{\rho} - \frac{1}{2}\hat{\rho}\hat{n}\right) \\ &\quad -2\Gamma \left[\hat{n}, \left[\hat{n}, \hat{\rho}\right]\right] - \sqrt{4\Gamma} \left(\hat{n}\hat{\rho} + \hat{\rho}\hat{n} - 2\hat{\rho} \left\langle \hat{n} \right\rangle (t)\right) \xi(t). \end{aligned} \tag{8.11}$$

For the rest of the derivation, we will drop the subscript s which denotes the signal mode. In the course of the adiabatic elimination calculation we also find the very useful identity

$$\sqrt{\kappa_{\mathrm{det}}} \langle \hat{a}_1 + \hat{a}_1^\dagger \rangle(t) = 2\sqrt{2\Gamma} \langle \hat{a}_0^\dagger \hat{a}_0 \rangle(t), \tag{8.12}$$

which allows us to write the measurement signal (rescaled) Eq. (6.4) as

$$X(t) \equiv \langle \hat{n} \rangle (t) + \frac{1}{4}\sqrt{\frac{1}{\Gamma}}\xi(t). \tag{8.13}$$

Having obtained the final form of the adiabatically eliminated stochastic master equation, we can turn to the detector logic and the evaluation of the photon detection efficiency. This will be done by numerically integrating Eqs. (8.14, 8.13) and applying a suitable non-linear filter to the signal followed by a statistical analysis of the dependence of the photon count rate on the physical parameters in the system, especially Γ/κ, as explained in the main text.

8.2 How to efficiently simulate master equations

8.2.1 Get a first fast idea about your system

The fast track to define your Hamiltonian/master equation without writing more code than the operator equation itself

Inspired by the Quantum Optics toolbox [211] package for Matlab, I started to build in the same kind of flexibility into my C++ library [212]. The goal was to allow rapid development while enabling the user to seamlessly go to an optimized version of his code without having to cross a system barrier. Usually, when writing something quick-and-dirty in e.g. Matlab, Mathematica or Maple it works until it gets numerically involved in terms of performance needed/CPU time which at a certain point often requires people to start all over again with their problem in C/C++ in order to finally get the performance they need to produce e.g. publication quality data.

Using my library, one only needs to optimize the way, the equation is composed of operators if needed. All the pre/post-processing code and the simulation steering can be kept the same and does not need to be touched. In essence one spends his time doing what one is supposed to do - getting the job done and spend as little time as possible dealing with technology. An extensive technical reference documentation can be found in [212].

Product Hilbert-spaces made up by combining subsystems of arbitrary dimensions

The key concept here is to exploit the object-oriented structure of C++. An instance of the class CComplexMat, for instance, can represent any (quantum mechanical) operator. Usually one starts to define such a matrix by supplying an STL std::vector<int> containing the dimensions of the subsystems. E.g. for a two qubits coupled to cavity with three resonator levels taken into account, one would pass a vector [2,2,3] to the constructor of CComplexMat.

Note that, no matter the 'real' composition of the matrix in terms of tensor-products of subsystem Hilbert spaces, everything is always stored internally in a linear array of type std::vector<std::complex<double> >. The individual matrix elements can be accessed by the single index, called *masterindex*, the pair of indices living in the product Hilbert space and the $2n$-tupel of indices, where n is the number of subsystems. This becomes especially useful when defining the terms on the right-hand side of the master equation in terms of matrix elements.

Obtaining creation and annihilation operators for the subsystems

Using the built-in method to retrieve an annihilation operator for a given subsystem given any initialized instance of CDensMat or CComplexMat, one obtains the following:

```
vector<int> dims;

dims.push_back(2); //one qubit
dims.push_back(2); //second qubit
dims.push_back(3); //resonator

CComplexMat H(dims); //construct (empty) Hamiltonian

//contruct a and a_dagger for each subsys
```

```
//annihilation operator for first qubit
CComplexMat a0 = H.m_Annihilation_operator(0);
```

a0 is an instance of CComplexMat itself and would physically mean

$$\hat{a}_0 \prod^{\otimes} \hat{\mathbb{1}},$$

where the tensor product is over all other subsystems. However, in rare cases it might be preferable to construct operators from tensor products by hand. Here, we have provided the tensor product operator &&.

Applying arbitrary functions to operators

In order to realize complicated nonlinear Hamiltonians, e.g. $\cos(\hat{a} + \hat{a}^{\dagger})$, one can apply arbitrary functions directly to arbitrary operators having defined your function:

```
double f(double in)
{
  return 4.0*cos(2.0*in);
};
```

Now the function can be used like this:

```
CComplexMat term_cosa0 = a0+a0_dagger; term_cosa0.m_Apply_function(f);
```

Note that this function evidently involves diagonalizing the operator which can be numerically costly.

Calculating arbitrary expectation values

Assuming we are working with a density matrix representation, e.g. when solving a master equation, arbitrary expectation values can be computed, e.g. for an operator $\hat{O}$, $\langle\hat{O}\rangle \equiv \mathrm{tr}\hat{\rho}\hat{O}$ will be computed straightforwardly coding (assuming that everything is defined and initialized properly before):

```
std::complex<double> expvalO = rho.m_expval(O);
```

Test the basic physics

Here is a code sniplet showing how to define a Tavis-Cummings Hamiltonian (two qubits coupled to a cavity). Here is a short example:

```
vector<int> dims;

dims.push_back(2); //one qubit
dims.push_back(2); //second qubit
dims.push_back(3); //resonator

CComplexMat H(dims); //construct (empty) Hamiltonian

//contruct a and a_dagger for each subsys

//annihilation operator for first qubit
CComplexMat a0 = H.m_Annihilation_operator(0);
CComplexMat a0_dag(dims);
a0_dag = a0;
a0_dag.m_Hermitian_Conjugate();

//annihilation operator for second qubit
CComplexMat a1 = H.m_Annihilation_operator(1);
CComplexMat a1_dag(dims);
a1_dag = a1;
a1_dag.m_Hermitian_Conjugate();

//annihilation operator for resonator
CComplexMat a2 = H.m_Annihilation_operator(2);
CComplexMat a2_dag(dims);
a2_dag = a2;
a2_dag.m_Hermitian_Conjugate();

//define the couplings
double  g0 = 2.0;
double  g1 = 3.0;

//define the transition frequencies
double w_0 = 10.0;
double w_1 = 30.0;
double w_r = 20.0;

//piece it together
H = w_0 * a0_dag*a0
  + w_1 * a1_dag*a1
  + w_r * (a2_dag*a2 + 0.5)
  + g0*(a0*a2_dag + a0_dag*a2)
  + g1*(a1*a2_dag + a1_dag*a2);

//now we can do spectroscopy or whatever...

CEigensystem eigsH = H.m_GetEigensystem();

cout << "eigenvalues ordered (smallest first)" << endl;
print_vector(eigsH.m_sort(true).m_eigenvalues);
```

8.2.2 Solve a deterministic master equation

Using the C++ libraries that have been developed in the course of this thesis, we can simply extend the example of the previous section to solve a master equation with the Tavis-Cummings-Hamiltonian. Details concerning the C++ class libraries can be found in the extensive documentation [212].

Implement a function container

The key concept of all solver classes in the libDESFrameWork library is that all the solver routines have been implemented in solving for a container class as the variable. It is now up to the user to put whatever he likes into this solver class , e.g. a density matrix for a simple master equation, two density matrices with different master equations to solve for simultaneously to e.g. check the accuracy of an approximation or to compare the ideal to a lossy evolution (see e.g. simulation for the Cavity Grid in Sec. 2). This keeps the solver itself readable and the user from touching solver routines. A sample function container (a class called CFuncCont) is already defined in libDESFrameWork so one just needs to implement it e.g. like this:

```
#include "CFuncCont.h"
#include "tools.h"
using namespace std;
CFuncCont::CFuncCont() { }
CFuncCont::CFuncCont(const vector<int>& dims)
{
  m_DensMat = CDensMat(dims);
  m_idealDensMat=CDensMat(dims);
  m_phases=vector<double>(dims.size());
  m_I_filtered = 0.0;
}
CFuncCont::~CFuncCont() { }

//... some other stuff ...
//..here is en example operator
CFuncCont CFuncCont::operator+(const CFuncCont& right) const
{
  CFuncCont retval(right.m_DensMat.m_dims);
  retval.m_DensMat=m_DensMat+right.m_DensMat;
  retval.m_idealDensMat=m_idealDensMat+right.m_idealDensMat;
  retval.m_I_filtered=m_I_filtered+right.m_I_filtered;
  for(int i=0;i<m_phases.size();++i)
  {
      retval.m_phases[i] = m_phases[i] + right.m_phases[i];
  }
  return retval;
}
```

As one can see, it is merely a task of passing all operations on to all elements of the container which is simple enough.

Implement the physical system container

The second necessary step is to define the system class which is supposed to inherit from CQuantumSystem. CQuantumSystem already defines some member variables. If we need more, we need to define them here. A sample definition could look like this:

```
class CCavity_Grid :  public CQuantumSystem
{
  public:
  virtual ~CCavity_Grid();
  CCavity_Grid();
  //A function to reset the added members
  void Reset(void);
  //for adding decoherence
  vector<double> m_kappa;
  vector<double> m_gamma_phi;
  //for adding a protocol
  CProtocol m_protocol;
  //to store the Hamiltonian
  CComplexMat m_H;
};
```

Combine system and solver

Now as we have defined the quantum system, we need to 'marry' it to a solver in order to get something to work with. This can be simply done e.g. by defining a class that inherits both from CCavityGrid and a solver class like CRungeKutta5. Its definition would look like this

```
class CCavityGridRungeKutta5 : virtual public CRungeKutta5, public CCavity_Grid
{
  public:
  CCavityGridRungeKutta5();
  virtual ~CCavityGridRungeKutta5();
  //a function that sets the internal member variables from
  //parameters from an ini-file stored in m_Parameters (explained later)
  void Set_Parameters(void);
  void m_Reset(void)
  {
    CDESBase::ResetBase();
    CCavity_Grid::Reset();
  };

  //most importantly: the right hand side and the processing of results

  virtual void m_rhs(const CFuncCont* FV /*Function Values to be used*/,CFuncCont* vTarget,
      const vector<double>& xi, double t);
  virtual void m_ProcessResultEachTimeStep(const double& t,  CFuncCont* Y, const vector<
      double>& v_xi);

};
```

Define the differential equation (master equation) and the way results are processed

```
CCavityGridRungeKutta5::CCavityGridRungeKutta5() { }
CCavityGridRungeKutta5::~CCavityGridRungeKutta5() { }

void CCavityGridRungeKutta5::m_rhs(const CFuncCont* FV /*Function Values to be used*/,
    CFuncCont* vTarget, const vector<double>& xi, double t)
{
  complex i = complex(0.,1.);
  vTarget->m_idealDensMat.m_set_to_zero();
  vTarget->m_idealDensMat += CDensMat(-i*m_H.m_Commutator(CComplexMat(FV->m_idealDensMat))
      ,0.0000001);
}
```

Say, we want to compute the entanglement between the two qubits at each time-step and write it to the screen, we use the function

```
 void CCavityGridRungeKutta5::m_ProcessResultEachTimeStep(const double& t,  CFuncCont* Y,
     const vector<double>& xi)
{
  //compute reduced density matrix, entanglement and output to screen
  cout << "entanglement at time" << "\t"
     << t << "\t"
     << Y->m_idealDensMat.m_Trace_out_System(2).m_GetLogNegativity(1)
    <<endl;
}
```

This is about it. Now we just need to steer this code from the main.

Start the simulation

Here, building on top of the example of the previous section, we instantiate CCavityGridRungeKutta5, set the Hamiltonian and initial values, time-steps and hit 'go'.

```
//initialize the system in the state |100>
vector<double> up_qb;
up_qb.push_back(0);
CParameterState MyInitialState("","Qubits_in_State_UP",up_qb);
double t_start=0.0;
double t_end=100.0;

CCavityGridRungeKutta5 MyRK;
MyRK.m_Initial_Values.m_idealDensMat.m_SetInitialState(MyInitialState);
MyRK.m_dims=dims;
MyRK.m_t.push_back(t_start);
MyRK.m_t_end=t_end;
MyRK.m_delta_t = 0.001;
//set the Hamiltonian
MyRk.m_H=H;

MyRK.m_kzRWA = false;
MyRK.m_eps=pow(10.0,double(-8));
MyRK.m_SetRK5Coefficients();

//solve the master equation
MyRK.m_evolve(true);
```

8.2.3 Introduce decoherence

Extend the function container and the right-hand side

If we had not already done this, we would need to extend the function container class CFuncCont to accommodate a second density matrix, which represents the lossy evolution such that we can simultaneously solve for both, the ideal and lossy evolution and compute fidelities at each time-step. Then, the only thing left to to is to extend the right-hand side to include the lossy evolution on the second density matrix. We assume that we have stored the loss rates in the member variables (vectors) m_kappa (for the decay rates) and m_gamma_phi (for the pure dephasing rates). We use built-in, optimized right-hand side terms for the decoherence and should do so also for the Hamiltonian part of the evolution once performance becomes important. Of course, also the initial state of the second density matrix has to be specified (e.g. in main, see previous section).

```
void CCavityGridRungeKutta5::m_rhs(const CFuncCont* FV /*Function Values to be used*/,
    CFuncCont* vTarget, const vector<double>& xi, double t)
{

complex i = complex(0.,1.);
complex one = complex(1.0,0.0);

vTarget->m_idealDensMat.m_set_to_zero();
vTarget->m_idealDensMat += CDensMat(-i*m_H.m_Commutator(CComplexMat(FV->m_idealDensMat))
    ,0.0000001);

vTarget->m_DensMat.m_set_to_zero();
vTarget->m_DensMat += CDensMat(-i*m_H.m_Commutator(CComplexMat(FV->m_DensMat)),0.0000001);
vTarget->m_DensMat.m_add_term_decay(0,m_kappa[0],one,&FV->m_DensMat);
vTarget->m_DensMat.m_add_term_pure_dephasing(0,m_gamma_phi[0],one,&FV->m_DensMat);
vTarget->m_DensMat.m_add_term_decay(1,m_kappa[1],one,&FV->m_DensMat);
vTarget->m_DensMat.m_add_term_pure_dephasing(1,m_gamma_phi[1],one,&FV->m_DensMat);
vTarget->m_DensMat.m_add_term_cavity_decay(2,m_kappa[2],one,&FV->m_DensMat);

}
```

Now that we solve for both density matrices, let us compute the fidelity and write it to stdout at every time step.

As one can see, it is merely a task of passing all operations on to all elements of the container which is simple enough.

```
 void CCavityGridRungeKutta5::m_ProcessResultEachTimeStep(const double& t,  CFuncCont* Y,
     const vector<double>& xi)
{
  //compute reduced density matrix, entanglement, and fidelity; then output to screen
  cout << "t=" << t << "\t" << logneg=
    << Y->m_idealDensMat.m_Trace_out_System(2).m_GetLogNegativity(1)
    << \t << fidelity=
    << fidelity(Y->m_DensMat,Y->m_idealDensMat)
    <<endl;
}
```

For completeness, we give the appropriately adapted part of main:

```
//initialize the system in the state |100>
vector<double> up_qb;
up_qb.push_back(0);
CParameterState MyInitialState("","Qubits_in_State_UP",up_qb);
double t_start=0.0;
double t_end=100.0;

CRungeKutta5_2qubitsCavitySwitchEnergies MyRK;
MyRK.m_Initial_Values.m_idealDensMat.m_SetInitialState(MyInitialState);
MyRK.m_Initial_Values.m_DensMat.m_SetInitialState(MyInitialState);

vector<double> decay_rates = vector<double>(3);
decay_rates[0]=1.0;
decay_rates[1]=1.0;
decay_rates[2]=1.0;


vector<double> dephasing_rates = vector<double>(3);
dephasing_rates[0]=1.0;
dephasing_rates[1]=1.0;
dephasing_rates[2]=1.0;

MyRK.m_kappa = decay_rates;
MyRK.m_gamma_phi = dephasing_rates;
MyRK.m_dims=dims;
MyRK.m_t.push_back(t_start);
MyRK.m_t_end=t_end;
MyRK.m_delta_t = 0.001;
//set the Hamiltonian
MyRk.m_H=H;

MyRK.m_kzRWA = false;
MyRK.m_eps=pow(10.0,double(-8));
MyRK.m_SetRK5Coefficients();

//solve the master equation
MyRK.m_evolve(true);
```

8.2.4 Solve a stochastic master equation

Change the example system

In order to give an illustrative example, we use the system introduced in Sec. 5 for the case of N qubits. We imagine to work in a rotating frame with respect to the qubit eigenfrequencies. Thus we do not need any Hamiltonian here which simplifies the main a lot. The system reads:

$$\begin{aligned}\dot{\hat{\rho}} &= \sum_{i=0}^{N}\gamma_1\left(\hat{\sigma}_i{}^{-}\hat{\rho}\hat{\sigma}_i{}^{+} - \frac{1}{2}\hat{\sigma}_i{}^{+}\hat{\sigma}_i{}^{-}\hat{\rho} - \frac{1}{2}\hat{\rho}\hat{\sigma}_i{}^{+}\hat{\sigma}_i{}^{-}\right)\\ &+ \sum_{i=0}^{N}\gamma^{\varphi}\left[2\hat{P}_i\hat{\rho}\hat{P}_i - \hat{P}_i\hat{\rho} - \hat{\rho}\hat{P}_i\right]\end{aligned}$$

$$
\begin{aligned}
&- \quad 2\bar{\Gamma}\left[\hat{N},\left[\hat{N},\hat{\rho}\right]\right] \\
&- \quad \sqrt{4\bar{\Gamma}}\left(\hat{N}\hat{\rho}+\hat{\rho}\hat{N}-2\hat{\rho}\left\langle\hat{N}\right\rangle(t)\right)\xi(t). \qquad (8.14)
\end{aligned}
$$

Here $\bar{\Gamma} \equiv \frac{\bar{g}^2|\varepsilon|^2}{\kappa_{cavity}}$ is the measurement rate, and $|\varepsilon|^2$ is the average photon number circulating inside the cavity mode. The stochastic master equation is conditioned on the measured signal

$$
X(t) \equiv \langle\hat{N}\rangle(t) + \frac{1}{4}\sqrt{\frac{1}{\bar{\Gamma}}}\xi(t). \qquad (8.15)
$$

$\xi(t)$ is white noise which is built-in and ready to use.

Extend the function container, change the solver and the right-hand side

Yet again, we would need to extend the function container class CFuncCont to hold an additional scalar function, which represents the classical integrated measurement signal $\bar{X}(t) \equiv \frac{1}{t}\int_0^t X(t')dt'$. We assume that we have changed our system to inherit from CEuler instead of CRungeKutta5 to solve a stochastic equation and to contain a vector of coupling m_v_g and the measurement rate m_Gamma.

```
class CCavityGridEuler : virtual public CEuler, public CCavity_Grid
{
  public:
  CCavityGridEuler();
  virtual ~CCavityGridEuler();
  //a function that sets the internal member variables from
  //parameters from an ini-file stored in m_Parameters (explained later)
  void Set_Parameters(void);
  void m_Reset(void)
  {
    CDESBase::ResetBase();
    CCavity_Grid::Reset();
  };

  //most importantly: the right hand side and the processing of results

  virtual void m_rhs(const CFuncCont* FV /*Function Values to be used*/,CFuncCont* vTarget,
      const vector<double>& xi, double t);
  virtual void m_ProcessResultEachTimeStep(const double& t,  CFuncCont* Y, const vector<
      double>& v_xi);

};
```

In addition, we only solve for one density matrix but with a switch m_b_dodecoherence, that tells the system to include decoherence or not.

```
void CCavityGridEuler::m_rhs(const CFuncCont* FV /*Function Values to be used*/,CFuncCont*
    vTarget, const vector<double>& xi, double t)
{

complex i = complex(0.,1.);
complex one = complex(1.0,0.0);

//contruct the operator N for arbitrary number of qubits
//depending on the individual couplings contained in m_v_g
  vector<CComplexMat> a;
  vector<CComplexMat> a_dag;

  vector<CComplexMat> n;
  CComplexMat N(m_dims);
  CComplexMat N_squared(m_dims);

  for(size_t it=0;it<m_dims.size();++it)
  {
    a.push_back(CComplexMat(m_dims));
    a.back().m_Annihilation_operator(it);
    a_dag.push_back(CComplexMat(m_dims));
    a_dag.back() = a.back();
    a_dag.back().m_Hermitian_Conjugate();
    n.push_back(a_dag.back()*a.back());
    N+=m_v_g[it]*n.back();
  }

  vTarget->m_DensMat.set_to_zero();
  double Gamma=m_Gamma;
  double expvalN = FV->m_DensMat.m_expval(N);

  (vTarget->m_DensMat) += CDensMat(-2.0 * Gamma * ( N.m_Commutator( N.m_Commutator(rho) ) )
      ,0.00001);
  (vTarget->m_DensMat) += CDensMat(-sqrt(4.0*Gamma)*( N*rho + rho*N - 2.0* expvalN * rho)*xi
      [0] ,0.00001);

  for(size_t it=0;it<m_dims.size() && m_bdodecoherence==true;it++)
  {
    vTarget->m_DensMat.m_add_term_decay(it,m_kappa[it],one,&(FV->m_DensMat));
    vTarget->m_DensMat.m_add_term_pure_dephasing(it,m_gamma_phi[it],one,&(FV->m_DensMat));
  }
  vTarget->m_I_filtered = expvalN + 1.0/4.0*(1.0/sqrt(Gamma))*xi[0] ;

}
```

Now say we want to print the integrated current as well as the entanglement between the two qubits (assuming we have $N = 2$). In addition, we want to apply Hadamard gates at the qubits at a certain time, which have been in the ground state previously. The member variable m_once, which is initialized in the constructor to be *false*, ensures that this only happens once.

```
 void CCavityGridEuler::m_ProcessResultEachTimeStep(const double& t,  CFuncCont* Y, const
     vector<double>& xi)
{
    if(t>3.0 && m_once==false)      //apply Hadamards
    {
      for(size_t it=0;it<m_dims.size();++it)
      {
        CComplexMat H(m_dims);
        H = H.m_Hadamard(it);
        Y->m_DensMat=CDensMat(H*CComplexMat(Y->m_DensMat)*H,0.0001);
      }
      cout << "t: " << t << " inserted Hadamards" << endl;
      m_once=true;
    }

    //compute entanglement and output to screen
    cout << "t=" << t << "\t" << Entanglement=
    << Y->m_idealDensMat.m_GetLogNegativity(1)
    << \t << X_bar=
    << Y->m_I_filtered)
    <<endl;
}
```

Appropriately adapt the main

```
CCavityGridEuler MyRK;

//we want to look at a two qubit experiment so
vector<int> dims;


dims.push_back(2); //one qubit
dims.push_back(2); //second qubit

//initialize the system in the state |00>
MyRK.m_Initial_Values.m_DensMat.m_mat[0]=1.0;

double t_start=0.0;
double t_end=100.0;

vector<double> decay_rates = vector<double>(2);
decay_rates[0]=1.0;
decay_rates[1]=1.0;


vector<double> dephasing_rates = vector<double>(2);
dephasing_rates[0]=1.0;
dephasing_rates[1]=1.0;

vector<double> couplings = vector<double>(2);
couplings[0]=1.0;
coupling[1]=1.0;

MyRK.m_Gamma = 1.0;
MyRK.m_v_g = couplings;
MyRK.m_kappa = decay_rates;
MyRK.m_gamma_phi = dephasing_rates;

MyRK.m_t.push_back(t_start);
MyRK.m_t_end=t_end;
MyRK.m_delta_t = 0.001;
MyRk.m_bdodecoherence=true;
MyRK.m_dims=dims;

//solve the stochastic master equation
MyRK.m_evolve(true);
```

8.2.5 Initialization-file handling

The example has already grown to a size that makes it desirable to organize parameters for a simulation not by hard-coding them into the main or into wherever, but instead write them to a human-readable initialization file. These files has to obey a certain syntax, e.g. XML. While XML is due to its hierarchical structure and validation possibilities certainly a good way to go if one were to improve the package I provide, I went for a simple text-based ini-file at the price of writing a parser myself. First, let us look at an appropriate example for an ini-file (following the stochastic master equation example).

```
# two-qubits
dims=2,2;
#same coupling -> Bell state |Phi+>
v_g=1.0,1.0;
#decay rates
kappa=0.0,0.0;
#dephasing rates
gamma_phi=0.0,0.0;
#time interval and step
```

```
t_start=0.0;
t_end=100.0;
delta_t=0.001;
```

This file is passed to the main by calling the program with (“-i <inifile.>”).

```
int main(int argc, char **argv)
{
  try
  {
    string IniFilename;
    CIniFileBase  MyIniFile;

    if(argc == 3)
    {
      if(!(string(argv[1])=="-i")
        throw string("First argument has to be -i");
      IniFilename = string(argv[2]);
    }
    else throw string("-i inifilename missing");

    MyIniFile.m_ReadIniFile(IniFilename);
    CCavityGridEuler MyRK;
    MyRK.m_kappa = MyIniFile.m_GetdvecParameter("kappa");
    MyRK.m_gamma_phi = MyIniFile.m_GetdvecParameter("gamma_phi");

    MyRK.m_t.push_back(MyIniFile.m_GetParameter("t_start");
    MyRK.m_t_end=MyIniFile.m_GetParameter("t_end");
    MyRK.m_delta_t = MyIniFile.m_GetParameter("delta_t");
    MyRK.m_v_g = MyIniFile.m_GetdvecParameter("v_g");
    MyRK.m_Gamma = MyIniFile.m_GetParameter("Gamma");
    MyRk.m_bdodecoherence = bool(MyIniFile.m_GetParameter("dodecoherence"));
    MyRK.m_dims=dims;


    //solve the stochastic master equation
    MyRK.m_evolve(true);

  }
  catch(string &e)
  {
    cout << "Error: " << e << endl;
  }
  catch(...)
  {
    cout << "Unknown error" << endl;
  }
  return 0;
}
```

The class CIniFileBase (see [212]) already provides the possibilities to pass vectors of values, scalar values, strings, initial states for density matrices and gate protocols to the program. Some of them are used here. Note that by specifying another array of dimensions in the ini-file, even the number of qubits or - in other cases - the number of levels for a special subsystem can be changed.

8.2.6 How to run more complicated gate sequences

Ini-file syntax for a protocol

In order to give an illustrative example, we use the system introduced in Sec. 5 for the case of N qubits. We will extend this system to include a flip-flop interaction (for the Hamiltonian see e.g. Sec. 2) between the qubits and realize an iSWAP around the corner using a SOPS protocol (see Sec. (2)). This needs the quantum gate library libQuantumGates which I have also documented in [212].

The syntax for the protocol in the ini-file is very simple. Here is the example for the adapted ini-file containing the protocol:

```
# two-qubits dims=2,2;
#same coupling -> Bell state |Phi+>
v_g=1.0,1.0;
#decay rates
kappa=0.0,0.0;
#dephasing rates
gamma_phi=0.0,0.0;
#time interval and step
t_start=0.0;
t_end=100.0;
delta_t=0.001;
#the protocol
Protocol="SWAP(0,1,-1.5,1.35)|ISWAPutp(1,2,1.35)|SWAP(0,1,-1.5,1.35)";
#reference frequency to tune qubits to when iSWAP is active
ref_freq_dispersive=100.0;
#qubit energies in the idle state
e=30.0,50.0,70.0;
#strength of flipflop-interaction
J=1.35,1.35;
```

As one can see, the single gates are like functions separated by a pipe symbol. Arbitrary gates can be concatenated. A separate protocol parser class is needed to decompose the string into a vector of gates. This is done e.g. by this definition and sample implementation of the class CParser which is itself not part of the quantum gate library. From the function CParser::m_Atom2Gate one can understand the syntax of the single gates in the ini-file and also extend it if one were to add new gates to the gate-library (the following code just shows how one particular gate is parsed. Others work analogously and can be obtained ifrom the author in an example project).

```
 class CParser
{
public:
  CParser();
  virtual ~CParser();

  void m_ParseExpression(const string& expression);
  CProtocol* m_ProtocolPtr

public:
  vector<string> m_GetAtoms(const string& expression);
  void m_Atom2Gate(const string& atom);
};


 CParser::CParser()
{
  m_ProtocolPtr = NULL;
  m_IniFilePtr = NULL;
}

CParser::~CParser()
{
}



void CParser::m_ParseExpression(const string& expression)
```

```
{
  //check for "'s

  if(expression.find_first_of("\"",0)!=string::npos)
    throw string("\" must not be part of an expression");

  vector<string> atoms = m_GetAtoms(expression);

  int i=0;

  for(i=0;i<atoms.size();++i)
  {
    m_Atom2Gate(atoms[i]);
  }
}

vector<string> CParser::m_GetAtoms(const string& expression)
{

  //.separates the single operations

  string operationbuffer=expression;

  vector<string> retval;

  if(operationbuffer.find_first_of("|",0)==string::npos)
  { //only one atom
    retval.push_back(operationbuffer);
  }
  else
  {
    while(operationbuffer.find_first_of("|",0)!=string::npos)
    {
      int endpos = operationbuffer.find_first_of("|",0);
      retval.push_back(operationbuffer.substr(0,endpos));
      operationbuffer.erase(0,endpos+1);
    }
    if(operationbuffer.length()>0)
      retval.push_back(operationbuffer);

  }

  return retval;

}

void CParser::m_Atom2Gate(const string& atom)
{
  string myatom=atom;
  string namebuffer;
  string arguments;

  int startpos=myatom.find("(",0);

  if(startpos==string::npos)
  {
    throw string("Atomic expression must contain (");
  }

  int endpos=myatom.find(")");

  if(endpos==string::npos)
  {
    throw string("Atomic expression must contain )");
  }
```

```
namebuffer=myatom.substr(0,startpos);

//myatom.erase(0,startpos);

arguments=myatom.substr(startpos+1,endpos-startpos-1);

//Komma-separiert

vector<string> v_arguments;

startpos=arguments.find_first_of(",",0);

while(startpos!=string::npos)
{

  v_arguments.push_back(arguments.substr(0,startpos));
  cout << v_arguments.back() << endl;
  arguments.erase(0,startpos+1);
  startpos=arguments.find_first_of(",",0);
}
if(arguments.size()>0)
{
  v_arguments.push_back(arguments);
}

cout << v_arguments.back() << endl;
//get time_offset

double time_offset=0.0;

int i=0;

for(i=0;i<m_ProtocolPtr->m_protocol.size();++i)
{
  time_offset+=m_ProtocolPtr->m_protocol[i]->m_Getduration();
}

string strtime_offset;

convert(time_offset,strtime_offset);

cout << "time_offset" << strtime_offset << endl;

if(namebuffer=="R")
{
  if(v_arguments.size()==4)//numb_of qubit,rotation axis,frequency,time = pi/frequency* x,
  {

    v_arguments.push_back("-1"); //no cavities explicitly in simulation
    v_arguments.push_back(strtime_offset);
  m_ProtocolPtr->m_protocol.push_back(new CGateZeroRiseTimeSingleQubitRotation(v_arguments
      ));
  }
  else if(v_arguments.size()==5)
  {
    //m_ProtocolPtr->m_protocol.push_back(new CGateFiniteRiseTimeSingleQubitRotation(
        v_arguments));
    v_arguments.push_back(strtime_offset);
    m_ProtocolPtr->m_protocol.push_back(new CGateZeroRiseTimeSingleQubitRotation(
        v_arguments));
  }
  else throw string("Function R must have 5 arguments");
}
else if(namebuffer=="rISWAPutp")
{
  if(v_arguments.size()==3)//numb_of qubit1, numb_of_qubit2,frequency,
    {
      v_arguments.push_back("-1"); //no cavities explicitly in simulation
      v_arguments.push_back(strtime_offset);
      m_ProtocolPtr->m_protocol.push_back(new CGateZeroRiseTimerISWAPutp(v_arguments));
    }
    else if(v_arguments.size()==4)//numb_of qubit1, numb_of_qubit2,frequency,
    {
      v_arguments.push_back(strtime_offset);
      m_ProtocolPtr->m_protocol.push_back(new CGateZeroRiseTimerISWAPutp(v_arguments));
    }
    else throw string("Function rISWAPutp must have 3 or 4 arguments");
  }
  else {
  // other gates
  }
  else throw string(string("Function")+namebuffer+string(" not known to Parser."));

  m_ProtocolPtr->m_protocol.back()->m_pProtocol=m_ProtocolPtr;

}
```

Extend the right-hand side

Now we need to adapt the right-hand side of the previous example in the sense that we do not look at measurement, so we can use the Runge-Kutta solver and include the protocol. This is straightforward:

```
CCavityGridRungeKutta5::CCavityGridRungeKutta5() { }
CCavityGridRungeKutta5::~CCavityGridRungeKutta5() { }

void CCavityGridRungeKutta5::m_rhs(const CFuncCont* FV /*Function Values to be used*/,
    CFuncCont* vTarget, const vector<double>& xi, double t)
{
  complex i = complex(0.,1.);
  complex one = complex(1.0,0.0);


  vTarget->m_DensMat.set_to_zero();
  vTarget->m_DensMat.m_add_term_qubit_energy(0,m_e[0],-i,&FV->m_DensMat);
  vTarget->m_DensMat.m_add_term_qubit_energy(1,m_e[1],-i,&FV->m_DensMat);
  vTarget->m_DensMat.m_add_term_qubit_energy(2,m_e[2],-i,&FV->m_DensMat);

  vTarget->m_DensMat.m_add_term_flipflop(0,1,m_J[0],-i,&FV->m_DensMat);
  vTarget->m_DensMat.m_add_term_flipflop(1,2,m_J[1],-i,&FV->m_DensMat);
  vTarget->m_DensMat += ( (-i)*(m_protocol.m_act(FV->m_DensMat, FV->m_phases,t) ));


  vTarget->m_phases[0] = m_e[m_switch_phases[0]];
  vTarget->m_phases[1] = m_e[m_switch_phases[1]];
  vTarget->m_phases[2] = m_e[m_switch_phases[2]];




  for(size_t it=0;it<m_dims.size() && m_bdodecoherence==true;it++)
  {
    vTarget->m_DensMat.m_add_term_decay(it,m_kappa[it],one,&(FV->m_DensMat));
    vTarget->m_DensMat.m_add_term_pure_dephasing(it,m_gamma_phi[it],one,&(FV->m_DensMat));
  }

}
```

Appropriately adapt the main

Here, among some other parameters, we need to parse the protocol and pass it to the system class.

```
int main(int argc, char **argv)
{
  try
  {
    string IniFilename;
    CIniFileBase  MyIniFile;

    if(argc == 3)
    {
      if(!(string(argv[1])=="-i")
        throw string("First argument has to be -i");
      IniFilename = string(argv[2]);
    }
    else throw string("-i inifilename missing");

    MyIniFile.m_ReadIniFile(IniFilename);
    CCavityGridRungeKutta5 MyRK;
    MyRK.m_kappa = MyIniFile.m_GetdvecParameter("kappa");
    MyRK.m_gamma_phi = MyIniFile.m_GetdvecParameter("gamma_phi");

    MyRK.m_t.push_back(MyIniFile.m_GetParameter("t_start");
    MyRK.m_t_end=MyIniFile.m_GetParameter("t_end");
    MyRK.m_delta_t = MyIniFile.m_GetParameter("delta_t");
    MyRK.m_v_g = MyIniFile.m_GetdvecParameter("v_g");
    MyRK.m_Gamma = MyIniFile.m_GetParameter("Gamma");
    MyRk.m_bdodecoherence = bool(MyIniFile.m_GetParameter("dodecoherence"));
    MyRK.m_dims=dims;

    //get the protocol from the ini-file
    string strproto = MyIniFile.m_GetStrParameter(Protocol);
    CProtocol MyProtocol;
    CParser MyParser;
    MyParser.m_pProtocol=&MyProtocol;
    MyParser.m_ParseExpression(strproto);


    //solve the master equation
    MyRK.m_eps=pow(10.0,double(-8));
    MyRK.m_SetRK5Coefficients();
    MyRK.m_evolve(true);

  }
  catch(string &e)
  {
    cout << "Error: " << e << endl;
  }
  catch(...)
  {
    cout << "Unknown error" << endl;
  }
  return 0;
}
```

8.2.7 How to optimize/profile the code

Optimization is nice and, of course, a goal of its own but most of the time optimization is the death of re-usability of the code. So, after getting the problems physically right, and if one realizes that the performance is too poor to produce publication quality data, one should never start optimizing without using a profiler. For this purpose, one can either use *gprof,* which unfortunately requires compiler options to be set, or if one is working on a Mac, one can use the great built-in profiler from the task manager (the option is called *process analysis*). It gives you a very convenient and fast overview where your code spends most CPU cycles. This way one can sort out the biggest problems first and most efficiently optimize the code. For the simulations used in this thesis, I have gained over a factor of 100, mainly by eliminating memory allocation for the built-in right-hand side terms of the master equation, which now use a lot of caching.

Bibliography

[1] L. DiCarlo, J.M. Chow, J.M. Gambetta, L.S. Bishop, D.I. Schuster, J. Majer, A. Blais, L. Frunzio, S.M. Girvin, and R.J. Schoelkopf. Demonstration of Two-Qubit Algorithms with a Superconducting Quantum Processor. *Arxiv preprint arXiv:0903.2030*, 2009.

[2] L. S. Bishop, J. M. Chow, J. Koch, A. A. Houck, M. H. Devoret, E. Thuneberg, S. M. Girvin, and R. J. Schoelkopf. Nonlinear response of the vacuum Rabi resonance. *Nature Physics*, 5:105–109, February 2009.

[3] DP DiVincenzo and C. Bennet. Quantum information and computation. *Nature*, 404: 247–255, 2000.

[4] I. Chuang and M.Q.C. Nielsen. *Quantum Information*. Cambridge University Press, 2000.

[5] J. Clarke and F. K. Wilhelm. Superconducting quantum bits. *Nature*, 453:1031–1042, June 2008.

[6] P.W. Shor. Polynomial-time algorithms for prime factorization and discrete logarithms on a quantum computer SIAM J. *Comp*, 26(5):1484–1509, 1997.

[7] C. Pomerance. A tale of two sieves. *Biscuits of Number Theory*, page 85, 2008.

[8] L.K. Grover. Quantum mechanics helps in searching for a needle in a haystack. *Physical Review Letters*, 79:325, 1993.

[9] L.K. Grover. A fast quantum mechanical algorithm for database search. In *Proceedings of the twenty-eighth annual ACM symposium on Theory of computing*, pages 212–219. ACM New York, NY, USA, 1996.

[10] D. Deutsch and R. Jozsa. Rapid solution of problems by quantum computation. In *Proceedings of the Royal Society: Mathematical and Physical Sciences (1990-1995)*, volume 439, pages 553–558. The Royal Society, 1992.

[11] DE DiVincenzo and D. Loss. Quantum information is physical. *Superlattices and Microstructures*, 23:419–432, 1998.

[12] N. Schuch and J. Siewert. Natural two-qubit gate for quantum computation using the xy interaction. *Physical Review A*, 67:032301, 2003.

[13] L.M.K. Vandersypen, M. Steffen, G. Breyta, C.S. Yannoni, M.H. Sherwood, and I.L. Chuang. Experimental realization of Shor's quantum factoring algorithm using nuclear magnetic resonance. *Nature*, 414:883–887, 2001.

[14] Chao-Yang Lu, Daniel E. Browne, Tao Yang, and Jian-Wei Pan. Demonstration of a compiled version of shor's quantum factoring algorithm using photonic qubits. *Physical Review Letters*, 99(25):250504, 2007.

[15] B. P. Lanyon, T. J. Weinhold, N. K. Langford, M. Barbieri, D. F. V. James, A. Gilchrist, and A. G. White. Experimental demonstration of a compiled version of shor's algorithm with quantum entanglement. *Physical Review Letters*, 99(25):250505, 2007.

[16] J.J. Vartiainen, A.O. Niskanen, M. Nakahara, and M.M. Salomaa. Implementing Shor's algorithm on Josephson charge qubits. *Physical Review A*, 70:012319, 2004.

[17] A.G. Fowler, S.J. Devitt, and L.C.L. Hollenberg. Implementation of Shor's algorithm on a linear nearest neighbor qubit array. *Quantum Information and Computation*, 4 (4):237–251, 2004.

[18] D. Kielpinski, C. Monroe, and D. J. Wineland. Architecture for a large-scale ion-trap quantum computer. *Nature*, 417:709, 2002.

[19] I. Cirac and P. Zoller. A scalable quantum computer with ions in an array of microtraps. *Nature*, 404:579, 2000.

[20] J. Bardeen, L. N. Cooper, and J. R. Schrieffer. Theory of superconductivity. *Physical Review*, 108(5):1175–1204, 1957.

[21] B.D. Josephson. Possible new effects in superconductive tunneling. *Physics Letters*, 1 (7):251, 1962.

[22] V. Ambegaokar and A. Baratoff. Tunneling between superconductors. *Physical Review Letters*, 10(11):486–489, 1963.

[23] V. Ambegaokar and A. Baratoff. Tunneling between superconductors (errata). *Physical Review Letters*, 11:104, 1963.

[24] P.W. Anderson and J.M. Rowell. Probable Observation of the Josephson Superconducting Tunneling Effect. *Physical Review Letters*, 10(6):230–232, 1963.

[25] F. London. On the problem of the molecular theory of superconductivity. *Physical Review*, 74(5):562–573, 1948.

[26] Y. Aharonov and D. Bohm. Significance of electromagnetic potentials in the quantum theory. *Physical Review*, 115(3):485–491, 1959.

[27] Michael Tinkham. *Introduction to Superconductivity*. McGraw-Hill, New York, 1996.

[28] W.C. Stewart. Current–voltage characteristics of Josephson junctions. *Appl. Phys. Lett*, 12, 1968.

[29] D.E. McCumber. Effect of ac impedance on dc voltage–current characteristics of superconductor weak-link junctions. *J. Appl. Phys*, 39, 1968.

[30] J.M. Martinis, M.H. Devoret, and J. Clarke. Energy-level quantization in the zero-voltage state of a current-biased Josephson junction. *Physical Review Letters*, 55(15): 1543–1546, 1985.

[31] M.H. Devoret, A. Wallraff, and J.M. Martinis. Superconducting qubits: A short review. *Arxiv preprint cond-mat/0411174*, 2004.

[32] B. Yurke and J.S. Denker. Quantum network theory. *Physical Review A*, 29(3):1419–1437, 1984.

[33] M.H. Devoret. Quantum fluctuations in electrical circuits. In *Quantum Fluctuations*, number LXIII in Les Houches Session, page 351, Amsterdam, 1995. Elsevier.

[34] R. W. Simmonds et al. Decoherence in Josephson phase qubits from junction resonators. *Physical Review Letters*, 93:077003, 2004.

[35] A. D. O'Connell et al. Microwave dielectric loss at single photon energies and millikelvin temperatures. *Applied Physics Letters*, 92:112903, 2008.

[36] J.M. Martinis, M.H. Devoret, and J. Clarke. Experimental tests for the quantum behavior of a macroscopic degree of freedom: The phase difference across a Josephson junction. *Physical Review B*, 35(10):4682–4698, 1987.

[37] J.M. Martinis, S. Nam, J. Aumentado, and C. Urbina. Rabi oscillations in a large Josephson-junction qubit. *Physical Review Letters*, 89(11):117901, 2002.

[38] M. Steffen, M. Ansmann, R. McDermott, N. Katz, R.C. Bialczak, E. Lucero, M. Neeley, E. M. Weig, A. N. Cleland, and J. M. Martinis. State tomography of capacitively shunted phase qubits with high fidelity. *Physical Review Letters*, 97(5):050502, 2006.

[39] A.J. Berkley, H. Xu, R.C. Ramos, M.A. Gubrud, F.W. Strauch, P.R. Johnson, J.R. Anderson, A.J. Dragt, C.J. Lobb, and F.C. Wellstood. Entangled macroscopic quantum states in two superconducting qubits. *Science*, 300:1548, 2003.

[40] R. McDermott, R.W. Simmonds, M. Steffen, K.B. Cooper, K. Cicak, K.D. Osborn, S. Oh, D.P. Pappas, and J.M. Martinis. Simultaneous state measurement of coupled Josephson phase qubits. *Science*, 307:1299, 2005.

[41] M.A. Sillanpaa, J.I. Park, and R.W. Simmonds. Coherent quantum state storage and transfer between two phase qubits via a resonant cavity. *Nature*, 449(7161):438–442, 2007.

[42] Yu. Makhlin, G. Schön, and A. Shnirman. Quantum-state engineering with Josephson-junction devices. *Rev. Mod. Phys.*, 73:357, 2001.

[43] J.R. Friedman, V. Patel, W. Chen, S.K. Tolpygo, and J.E. Lukens. Quantum superposition of distinct macroscopic states. *Nature*, 46:43, 2000.

[44] J. E. Mooij, T. P. Orlando, L. Levitov, L. Tian, C. H. van der Wal, and S. Lloyd. Josephson persistent-current qubit. *Science*, 285:1036, 1999.

[45] T. P. Orlando et al. Superconducting persistent current qubit. *Physical Review B*, 60: 15398, 1999.

[46] E. Il'ichev, N. Oukhanski, A. Izmalkov, Th. Wagner, M. Grajcar, H.-G. Meyer, A.Yu. Smirnov, Alec Maassen van den Brink, M.H.S. Amin, and A.M. Zagoskin. Continuous observation of Rabi oscillations in a Josephson flux qubit. *Physical Review Letters*, 91:097906, 2003.

[47] M. Grajcar, A. Izmalkov, E. Il'ichev, Th. Wagner, N. Oukhanski, U. Hübner, T. May, I. Zhilyaev, H. E. Hoenig, Ya. S. Greenberg, V. I. Shnyrkov, D. Born, W. Krech, H.-G. Meyer, Alec Maassen van den Brink, and M. H. S. Amin. Low-frequency measurement of the tunneling amplitude in a flux qubit. *Physical Review B*, 69(6):060501, 2004.

[48] D.A. Ivanov, L.B. Ioffe, V.B. Geshkenbein, and G. Blatter. Interference effects in isolated Josephson junction arrays with geometric symmetries. *Physical Review B*, 65 (2):24509, 2001.

[49] D.A. Ivanov and M.V. Feigel'man. Phonon relaxation of subgap levels in superconducting quantum point contacts. *Journal of Experimental and Theoretical Physics Letters*, 68(11):890–894, 1998.

[50] L. B. Ioffe, V. B. Geshkenbein, M. V. Feigel'man, A. L. Fauchere, and G. Blatter. Environmentally decoupled sds-wave Josephson junctions for quantum computing. *Nature*, 398:679, 1999.

[51] I. Chiorescu, Y. Nakamura, C.J.P.M. Harmans, and J.E. Mooij. Coherent Quantum Dynamics of a Superconducting Flux Qubit. *Science*, 299:1869, 2003.

[52] Y. Yu, D. Nakada, J.C. Lee, B. Singh, D.S. Crankshaw, T.P. Orlando, K.K. Berggren, and W.D. Oliver. Energy relaxation time between macroscopic quantum levels in a superconducting persistent current qubit. *Physical Review Letters*, 92:117904, 2004.

[53] J.C. Lee, W.D. Oliver, T.P. Orlando, and K.K. Berggren. Resonant readout of a persistent current qubit. *IEEE Trans. Appl. Superc.*, 15:841, 2005.

[54] H. Tanaka, S. Saito, H. Nakano, K. Semba, M. Ueda, and H. Takayanagi. Single-shot readout of macroscopic quantum superposition state in a superconducting flux qubit. cond-mat/0407299.

[55] C.H. van der Wal, A.C.J. ter Haar, F.K. Wilhelm, R.N. Schouten, C.J.P.M.Harmans, T.P. Orlando, S. Lloyd, and J.E.Mooij. Quantum superposition of macroscopic persistent-current states. *Science*, 290:773, 2000.

[56] G. Blatter, V.B. Geshkenbein, and L.B. Ioffe. Design aspects of superconducting-phase quantum bits. *Physical Review B*, 63(17):174511, 2001.

[57] J.B. Majer, F.G. Paauw, A.C.J. ter Haar, C.J.P.M. Harmans, and J.E. Mooij. Spectroscopy of coupled flux qubits. *Physical Review Letters*, 94:090501, 2005.

[58] C. H. van der Wal et al. Quantum superposition of macroscopic persistent-current states. *Science*, 290:773, 2000.

[59] C.H. van der Wal. *Quantum Superpositions of Persistent Josephson Currents*. PhD thesis, Technische Universiteit Delft, 2001.

[60] I. Chiorescu et al. Coherent dynamics of a flux qubit coupled to a harmonic oscillator. *Nature*, 431(7005):159–162, 2004.

[61] P. Bertet, I. Chiorescu, K. Semba, C.J.P.M. Harmans, and J.E. Mooij. Detection of a persistent-current qubit by resonant activation. *Physical Review B*, 70:100501(R), 2004.

[62] J.B. Majer, F.G. Paauw, A.C.J. ter Haar, C. Harmans, and J.E. Mooij. Spectroscopy on two coupled superconducting flux qubits. *Physical Review Letters*, 94(9):90501, 2005.

[63] M. Grajcar, A. Izmalkov, S.H.W. van der Ploeg, S. Linzen, E. Il'ichev, T. Wagner, U. Hübner, H.G. Meyer, A. Maassen van den Brink, S. Uchaikin, et al. Direct Josephson coupling between superconducting flux qubits. *Physical Review B*, 72(2):20503, 2005.

[64] S.H.W. van der Ploeg, A. Izmalkov, A.M. van den Brink, U. Hübner, M. Grajcar, E. Il'ichev, H.G. Meyer, and A.M. Zagoskin. Controllable coupling of superconducting flux qubits. *Physical Review Letters*, 98(5):57004, 2007.

[65] J. H. Plantenberg, P. C. de Groot, C. J. P. M. Harmans, and J. E. Mooij. Demonstration of controlled-not quantum gates on a pair of superconducting quantum bits. *Nature*, 447(7146):836–839, 2007.

[66] Markus János Storcz. *Decoherence, encoding and control of coupled solid-state quantum bits*. PhD thesis, Ludwig-Maximilians-Universität München, 2005.

[67] G. Wendin and V.S. Shumeiko. Superconducting quantum circuits, qubits and computing. *Arxiv preprint cond-mat/0508729*, 2005.

[68] J. Johansson, S. Saito, T. Meno, H. Nakano, M. Ueda, K. Semba, and H. Takayanagi. Vacuum Rabi Oscillations in a Macroscopic Superconducting Qubit LC Oscillator System. *Physical Review Letters*, 96(12):127006, 2006.

[69] M. Grajcar et al. Four-qubit device with mixed couplings. *Physical Review Letters*, 96:047006, 2006.

[70] P. Lafarge, P. Joyez, D. Esteve, C. Urbina, and M.H. Devoret. Two-electron quantization of the charge on a superconductor. *Nature*, 365(6445):422–424, 1993.

[71] Y. Nakamura, Yu. A. Pashkin, and J. S. Tsai. Coherent control of macroscopic quantum states in a single-Cooper-pair box. *Nature*, 398:786, 1999.

[72] V. Bouchiat, D. Vion, P. Joyez, D. Esteve, and M. H. Devoret. Quantum Coherence with a Single Cooper Pair. *Physica Scripta*, T76:165, 1998.

[73] Y. Nakamura, Y.A. Pashkin, and J.S. Tsai. Rabi Oscillations in a Josephson-Junction Charge Two-Level System. *Physical Review Letters*, 87:246601, 2001.

[74] Y. Nakamura, Yu. A. Pashkin, T. Yamamoto, and J. S. Tsai. Charge echo in a Cooper-pair box. *Physical Review Letters*, 88:047901, 2002.

[75] M. Büttiker. Zero-current persistent potential drop across small-capacitance Josephson junctions. *Physical Review B*, 36(7):3548–3555, 1987.

[76] M.S. Choi, R. Fazio, J. Siewert, and C. Bruder. Coherent oscillations in a Cooper-pair box. *Europhysics Letters*, 53(2):251–256, 2001.

[77] Y. Nakamura, C. D. Chen, and J. S. Tsai. Spectroscopy of energy-level splitting between two macroscopic quantum states of charge coherently superposed by Josephson coupling. *Physical Review Letters*, 79(12):2328–2331, 1997.

[78] A. Blais, R. S. Huang, A. Wallraff, S. M. Girvin, and R. J. Schoelkopf. Cavity quantum electrodynamics for superconducting electrical circuits: an architecture for quantum computation. *Physical Review A*, 69:062320, 2004.

[79] A. Wallraff, D. I. Schuster, A. Blais, L. Frunzio, R. S. Huang, J. Majer, S. Kumar, S. M. Girvin, and R. J. Schoelkopf. Strong coupling of a single photon to a superconducting qubit using circuit quantum electrodynamics. *Nature*, 431:162, 2004.

[80] J. Koch, T.M. Yu, J. Gambetta, A. A. Houck, D. I. Schuster, J. Majer, A. Blais, M. H. Devoret, S. M. Girvin, and R. J. Schoelkopf. Charge-insensitive qubit design derived from the Cooper pair box. *Physical Review A*, 76(4):042319, 2007.

[81] J.Q. You, X. Hu, S. Ashhab, and F. Nori. Low-decoherence flux qubit. *Physical Review B*, 75(14):140515, 2007.

[82] J. Majer et al. Coupling superconducting qubits via a cavity bus. *Nature*, 449(7161): 443–447, 2007.

[83] J. M. Chow, J. M. Gambetta, L. Tornberg, J. Koch, L. S. Bishop, A. A. Houck, B. R. Johnson, L. Frunzio, S. M. Girvin, and R. J. Schoelkopf. Randomized benchmarking and process tomography for gate errors in a solid-state qubit. *Physical Review Letters*, 102(9):090502, 2009.

[84] J.M. Fink, M. Baur, R. Bianchetti, P.J. Leek, A. Blais, and A. Wallraff. Climbing the Jaynes-Cummings ladder and observing its nonlinearity in a cavity QED system. *Nature*, 454(7202):315, 2008.

[85] S. Filipp, P. Maurer, P. J. Leek, M. Baur, R. Bianchetti, J. M. Fink, M. Göppl, L. Steffen, J. M. Gambetta, A. Blais, and A. Wallraff. Two-Qubit State Tomography using a Joint Dispersive Read-Out. *ArXiv cond-mat/0812.2485*, December 2008.

[86] P. J. Leek, S. Filipp, P. Maurer, M. Baur, R. Bianchetti, J. M. Fink, M. Göppl, L. Steffen, and A. Wallraff. Using Sideband Transitions for Two-Qubit Operations in Superconducting Circuits. *ArXiv cond-mat/0812.2678*, December 2008.

[87] M. Baur, S. Filipp, R. Bianchetti, J. M. Fink, M. Göppl, L. Steffen, P. J. Leek, A. Blais, and A. Wallraff. Measurement of Autler-Townes and Mollow transitions in a strongly driven superconducting qubit. *ArXiv cond-mat/0812.4384*, December 2008.

[88] J.A. Schreier, A.A. Houck, J. Koch, D.I. Schuster, B.R. Johnson, J.M. Chow, J.M. Gambetta, J. Majer, L. Frunzio, M.H. Devoret, et al. Suppressing charge noise decoherence in superconducting charge qubits. *Physical Review B*, 77(18):180502, 2008.

[89] A. A. Houck, J. A. Schreier, B. R. Johnson, J. M. Chow, Jens Koch, J. M. Gambetta, D. I. Schuster, L. Frunzio, M. H. Devoret, S. M. Girvin, and R. J. Schoelkopf. Controlling the spontaneous emission of a superconducting transmon qubit. *Physical Review Letters*, 101(8):080502, 2008.

[90] A. A. Houck, J. Koch, M. H. Devoret, S. M. Girvin, and R. J. Schoelkopf. Life after charge noise: recent results with transmon qubits. *ArXiv cond-mat/0812.1865*, December 2008.

[91] A. Wallraff, D. I. Schuster, A. Blais, J. M. Gambetta, J. Schreier, L. Frunzio, M. H. Devoret, S. M. Girvin, and R. J. Schoelkopf. Sideband Transitions and Two-Tone Spectroscopy of a Superconducting Qubit Strongly Coupled to an On-Chip Cavity. *Physical Review Letters*, 99(5):050501, August 2007.

[92] A. Cottet. *Implementation of a quantum bit in a superconducting circuit.* PhD thesis, Universite Paris 6, Paris, 2002.

[93] E.T. Jaynes and F.W. Cummings. Comparison of quantum and semiclassical radiation theories with application to the beam maser. *Proceedings of the IEEE*, 51(1):89–109, 1963.

[94] J.M. Raimond, M. Brune, and S. Haroche. Manipulating quantum entanglement with atoms and photons in a cavity. *Reviews of Modern Physics*, 73(3):565–582, 2001.

[95] P. Berman. Cavity Quantum Electrodynamics, Advances in Atomic, Molecular and Optical Physics, suppl. 2, 1994.

[96] R.J. Thompson, G. Rempe, and H.J. Kimble. Observation of normal-mode splitting for an atom in an optical cavity. *Physical Review Letters*, 68(8):1132–1135, 1992.

[97] P. Münstermann, T. Fischer, P. Maunz, P.W.H Pinkse, and G. Rempe. Dynamics of single-atom motion observed in a high-finesse cavity. *Physical Review Letters*, 82 (19):3791–3794, 1999.

[98] C.J. Hood, T.W. Lynn, A.C. Doherty, A.S. Parkins, and H.J. Kimble. The atom-cavity microscope: single atoms bound in orbit by single photons. *Science*, 287(5457):1447, 2000.

[99] C. J. Hood, H. J. Kimble, and J. Ye. Characterization of high-finesse mirrors: Loss, phase shifts and mode structure in an optical cavity. *Physical Review A*, 64:033804, 2001.

[100] P. Nussenzveig, F. Bernardot, M. Brune, J. Hare, J.M. Raimond, S. Haroche, and W. Gawlik. Preparation of high-principal-quantum-number "circular" states of rubidium. *Physical Review A*, 48(5):3991–3994, 1993.

[101] G. Rempe, H. Walther, and N. Klein. Observation of quantum collapse and revival in a one-atom maser. *Physical Review Letters*, 58(4):353–356, 1987.

[102] S. Haroche, M. Brune, and J.M. Raimond. Manipulation of optical fields by atomic interferometry: Quantum variations on a theme by Young. *Applied Physics B: Lasers and Optics*, 54(5):355–365, 1992.

[103] M. Brune, F. Schmidt-Kaler, A. Maali, J. Dreyer, E. Hagley, J.M. Raimond, and S. Haroche. Quantum Rabi oscillation: a direct test of field quantization in a cavity. *Physical Review Letters*, 76(11):1800–1803, 1996.

[104] S. Gleyzes, S. Kuhr, C. Guerlin, J. Bernu, S. Deléglise, U. Busk Hoff, M. Brune, J.-M. Raimond, and S. Haroche. Quantum jumps of light recording the birth and death of a photon in a cavity. *Nature*, 446:297–300, March 2007.

[105] V.B. Braginsky, Yu. I. Vorontsov, and F. Ya. Khalili. Kvantovye osobennosti ponderomotornogo izmeritelia electromagnitnoi energii (Quantum particularities of ponderomotive measuring device for electromagnetic energy). *Sov. Phys. JETP*, 73:1340–1343, 1977.

[106] V. B. Braginsky and F. Y. Khalili. *Quantum Measurement*. Cambridge University Press, Cambridge, 1992.

[107] G. Nogues, A. Rauschenbeutel, S. Osnaghi, M. Brune, J.M. Raimond, and S. Haroche. Seeing a single photon without destroying it. *Nature*, 400(6741):239–242, 1999.

[108] C. Monroe, D. M. Meekhof, B. E. King, W. M. Itano, and D. J. Wineland. Demonstration of a fundamental quantum logic gate. *Physical Review Letters*, 75(25):4714–4717, 1995.

[109] A. Rauschenbeutel et al. Coherent operation of a tunable quantum phase gate in cavity QED. *Physical Review Letters*, 83:5166, 1999.

[110] G. Jundt, L. Robledo, A. Hogele, S. Falt, and A. Imamoglu. Observation of dressed excitonic states in a single quantum dot. *Physical Review Letters*, 100(17):177401–177401, 2008.

[111] D. Englund, A. Majumdar, A. Faraon, M. Toishi, N. Stoltz, P. Petroff, and J. Vuckovic. Coherent excitation of a strongly coupled quantum dot - cavity system. *ArXiv cond-mat/0902.2428*, February 2009.

[112] M. Kaniber, A. Neumann, A. Laucht, M. F. Huck, M. Bichler, M.-C. Amann, and J. J. Finley. Efficient and selective cavity-resonant excitation for single photon generation. *New Journal of Physics*, 11(1):013031, January 2009.

[113] B.D. Gerardot, D. Brunner, P.A. Dalgarno, P. Öhberg, S. Seidl, M. Kroner, K. Karrai, N.G. Stoltz, P.M. Petroff, and R.J. Warburton. Optical pumping of a single hole spin in a quantum dot. *Nature*, 451:441, 2008.

[114] A. Laucht, F. Hofbauer, N. Hauke, J. Angele, S. Stobbe, M. Kaniber, G. Böhm, P. Lodahl, M. Amann, and J. Finley. Electrical control of spontaneous emission and strong coupling for a single quantum dot. *New Journal of Physics*, 11(2):023034, February 2009.

[115] I. Fushman, D. Englund, A. Faraon, N. Stoltz, P. Petroff, and J. Vuckovic. Controlled phase shifts with a single quantum dot. *Science*, 320(5877):769, 2008.

[116] P.K. Day, H.G. LeDuc, B.A. Mazin, A. Vayonakis, and J. Zmuidzinas. A broadband superconducting detector suitable for use in large arrays. *Nature*, 425(6960):817–821, 2003.

[117] S.M. Girvin, R.S. Huang, A. Blais, A. Wallraff, and R.J. Schoelkopf. Prospects for Strong Cavity Quantum Electrodynamics with Superconducting Circuits. *eprint arXiv: cond-mat/0310670*, 2003.

[118] J. Q. You and F. Nori. Quantum information processing with superconducting qubits in a microwave field. *Physical Review B*, 68(6):064509, Aug 2003.

[119] O. Astafiev et al. Single artificial-atom lasing. *Nature*, 449:588, 2007.

[120] J. Hauss, A. Fedorov, S. Andre, V Brosco, C. Hutter, R. Kothari, S. Yeshwanth, A. Shnirman, and G. Schön. Dissipation in circuit quantum electrodynamics: Lasing and cooling of a low-frequency oscillator. *New Journal of Physics*, 10(9):095018 (17pp), 2008.

[121] D. I. Schuster et al. Resolving photon number states in a superconducting circuit. *Nature*, 445:515, 2007.

[122] J. Gambetta, A. Blais, D. I. Schuster, A. Wallraff, L. Frunzio, J. Majer, M. H. Devoret, S. M. Girvin, and R. J. Schoelkopf. Qubit-photon interactions in a cavity: Measurement-induced dephasing and number splitting. *Physical Review A*, 74(4): 042318, October 2006.

[123] A. A. Houck, D. I. Schuster, J. M. Gambetta, J. A. Schreier, B. R. Johnson, J. M. Chow, L. Frunzio, J. Majer, M. H. Devoret, S. M. Girvin, and R. J. Schoelkopf. Generating single microwave photons in a circuit. *Nature*, 449(7160):328–331, 2007.

[124] F. Helmer, M. Mariantoni, A.G. Fowler, J. von Delft, E. Solano, and F. Marquardt. Two-dimensional cavity grid for scalable quantum computation with superconducting circuits. *Europhysics Letters*, 85(5), 03 2009.

[125] J.M. Fink, R. Bianchetti, M. Baur, M. Göppl, L. Steffen, S. Filipp, P.J. Leek, A. Blais, and A. Wallraff. Collective Qubit States and the Tavis-Cummings Model in Circuit QED. *arxiv.org/cond-mat*, 0812.2651v1, 2008.

[126] J. Siewert and R. Fazio. Implementation of the Deutsch-Jozsa algorithm with Josephson charge qubits. *Journal of Modern Optics*, 49(8):1245–1254, 2002.

[127] M. Tavis and F.W. Cummings. Exact solution for an N-molecule-radiation-field Hamiltonian. *Physical Review*, 170(2):379–384, 1968.

[128] W.E. Lamb and R.C. Retherford. Fine structure of the hydrogen atom by a microwave method. *Physical Review*, 72(3):241–243, 1947.

[129] H.A. Bethe. The electromagnetic shift of energy levels. *Physical Review*, 72:339, 1947.

[130] A. Fragner, M. Goppl, J.M. Fink, M. Baur, R. Bianchetti, P.J. Leek, A. Blais, and A. Wallraff. Resolving Vacuum Fluctuations in an Electrical Circuit by Measuring the Lamb Shift. *Science*, 322(5906):1357, 2008.

[131] T. Lindstrom, C.H. Webster, J.E. Healey, M.S. Colclough, C.M. Muirhead, and A.Y. Tzalenchuk. Circuit QED with a flux qubit strongly coupled to a coplanar transmission line resonator. *Superconductor Science and Technology*, 20(8):814–821, 2007.

[132] F. Deppe, M. Mariantoni, E.P. Menzel, A. Marx, S. Saito, K. Kakuyanagi, H. Tanaka, T. Meno, K. Semba, H. Takayanagi, et al. Two-photon probe of the Jaynes–Cummings model and controlled symmetry breaking in circuit QED. *Nature Physics*, 4(9):686, 2008.

[133] John M. Martinis, K. B. Cooper, R. McDermott, Matthias Steffen, Markus Ansmann, K. D. Osborn, K. Cicak, Seongshik Oh, D. P. Pappas, R. W. Simmonds, and Clare C. Yu. Decoherence in Josephson Qubits from Dielectric Loss. *Physical Review Letters*, 95(21):210503, Nov 2005.

[134] M. Steffen et al. Measurement of the entanglement of two superconducting qubits via state tomography. *Science*, 313:1423, 2006.

[135] E. Lucero, M. Hofheinz, M. Ansmann, R.C. Bialczak, N. Katz, M. Neeley, A.D. O'Connell, H. Wang, A.N. Cleland, and J.M. Martinis. High-fidelity gates in a Josephson qubit. *Physical Review Letters*, 100:247001, 06 2008.

[136] M. Hofheinz, E.M. Weig, M. Ansmann, R.C. Bialczak, E. Lucero, M. Neeley, H. Wang, J.M. Martinis, and A.N. Cleland. Generation of Fock states in a superconducting quantum circuit. *Nature*, 454(7202):310, 2008.

[137] H. Wang, M. Hofheinz, M. Ansmann, RC Bialczak, E. Lucero, M. Neeley, AD O'Connell, D. Sank, J. Wenner, A.N. Cleland, et al. Measurement of the decay of Fock states in a superconducting quantum circuit. *Physical Review Letters*, 101 (24):240401, 2008.

[138] D. Vion et al. Manipulating the quantum state of an electrical circuit. *Science*, 296: 886, 2002.

[139] J. M. Martinis, S. Nam, J. Aumentado, and C. Urbina. Rabi oscillations in a large Josephson-junction qubit. *Physical Review Letters*, 89:117901, 2002.

[140] T. Hime et al. Solid-state qubits with current-controlled coupling. *Science*, 314:1427, 2006.

[141] A. O. Niskanen, K. Harrabi, F. Yoshihara, Y. Nakamura, S. Lloyd, and J. S. Tsai. Quantum coherent tunable coupling of superconducting qubits. *Science*, 316:723, 2007.

[142] F Marquardt and C. Bruder. Superposition of two mesoscopically distinct quantum states: Coupling a Cooper-pair box to a large superconducting island. *Physical Review B*, 63:054514, 2001.

[143] O. Buisson and F. Hekking. *in: Macroscopic Quantum Coherence and Quantum Computing (eds. D. V. Averin and B. Ruggiero and P. Silvestrini)*. Kluwer, New York, 2001.

[144] A. Wallraff et al. Approaching unit visibility for control of a superconducting qubit with dispersive readout. *Physical Review Letters*, 95:060501, 2005.

[145] M. Wallquist, V. S. Shumeiko, and G. Wendin. Selective coupling of superconducting qubits via tunable stripline cavity. *Physical Review B*, 74:224506, 2006.

[146] D. Jaksch, H.-J. Briegel, J. I. Cirac, C. W. Gardiner, and P. Zoller. Entanglement of atoms via cold controlled collisions. *Physical Review Letters*, 82:1975, 1999.

[147] J. M. Taylor et al. Fault-tolerant architecture for quantum computation using electrically controlled semiconductor spins. *Nature Physics*, 1:177, 2005.

[148] M. Wallquist, J. Lantz, V. S. Shumeiko, and G. Wendin. Superconducting qubit network with controllable nearest-neighbour coupling. *New Journal of Physics*, 7(1):178, August 2005. ISSN 1367-2630.

[149] A. Imamoğlu et al. Quantum information processing using quantum dot spins and cavity QED. *Physical Review Letters*, 83:4204, 1999.

[150] S. Osnaghi et al. Coherent control of an atomic collision in a cavity. *Physical Review Letters*, 87:037902, 2001.

[151] A. Blais et al. Quantum-information processing with circuit quantum electrodynamics. *Physical Review A*, 75(3):032329, March 2007.

[152] A. Gilchrist, N. K. Langford, and M. A. Nielsen. Distance measures to compare real and ideal quantum processes. *Physical Review A*, 71:062310, 2005.

[153] M. J. Storcz, M. Mariantoni, et al. Orthogonally-driven superconducting qubit in circuit QED. *cond-mat/0612226*, 2006.

[154] M. Mariantoni, F. Deppe, A. Marx, R. Gross, F. K. Wilhelm, and E. Solano. Two-resonator circuit qed: A superconducting quantum switch. *Physical Review B*, Sep 2008.

[155] A. Steane. Multiple particle interference and quantum error correction. *Proc. Royal Society A*, 452:2551, 1996.

[156] D. P. DiVincenzo and P. Aliferis. Effective fault-tolerant quantum computation with slow measurements. *Physical Review Letters*, 98(020501), 2007.

[157] A. M. Stephens, A. G. Fowler, and L. C. L. Hollenberg. Universal fault tolerant quantum computation on bilinear nearest neighbor arrays. *Quant. Inf. Comp.*, 8:330, 2008.

[158] A. G. Fowler et al. Long-range coupling and scalable architecture for superconducting flux qubits. *Physical Review B*, 76:174507, 2007.

[159] Geraldine Haack. Faster gates for quantum computing and simulation in circuit QED. Master's thesis, Ludwig-Maximilians-Universität München, 2008.

[160] P. Rebentrost and F.K. Wilhelm. Optimal control of a leaking qubit. *Physical Review B*, 79:060507, 2009.

[161] N. Khaneja, T. Reiss, C. Kehlet, T. Schulte-Herbrüggen, and S.J. Glaser. Optimal control of coupled spin dynamics: design of NMR pulse sequences by gradient ascent algorithms. *Journal of Magnetic Resonance*, 172(2):296–305, 2005.

[162] T. Schulte-Herbrüggen, A. Spörl, N. Khaneja, and S.J. Glaser. Optimal Control-Based Efficient Synthesis of Building Blocks of Quantum Algorithms Seen in Perspective from Network Complexity towards Time Complexity. *Physical Review A*, 72 (042331/1):7, 2005.

[163] L.S. Pontryagin, V.G. Boltyanskii, R.V. Gamkrelidze, and E.F. Mishchenko. The Mathematical Theory of Optimal Processes. Fizmatgiz, Moscow. *English translation: Pergamon Press, New York*, 1964.

[164] A.G. Butkovskii and I.U.I. Samoilenko. *Control of quantum-mechanical processes and systems*. Kluwer Academic, Dordrecht, 1990.

[165] Navin Khaneja, Roger Brockett, and Steffen J. Glaser. Time optimal control in spin systems. *Physical Review A*, 63(3):032308, Feb 2001.

[166] V. B. Braginskii, I. I. Vorontsov, and K. S. Thorne. Quantum nondemolition measurements. *Science*, 209:547–557, 1980.

[167] T.A. Brun. A simple model of quantum trajectories. *American Journal of Physics*, 70: 719, 2002.

[168] H. M. Wiseman and G. J. Milburn. Quantum theory of field-quadrature measurements. *Physical Review A*, 47(1):642–662, Jan 1993.

[169] Ferdinand Helmer and Florian Marquardt. Measurement-based synthesis of multi-qubit entangled states in superconducting cavity QED. *Physical Review A*, 79(5), 2009.

[170] H. Mabuchi and A. C. Doherty. Cavity quantum electrodynamics: Coherence in context. *Science*, 298:1372, 2002.

[171] D. I. Schuster et al. ac stark shift and dephasing of a superconducting qubit strongly coupled to a cavity field. *Physical Review Letters*, 94:123602, 2005.

[172] P.J. Leek, J.M. Fink, A. Blais, R. Bianchetti, M. Goppl, J.M. Gambetta, D.I. Schuster, L. Frunzio, R.J. Schoelkopf, and A. Wallraff. Observation of Berry's phase in a solid-state qubit. *Science*, 318(5858):1889, 2007.

[173] F. Helmer, M. Mariantoni, E. Solano, and F. Marquardt. Quantum nondemolition photon detection in circuit qed and the quantum zeno effect. *Physical Review A*, 79 (5), 2009.

[174] M. Sarovar, H.S. Goan, T.P. Spiller, and G.J. Milburn. High-fidelity measurement and quantum feedback control in circuit qed. *Physical Review A*, 72(6):62327, 2005.

[175] C. L. Hutchison, J. M. Gambetta, A. Blais, and F. K. Wilhelm. Quantum trajectory equation for multiple qubits in circuit QED: Generating entanglement by measurement. *ArXiv cond-mat/0812.0218*, December 2008.

[176] D.A. Rodrigues, C.E.A. Jarvis, B.L. Gyorffy, T.P. Spiller, and J.F. Annett. Entanglement of superconducting charge qubits by homodyne measurement. *Journal of Physics of Condensed Matter*, 20(7):75211, 2008.

[177] J. Lantz, M. Wallquist, V.S. Shumeiko, and G. Wendin. Josephson junction qubit network with current-controlled interaction. *Physical Review B*, 70(14):140507, 2004.

[178] L.F. Wei, Y. Liu, and F. Nori. Generation and control of Greenberger-Horne-Zeilinger entanglement in superconducting circuits. *Physical Review Letters*, 96(24):246803, 2006.

[179] M. Steffen, M. Ansmann, R.C. Bialczak, N. Katz, E. Lucero, R. McDermott, M. Neeley, E.M. Weig, A.N. Cleland, and J.M. Martinis. Measurement of the entanglement of two superconducting qubits via state tomography. *Science*, 313(5792):1423–1425, 2006.

[180] K. Maruyama, T. Iitaka, and F. Nori. Enhancement of entanglement transfer in a spin chain by phase-shift control. *Physical Review A*, 75(1):12325, 2007.

[181] J.Q. You, X. Wang, T. Tanamoto, and F. Nori. Efficient one-step generation of large cluster states with solid-state circuits. *Physical Review A*, 75(5):52319, 2007.

[182] Howard M. Wiseman. *Quantum Trajectories and Feedback.* PhD thesis, University of Queensland, Brisbane, 1994.

[183] D. H. Santamore, A. C. Doherty, and M. C. Cross. Quantum nondemolition measurement of Fock states of mesoscopic mechanical oscillators. *Physical Review B*, 70: 144301, 2004.

[184] B. Misra and E. C. G. Sudarshan. Zeno's paradox in quantum theory. Technical report, July 1976.

[185] M. Mariantoni et al. On-chip microwave Fock states and quantum homodyne measurements. *Arxiv preprint cond-mat/0509737*, 2005.

[186] F. Marquardt. Efficient on-chip source of microwave photon pairs in superconducting circuit QED. *Physical Review B*, 76:205416, 2007.

[187] F. Mallet et al. (priv. comm.), 2008.

[188] E. Buks, R. Schuster, M. Heiblum, D. Mahalu, and V. Umansky. Dephasing in electron interference by a "which-path" detector. *Nature*, 391:871, 1998.

[189] J. D. Thompson et al. Strong dispersive coupling of a high-finesse cavity to a micromechanical membrane. *Nature*, 452:72–75, March 2008.

[190] J. Gambetta, W.A. Braff, A. Wallraff, S.M. Girvin, and R.J. Schoelkopf. Protocols for optimal readout of qubits using a continuous quantum nondemolition measurement. *Physical Review A*, 76(1):12325, 2007.

[191] J. Gambetta et al. Quantum trajectory approach to circuit QED: Quantum jumps and the Zeno effect. *Physical Review A*, 77(1):012112, January 2008.

[192] J. I. Cirac, R. Blatt, A. S. Parkins, and P. Zoller. Preparation of Fock states by observation of quantum jumps in an ion trap. *Physical Review Letters*, 70:762–765, February 1993.

[193] W. Nagourney, J. Sandberg, and H. Dehmelt. Shelved optical electron amplifier - Observation of quantum jumps. *Physical Review Letters*, 56:2797–2799, June 1986.

[194] M. Porrati and S. Putterman. Wave-function collapse due to null measurements: The origin of intermittent atomic fluorescence. *Physical Review A*, 36(2):929–932, 1987.

[195] S. Peil and G. Gabrielse. Observing the Quantum Limit of an Electron Cyclotron: QND Measurements of Quantum Jumps between Fock States. *Physical Review Letters*, 83:1287–1290, August 1999.

[196] W. M. Itano, D. J. Heinzen, J. J. Bollinger, and D. J. Wineland. Quantum Zeno effect. *Physical Review A*, 41:2295–2300, March 1990.

[197] K. Jacobs, P. Lougovski, and M. Blencowe. Continuous measurement of the energy eigenstates of a nanomechanical resonator without a nondemolition probe. *Physical Review Letters*, 98(14):147201, 2007.

[198] R. Rossi Jr, M.C. Nemes, and A.R.B. de Magalhaes. Quantum Zeno effect in cavity qed: Experimental proposal with non ideal cavities and detectors. *eprint arXiv: 0710.0275*, 2007.

[199] J.A. Damborenea, I.L. Egusquiza, G.C. Hegerfeldt, and J.G. Muga. Measurement-based approach to quantum arrival times. *Physical Review A*, 66(5):52104, 2002.

[200] X.B. Wang, J. Q. You, and F. Nori. Deterministic generation of large cluster states using non-deterministic collective measurements based on quantum Zeno effect. *ArXiv preprint quant-ph/0701007*, January 2007.

[201] N. Imoto, HA Haus, and Y. Yamamoto. Quantum nondemolition measurement of the photon number via the optical Kerr effect. *Physical Review A*, 32(4):2287–2292, 1985.

[202] P. Yeh. Exact solution of a nonlinear model of two-wave mixing in Kerr media. *J. Opt. Soc. Am. B*, 3:747, 1986.

[203] H.A. Bachor, M.D. Levenson, D.F. Walls, S.H. Perlmutter, and R.M. Shelby. Quantum nondemolition measurements in an optical-fiber ring resonator. *Physical Review A*, 38 (1):180–190, 1988.

[204] A. Barchielli. Measurement theory and stochastic differential equations in quantum mechanics. *Physical Review A*, 34:1642–1649, September 1986.

[205] H. Carmichael. *An Open Systems Approach to Quantum Optics*. Number 18 in Springer Lecture Notes Monographs Series. Springer-Verlag, Berlin, Heidelberg, 1993.

[206] D. F. Walls and G. J. Milburn. *Quantum optics*. Springer, Berlin, 1995.

[207] H.M. Wiseman and G.J. Milburn. Squeezing via feedback. *Physical Review A*, 49(2): 1350–1366, 1994.

[208] AC Doherty and K. Jacobs. Feedback control of quantum systems using continuous state estimation. *Physical Review A*, 60(4):2700–2711, 1999.

[209] Deborah H. Santamore. *Quantum transport and dynamics of phonons in mesoscopic systems*. PhD thesis, California Institute of Technology, Pasadena, CA, USA, 2003.

[210] Howard M. Wiseman and J. M. Gambetta. Pure-state quantum trajectories for general non-Markovian systems do not exist. *Physical Review Letters*, 101(14), 2008.

[211] Sze M. Tan. Quantum optics and computation toolbox for matlab. `http://www.qo.phy.auckland.ac.nz/qotoolbox.html`, 2002.

[212] Ferdinand Helmer. A framework to efficiently simulate deterministic and stochastic master equations - technical reference. Technical report, Ludwig-Maximilians-Universität München, 03 2009.

Acknowledgements

I want to express my deep gratitude to my advisor Florian Marquardt, who with his insight and extraordinary expertise has guided me through this thesis. Countless times he motivated me to settle not for 'almost understood' but to go all the way to really understand the subject matter. Numerous discussions with Jan von Delft, Michael Möckel and Miles P. Blencowe have inspired me through the whole process.

I want to thank the LMU, CeNS, NIM, the Arnold-Sommerfeld-Center for Theoretical Physics and the SFB 631, project A2, for their financial and infrastructural support which made it possible to travel to conferences, meet the most productive experimentalists and theorists in the field and thus establish and keep contact with the community.

Looking back on the last three years, I must not forget to mention the superb support by the Institute Prof. Dr. E. Neuburger & Partner, a finance mathematics company for which I have been working since I started studying. They showed the utmost understanding towards my academic work - not to mention offering me a great perspective for the years to come.

Last but not least the everlasting and constant support of my parents has made my studies and this thesis possible. Moreover, the tedious proof-reading was done to a large degree by my dear father.

Finally and most importantly I want to thank my wife Anna for her patient and true support. I realize that being in academia, and especially writing a thesis, puts private life and relationships to a hard test. I cannot thank my friends and especially my wife enough for putting up with this for so long.

Franz Ferdinand Helmer

Curriculum Vitae

Personal Data

Date of birth	12.5.1980 in Munich, Germany
Family status	married
Citizenship	German

Education

01/2006-07/2009	PhD at the chair for theoretical solid state physics of Prof. Dr. Jan von Delft at the LMU, Munich. Advisor: Dr. Florian Marquardt
11/2005	Diploma in physics from LMU Munich
09/2003–07/2004	Master of Science at Dartmouth College, NH, USA, supported by a Fulbright-scholarship and a Dartmouth fellowship
04/2002	Pre-diploma in physics, grade „Sehr gut“
10/2000–11/2005	Diploma studies in physics and philosophy at LMU Munich
09/1999	High School “Abitur”, grade 1.2
09/1990–06/1999	Attending the Maximiliansgymnasium in Munich
09/1986–06/1990	Attending primary school in Munich (Grundschule an der Wilhelmstrasse)

FRANZ FERDINAND HELMER

EXPERIENCE

since 06/2006	Associate at Institute Prof. Neuburger & Partner, Munich
08/2001–10/2001	Scientific assistant at the pellet laboratory at the ASDEX Upgrade fusion reactor experiment at Max-Planck-Institute for plasma physics, Garching near Munich
09/2000–10/2000	Internship at the ASDEX Upgrade experiment at the Max-Planck-Institute for plasma physics, Garching near Munich
06/2000–06/2006	Analyst at Institute Prof. Neuburger & Partner, Munich
09/1999–07/2000	Alternative service at the 'Club of the Handicapped and their Friends' (Club Behinderter und ihrer Freunde), Munich

LANGUAGES

German	native tongue
Englisch	fluent
Spanish	basic knowlegde
French	basic knowledge
Latin	Latinum
Ancient Greek	Graecum

Munich, 18.05.2009